Bearing capacity of perforated offshore foundations under combined loading

Laith Tapper

Worcester College
University of Oxford

A thesis submitted for the degree of

Doctor of Philosophy

Trinity Term, 2013

Abstract

Bearing capacity of perforated offshore foundations under combined loading

A thesis submitted for the degree of Doctor of Philosophy

Laith Tapper
Worcester College, Oxford
Trinity Term, 2013

This thesis presents experimental work and numerical analysis that has been undertaken to assess the bearing capacity of perforated offshore foundations. Perforated foundations may be used to support subsea infrastructure, including as mudmats into which a number of perforations have been made, or as grillages which consist of a series of structurally connected strip footings. Larger gravity base foundations, such as for offshore wind turbines or oil and gas platforms, may adopt a single central perforation. The advantages of using perforated foundations can include reduced material requirements and easier offshore handling as a result of smaller weight and lower hydrodynamic forces during deployment. Limited guidance currently exists for assessing the bearing capacity of these foundation types.

Bearing capacity of perforated foundations has been examined in this thesis under conditions of combined vertical, horizontal and moment loading which is typical in offshore settings. Undrained soil conditions have been considered, except for the case of grillages in which drained conditions are often most relevant. Experimental work has included centrifuge testing of ring and square annular foundations on clay, and 1g testing of grillage foundations on sand. Finite element modelling has also been undertaken to assess perforated foundation capacity. A Tresca material subroutine (UMAT) and an adaptive meshing scheme have been developed to improve the accuracy of the finite element analysis carried out.

The results showed that perforated foundations can be an efficient foundation solution for accommodating combined loading. As a ratio of their vertical load capacity, perforated foundations may be able to withstand higher moment and horizontal loads compared with unperforated foundations. The experimental and numerical results have been used to develop design expressions that could be employed by practitioners to estimate the vertical and combined load bearing capacity of these foundation types.

Acknowledgements

I would like to thank my supervisors Prof. Byron Byrne and Prof. Chris Martin for their invaluable guidance and patient advice throughout the course of this research. Thanks also to Prof. Barry Lehane at the University of Western Australia for his support and advice with the centrifuge work undertaken in this thesis.

The friendship and advice I received from my fellow Room 11 students in the Civil Engineering Research Group is gratefully appreciated. Thanks also to my friends at Worcester College for their enjoyable company and friendship over the last few years.

Finally I would like to express my thanks to my family for all the support they have given me.

Notation

Nomenclature used in this thesis (excluding those which only appear once):

A	contact foundation area
a	yield plane gradient
A_i	foundation void area
A_o	gross foundation area
B	foundation width
b	plastic potential gradient
B^*	effective strip width
B'	effective foundation width
c_v	coefficient of consolidation
d	depth of foundation base below soil surface
D	foundation diameter
D	elastic constitutive matrix
d_c, d_q, d_γ	depth factors
D^{ep}	elasto-plastic constitutive matrix
D^{epc}	consistent elasto-plastic constitutive matrix
e	eccentricity of foundation load
E	Young's modulus
e_1, e_2, $\bar{e}$	yield surface fitting parameters
f	yield function
g	plastic potential function
H	horizontal load
h	grille height
H_0	maximum horizontal load capacity
h_0	normalised horizontal capacity
i_c, i_q, i_γ	inclination factors
k	rate of s_u increase with depth
L	foundation length
M	moment load
M_0	maximum moment load capacity
m_0	normalised moment capacity
N	number of cycles
N_c, N_q, N_γ	bearing capacity factors

$N_{T\text{-}bar}$	T-bar bearing capacity factor
Q	Torsion load
q	surcharge
q_u	ultimate bearing capacity
R	perforation ratio
s	grille spacing
s_c, s_q, s_γ	shape factors
s_u	undrained shear strength
s_{u0}	s_u at base of embedded foundation level
s_{um}	s_u at surface (mudline) level
t	grille width
V	vertical load
V_0	maximum vertical load capacity
V_{max}	maximum vertical bearing capacity
z	vertical depth
α	Soil adhesion factor
β_1, β_2, $\bar{\beta}$	shaping factors for yield surface
γ'	submerged unit weight
ε	strain
ε^e	elastic strain
ε^p	plastic strain
λ	plastic multiplier
σ	normal stress
σ_1, σ_2, σ_3	principal stresses
σ^A, σ^B, σ^C	return mapping stresses
σ^e	elastic stress
σ^p	plastic stress
σ_x, σ_y, σ_z	normal stresses
τ_{xy}, τ_{xz}, τ_{yz}	shear stresses
ϕ	friction angle
ϕ'_{cs}	critical state friction angle
θ	rotation
ν	Poisson's ratio

Contents

Chapter 1. Introduction

The continual drive to improve the cost effectiveness and functionality of offshore foundations has meant that a diverse range of foundation types has emerged for use offshore. To accommodate challenges posed by the offshore environment, these foundation types are often less conventional in arrangement compared to onshore foundations (such as suction caissons for example) and have required rigorous investigation to properly understand their performance in offshore conditions.

Perforated shallow foundations are one such group of less conventional foundations that find application in offshore settings. The term ‘perforated foundation’ has been used to describe foundations that have voids within the plan foundation area. In particular, attention has been given in this thesis to the perforated foundation types of i) ring foundations, ii) square annular foundations, iii) perforated mudmats and iv) grillages as illustrated in Figure 1.1.

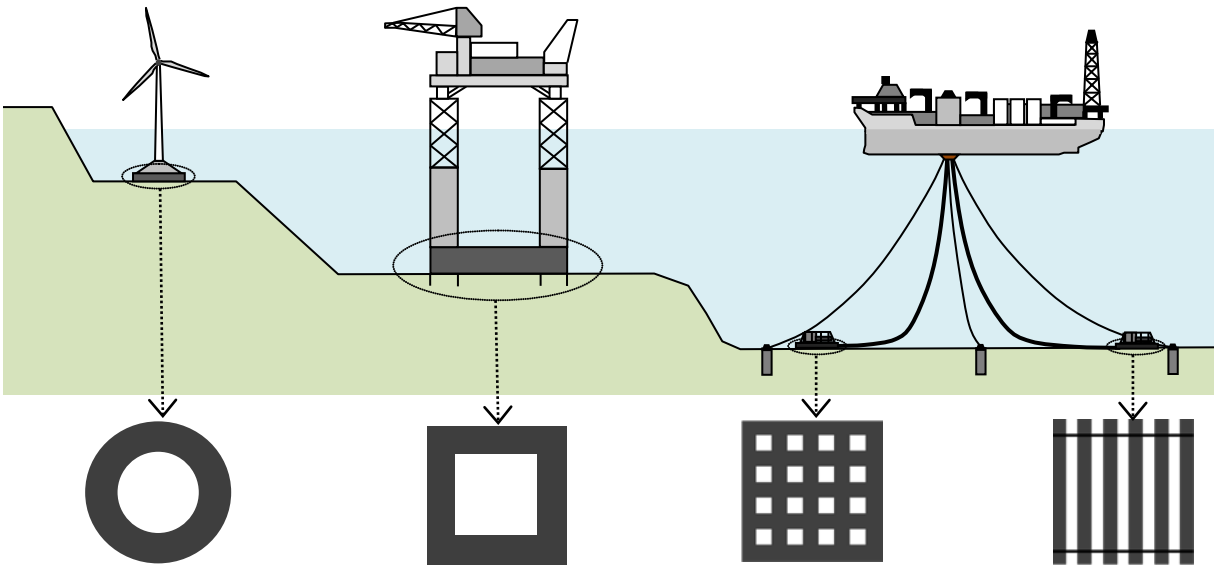

Figure 1.1: Offshore applications of perforated foundations

Quantifying bearing capacity is a key component of foundation design as it defines how much load the foundation can support before the soil beneath it will fail. There is no generally accepted method for assessing the bearing capacity of perforated foundations and limited published research is available to provide guidance for designers. As a result, conservative design approaches may be adopted leading to higher project costs.

This thesis presents numerical analysis and experimental work that has been undertaken to better understand the bearing capacity of perforated foundations when subject to the combined vertical, horizontal and moment loading that is typically applied in offshore conditions. Finite element modelling of perforated foundations has been undertaken in which a Tresca material subroutine (UMAT) and adaptive meshing has been implemented to improve the accuracy of the analysis. Perforated foundations have also been modelled experimentally using centrifuge and 1g testing. Undrained soil conditions have been considered, except for the case of grillages in which drained conditions are most applicable. The results have been used to develop design guidelines to assist practitioners achieve more efficient designs for these types of foundations.

1.1 Perforated foundations

1.1.1 Description

Perforated foundations, which can be described as foundations with void spaces, are increasingly finding application in offshore settings. A common use for perforated foundations is to support subsea infrastructure including pipeline end manifolds (PLEMs) and terminations (PLETs). These can take the form of mudmats in which a series of perforations have been made (Figure 1.1(iii)), or grillages which consist of a series of structurally connected strip footings (Figure 1.1(iv)). Perforated foundations are also a practical design solution for larger gravity base foundations such as for offshore wind turbines or oil and gas platforms. These foundations often comprise a single central perforation resulting in a ring or

annular type foundation (Figure 1.1(i) & (ii)). It may be the case that these foundations are skirted with vertical plates penetrating into the seabed to achieve additional bearing capacity.

The motivation for designers to adopt perforated foundations is to take advantage of benefits that can exist over solid foundations. These can include reduced material requirements and easier offshore handling due to less weight and lower hydrodynamic forces during deployment. The uplift resistance can also be reduced by perforations, which affords a sustainability advantage of easier foundation retrieval for re-use or to enable material recycling.

1.1.2 Perforation ratio

It is useful to characterise perforated foundations in terms of their perforation ratio, R (the notation R is adopted to be consistent with previous studies (Martin and Hazell, 2005, White et al., 2005)). This ratio relates the area of the void space A_i to the gross foundation area A_o as follows:

$$R = \frac{A_i}{A_o} \tag{1.1}$$

A perforation ratio of R = 0 represents a solid foundation with no void, whilst as R approaches 1 the void area becomes largest. The void area subtracted from the gross area gives the foundation contact area, A (Figure 1.2).

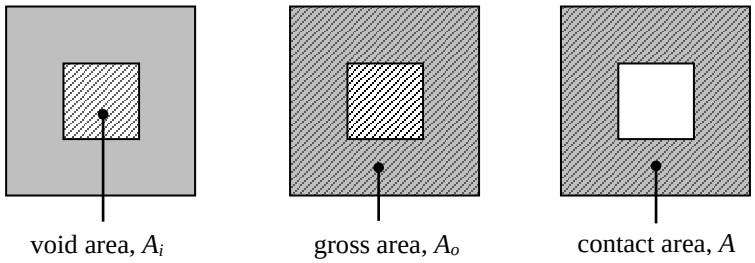

Figure 1.2: Area definitions for perforated foundations

The perforation ratio R of foundations used offshore may vary depending on the functional requirements and loading conditions of the foundation (Figure 1.3). Foundations

for larger infrastructure might be expected to have lower values of *R*, whilst smaller foundations such as grillages and perforated mudmats may be more likely to have larger values of *R*. However this can depend on the nature of the loading conditions the foundation will be subject to and soil conditions present at the foundation location.

Yolla Platform	Maari Platform	MCR-A Platform	Atlas CTB wind turbine*	Concept Platform	Subsea frame with grillage
	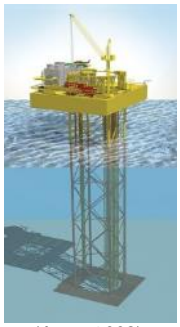	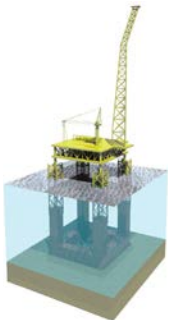			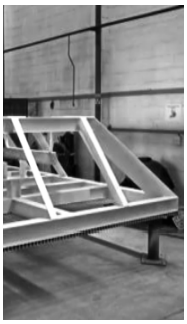
(Watson and Humpheson, 2007)	(Arup, 2009)	(Pinna et al., 2009)	(Tindall, 2013) *Design for onshore	(Arup and Clough, 2008)	(Bransby et al., 2012)
R = 0	*R* = 0.27	*R* = 0.40	*R* = 0.42	*R* = 0.64	*R* = 0.75
		Increasing *R* →			

Figure 1.3: Examples of perforation ratios (*R*) for perforated foundations

1.1.3 Loading conditions

Foundations must be designed to withstand applied loads without experiencing bearing failure. Foundations must also provide adequate stiffness to meet serviceability requirements, although this aspect is not a focus of this thesis. The offshore environment can subject foundations to arduous loading conditions, primarily as a result of waves, wind and currents (Figure 1.4(a)). In addition to the structural self weight, other loads may need to be withstood, for example thermally-induced axial loads in the case of pipeline subsea foundations. It is convenient for design to resolve the loads acting on the structure to a single reference point on the foundation. The applied loads may be two dimensional, or can be simplified as acting in-plane. This enables a more straightforward plane strain assessment as shown in Figure 1.4(b). However, significant loading acting in three dimensions may be imposed on the foundation, leading to the application of vertical (*V*), horizontal (*H*), moment

(*M*) and torsional (*Q*) loads as represented in Figure 1.4(c). In addition, applied loads may be cyclic in nature which can add further complexity (see for example Andersen (2009)). Understanding the response of perforated foundations under two dimensional and three dimensional loading is therefore an important consideration.

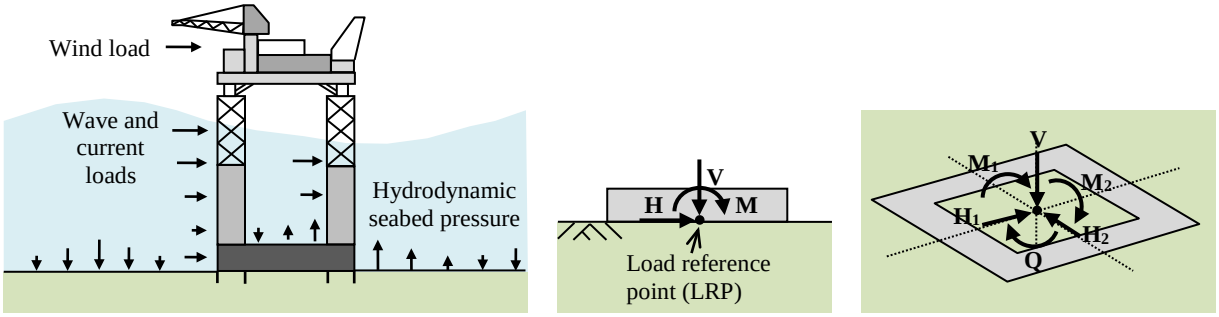

(a) Environmental load components (b) 2D loading (c) 3D loading

Figure 1.4: In-plane and three dimensional loading on offshore structures

1.1.4 Soil conditions

For the assessment of bearing capacity, it is necessary to distinguish whether the seabed soil being loaded by the foundation behaves in a drained or an undrained manner. The drainage state of the soil can depend on factors such as the soil permeability, the rate of which the load is applied, and the length of the drainage path. Clays and silts have low permeability and so are typically associated with undrained conditions. Sands and gravels on the other hand have high permeability and so are often associated with drained conditions. Bearing capacity is assessed differently depending if drained or undrained conditions are present. In undrained conditions it is convenient to use stress-strain behaviour defined in terms of total stress whilst in drained conditions it is defined in terms of effective stress.

In this thesis the bearing capacity of perforated foundations has been primarily assessed under the assumption of undrained conditions. This is appropriate as clay ground conditions are commonly present offshore. In addition, where sand conditions are present it can still be applicable for an undrained bearing capacity assessment to be undertaken. This is because

environmental loading periods can result in the rate of loading being too rapid to allow any significant outflow of pore water, particularly for larger foundations with long drainage paths. In this instance undrained conditions are generated.

The bearing capacity analysis of grillage foundations however has been assessed under drained conditions. Grillage foundations rely upon enhanced bearing capacity due to interference effects that occur more substantially in frictional soil such as sand. The regularly spaced voids between grilles also mean that very short drainage paths are present. Drained conditions are therefore often relevant for this type of perforated foundation. A more detailed description of grillage foundations is given in Section 2.3.2.

1.1.5 Current design approaches and limitations

The bearing capacity of shallow foundations under vertical loads is commonly assessed using a modified version of the classical Terzaghi bearing capacity equation (see Equation 2.1). Combined loading is typically addressed by including load inclination factors to account for the effects of horizontal loading, and the effective width principle to incorporate moment loading. Offshore foundation design codes adopt this classical approach, but it has not always been found to provide an accurate assessment of foundation capacity, particularly under combined loading. This is illustrated in Figure 1.5 which shows typical experimental results for a shallow foundation in undrained and drained conditions when loaded to failure under different combinations of horizontal and moment load. The failure loads calculated from a classical bearing capacity solution are also included in this figure and are seen to provide a poor match with the elliptical trend of experimental results. An alternative approach is to consider bearing capacity within a three dimensional V:H:M load space by defining the envelope of the failure surface directly in this space. The failure envelope approach can be used to provide a better match with observed combined load capacity results as shown in Figure 1.5. It also allows a physically meaningful factor of safety against bearing failure

under different loading paths to be visualised. A more detailed discussion on assessing shallow foundation bearing capacity is provided in Chapter 2.

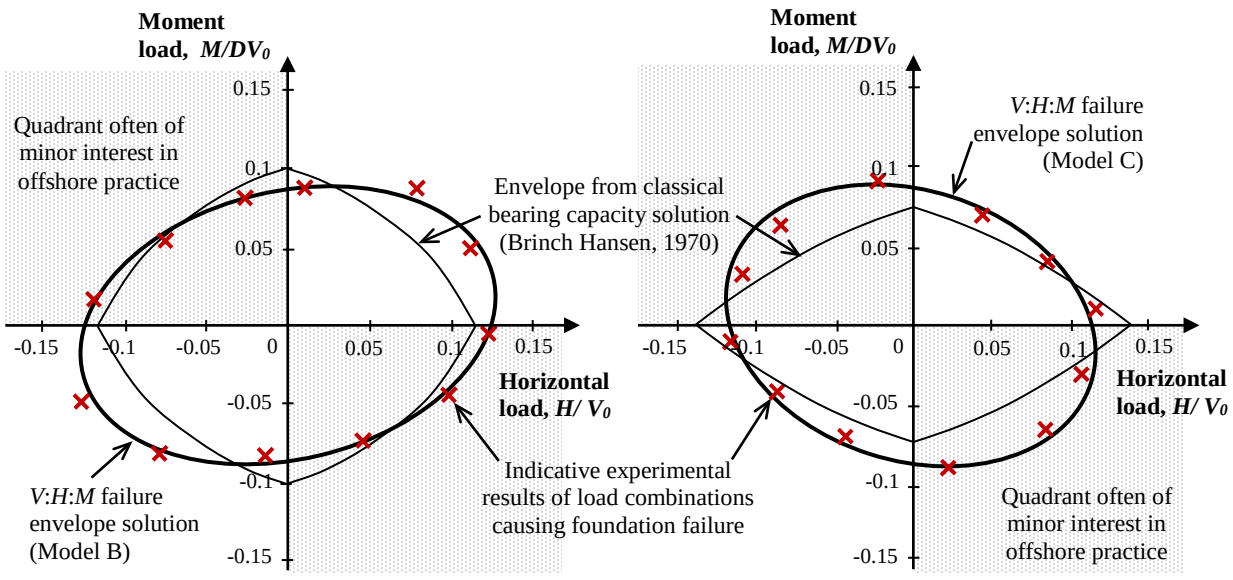

(a) Undrained conditions (Martin, 1994) (b) Drained conditions (Cassidy, 1999)

Figure 1.5: Schematic of circular foundation capacity in the *H*:*M* load space (at $V/V_0 = 0.5$)

Researchers have used the failure envelope approach to determine the bearing capacity of regular-shaped shallow foundations such as strip, square and circular foundations. This has taken the form of experimental work and numerical analysis to explore the shape of the failure envelope. However there has only been limited research of this type for perforated foundations. A focus of the research in this thesis is to examine the bearing capacity of perforated foundations under combined loading within the framework of *V*:*H*:*M* failure envelopes.

1.2 Research aims

The overall aim of the research presented in this thesis was to perform experimental work and numerical analysis to understand the bearing capacity of perforated foundations over a range of perforation ratios, *R*. This has been approached in four parts:

1) Finite element analysis (FEA) is regularly used to numerically analyse foundation bearing capacity and is adopted in this thesis to investigate perforated foundations. For undrained conditions the Tresca model (a special case of the Mohr-Coulomb model) is a common choice for defining the yield criterion of the soil. A disadvantage of the Tresca failure criterion is that the yield (and plastic potential) surface contains corners which can create numerical difficulties, e.g. if smoothing is required. In addition, the accuracy of FEA solutions is sensitive to the refinement of the soil mesh in terms of the number and size of elements. This can require the modeller to experiment to find the best distribution of elements. An aim of this research was to implement measures to address these two aspects such that modelling errors could be reduced in FEA of perforated foundations.
2) It is necessary to understand the bearing capacity of perforated foundations under vertical load before their response to combined loads can be properly understood. An aim of this thesis was to investigate both experimentally and numerically the undrained vertical capacity of perforated foundations. This was to include consideration of foundation embedment such that the results could be applicable to both surface and skirted foundations.
3) After establishing an understanding of vertical load capacity, an aim of this thesis was to investigate experimentally and numerically the combined load capacity of surface and skirted perforated foundations. The purpose of this was to provide guidance to designers for analysing these types of foundations by interpreting the results within the V:H:M failure envelope framework.
4) Recent research on grillage foundations has proposed a method for calculating vertical bearing capacity on sand. An aim of the thesis was to investigate grillage capacity under vertical loading and compare the results to those predicted by the

existing method. A further aim was to extend previous work by conducting experiments and numerical analyses for combined loading and interpreting the results within the *V*:*H*:*M* failure envelope framework.

1.3 Thesis outline

In line with the above research aims, the work in this thesis has been arranged as follows:

- **Chapter 2:** Provides background on the foundation capacity of shallow foundations, and is presented in two parts. The first part provides a general summary on shallow foundation capacity assessment including classical and failure envelope approaches. Attention has been given to the effect on bearing capacity of factors including foundation shape, embedment and soil strength heterogeneity. The second part includes a literature review to summarise previous work specific to the bearing capacity of perforated foundations.
- **Chapter 3:** Summarises a Tresca user material (UMAT) subroutine and an adaptive meshing strategy that have been implemented with the FEA software Abaqus (Dassault, 2009). It is shown that these measures improve the accuracy of FEA for the assessment of bearing capacity. Analysis that has been undertaken for verification purposes is also presented.
- **Chapter 4:** Presents a FEA study using Abaqus to investigate the undrained vertical bearing capacity of ring and annular foundations. Consideration has been given to the effect of interface roughness, soil strength heterogeneity and foundation embedment. A design approach to calculate vertical bearing capacity is presented.
- **Chapter 5:** Considers the undrained capacity of perforated foundations under combined loading. The results of centrifuge tests are presented and interpretation is undertaken with comparison to results from FEA using Abaqus. An expression for calculating *V*:*H*:*M* failure envelopes for perforated foundations is suggested.

- **Chapter 6:** Examines the capacity of grillage foundations under drained conditions. Experiments carried out under 1g conditions are used to investigate vertical and combined loading. The vertical loading results are compared to existing solutions. The combined loading results are used to propose an expression describing *V*:*H*:*M* failure envelopes for grillage foundations. Finite element limit analysis using OxLim (Martin, 2010, Martin, 2011) is also undertaken for comparison with the experimental results.
- **Chapter 7:** Summarises the main findings of the research presented in this thesis and suggests areas for future research.

Chapter 2. Background

Assessing the bearing capacity of shallow foundations is a fundamental aspect of geotechnical engineering. This chapter briefly reviews classical bearing capacity theory which is commonly adopted in foundation design codes. The more recent failure envelope approach for bearing capacity assessment is also discussed. Reference is made to both surface foundations and skirted foundations, where the skirts are used for embedment into the seabed to generate increased capacity. Emphasis is given to bearing capacity under undrained conditions as this is a principal focus of the research in this thesis. Finally a review of the literature pertaining specifically to the bearing capacity of perforated foundations is presented.

2.1 Bearing capacity of shallow foundations

Ultimate bearing capacity is defined as the average bearing pressure at which the soil supporting a rigid foundation would be expected to fail in shear. The foundation design should ensure safety against ultimate shear failure occurring. Classical bearing capacity theory is often drawn upon to assess foundation capacity, but new approaches such as failure envelopes are increasingly being used. Design factors other than ultimate bearing capacity should also be considered, such total or differential settlement limitations, although these are not within the scope of this thesis.

2.1.1 Classical bearing capacity theory

Shallow foundation bearing capacity is commonly assessed using a modified version of the classical Terzaghi bearing capacity equation (Terzaghi, 1943). This uses superposition to combine (in an appropriate, but conservative, manner) the effects of cohesion, surcharge and

soil weight. The soil is assumed to act as a rigid-plastic Mohr-Coulomb material in drained conditions, or as a rigid-plastic Tresca material in undrained conditions.

The original calculation applied to a surface strip footing subject to vertical load. To extend its application to a broader range of foundation types, a number of mostly empirical and semi-empirical modification factors are used. With the inclusion of these factors, the ultimate capacity q_u for a footing of width B is given by:

$$q_u = cN_c \cdot s_c d_c i_c + qN_q \cdot s_q d_q i_q + 0.5\gamma B N_\gamma \cdot s_\gamma d_\gamma i_\gamma \quad (2.1)$$

where N_c, N_q and N_γ are bearing capacity factors corresponding to cohesion c, surcharge pressure at footing level q, and soil unit weight below footing level γ. The bearing capacity factors are each a function of the friction angle, ϕ. Equation 2.1 is written in a general form and can be applied to assess both drained and undrained capacity. Parameters are typically adopted according to the type of analysis undertaken as summarised in Table 2.1.

Table 2.1: Drained and undrained parameters for Equation 2.1

Parameter	**Drained analysis**	**Undrained analysis**
Friction angle, ϕ	$\phi = \phi' > 0$	$\phi = \phi_u = 0$
Cohesion, c	$c = c' = 0$	$c = s_u > 0$
Surcharge, q	q' (effective stress)	q (total stress)
Unit weight, γ	γ' (effective weight)	γ (total weight)

In Equation 2.1 the shape and depth modification factors are given by s_q, s_γ, s_c and d_c, d_q, d_γ respectively. Load inclination modification factors, i_q, i_γ and i_c are used to account for the effects of horizontal loading. Several different expressions for the modification factors have been proposed, including those by Meyerhof (1953), Brinch Hansen (1970) and Vesic (1973). The effective width principle (Meyerhof, 1953) incorporates moment loading where an equivalent footing width $B' = B - 2e$ is used in place of B in Equation 2.1, where $e = M/V$. The load inclination and the effective width implementation are illustrated in Figure 2.1.

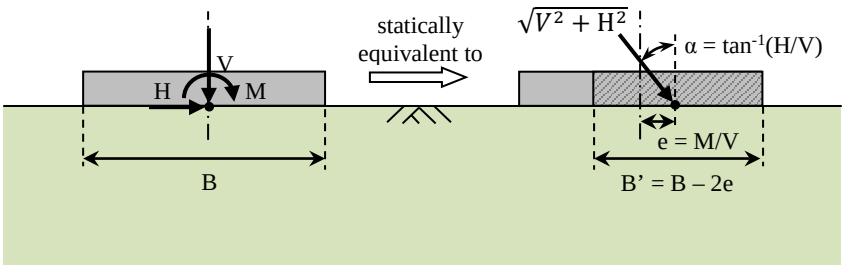

Figure 2.1: Implementation of combined loading by the classical bearing equation

The bearing capacity factors N_c and N_q, which pertain to a weightless soil, have been solved analytically using the method of characteristics when assuming the soil satisfies an associated flow rule (angle of dilation equal to angle of friction). These expressions are well known. For the case of N_γ however, consideration of soil self weight is required and there are a range of proposed solutions (Bolton and Lau, 1993, Frydman and Burd, 1997, Ukritchon et al., 2003, Hjiaj et al., 2005, Lyamin et al., 2007). Martin (2005) found accurate values of N_γ based on the method of characteristics, though again these solutions assume an associated flow rule.

Recommended practices for assessing the bearing capacity of shallow offshore foundations are given in design codes that include DNV (1992), ISO (2003) and API (2007). The solutions are based on the classical bearing capacity equation, but this approach is not straightforward. Variations in soil strength with depth can be difficult to incorporate for example, as are non-standard foundation arrangements such as perforated foundations.

2.1.2 Failure envelopes

An alternative to the classical bearing capacity equation is to consider bearing capacity directly within a three dimensional *V:H:M* load space by defining the envelope of the failure surface in this space (Figure 2.2). The failure envelope shows how the foundation capacity varies with different loading combinations. Load combinations located on or outside the envelope result in foundation failure, whilst load combinations within the envelope can be considered stable.

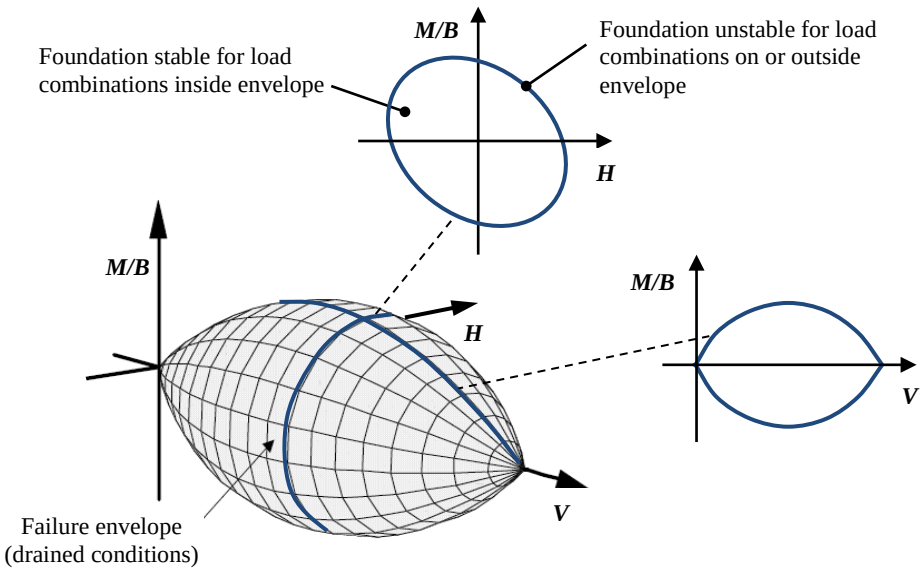

Figure 2.2: Failure envelope for combined loading (drained conditions)

A number of studies have been undertaken to investigate the shape of the failure envelope for strip and circular footings on both clay and sand. Failure envelopes for foundations on clay have been determined by fitting curves to experimental results, or by using numerical or theoretical techniques (Martin, 1994, Murff, 1994, Bransby and Randolph, 1998, Ukritchon et al., 1998, Taiebat and Carter, 2000, Gourvenec and Randolph, 2003, Gourvenec, 2007a). Failure envelopes for foundations on sand have mostly been derived based on experimental results (Nova and Montrasio, 1991, Butterfield and Gottardi, 1994, Gottardi et al., 1999, Byrne, 2000). The form of failure envelopes has generally been found to be approximately parabolic in the *H*:*V* and *M*/*B*:*V* load space, and elliptical in the *M/B*:*H* load space (Figure 2.2). The elliptical *M/B*:*H* failure envelope for clay has been found to have a positive eccentricity (as defined by the sign convention shown in Figure 2.2) whilst for sand the eccentricity has been shown to be negative (see Figure 1.5).

The shape of failure envelopes can be defined experimentally or numerically using i) swipe tests, ii) displacement-controlled probe tests, or iii) load-controlled probe tests. An illustration of exploring the failure envelope numerically using these approaches is given in Figure 2.3. This figure shows finite element analysis results in the *V*:*H* load space for a rough

strip footing of width B (see for example Bransby and Randolph (1998) where this case has been analysed previously). The analysis was undertaken in Abaqus using a homogeneous soil of undrained shear strength s_u, with a full tension interface.

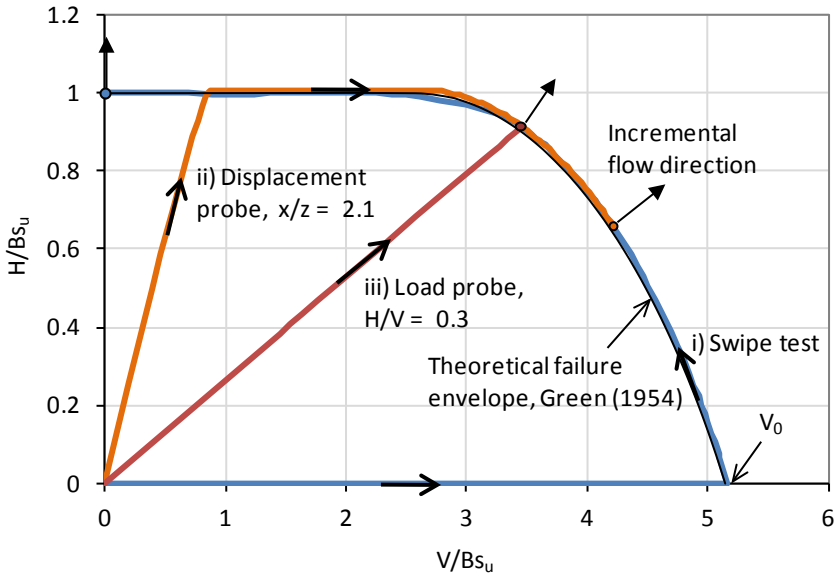

Figure 2.3: Numerical swipe and probe tests of a strip foundation (undrained soil)

Swipe tests are carried out by first loading the foundation vertically until a failure load V_0 is reached (Figure 2.3(i)). The vertical displacement is then kept constant, and when the foundation is translated or rotated it has been found the load path will track closely along the failure envelope (Tan, 1990, Martin, 1994). Probe tests are undertaken by applying a fixed ratio of displacement or load until failure occurs. For displacement-controlled probes (Figure 2.3(ii)), once the failure surface has been reached the load path will continue to track along the failure envelope until a point where the imposed displacements match the incremental flow direction. With an associated flow rule this occurs when the displacement vector is perpendicular to the failure envelope. For load controlled probes (Figure 2.3(iii)), when failure is reached a single point will be defined on the failure envelope, and the corresponding incremental displacement vector obtained. Figure 2.3 shows that the failure envelope defined by these three types of tests matches the theoretical solution for this case given by Green (1954).

A number of expressions have been proposed to describe the shape of failure envelopes determined numerically or experimentally as a function of the loads *V*, *H* and *M*. Establishing an algebraic expression is not always straightforward. It has been found that different expressions are required for different foundation configurations and soil types.

2.2 Bearing capacity in undrained conditions

The bearing capacity of foundations in undrained conditions is a primary focus of this thesis and is reviewed in further detail in this section. Consideration has been given to both surface and embedded foundations as shown in Figure 2.4. Foundation embedment is commonly achieved offshore by the use of thin-walled skirts beneath the foundation base which penetrate into the seabed. Skirt penetration is achieved either under the structural self weight or by pumping water out from within the skirted compartment. This generates an under-pressure thereby creating an additional penetrating force. The skirts improve foundation capacity by trapping the soil within the skirted compartment such that it can act as a solid embedded foundation with loads transferred to the foundation base.

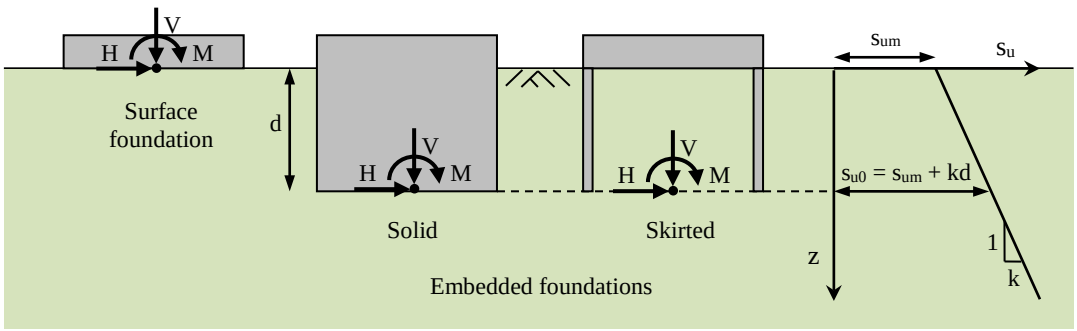

Figure 2.4: Surface and embedded foundations with undrained shear strength assumption

2.2.1 Undrained soil strength

In undrained conditions the soil friction angle ϕ is taken to be zero and the variation of undrained shear strength s_u with depth is a key parameter. The undrained strength can be determined by undertaking laboratory tests, such as an undrained triaxial test. The vertical

stress σ_v (= σ_1) and horizontal stress σ_h (= σ_3) of the triaxial sample at failure can be plotted on a Mohr's circle (Figure 2.5). The undrained strength s_u is defined by the radius of the Mohr's circle which can be expressed as:

$$s_u = \frac{\sigma_1 - \sigma_3}{2} \tag{2.2}$$

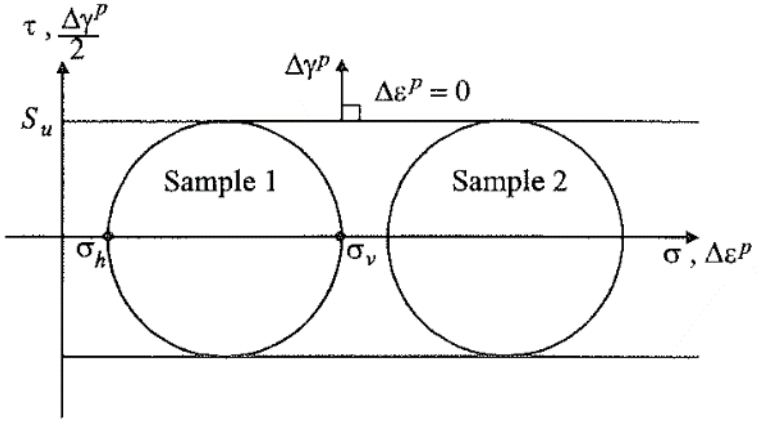

Figure 2.5: Mohr's circles of total stress results for two similar soil samples without allowing any consolidation (Potts and Zdravkovic, 1999)

For ease of assessment in bearing capacity calculations the soil strength profile variation is often assumed to be either homogeneous or to increase linearly with depth such that:

$$s_u = s_{um} + kz \tag{2.3}$$

where s_{um} is the undrained strength at the soil surface (often referred to as mudline), k is the rate of strength increase with depth, and z is the depth below the soil surface (Figure 2.4). In the case of homogeneous soil k = 0. For normally consolidated (NC) soils a linearly increasing soil strength profile with zero mudline strength, s_{um} = 0, can often give a good approximation of the soil strength variation with depth. The strength profile for over consolidated (OC) soils is typically less linear in its variation with depth, but often a reasonable linear approximation can still be made. In other cases assuming a constant homogeneous profile (k = 0) might provide an adequate approximation.

2.2.1.1 Tresca model

The Tresca model is a special case of the Mohr-Coulomb criterion and is applied in the classical undrained bearing capacity solution. The model adopts the failure criterion given by Equation 2.2 as a yield surface such that the yield function becomes:

$$f = \sigma_1 - \sigma_3 - 2s_u = 0 \tag{2.4}$$

In three dimensional principal stress space the Tresca yield function plots as a hexagonal cylinder, with the space diagonal (where $\sigma_1 = \sigma_2 = \sigma_3$) as its axis (Figure 2.6). When plotted in the deviatoric plane, the vertices of the hexagon correspond to triaxial compression and extension points.

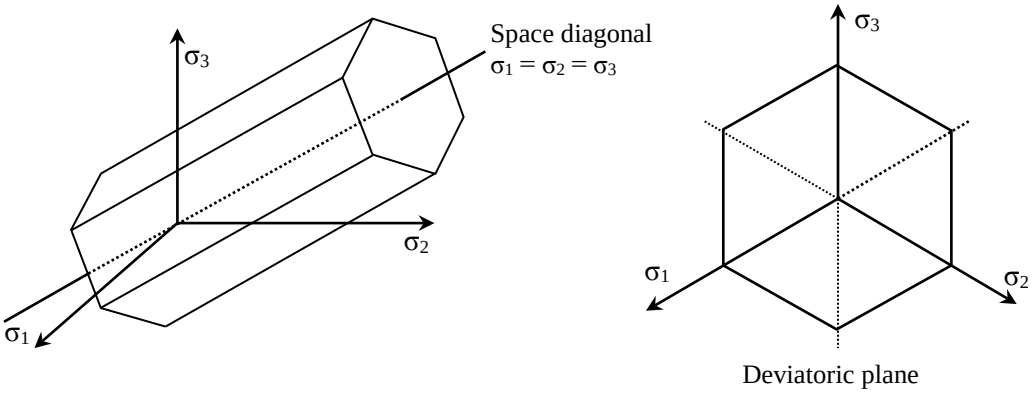

Figure 2.6: Tresca failure criterion in a three dimensional stress space

In finite element analysis (FEA) the Tresca model is a common choice of constitutive model for the analysis of undrained problems. Although it is a simple model, it is useful for determining failure loads of soils in undrained conditions. The Tresca model is perfectly plastic so there is no hardening or softening law required. The plastic potential function used should predict zero volumetric strain. A convenient choice is to assume associated flow and adopt the yield function as the plastic potential function. A disadvantage of the Tresca model in FEA is that the yield and plastic potential surface corners can create implementation problems and numerical difficulties for the analysis software. This is discussed further in Chapter 3.

2.2.2 Vertical load capacity

In undrained conditions the surcharge and unit weight components of Equation 2.1 become zero so the bearing capacity of a vertically loaded surface foundation is given by

$$V_{max} = AN_c s_u \tag{2.5}$$

where V_{max} is the load at failure, A is foundation area and N_c is the bearing capacity factor. N_c is commonly used to denote the bearing capacity factor for an infinite strip foundation on undrained soil with a constant strength. For this case it can be shown from limit analysis that a theoretically exact solution exists of $N_c = 2 + \pi$ (= 5.142) (Prandtl, 1921, Bishop, 1953).

The bearing capacity factor can vary depending on foundation roughness, as the soil-foundation interface influences the failure mechanism within the soil. For smooth foundations a Hill type mechanism (Hill, 1950) is typical whilst for a rough foundation a Prandtl type mechanism (Prandtl, 1921) is expected (Figure 2.7). In the Hill failure mechanism the soil immediately beneath the foundation has both vertical and horizontal components of displacement. The soil immediately below the foundation in the Prandtl mechanism has only vertical movement. As a result the mechanism for a rough foundation penetrates deeper into the soil compared with that for a smooth foundation. For a strip footing on homogeneous soil however, the bearing capacity factor N_c turns out to be the same for both mechanisms. Various hybrid and one-sided mechanisms can also be derived that give the same value of N_c for this particular case.

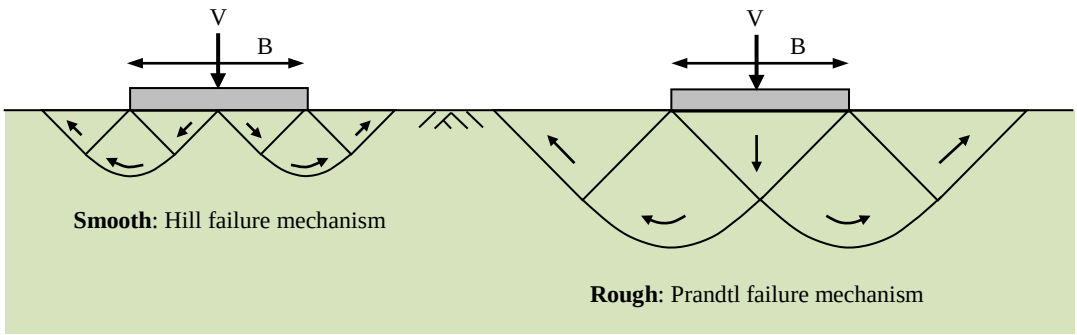

Figure 2.7: Possible failure mechanisms for smooth and rough strip foundations

2.2.2.1 Effect of foundation shape

The failure mechanism also varies depending on the foundation shape. This results in varying bearing capacity factors N_c for different geometries (in Equation 2.1 the variation is achieved by multiplying $N_c = 5.142$ for a strip foundation by the shape factor s_c). A summary of N_c values for three key foundation shapes is given in Table 2.2.

Table 2.2: Bearing capacity factors for surface foundations

Interface condition	**Bearing capacity factor, N_c**		
	Strip 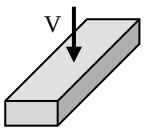	Circle 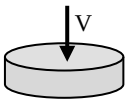	Square 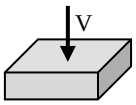
Smooth	2 + π (= 5.142)	5.689 [a]	5.56 [b]
Rough	2 + π (= 5.142)	6.048 [a]	5.91 [b]

[a] Results from Martin (2004)
[b] Results from Gourvenec et al. (2006) - exact solution unknown

As with a strip foundation, exact solutions have been determined for smooth and rough circular foundations (Shield, 1955, Eason and Shield, 1960). Martin (2004) undertook rigorous slip-line analysis of circular foundations to more accurately determine bearing capacity factors of 5.689 and 6.048 for smooth and rough foundations respectively. The stress characteristics for each case are shown in Figure 2.8.

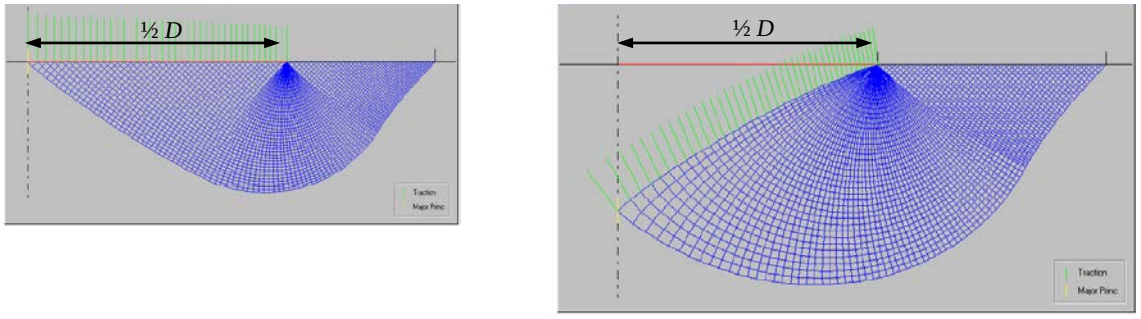

(a) Smooth interface (b) Rough interface

Figure 2.8: Circular foundation (of diameter D) slip line solutions (Martin, 2004)

No exact solution has yet been found for the undrained bearing capacity of a square foundation, and a range of N_c values exists in the literature. A summary is given in Table 2.3 for smooth square foundations and Table 2.4 for rough square foundations.

Table 2.3: Comparison of N_c for smooth square foundations

Study	Method	Bearing capacity factor, N_c
Gourvenec et al. (2006)	FEA - Abaqus	5.56
Puzrin & Randolph (2003)	UB limit analysis	UB: 6.13
Michalowski & Dawson (2002)	Finite difference - FLAC	5.43
Shield & Drucker (1953)	UB limit analysis	UB: 5.71
Skempton (1951)	Empirical	6.17

Table 2.4: Comparison of N_c for rough square foundations

Study	Method	Bearing capacity factor, N_c
Nguyen & Merifield (2012)	FEA - Abaqus	5.950
Gourvenec et al. (2006)	FEA - Abaqus	5.91
Salgado et al. (2004)	FELA	LB: 5.523 UB: 6.221
Michalowski (2001)	Limit analysis	Continuous mechanism, UB: 6.830 Multi-block mechanism: 4 symmetry planes, UB: 6.823 2 symmetry planes, UB: 6.561
Skempton (1951)	Empirical	6.17

The complication in solving this problem is in part due to uncertainty surrounding the nature of the failure mechanism occurring. Figure 2.9(a) shows contours of velocity magnitude at the soil surface from the finite difference analysis (FDA) of a smooth square foundation undertaken by Michalowski & Dawson (2002). The deformation field showing the nature of the failure mechanism exhibits four planes of symmetry, with two being diagonal. Figure 2.9(b) gives displacement contours from FEA undertaken by Gourvenec et al. (2006) for comparison. It is seen that diagonal symmetry is also obtained, although the shape of the

failure mechanism implied by the displacement profile is different since it does not taper appreciably towards the corners.

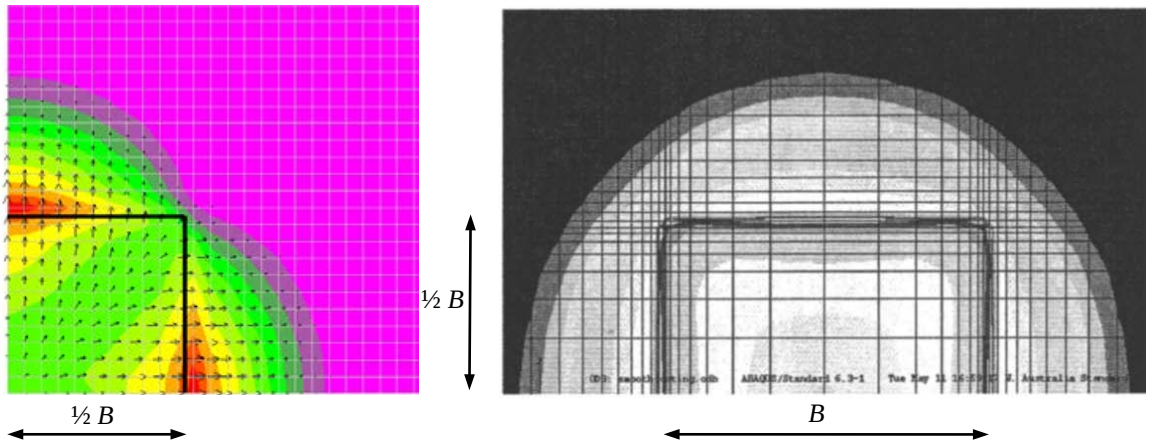

(a) Total velocity magnitude contours (¼ foundation) from FDA, Michalowski & Dawson (2002)

(b) Displacement contours (½ foundation) from FEA, Gourvenec et al. (2006)

Figure 2.9: Numerical results for a smooth square foundation (plan view)

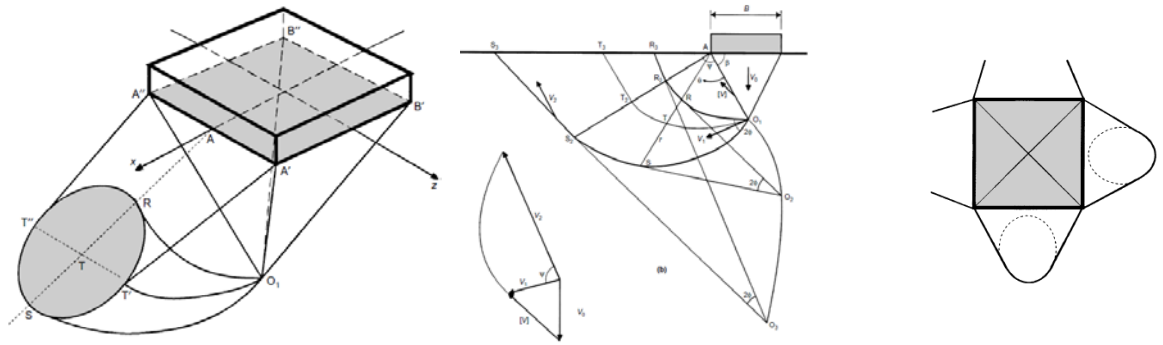

(a) Continuous deformation mechanism

i. 4 symmetry planes

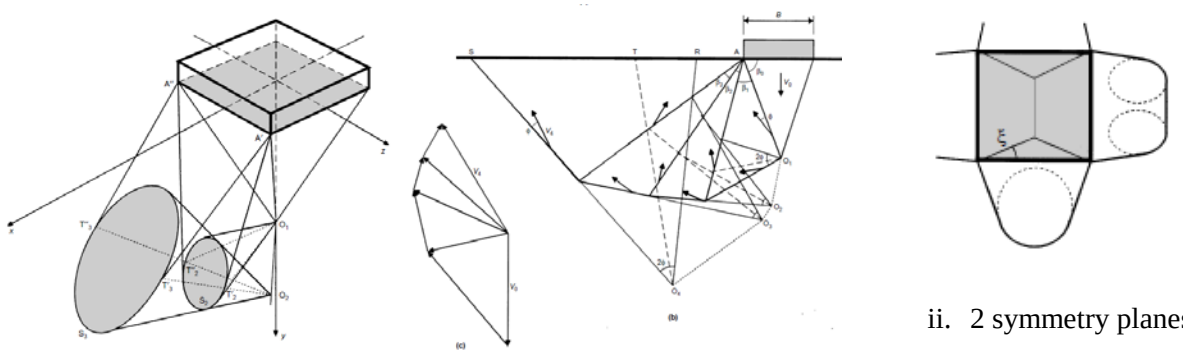

(b) Multi-block failure mechanism

ii. 2 symmetry planes

(c) Collapse mechanism

Figure 2.10: Rough square foundation mechanisms used in limit analysis by Michalowski (2001)

For the case of a rough square foundation, Michalowski (2001) investigated different types of mechanisms using limit analysis as shown in Figure 2.10. A multi-block mechanism was found to produce a better upper bound solution than the continuous mechanism (Table 2.4). For the multi-block mechanism both the cases of 2 symmetry planes and 4 symmetry planes with diagonal symmetry were considered. Surprisingly, it was found that the lowest upper bound estimate of the failure load occurred for the mechanism with no symmetry with respect to the diagonal planes.

The displacement contours obtained from the Abaqus study by Gourvenec et al. (2006) for a rough square foundation are shown in Figure 2.11. Four symmetry planes were obtained. As with the case for the smooth foundation, the displacement profile did not taper toward the corners of the square.

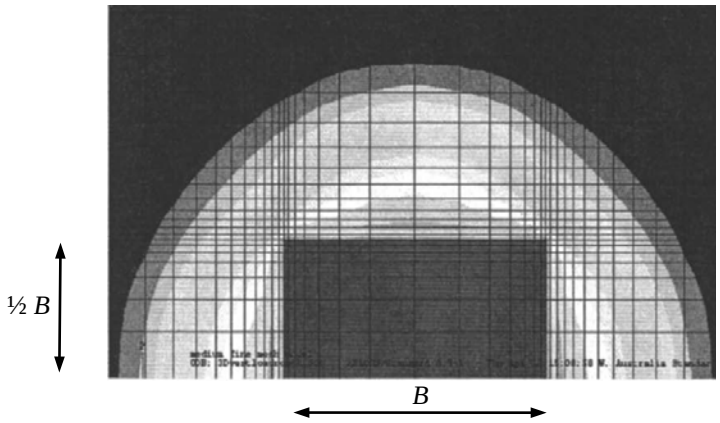

Figure 2.11: Plan view of displacement contours for a rough square from Gourvenec et al. (2006)

2.2.2.2 Effect of soil strength heterogeneity

It can be common when assessing undrained bearing capacity to represent the soil strength as increasing linearly with depth rather than being homogeneous (see Section 2.2.1). The degree of heterogeneity can be defined by the dimensionless quantity kB/s_{um} (or kD/s_{um}). A number of studies have considered the impact of soil strength heterogeneity on the bearing capacity factor N_c and solutions have been found for strip and circular foundations (Davis and Booker, 1973, Salencon and Matar, 1982, Houlsby and Wroth, 1983, Tani and Craig, 1995). Martin

(2004) examined the case of smooth and rough foundations on heterogeneous soil using the software ABC. The results for strip and circular foundations are given in Figure 2.12. Rough foundations are seen to have a greater increase in bearing capacity. This is expected given that the rough mechanism penetrates deeper into the soil of increasing strength compared to the failure mechanism of a smooth foundation (see Figure 2.7). As found by Houlsby & Wroth (1983), for kB/s_{um} greater than about 2 the capacity of a strip foundation starts to exceed that of a circular foundation. FEA results on the capacity of a square foundation with varying soil strength heterogeneity were not found to be reported in the literature.

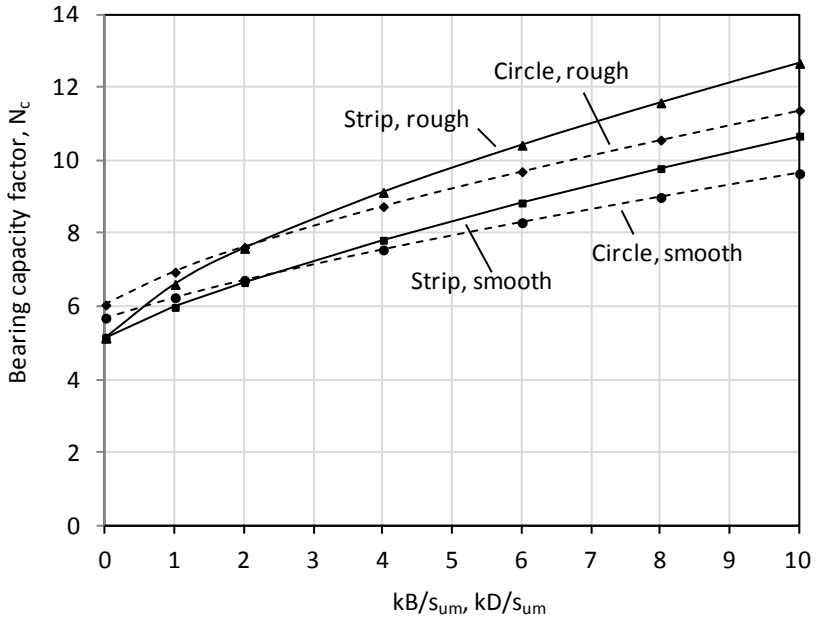

Figure 2.12: Bearing capacity factors for soil strength heterogeneity, results from Martin (2004)

2.2.2.3 Effect of foundation embedment

Foundation embedment results in an increase in vertical capacity. This is due to the additional overburden stress acting at foundation base level γd, which is added to Equation 2.5 (although depending on the foundation arrangement this may largely be negated by backfill or soil plug weight). In addition, the bearing capacity factor N_c increases with depth due to the extra shearing required for failure in the soil above the foundation base level. A number of studies have examined the influence of embedment on N_c for strip and circular foundations

(Hu et al., 1999, Martin, 2001, Houlsby and Martin, 2003, Salgado et al., 2004, Edwards et al., 2005). Gourvenec and Mana (2011) used Abaqus to assess the influence of foundation embedment on the bearing capacity factor N_c. The results for circular and strip foundations with smooth sides in homogeneous soil are shown in Figure 2.13. The circular foundation capacity remains consistently higher than that of a strip foundation. Negligible difference between rough-based and smooth-based strip foundations is observed. The average of lower and upper bound results determined from finite element limit analysis (FELA) by Salgado et al. (2004) for a rough square foundation are also shown in Figure 2.13. These fall between the smooth and rough circular foundation results.

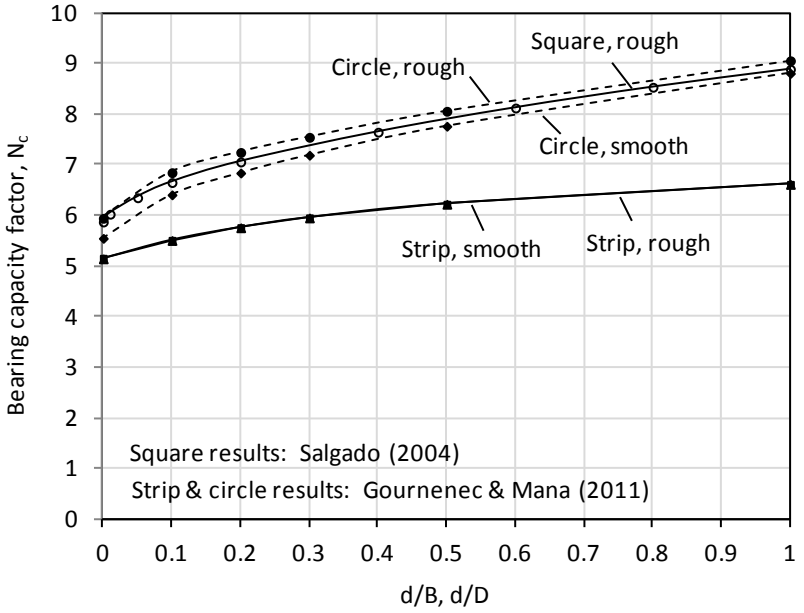

Figure 2.13: Bearing capacity factors for varying embedment depth

For the case of the vertical capacity of skirted foundations on homogeneous soil the same bearing capacity factors N_c apply as for an equivalent solid embedded foundation due to the soil being trapped by the skirts (Yun and Bransby, 2007). However, when soil strength increases with depth the capacity of skirted foundations at shallower embedment depths ($d/B < 0.3$) can be lower than a solid foundation. This is due to soil deformation occurring within the soil plug (Mana et al., 2013).

2.2.3 Combined load capacity

2.2.3.1 Classical approach

Combined loading is incorporated into the classical approach using an inclination factor (for horizontal loading) and the effective width principle (for moment loading) as described in Section 2.1.1. Based on the classical approach, the DNV (1992) guidelines suggest the following expression to be used for undrained foundation capacity under combined loads:

$$V_{max} = F\left(N_c s_{u0} + \frac{kB'}{4}\right)(1 + s_{ca} + d_{ca} - i_{ca})A \tag{2.6}$$

where F is a correction factor to account for interface roughness and the degree of heterogeneity (Davis and Booker, 1973), N_c is the bearing capacity for a strip on homogeneous soil = 5.14, and B' is the effective width of the foundation. The shape factor s_{ca} can be calculated as follows

$$s_{ca} = s_{cv}(1 - 2i_{ca})\frac{B'}{L} \tag{2.7}$$

and is dependent on the coefficient s_{cv} which is a function of the strength heterogeneity. In homogeneous soil s_{cv} = 0.2. The depth factor is given by

$$d_{ca} = \frac{s_{u1}}{s_{u2}} 0.3 \tan^{-1}\left(\frac{d}{B'}\right) \tag{2.8}$$

where s_{u1} is the average undrained shear strength above base level and s_{u2} is the equivalent shear strength below base level which is described by

$$s_{u2} = \frac{1}{5.14}\left(5.14 s_{u0} + \frac{kB'}{4}\right) \tag{2.9}$$

The inclination factor i_{ca} is given by

$$i_{ca} = 0.5 - 0.5\sqrt{1 - \frac{H}{A' s_{u0}}} \tag{2.10}$$

For purely vertical loading on homogeneous soil Equation 2.6 reduces to V_{max} = $5.14As_{um}$ which matches the exact solution for a surface strip foundation. For circular and square surface foundations on homogeneous soil, the equation becomes V_{max} = $6.17As_{um}$

which is an overestimation compared with the values in Table 2.2. When horizontal loading is introduced, the inclination factor i_{ca} is equivalent to the solution by Green (1954) and so is accurate for the case of a strip foundation on homogeneous soil (see Figure 2.3), but does not take into account change for other foundation geometries. For purely eccentric loading (H = 0), Equation 2.6 gives a maximum moment M_{max} of $M_{max} = 0.64B^2 s_{um}$ for a strip foundation and $M_{max} = 0.61ADs_{um}$ for a circular foundation. These are close to solutions for a strip found from plasticity analysis of about $M_{max} = 0.66ABs_{um}$ (Houlsby and Puzrin, 1999) and for a circle found from finite element analysis of about $M_{max} = 0.63ADs_{um}$ (Taiebat and Carter, 2002). These solutions are for the case where no tensile stresses are allowed between the foundation and the soil. Plasticity solutions for unlimited tensile capacity have been found as $M_{max} = 0.69ABs_{u0}$ and $M_{max} = 0.67ADs_{u0}$ for strip and circular foundations respectively (Randolph and Puzrin, 2003). The effective width principle (and therefore Equation 2.6) does not accommodate any tensile capacity, which can be a drawback as tensile capacity can often be incorporated into the design of offshore foundations, particularly if they are embedded or if skirts are present.

Whilst Equation 2.6 is seen to provide a reasonable match with analytical solutions for the case of inclined loading (V:H) or eccentric loading (V:M) on homogeneous soil, this is less the case for heterogeneous soil (as described in Randolph et al. (2005) for example). Furthermore, loading cases where inclined and eccentric loading occur in combination (V:H:M) are also not handled well, as evidenced in Figure 1.5(a). Given the shortcomings of the classical approach, the failure envelope framework has become popular for understanding the combined loading capacity of a foundation. This is particularly the case for offshore foundations where environmental conditions can impose high horizontal and moment loads.

2.2.3.2 Failure envelopes

Failure envelopes for undrained conditions have been investigated i) experimentally, ii) numerically, and iii) analytically using plasticity solutions. A number of expressions have been proposed to describe the form of the failure envelope for various foundation shapes, embedment ratios and strength profiles, although the shape of these envelopes can be complex and difficult to describe mathematically.

i) Experimental: Martin (1994) undertook 1g experiments by conducting swipe tests on model circular foundations on clay. Using a fit to the experimental data a failure envelope termed Model B was proposed as shown in Figure 2.14. The envelope indicates that no tension can be sustained. It also shows that as the vertical load approaches zero the horizontal capacity approaches zero. Theoretically this would be expected in a drained soil rather than an undrained soil. Martin & Houlsby (2000) suggested that undrained loading conditions may not have been maintained at this loading condition due to the shallow nature of the sliding failure mechanism.

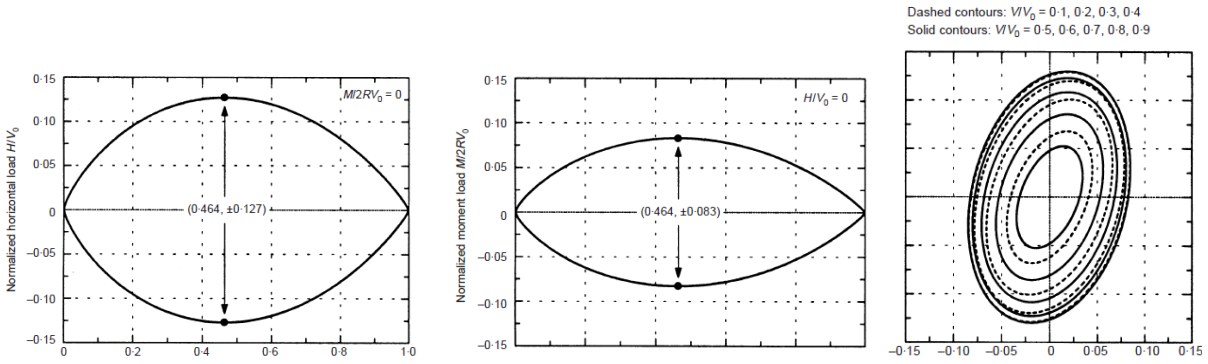

(a) *V*:*H* load space (b) *V*:*M* load space (c) *V*:*H*:*M* load space

Figure 2.14: Model B normalised failure envelope (Martin and Houlsby, 2000)

The equation describing the Model B failure envelope in dimensionless terms is as follows (Martin and Houlsby, 2000, Martin and Houlsby, 2001):

$$f = \left(\frac{H}{H_0}\right)^2 + \left(\frac{M}{M_0}\right)^2 - 2\bar{e}\frac{H}{H_0}\frac{M}{M_0} - \bar{\beta}^2\left(\frac{V}{V_0}\right)^{2\beta_1}\left(1 - \frac{V}{V_0}\right)^{2\beta_2} = 0 \tag{2.11}$$

where

$$\bar{e} = e_1 + e_2\left(\frac{V}{V_0}\right)\left(\frac{V}{V_0} - 1\right) \tag{2.12}$$

and

$$\bar{\beta} = \frac{(\beta_1 + \beta_2)^{(\beta_1+\beta_2)}}{{\beta_1}^{\beta_1}{\beta_2}^{\beta_2}} \tag{2.13}$$

and $H_0 = h_0V_0$, $M_0 = m_0DV_0$. The parameter values obtained from regression analysis were h_0 = 0.127, m_0 = 0.083, e_1 = 0.518, e_2 = 1.180, β_1 = 0.764 and β_2 = 0.882.

ii) Numerical: A number of numerical studies have been undertaken using FEA to map out the shape of failure envelopes under *V*:*H*:*M* loading (Bransby and Randolph, 1998, Ukritchon et al., 1998, Taiebat and Carter, 2000, Gourvenec and Randolph, 2003, Gourvenec and Barnett, 2011). Taiebat & Carter (2000) undertook FEA of a surface circular foundation on homogeneous soil. Different load combinations were applied to the foundation and used to define the failure envelope as shown in Figure 2.15. The form of this differs from the experimental results of Martin (1994) because unlimited tension is allowed and horizontal load can be sustained at zero vertical loading. The resulting degree of asymmetry of the failure envelope in the *H*:*M* load space was not observed in the results of Martin (1994).

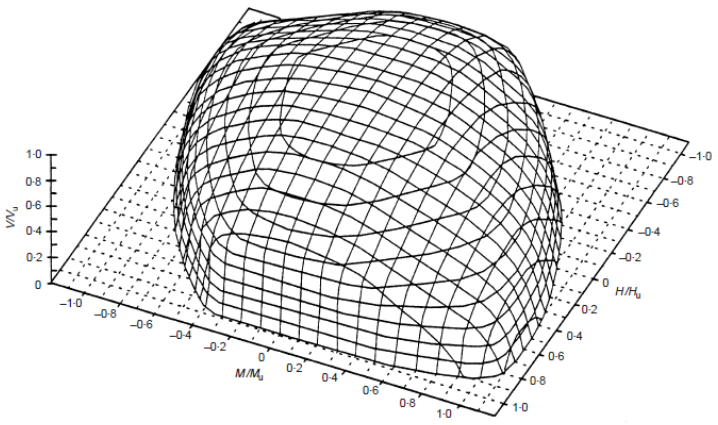

Figure 2.15: Circular foundation failure envelope on homogeneous soil (Taiebat and Carter, 2000)

Taiebat and Carter (2000) proposed the following expression to approximate the numerically derived circular foundation failure envelope:

$$f = \left(\frac{V}{V_u}\right)^2 + \left[\frac{M}{M_u}\left(1 - \alpha_1 \frac{HM}{H_u|M|}\right)\right]^2 + \left|\left(\frac{H}{H_u}\right)^3\right| = 0 \tag{2.14}$$

where α_1 is a factor adjusting the eccentricity of the failure envelope. A value of $\alpha_1 = 0.3$ was considered to provide a good fit to the homogeneous soil profile studied (Taiebat and Carter, 2000). Gourvenec (2007a) undertook finite element analysis of the same problem and compared the results to the failure envelope approximation given by Taiebat & Carter (2000). The comparison is given in Figure 2.16 and shows that there is a reasonable match but that the asymmetry of the failure envelope is not always well captured by Equation 2.14.

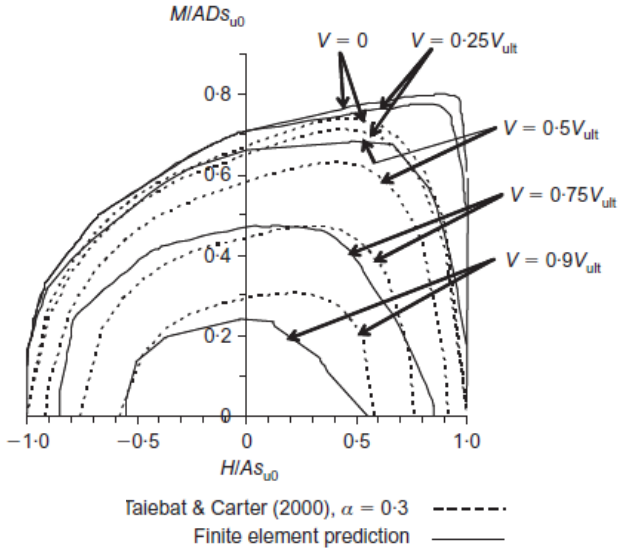

Figure 2.16: Comparison of Equation 2.14 with finite element results (Gourvenec, 2007a)

iii) Plasticity theory: Plasticity theory has been used as another approach to investigate undrained failure envelopes (Bransby and Randolph, 1998, Houlsby and Puzrin, 1999, Randolph and Puzrin, 2003). Bransby & Randolph (1998) used upper bound plasticity calculations to estimate upper bound failure envelopes for a surface strip foundation under combined loading with full tension capacity. The mechanisms adopted were informed from the results of FEA for different load combinations. Each mechanism was derived from either

'scoop' or 'wedge' components (Figure 2.17). The results from the upper bound analysis provide a good match with the failure envelope derived from FEA.

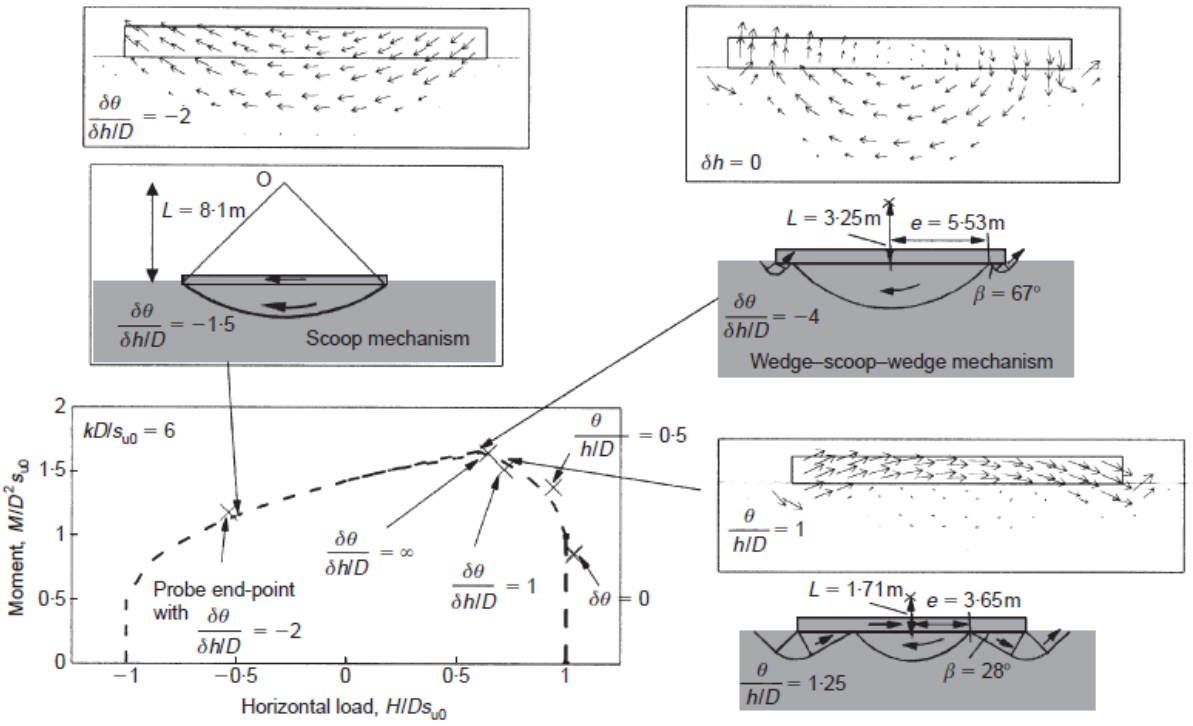

Figure 2.17: Comparison between upper bound and finite element analysis failure mechanisms for a strip foundation (of width *D*) under *H*:*M* loading (Bransby and Randolph, 1998)

2.2.3.3 Effect of foundation tension capacity

Several studies have investigated the impact that the tension capacity of a foundation has on its performance under combined loading (Salencon and Pecker, 1995a, Salencon and Pecker, 1995b, Michalowski and You, 1998, Houlsby and Puzrin, 1999). The bounding cases are for a foundation sustaining either full or zero-tension capacity (the latter is imposed when adopting the effective width rule). Ukrtichon et al. (1998) considered these two cases by undertaking finite element limit analysis of a strip foundation where both full and zero-tension soil-foundation interfaces were modelled. Figure 2.18 shows the *V*:*H*:*M* failure envelope obtained from the analysis. The results illustrate that there is reduced moment capacity for the case where no tension is sustained.

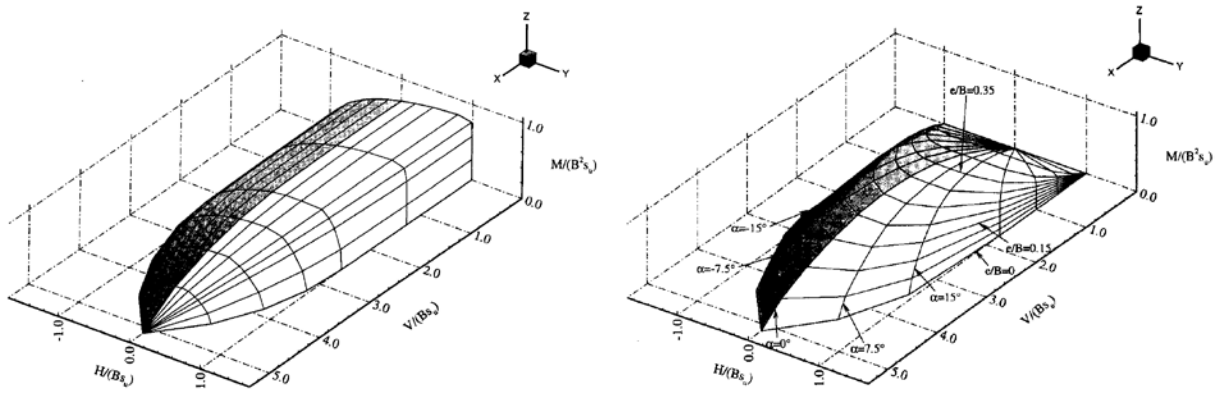

(a) Full tension interface (b) Zero-tension interface

Figure 2.18: Failure envelopes for strip foundations on homogeneous soil (Ukritchon et al., 1998)

2.2.3.4 Effect of foundation shape

The combined loading of strip foundations can be assessed in plane strain which makes the analysis more straightforward. Previous studies have also addressed circular foundations, and less commonly square and rectangular foundations. Gourvenec (2007b) undertook FEA of strip, circular and square foundations to investigate the effect of foundation shape on bearing capacity under combined loading (Figure 2.19).

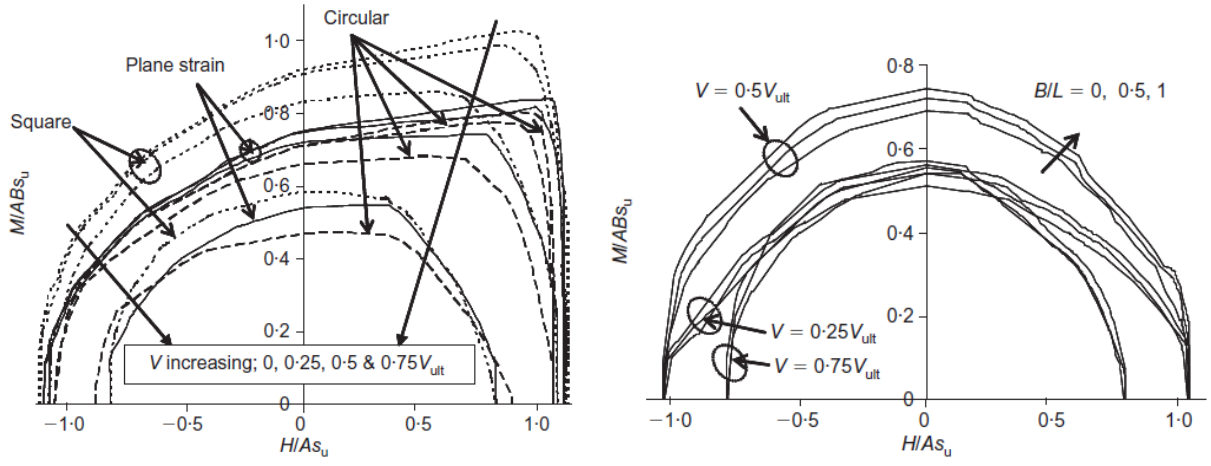

(a) Full tension capacity (b) Zero-tension capacity

Figure 2.19: Shape effects on *V*:*H*:*M* failure envelopes (Gourvenec, 2007b)

The results show that bearing capacity determined under plane strain conditions may not be reliably applied for the case of circular and square foundations. When full interface tension was permitted, the normalised moment capacity of a square foundation was found to

be significantly larger than a strip (by about 30%), whilst the capacity of a circular foundation was similar, although slightly lower (Figure 2.19(a)). For a zero-tension interface, the moment capacity of a square foundation (B/L = 1) was only marginally greater than that of a strip foundation (B/L = 0) (Figure 2.19(b)).

2.2.3.5 Effect of soil strength heterogeneity

Gourvenec and Randolph (2003) undertook FEA to investigate the effect of soil strength heterogeneity on bearing capacity of strip and circular foundations under combined loading. The shape of the failure envelope in the V:H plane was found to be independent of the degree of heterogeneity. In the H:M plane the degree of heterogeneity was found to have a significant effect on the shape of the failure envelope. When normalised by As_{uo}, the failure envelope expands with heterogeneity due to increasing moment capacity (Figure 2.20(a)). When normalised by the peak capacities H_0 and M_0, the failure envelope is seen to contract in the positive quadrant (Figure 2.20(b)).

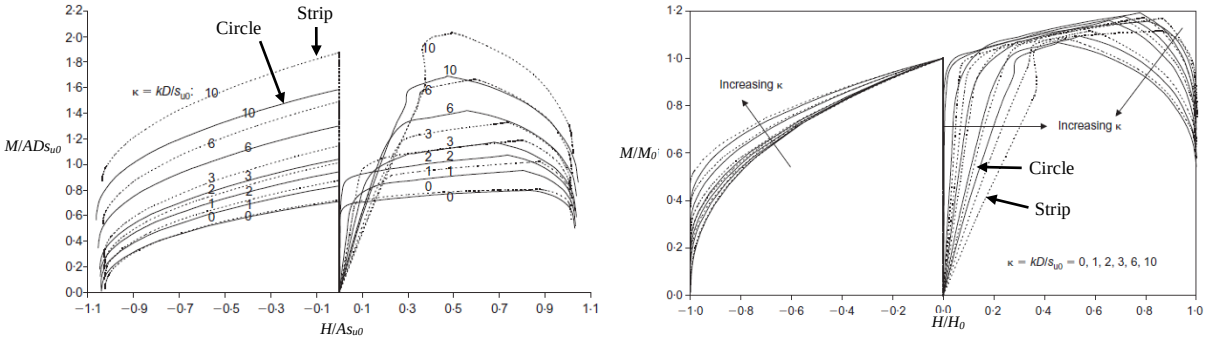

(c) Normalised by As_{uo} (d) Normalised by peak capacities H_0 and M_0

Figure 2.20: Soil heterogeneity effects on V:H:M failure envelopes (Gourvenec and Randolph, 2003)

2.2.3.6 Effect of foundation embedment

Several numerical studies have been undertaken investigating the impact of embedment depth on failure envelopes (Bransby and Randolph, 1999, Gourvenec, 2008, Mana et al., 2013) Bransby & Yun (2009) carried out a series of finite element and upper bound plasticity

calculations to investigate the capacity of embedded strip foundations under combined loading. Consideration was given to both solid and skirted embedded foundations, for which the load reference point was taken at skirt tip level. The failure envelope in the *H*:*M* plane was seen to expand and the eccentricity increase with increasing embedment ratio. It was found that the capacities for skirted foundations could be significantly less than those for solid embedded foundations, particularly for the case of non-homogeneous soil (Figure 2.21). The lower capacity was due to failure mechanisms in which deformation of the soil occurred between the skirts.

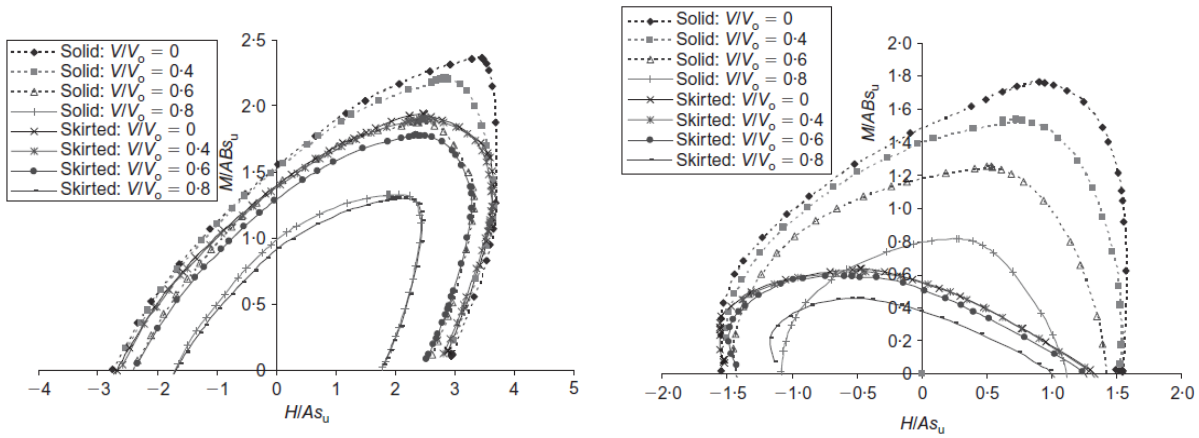

(a) *H*:*M* load space at *d*/*B* = 1 (b) *H*:*M* load space at *d*/*B* = 0.2

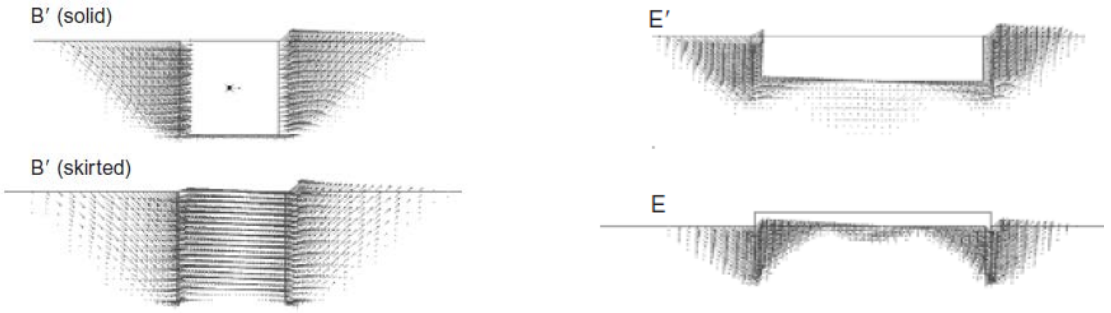

(c) Displacement mechanism at *d*/*B* = 1 (d) Displacement mechanism at *d*/*B* = 0.2

Figure 2.21: Solid and skirted strip footing in normally consolidated soil (Bransby and Yun, 2009)

The difference between the solid and skirted foundation capacity decreased with increasing embedment depth (and therefore increasing aspect ratio). For pure moment capacity M_0, an embedment depth ratio of greater than about *d*/*B* = 0.75 was required before

the calculated capacities were approximately the same as an equivalent solid foundation (Figure 2.22).

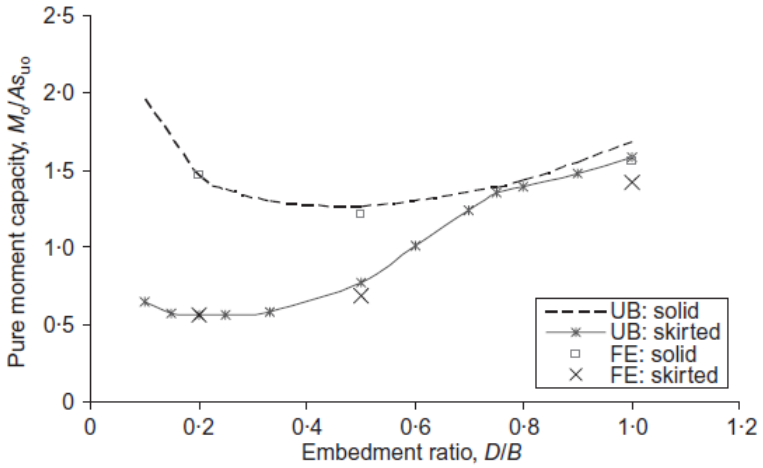

Figure 2.22: Comparison between solid and skirted foundation moment capacity for normally consolidated soil (Bransby and Yun, 2009)

2.3 Bearing capacity of perforated foundations

In the literature, limited attention has been given to the bearing capacity of perforated foundations, and no geotechnical design guidance is provided in design codes. Other design aspects of perforated foundations have been addressed in design codes, such as DNV (2009) which provides guidance on hydrodynamic loading during installation based on percentage foundation perforation. However, concepts for conventional foundation bearing capacity described previously in this chapter may also be adopted for perforated foundations. This section gives a summary of research that has been undertaken, firstly for undrained conditions, then for grillages on sand.

2.3.1 Undrained bearing capacity of perforated foundations

Perforated foundations can be an attractive foundation solution for offshore environments. Compared with equivalent solid foundations, they can have reduced material requirements (thereby reducing cost). This also allows for easier offshore handling due to the lower weight. Hydrodynamic forces are also decreased during deployment as waves and currents can pass

through the perforated area. If required, perforations can be configured to reduce uplift resistance. This allows easier foundation retrieval for re-use, or to enable material recycling.

Perforated foundations are commonly used as mudmats to support subsea infrastructure including pipeline end manifolds and terminations (Figure 2.23(a)). Subsea mudmats such as these are often limited to dimensions of approximately width, B = 5 m and length L = 10 m so that handling offshore is manageable. They should be designed to include sufficient perforations to allow water to escape during installation and allow release of under-base suction on decommissioning (Fisher and Cathie, 2002). Perforated foundations can also be functional design solution for larger fixed-bottom foundations, such as those for offshore wind turbines or oil and gas platforms (Figure 2.23(b)). These foundations often have a single central perforation resulting in a ring or annular type foundation. Foundations for this type of structure may have a width in excess of 50 m (Tuturea and Jackson, 2002, Pinna et al., 2009).

In some cases skirts may be used beneath perforated foundations to achieve additional bearing capacity, or to address other design issues such as scour protection. For subsea infrastructure, the skirt embedment depth d is typically in the range of $0.05 \leq d/B \leq 0.2$. For larger fixed-bottom foundations this range is typically $0.2 \leq d/B \leq 0.5$ (Mana et al., 2013).

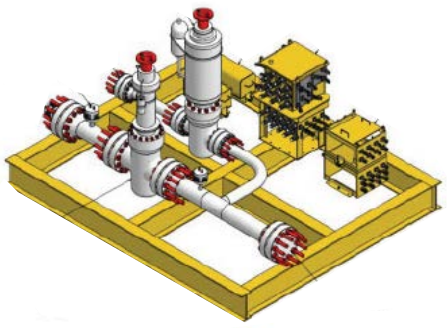

(a) Perforated foundation supporting subsea pipline valve (Banimahd et al., 2010)

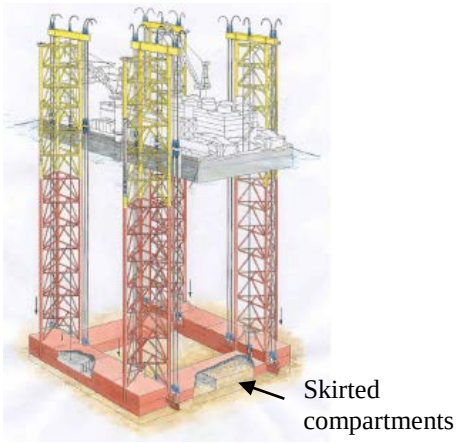

(b) Hang Tuah platform (Tuturea and Jackson, 2002)

Figure 2.23: Perforated offshore foundations

2.3.1.1 Vertical load capacity

Martin and Hazell (2005) used plasticity analysis to examine the vertical bearing capacity of closely spaced parallel strip foundations. This case can represent a simplification of 3D geometries such as a perforated mudmat constructed from bi-directional beams. Although simplified, analysis in 2D can be used to examine the general effect of the perforations. The cases of two strips and of regularly spaced multiple strips that were analysed are shown in Figure 2.24. Strips of width B^* (assumed to be rigidly connected by some superstructure) are arranged at an edge to edge spacing S to make up the overall foundation of width W.

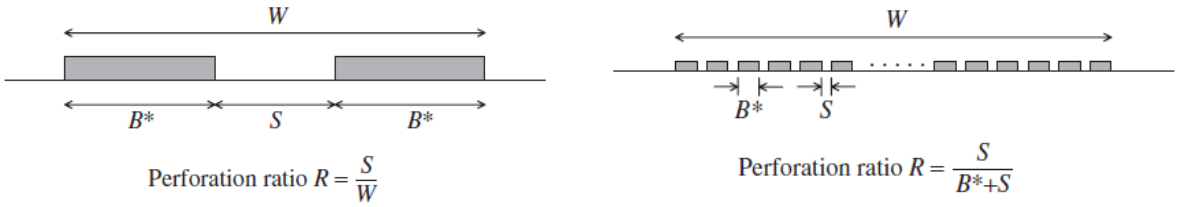

(a) Two strip foundation (b) Multiple strip foundation

Figure 2.24: 2D geometry of perforated foundations (Martin and Hazell, 2005)

Two closely spaced strip foundations can provide greater bearing capacity than the same two footings acting independently. The benefit can be quantified in terms of the 'efficiency' provided, being the ratio of overall capacity of the two strips together to the sum of their individual capacities. Martin and Hazell (2005) found a peak efficiency for parallel rough strip foundations of 1.07 at a spacing of 0.15B (Figure 2.25(a)), a result first obtained by Mandel (1963). The initial increase in efficiency reflects soil arching over the gap resulting in overall failure occurring. Efficiency diminishes once the spacing has increased such that there is a transition from overall failure to squeezing type failure. Gourvenec and Steinepreis (2007) found the peak efficiency using finite element modelling to be 1.05 at a spacing of 0.25B as shown in Figure 2.25(b). When embedded, the strip footings were found to exhibit a lower peak efficiency value (Gourvenec and Jensen, 2009). Martin and Hazell

(2005) indicated there to be no increase in efficiency for smooth strip foundations on homogeneous clay.

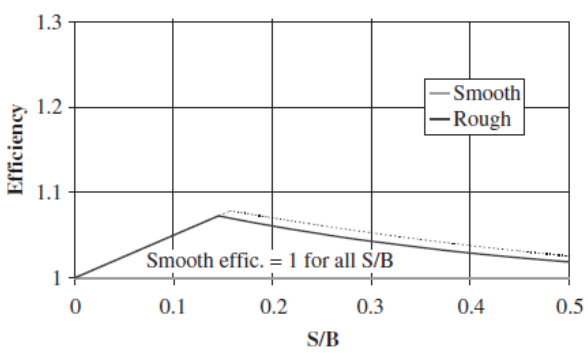

(a) Martin and Hazell (2005)

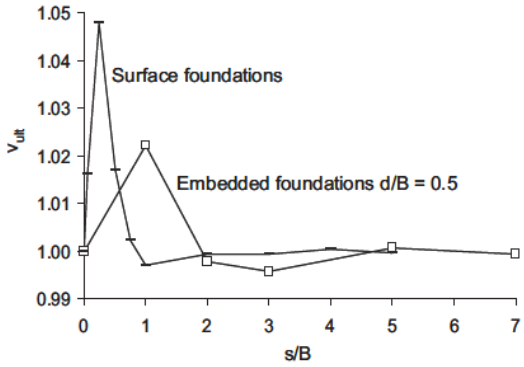

(b) Gourvenec and Jensen (2009)

Figure 2.25: Efficiency of two spaced strip foundations on homogeneous soil

Results by Martin and Hazell (2005) for a mudmat with multiple strips are given in Figure 2.26. A 'gross' bearing capacity factor $N_c = Q_u/Ws_{u0}$ has been defined from the ultimate vertical load Q_u using the overall foundation width W. The results show that at smaller perforation there is no reduction in capacity due to overall failure occurring, although this reduces with increasing non-homogeneity. Once squeezing failure occurs the bearing capacity reduces with increasing perforation ratio.

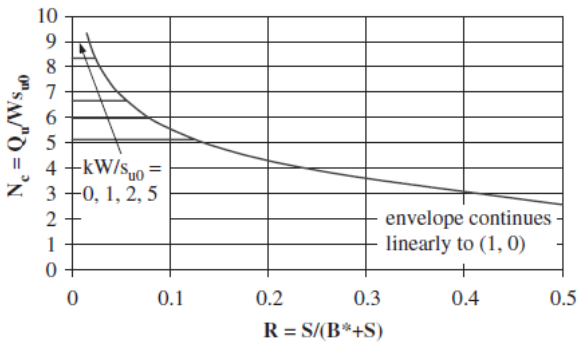

(a) Smooth

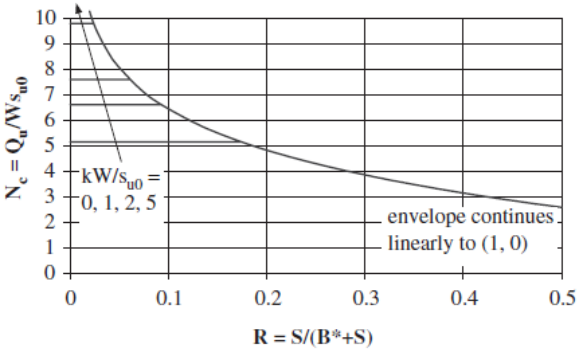

(b) Rough

Figure 2.26: 2D geometry of perforated foundations (Martin and Hazell, 2005)

White et al. (2005) conducted 1g experiments using model square mudmat foundations with square or circular perforations. Each model was penetrated into heterogeneous clay at a constant rate, held for an hour, and then extracted at the same rate. The results from the

experiments are shown in Figure 2.27 (the specific results for each geometry type were not disclosed by the authors). These results are also given in terms of a 'gross' bearing capacity factor N_c. The impact of the perforation was to reduce the bearing capacity factor N_c in proportion to the perforated area, although arching and shape effects were ignored.

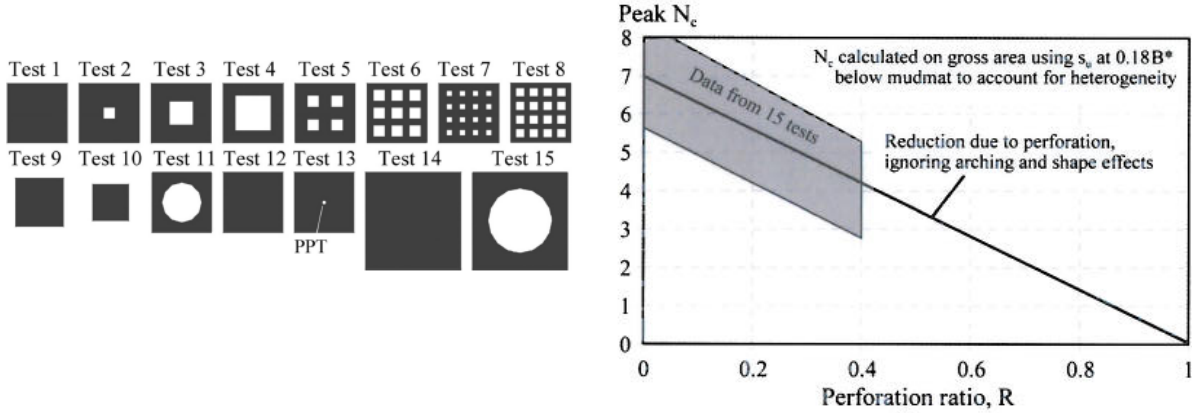

(a) Model details (b) Vertical loading results

Figure 2.27: Vertical loading experiments on perforated mudmat models (White et al., 2005)

The decrease in capacity with increasing perforation was expected because of two reasons:

i. The perforations reduced the actual contact area over which bearing resistance could be mobilised.

ii. Perforations, which reduce the effective strip width B^*, decreased the depth of the failure mechanism. This leads to a change in operative strength in the heterogeneous conditions.

For the extraction tests, increasing perforation reduced the peak pullout resistance. This reduction was more dependent on the effective strip width B^* than on the perforated ratio, R. Other studies such as that by Lieng and Bjorgen (1995) have found mudmat perforations to be effective in reducing pullout resistance.

Limited work is available on the vertical load capacity of ring foundations. A FEA study was undertaken on smooth and rough ring foundations by Galloway (2004). Some results from this study are discussed further in Section 4.2.

2.3.1.2 Combined load capacity

Several studies have used 2D numerical analysis to examine the ultimate bearing capacity of parallel strip foundations on homogeneous clay under combined loading (Gourvenec and Steinepreis, 2007, Gourvenec and Jensen, 2009, Kelly, 2009). Failure envelopes were investigated under *V*:*H*:*M* loading for the case of strips with width *B* in which the clear spacing between them, *s*, was varied. The results showed that the moment capacity increases significantly with increased spacing (Figure 2.28, noting that the vertical axes have different scales). This was a result of the assumed kinematic constraint provided by the rigid connection between the two strip foundations. For embedded multiple foundations an additional increase in moment capacity is experienced. When embedded the horizontal capacity was also found to be enhanced as the kinematic constraint restricted the degree of rotation possible under horizontal load (Gourvenec and Jensen, 2009).

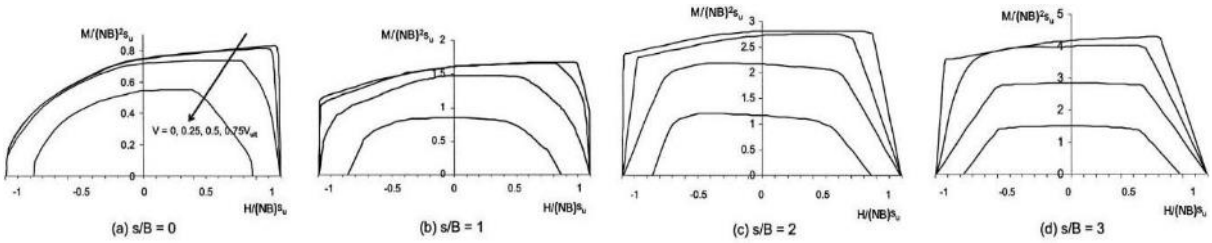

Figure 2.28: Failure envelopes for two strip foundations on clay (Gourvenec and Steinepreis, 2007)

In the above cases plane strain analysis was undertaken. Limited research has been undertaken to examine the capacity of 3D perforated foundations under combined loading, which is the focus of the research presented in this thesis.

2.3.2 Drained bearing capacity of grillage foundations

Grillage foundations consist of a series of vertical grilles, often vertical plates or steel beams, that are structurally connected together to form the foundation. They find application principally as mudmats for subsea infrastructure such as pipeline end manifolds or terminations (Figure 2.29). Grillage foundations used offshore are reported to have a typical

grille width, *t*, of 5 mm to 10 mm and height of 50 mm, with centre to centre spacing, *s*, ranging from 20 mm to 80 mm (Bransby et al., 2012). This corresponds to a perforation ratio *R* ranging from about 0.5 to 0.8.

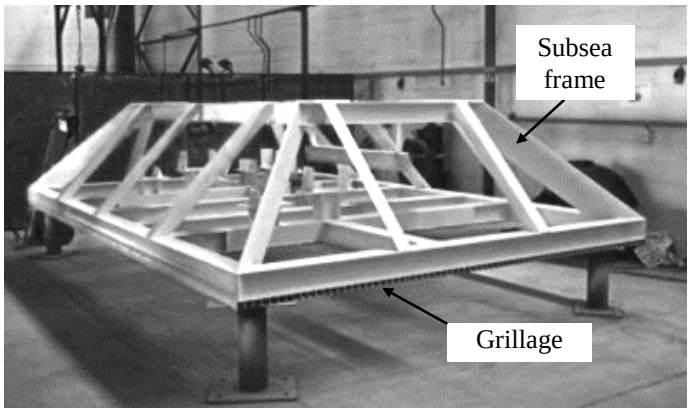

Figure 2.29: Subsea frame with grillage foundation (Bransby et al., 2012)

Grillages may be installed in i) a normally penetrated state, where the foundation (plus superstructure) is allowed to settle under its own weight, or ii) an over-penetrated state, in which the foundation is first preloaded to achieve a target embedment before being unloaded to the operating condition. During operation, offshore grillages are primarily subjected to combinations of vertical and horizontal load, but moment loading must also be accounted for in the design.

2.3.2.1 Vertical load capacity

The degree of interaction occurring between strip foundations on sand is much greater than for clay. Initial work on the vertical capacity of adjacent strip foundations on sand was undertaken by Stuart (1962), involving theoretical and small scale model investigations. The results showed that the bearing capacity of closely spaced footings increased by up to a factor of two compared with isolated footings. Similar tests were undertaken by Das and Larbi–Cherif (1983) which produced comparable results. More recently upper bound limit analysis and finite element analysis has also been used to investigate the problem (Kumar and Ghosh, 2007, Kumar and Kouzer, 2008).

The above studies involved minimal embedment and so their findings are not readily transferable to the case of grilles, which may penetrate to a depth several times their width. Grillage foundations exhibit two modes of behaviour as the grilles penetrate into the sand. As described by Bransby et al. (2012), initially upon penetration the sand moves easily up between the grilles and the foundation acts in 'coring' mode (Figure 2.30(a)). With increased penetration, the close grille spacing increases the vertical and horizontal stresses between grilles such that arching of the sand begins to develop (Figure 2.30(b)). With further penetration the grillage foundation exhibits 'plugging' behaviour (Figure 2.30(c)). Once the grillage foundation is in a plugged state it can be expected to have the same capacity as a flat plate foundation of equivalent overall width.

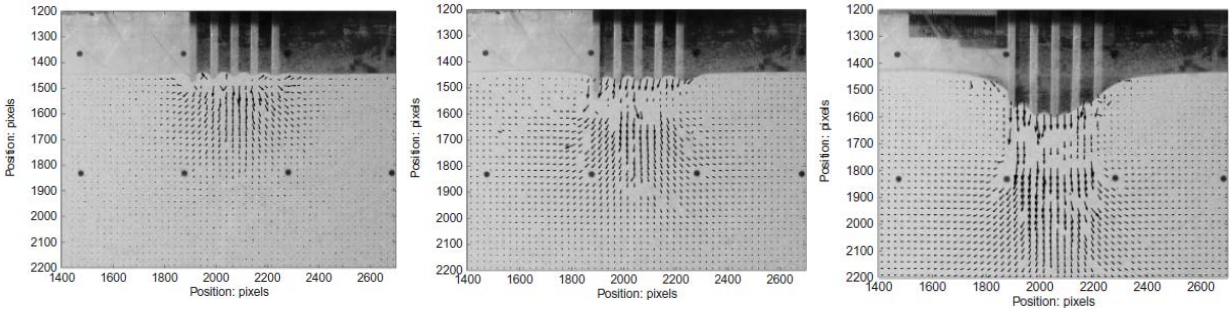

(a) Coring behaviour (b) Onset of plugging (c) Plugging behaviour

Figure 2.30: Incremental soil displacements during grillage penetration (Bransby et al., 2012)

Laboratory experiments were undertaken by Bransby et al. (2011, 2012) to assess the vertical bearing capacity of grillage foundations in loose and dense sand. The experiments consisted of measuring the penetration resistance of a grillage foundation section with the number of grilles ranging from $N = 2 – 8$ at spacing ratios ranging from $s/t = 2.5 – 8$. The results of these tests were used to develop an approximate design solution for the vertical capacity of a grillage foundation. The solution involved treating the grilles as plane strain piles such that the capacity of each grille is determined by summing the base resistance, Q_b and the side friction, Q_s. The total capacity of a foundation with N grilles is then given by:

$$V_o = N(Q_b + 2Q_s) \tag{2.15}$$

The base capacity of a grille of length L is determined using a standard pile end bearing equation:

$$Q_b = tL\sigma'_{vb}N_{qB} + 0.3\gamma' BN_\gamma tL \tag{2.16}$$

where σ'_{vb} is the vertical effective stress at the level of the grille tips and N_{qB} is taken from Berezantzev et al. (1961). The side friction component on each side of the grille with penetration depth z is:

$$Q_s = (0.5K\gamma' z\tan\delta)zL \tag{2.17}$$

where K is the lateral earth pressure coefficient and δ is the interface friction angle.

To account for the arching effect between closely spaced grilles, Bransby et al. (2012) considered the forces acting on a soil block of thickness dz as shown in Figure 2.31(a). Assessing the vertical equilibrium of the soil element, and taking $\tau = K\sigma'_v\tan\delta$, the vertical stress can be expressed as:

$$\sigma'_v = (e^{az} - 1)\frac{\gamma'}{a} \tag{2.18}$$

where $a = 2K\tan\delta/(s-t)$. This results in an increase in vertical stress and is a solution similar to that given by Randolph et al. (1991) for pipe piles.

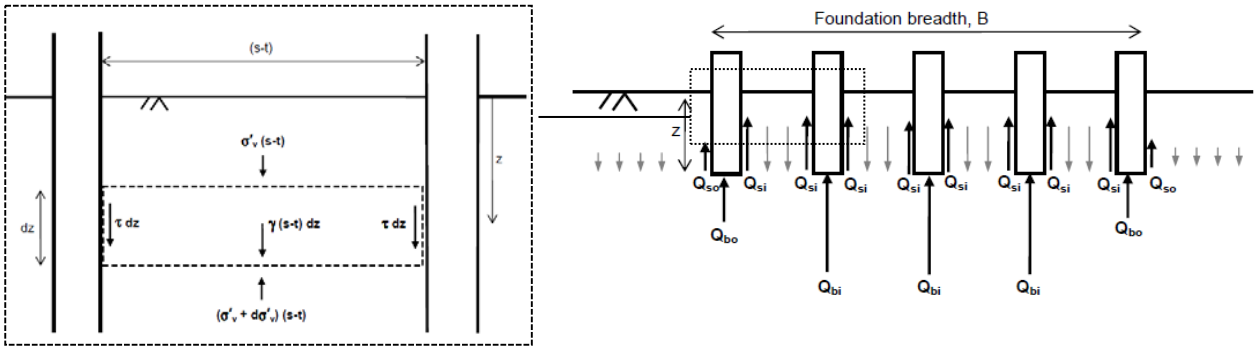

(a) Forces acting on soil block (b) Components of penetration resistance

Figure 2.31: Schematic of grillage penetration resistance (after Bransby et al. (2012))

The stress increase is incorporated into the design solution by accounting for the influence of increased overburden stress on end bearing and the influence of increased normal stress between the grilles on side friction. The end bearing and outside side friction of the grille at each end is considered not to be influenced by the arching effect. Subsequently, the total capacity of the grillage foundation is given by:

$$V_o = (N-2)Q_{bi} + 2Q_{bo} + 2(N-1)Q_{si} + 2Q_{so} \tag{2.19}$$

where the outside grille end bearing, Q_{bo} and side resistance, Q_{so} are given by Equations 2.16 and 2.17 respectively, the internal grille end bearing, Q_{bi} is given by Equation 2.17 with the σ'_{vb} term determined using Equation 2.18, and the internal side friction can be found to be:

$$Q_{si} = \frac{\gamma' L(s-t)}{2a}(e^{az} - az - 1) \tag{2.20}$$

These different components of penetration resistance are illustrated in Figure 2.31(b).

It was observed in the experiments that during the initial coring penetration the soil heaved between the grilles above the initial ground level. A modification to the analytical solution was proposed by Bransby et al. (2011) to account for the observed soil heave. The final height of the soil plug, z^* is calculated by:

$$z^* = z + \Delta H \tag{2.21}$$

where $\Delta H = z/(s/t - 1)$ which assumes the soil is displaced by the grille causing heave in a constant volume process. This can be considered appropriate for loose sand with no dilation.

A grillage foundation in the field would comprise a large number of grilles. Bransby et al. (2012) outlined a simplification to the full analytical load penetration solution (Equation 2.19) for such a case that $N>>1$ which is given by:

$$V_o = NtL\left(e^{az^*} - 1\right)\frac{\gamma'}{a}N_{qb} \tag{2.22}$$

Approximating the breath of a grillage foundation as $B \approx Ns$ for large values of N, Equation 2.22 can be expressed as a bearing stress as follows:

$$q = N_{qb}\frac{t}{s}\left(e^{az^*} - 1\right)\frac{\gamma'}{a} \tag{2.23}$$

When full plugging has occurred the capacity can be determined using existing methods for a flat plate footing.

2.3.2.2 Combined load capacity

Knappett et al. (2012) undertook experiments to investigate the capacity of grillages subject to *V*:*H* loading, using a range of sand densities. Based on the results, an expression for the *V*:*H* failure envelope was proposed. This was adapted from a general *V*:*H*:*M* failure surface expression employed by Martin (1994) as described in Section 2.2.3.2. The expression used by Knappett et al. (2012) is as follows:

$$f = \left(\frac{H}{H_0}\right)^2 - \beta\left(\frac{V}{V_0} + \chi\right)^{\beta_1}\left(1 - \frac{V}{V_0}\right)^{B_2} = 0 \tag{2.24}$$

where

$$\beta = \frac{(\beta_1 + \beta_2)^{(\beta_1+\beta_2)}}{{\beta_1}^{\beta_1}{\beta_2}^{\beta_2}(1+\chi)^{(\beta_1+\beta_2)}} \tag{2.25}$$

$H_0 = h_0 V_0$, and χ is an uplift capacity parameter. The failure surface shaping parameters β_1 and β_2 were both assumed to be 1. From regression analysis of the experimental data the normalised horizontal load capacity parameter h_0 and was found to be 0.23, 0.15 and 0.12 for loose, medium dense and dense soils respectively.

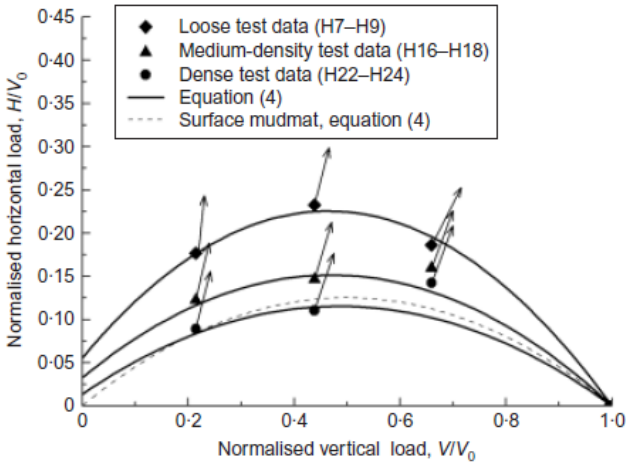

Figure 2.32: Normalised failure envelopes for a grillage (*s*/*t* = 4) (Knappett et al., 2012)

The results for the three soil conditions are shown in Figure 2.32. The loose soil condition gave the largest normalised failure envelope, and showed a significant increase in comparison to a solid surface mudmat. The result for the dense soil, having the smallest normalised failure envelope, was similar to that of a solid mudmat.

A numerical study by Banimahd et al. (2010) examined the combined loading capacity of grillage foundations using the FEA program Abaqus. Plane strain analysis of up to five adjacent strips was undertaken with width *b* and spacing *s* resting on the surface of loose sand with $\phi = 30°$. Load controlled simulations were conducted to define points on the *V*:*H* and *V*:*M* failure envelopes.

The *V*:*H* results are shown in Figure 2.33(a) for rough and relatively rough grillages. The results have been fitted with a failure envelope for each roughness condition. The proposed failure envelope is similar to that given by Gottardi and Butterfield (1993) for a single strip. This indicated that the grillage spacing did not have an important effect on the interaction between normalised vertical and horizontal loads. For the case of the *V*:*M* results shown in Figure 2.33(b) there is seen to be a more significant influence due to grillage spacing on the normalised moment capacity. From these results greater moment capacity is expected from a grillage compared to a strip foundation. The expressions defining the failure envelopes were not disclosed by Banimahd et al. (2010).

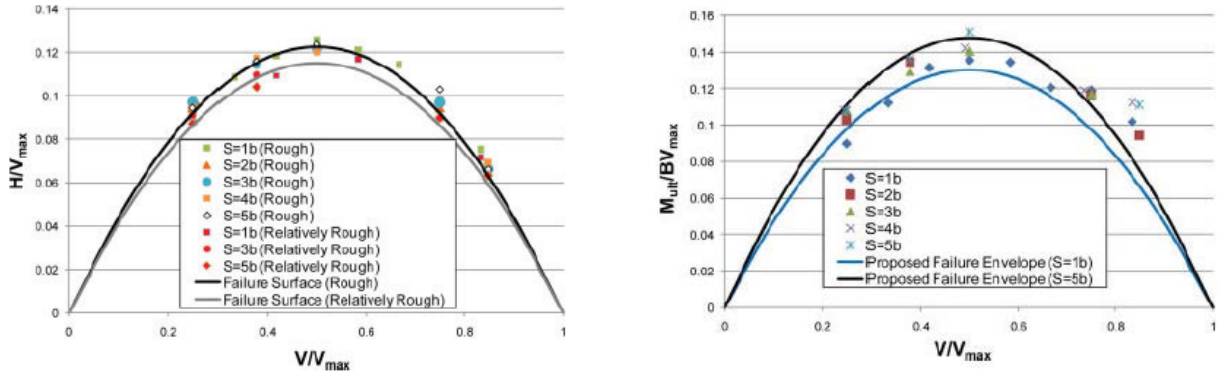

(a) *V*:*H* results (b) *V*:*M* results

Figure 2.33: Failure points for grillages of different spacing (Banimahd et al. (2010))

2.4 Summary

This chapter has provided a summary of key aspects of shallow foundation bearing capacity under conditions of both vertical and combined loading. Classical bearing capacity theory, which is commonly adopted in foundation design codes, has been discussed along with the more recent failure envelope assessment approach. Failure envelopes have been found to more accurately capture foundation capacity under combined loading. The shape of the failure envelope varies depending on the foundation geometry, embedment depth and the type of soil. Deriving an expression that is able to mathematically describe the form of the failure envelope for these different aspects is not straightforward.

The introduction of perforations can result in a decrease in vertical capacity due to the reduction of the net area over which bearing resistance can be mobilised. Perforations can also act to decrease the depth of the failure mechanism which leads to a lower operative strength in the case of a heterogeneous undrained strength profile. This can further add to the reduction in vertical capacity for the perforated foundation compared with a solid foundation of equivalent overall width. For the case of grillage foundations on sand, if the foundation is penetrated a sufficient depth then plugging of the sand between the grilles can occur. In this instance the same capacity as an equivalent solid foundation can be achieved. The moment capacity of strip foundations is increased as the spacing between them is increased. Limited research has been undertaken however for 3D perforated foundations under combined loading. This will be a focus of the thesis in subsequent chapters.

Chapter 3. Tresca plasticity and adaptive meshing in finite element analysis

The finite element method is widely used for the assessment of foundation bearing capacity and is adopted in this thesis to analyse perforated foundations. When analysing undrained problems the Tresca model is a common choice for defining the yield criterion of the soil. A disadvantage of adopting the Tresca failure criterion in finite element analysis (FEA) however is that the yield (and plastic potential) surface contains corners. Simplifications are commonly made to the yield and/or plastic potential functions in order to overcome this problem. It has been found though that such approaches may under-predict the collapse loads of shallow foundations. In addition, the accuracy of an FEA solution is sensitive to the refinement of the soil mesh and can require the analyst to experiment with the size and distribution of elements to try to find the best estimate bearing capacity solution.

In order to address i) the numerical implementation of Tresca soil and ii) the sensitivity of FEA solutions to mesh refinement, the following items have been developed:

1. A user material subroutine (UMAT) to implement the Tresca failure criterion for 2D and 3D models in Abaqus without it being necessary for the surface corners to be approximated.
2. An adaptive meshing scheme that automatically guides mesh refinement of the bearing capacity analysis by introducing more elements with successive iterations on the basis of plastic shear strain concentration.

This chapter describes the UMAT and the adaptive meshing scheme that have been implemented for use with Abaqus (although the methodology is not specific to this software). Analyses undertaken to verify the accuracy of the Tresca implementation are presented. Used

in combination, the Tresca UMAT and the adaptive meshing facility allow the Abaqus solutions to converge rapidly towards the exact plasticity solution as the mesh is refined. Particular attention is also given to assessing the suitability of this scheme to model square foundation geometry. This is because a square geometry is used extensively in this thesis for the purpose of investigating perforated foundations.

3.1 Tresca material subroutine (UMAT)

3.1.1 Finite element implementation of elasto-plastic models

Typically it is not appropriate to model soil as a purely elastic material, and plasticity theory is commonly drawn upon to enable the soil being modelled to exhibit yielding behaviour. In order to implement an elasto-plastic constitutive model (such as the Tresca criterion in this case) the following two key components must be established:

i) An elasto-plastic constitutive matrix, $\boldsymbol{D}^{ep}$ defining the relationship between stresses and strains:

Elasto-plastic models require the definition of a yield function, $f(\boldsymbol{\sigma})$ to separate purely elastic from elasto-plastic behaviour. The onset of inelastic behaviour occurs when

$$f(\boldsymbol{\sigma}) = 0 \tag{3.1}$$

A plastic potential, g must also be incorporated to define the direction of plastic straining. The plastic strain increments $d\boldsymbol{\varepsilon}^{\boldsymbol{p}}$ are derived from the plastic potential as given by Equation 3.2 (assuming g is smooth everywhere), which is referred to as the flow rule.

$$d\boldsymbol{\varepsilon}^{\boldsymbol{p}} = d\lambda \frac{\partial g}{\partial \boldsymbol{\sigma}} \tag{3.2}$$

In this equation $d\lambda$ is a positive plastic multiplier and $\frac{\partial g}{\partial \sigma}$ is the gradient of the plastic potential function. It is assumed that g is smooth everywhere, otherwise $\frac{\partial g}{\partial \sigma}$ may not be defined. For the case that $g = f$, the flow rule is considered associated. Otherwise if $g \neq f$ the flow rule is non-associated.

The elasto-plastic constitutive matrix $\boldsymbol{D}^{ep}$ provides a relationship between incremental stresses and strains as per Equation 3.3.

$$d\sigma = \boldsymbol{D}^{ep} d\varepsilon \tag{3.3}$$

Having defined the yield function, *f*, and the plastic potential function, *g*, the matrix for a perfectly plastic model can be given by (see e.g. Potts and Zdravovic, 1999):

$$\boldsymbol{D}^{ep} = \boldsymbol{D} - \frac{\boldsymbol{D}\frac{\partial g}{\partial \sigma}\left(\frac{\partial f}{\partial \sigma}\right)^{T}\boldsymbol{D}}{\left(\frac{\partial f}{\partial \sigma}\right)^{T}\boldsymbol{D}\frac{\partial g}{\partial \sigma}} \tag{3.4}$$

where $\boldsymbol{D}$ is the elastic constitutive matrix.

ii) A numerical method for integrating the stresses over a strain increment in the elasto-plastic finite element calculations:

A solution strategy is required to solve the governing finite element equations which are reduced to incremental form due to nonlinearity introduced by the elasto-plastic constitutive matrix:

$$\boldsymbol{K}_G{}^{i}\Delta\boldsymbol{d}_{nG}^{i} = \Delta\boldsymbol{R}_G{}^{i} \tag{3.5}$$

where $\boldsymbol{K}_G{}^{i}$ is the incremental global system stiffness matrix, $\Delta\boldsymbol{d}_{nG}^{i}$ is the vector of incremental nodal displacements, $\Delta\boldsymbol{R}_G{}^{i}$ is the vector of incremental nodal forces and *i* is the increment number. As the material behaviour is nonlinear, $\boldsymbol{K}_G{}^{i}$ is not constant but varies with the incremental stress and strain changes. For each strain increment from the solution of the governing equations, the stress must be updated at each integration point. A number of methods have been proposed for performing this integration. One approach is the return mapping method, which belongs to the class of implicit integration schemes.

The return mapping stress return scheme is illustrated in Figure 3.1. The stress point under consideration at the start of the increment is σ^A. This is shown in the elastic region ($f < 0$) but it could also lie on the yield surface ($f = 0$). The return mapping method involves first updating the stress, assuming that the material remains elastic. The elastic predictor

increment is shown as $\Delta\sigma^e$, which leads to the trial stress σ^B. If the elastic trial stress obtained lies outside the yield surface, the stress is projected onto the closest point on the yield surface. The addition of the plastic corrector increment $\Delta\sigma^p$ returns the stress to the final increment on the yield surface σ^C. This requires knowing the gradient of the yield surface. This projection or stress return ensures that the stress at the end of the increment does not violate the yield criterion. The plastic strains over the increment are calculated from the stress conditions corresponding to the end of the increment.

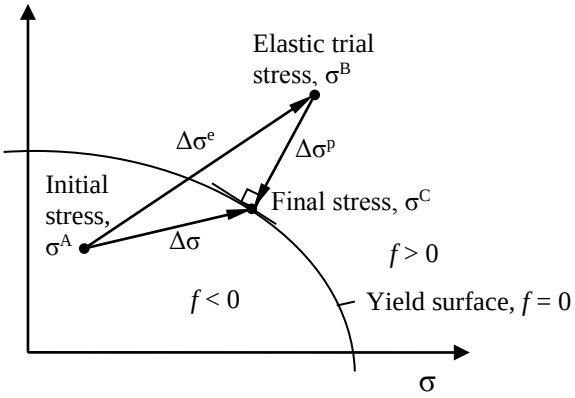

Figure 3.1: Principle of return mapping (after Clausen et al., 2006)

It is seen above that the formation of the elasto-plastic constitutive matrix and the stress update from the return mapping scheme requires the derivatives of the yield and plastic potential functions. This is problematic with Tresca as these derivatives cannot be uniquely defined at the vertices of the yield and plastic potential functions (refer to Figure 2.6).

3.1.2 Accommodating yield criterion with singularities

The Tresca criterion is regularly used in non-linear analyses of geotechnical problems and so several approaches have been used to tackle the numerical difficulties caused by the vertices. Three of these are summarised briefly:

i) Rounded Tresca: The non-differentiable corners are smoothed using analytical rounding techniques in order to make the failure surface continuously differentiable as indicated in Figure 3.2 (Sloan and Booker, 1986, Abbo and Sloan, 1995). A shorter

smoothing transition angle θ_T (i.e. θ_T closer to 30°) will providesimproved accuracy, although a transition too acute may result in ill-conditioning of the approximation (Taiebat and Carter, 2008). A 3D circular foundation was modelled in Abaqus by Andersen and Clausen (2009) using the rounded Tresca approach for the cases of θ_T = 25° and 29.5°. The result for θ_T = 25° was found to under-predict the result determined using a direct implementation of Tresca by about 2%, with a smaller under-prediction obtained when θ_T = 29.5° was used.

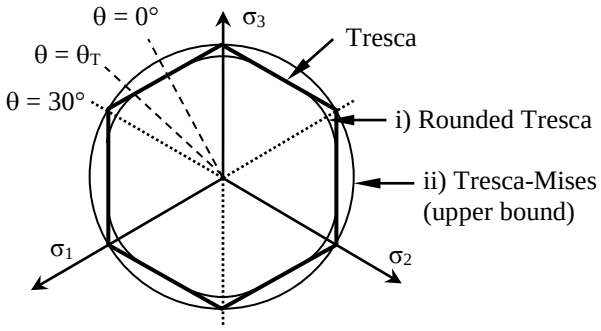

Figure 3.2: Methods for singularity removal from the Tresca criterion (after Taiebat and Carter, 2008)

ii) Tresca–Mises hybrid: The von Mises failure surface (which has a circular cross section in the deviatoric plane) is used to approximate the Tresca criterion by adjusting the radius of the circular failure surface, for example to circumscribe the Tresca hexagon as shown in Figure 3.2 (Taiebat and Carter, 2008). The built-in Abaqus implementation of Tresca (achieved using the Mohr-Coulomb model by setting the friction and dilation angles to 0) partially adopts this approach by using a von Mises surface for the plastic potential (though not the yield function). Analysis using this approach, for cases other than plane strain where the plastic strain vectors are the same in either case, has been found to under-predict the bearing capacity of shallow foundations (Taiebat and Carter, 2000, Gourvenec and Randolph, 2003, Mana et al., 2010). This is in contrast with the expectation that displacement based finite element solutions will tend to give too stiff a response and over-estimate plastic collapse loads (Randolph and Puzrin, 2003).

This was investigated in Abaqus by examining the bearing capacity of a rough circular footing of radius r = 1 m on uniform Tresca soil having an undrained shear strength of s_u = 1 kPa, a Young's modulus E =1000 kPa, and a Poisson's ratio v = 0.49. The mesh was created with second-order quadratic elements, where both full and reduced integration were used. The exact solution for the bearing capacity factor for this problem has been established as N_c = 6.048 (Table 2.2), where N_c relates to the maximum vertical bearing capacity V_{max} as per Equation 2.5. The results of the analysis, using manual refinement of a structured mesh, are shown in Figure 3.3. It can be seen that for both the cases of reduced and full integration the analysis results fall below the exact value for a rough circular foundation, approaching a value of around N_c = 5.83 (3.6% low). Taiebat and Carter (2008) also examined this case of a circular foundation in Abaqus and obtained a comparable result of N_c = 5.87 (2.9% low).

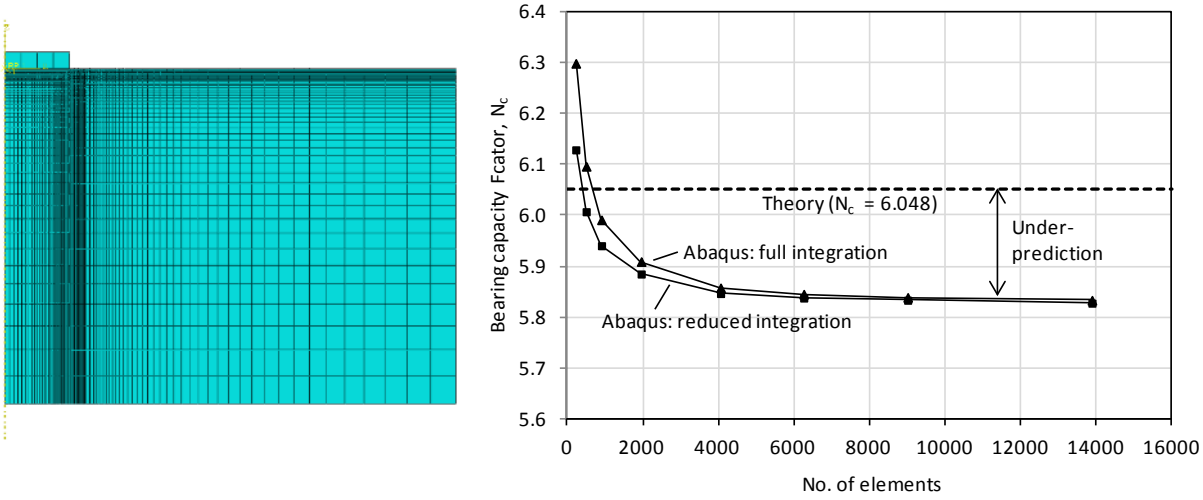

(a) Finite element mesh example (6,250 elements)

(b) Bearing capacity factor, N_c

Figure 3.3: Axisymmetric analysis of a rough circular foundation on Tresca soil

Gourvenec & Randolph (2003) noted that adopting fully integrated elements reduces the under-prediction of the exact solution compared with reduced integration elements. In Figure 3.3 however, the difference is seen to diminish with increasing mesh refinement, and full and reduced integration tend towards the same solution.

iii) Direct treatment of singularities: Several solutions have been proposed that are based on theory by Koiter (1953) enabling the vertex singularities to be accommodated. This theory says that a plastic strain vector at a vertex has to be a linear combination of the strain vectors on the two planes forming the vertex. Approaches such as Crisfield (1991) perform the derivations necessary for the stress return and formation of the constitutive matrices in the general six dimensional stress space with the singularities remaining present. For isotropic materials, equivalent derivations can be carried out with a geometric approach in the three-dimensional principal stress space (Clausen et al., 2006, Clausen et al., 2007, Hazell, 2008). This is advantageous as it reduces the dimensionality of the problem from six to three, and enables the stress states to be visualised graphically. This approach has been adopted in the UMAT described in this chapter.

3.1.3 Tresca UMAT subroutine

A user material subroutine (UMAT) was developed to implement the Tresca model in Abaqus without smoothing or other approximations. The subroutine, written in Fortran, is called by Abaqus/Standard to implement the constitutive model. It takes the stresses at an integration point at the start of an increment, together with the strains to be applied during the increment, and returns the updated stress at the end of the increment. The implementation is valid for three-dimensional, two-dimensional plane strain and axisymmetric stress states. The algorithm used in the UMAT follows the approach described by Clausen et al. (2006)who apply the method to a Mohr-Coulomb material. Simplifications can be made for the case of a Tresca material. Simplifications similar to those used by Hazell (2008) have been implemented, with extensions made to enable three-dimensional stress cases. The basic steps implemented by the UMAT are as follows:

1. The initial stress $\boldsymbol{\sigma}^A$ and the total strain increment $\Delta\varepsilon$ are used to calculate the elastic trial stress, $\boldsymbol{\sigma}^B$

2. The elastic trial stress $\boldsymbol{\sigma}^B$ is transformed into principal stress space to become $\boldsymbol{\sigma'}^B$
3. If $\boldsymbol{\sigma'}^B$ lies outside the yield surface, the plastic corrector $\Delta\boldsymbol{\sigma}^p$ is determined such that $\boldsymbol{\sigma'}^C$ is on the yield surface. Otherwise, $\boldsymbol{\sigma}^C = \boldsymbol{\sigma}^B$ is returned
4. The elasto-plastic constitutive matrix, $\boldsymbol{D'}^{ep}$ is calculated
5. The consistent elasto-plastic constitutive matrix, $\boldsymbol{D'}^{epc}$ is calculated
6. $\boldsymbol{\sigma'}^C$ and $\boldsymbol{D'}^{epc}$ are transformed back into Cartesian stress space so the inputs are returned as $\boldsymbol{\sigma}^C$ and $\boldsymbol{D}^{epc}$

The above steps are described in more detail in the following sections. The derivations presented follow the notation used by Clausen et al. (2007) where bold symbols are used to denote vectors or matrices. The formulations presented are for the case of a three-dimensional stress space where stress and strain vectors are ordered according to:

$$\boldsymbol{\sigma} = [\sigma_x \quad \sigma_y \quad \sigma_z \quad \tau_{xy} \quad \tau_{xz} \quad \tau_{yz}]^T \tag{3.6}$$
$$\boldsymbol{\varepsilon} = [\varepsilon_x \quad \varepsilon_y \quad \varepsilon_z \quad 2\varepsilon_{xy} \quad 2\varepsilon_{xz} \quad 2\varepsilon_{yz}]^T$$

For plane strain or axisymmetric problems, the stress and strain vectors in two dimensions are:

$$\boldsymbol{\sigma} = [\sigma_x \quad \sigma_y \quad \sigma_z \quad \tau_{xy}]^T \tag{3.7}$$
$$\boldsymbol{\varepsilon} = [\varepsilon_x \quad \varepsilon_y \quad \varepsilon_z \quad 2\varepsilon_{xy}]^T$$

In the case of axisymmetry *x*, *y*, *z* are taken as cylindrical coordinates of *r* (radial direction), *z* (vertical direction) and θ (circumferential direction) respectively. The details described next for a three-dimensional stress space are also applicable for two dimensions, although some adjustment is required for the transformation between stress spaces and the formulation of the consistent constitutive matrix (see Clausen et al. (2007) for example).

3.1.3.1 Return mapping details

The basic assumption of a return mapping scheme is that a strain increment, $d\boldsymbol{\varepsilon}$ is made up of a elastic component, $d\boldsymbol{\varepsilon}^e$ and a plastic component $d\boldsymbol{\varepsilon}^p$ such that

$$d\boldsymbol{\varepsilon} = d\boldsymbol{\varepsilon}^{\boldsymbol{e}} + d\boldsymbol{\varepsilon}^{\boldsymbol{p}} \tag{3.8}$$

The elastic stress increment can be determined by using Hooke's law

$$d\boldsymbol{\sigma} = \boldsymbol{D}d\boldsymbol{\varepsilon}^{\boldsymbol{e}} = \boldsymbol{D}(d\boldsymbol{\varepsilon} - d\boldsymbol{\varepsilon}^{\boldsymbol{p}}) \tag{3.9}$$

where $\boldsymbol{D}$ is the elastic constitutive matrix. Integration of Equation 3.9 for a finite strain increment yields a finite stress increment

$$\Delta\boldsymbol{\sigma} = \boldsymbol{D}\Delta\boldsymbol{\varepsilon} - \boldsymbol{D}\Delta\boldsymbol{\varepsilon}^{\boldsymbol{p}} = \Delta\boldsymbol{\sigma}^{\boldsymbol{e}} - \Delta\boldsymbol{\sigma}^{\boldsymbol{p}} \; or \; \Delta\boldsymbol{\sigma}^{\boldsymbol{C}} = \Delta\boldsymbol{\sigma}^{\boldsymbol{B}} - \Delta\boldsymbol{\sigma}^{\boldsymbol{p}} \tag{3.10}$$

where $\Delta\boldsymbol{\sigma}^{\boldsymbol{e}} = \boldsymbol{D}\Delta\boldsymbol{\varepsilon}$ is the elastic predictor increment and $-\Delta\boldsymbol{\sigma}^{\boldsymbol{p}}$ is the plastic corrector. The final stress $\boldsymbol{\sigma}^{\boldsymbol{C}}$ is obtained from the trial stress by subtracting $\boldsymbol{\Delta\sigma}^{\boldsymbol{p}}$ which is given by:

$$\Delta\boldsymbol{\sigma}^{\boldsymbol{p}} = \int_{\lambda}^{\lambda+\Delta\lambda} \boldsymbol{D}\frac{\partial g}{\partial \boldsymbol{\sigma}} d\lambda \tag{3.11}$$

This can be evaluated numerically as

$$\Delta\boldsymbol{\sigma}^{\boldsymbol{p}} = \Delta\lambda \boldsymbol{D}\frac{\partial g}{\partial \boldsymbol{\sigma}}\bigg|_{P} \tag{3.12}$$

where the subscript P indicates the point on the integration path at which the gradient of the plastic potential function is to be evaluated. For fully implicit integration (backward Euler scheme), P corresponds to evaluation at the (initially unknown) updated stress state $\boldsymbol{\sigma}^{\boldsymbol{C}}$ and so iteration is required. Otherwise, P could refer to evaluation at the predictor point $\boldsymbol{\sigma}^{B}$. For the case of a yield criterion such as Tresca that is linear in the principal stress space , the potential function gradient is constant along the integration path. As such it can be evaluated at $\boldsymbol{\sigma}^{B}$ with no loss of accuracy.

3.1.3.2 Return mapping with linear yield functions

Once the elastic predictor stress has been determined from Equation 3.9, the stresses must be transformed into principal stress space (see Section 3.1.3.7). Whilst in principal stress space, the stress point is returned to the yield surface before then being transformed back to the original coordinate system. The change back to the original coordinate system is

straightforward as the principal stress directions are unchanged during the return to the yield surface, with the shear stresses remaining zero.

For yield functions that are linear in the principal stresses, there are three possibilities for stress return (Figure 3.4):

1. Return to a yield plane
2. Return to a line (the intersection of two yield planes)
3. Return to a point (the intersection of three or more yield planes). This case is not required for a Tresca material. However, if a stress is to be returned to a singularity point $\boldsymbol{\sigma}^a$ (as may be the case for a Mohr-Coulomb material) then the returned stress would be $\boldsymbol{\sigma}^C = \boldsymbol{\sigma}^a$.

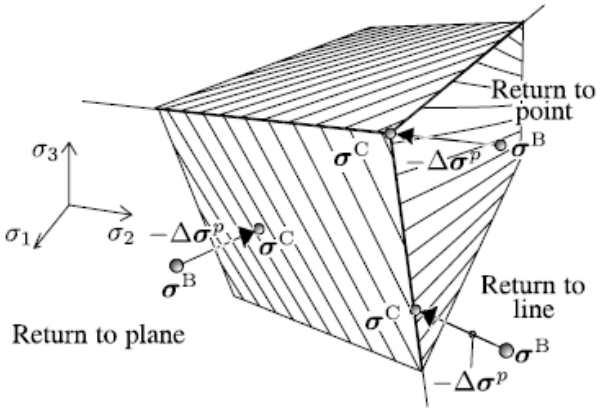

Figure 3.4: Intersecting yield planes with three types of stress return (Clausen et al., 2007)

The hexagonal prism formed by the Tresca criterion in the principal stress space can be defined by six yield functions. Following the notation of Hazell (2008):

$$\begin{aligned} f_1(\boldsymbol{\sigma}, s_u) &= \sigma_1 - \sigma_2 - 2s_u & f_2(\boldsymbol{\sigma}, s_u) &= \sigma_2 - \sigma_1 - 2s_u \\ f_3(\boldsymbol{\sigma}, s_u) &= \sigma_2 - \sigma_3 - 2s_u & f_4(\boldsymbol{\sigma}, s_u) &= \sigma_3 - \sigma_2 - 2s_u \\ f_5(\boldsymbol{\sigma}, s_u) &= \sigma_3 - \sigma_1 - 2s_u & f_6(\boldsymbol{\sigma}, s_u) &= \sigma_1 - \sigma_3 - 2s_u \end{aligned} \tag{3.13}$$

The six yield planes, S_1 – S_6, are shown in Figure 3.5 along with the six lines formed between the edges of the planes. If the principal stresses are ordered according to $\sigma_1 \geq \sigma_2 \geq \sigma_3$ then the stresses can only return to one of the stress planes or its two adjacent lines. This stress plane is referred to as the primary yield plane and in Figure 3.5 corresponds to plane surface S_6.

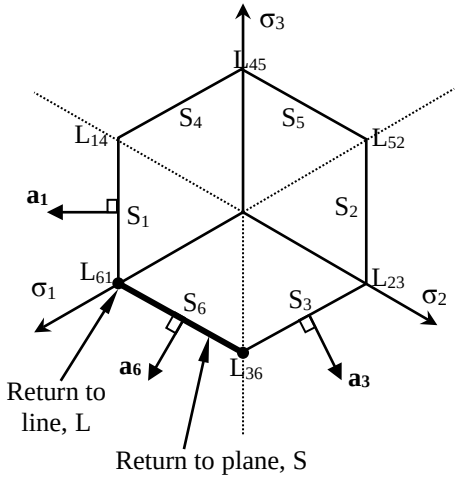

Figure 3.5: Plane surfaces forming the Tresca yield surface with primary plane S_6 in bold, and the directions of the gradients $\boldsymbol{a}$ of applicable yield functions (after Hazell, 2008)

3.1.3.3 Return to a plane

When returning the stress state to a plane, the following solution for the incremental plastic multiplier $\Delta\lambda$ can be used (Clausen et al., 2007):

$$\Delta\boldsymbol{\lambda} = \frac{f}{\boldsymbol{b}^T\boldsymbol{D}\boldsymbol{a}}\boldsymbol{D}\boldsymbol{b} \tag{3.14}$$

where $\boldsymbol{a} = \frac{\partial f}{\partial \sigma}$ and $\boldsymbol{b} = \frac{\partial g}{\partial \sigma}$ are the yield plane and plastic potential gradients in principal stress space respectively, and $\boldsymbol{D}$ is the elastic constitutive matrix. For the case of associated flow $\boldsymbol{b} = \boldsymbol{a}$, such that together with Equation 3.12, the plastic corrector can be found by

$$\Delta\boldsymbol{\sigma^p} = \frac{f(\boldsymbol{\sigma}^B)}{\boldsymbol{a}^T\boldsymbol{D}\boldsymbol{a}}\boldsymbol{D}\boldsymbol{a} = f(\boldsymbol{\sigma}^B)\boldsymbol{r}^p, \qquad \text{where } \boldsymbol{r}^p = \frac{\boldsymbol{D}}{\boldsymbol{a}^T\boldsymbol{D}\boldsymbol{a}} \tag{3.15}$$

where $\boldsymbol{r}^p$ is the direction of the plastic corrector in principal stress space. For the principal plane S_6 (see Figure 3.5), the surface gradient is $\boldsymbol{a} = [1, 0, -1]^T$. Substituting $\boldsymbol{a}$ along with $\boldsymbol{D}$ in

Equation 3.15 results in $\boldsymbol{r}^p = [½, 0, -½]^T$. The stress at the end of the increment is therefore expressed by

$$\boldsymbol{\sigma}^C = \begin{bmatrix} \sigma_1^B \\ \sigma_2^B \\ \sigma_3^B \end{bmatrix} - \begin{bmatrix} ½ \\ 0 \\ -½ \end{bmatrix} f_6 \tag{3.16}$$

where the yield function f_6 is evaluated at the trial stress $\boldsymbol{\sigma}^B$.

When the updated stress is located on a yield plane, the elasto-plastic matrix $\boldsymbol{D}_f^{ep}$ is as per Equation 3.4, although for the case with an associated flow it can be expressed as

$$\boldsymbol{D}_f^{ep} = \boldsymbol{D} - \frac{\boldsymbol{D}\boldsymbol{a}\boldsymbol{a}^T\boldsymbol{D}}{\boldsymbol{a}^T\boldsymbol{D}\boldsymbol{a}} \tag{3.17}$$

3.1.3.4 Return to a line

When returning to a line the plastic corrector $\Delta\boldsymbol{\sigma}^{\boldsymbol{p}} = \Delta\lambda\boldsymbol{D}\mathbf{a}$ is unknown. However, with an associated flow rule the direction of the plastic strain increment $\boldsymbol{a}$ must be perpendicular to the line in principal stress space. Using this orthogonality condition the final stress $\boldsymbol{\sigma}^C$ can be obtained.

In principal stress space a line can be represented as

$$\sigma = t\boldsymbol{r}^l + \boldsymbol{\sigma}^l \tag{3.18}$$

where t is a parameter with the dimensions of stress, $\boldsymbol{r}^l$ is a vector in the direction of the line, and $\boldsymbol{\sigma}^l$ is a point in principal stress space that lies on the line. It is shown in Clausen et al. (2007) that t is described by

$$t = \frac{\left(\boldsymbol{r}_g^l\right)^T \boldsymbol{D}^{-1}\left(\boldsymbol{\sigma}^B - \boldsymbol{\sigma}^l\right)}{\left(\boldsymbol{r}_g^l\right)^T \boldsymbol{D}^{-1}\boldsymbol{r}^l} \tag{3.19}$$

such that the final stress $\boldsymbol{\sigma}^C$ is obtained by inserting this value of t into Equation 3.18. In this expression $\boldsymbol{r}_g^l$ is the direction of the plastic potential line. With an associated flow rule, $\boldsymbol{r}_g^l$ is perpendicular to the direction $\boldsymbol{a}$ of the plastic strain increment, and is thereby in the same directions as $\boldsymbol{r}^l$.

For the Tresca model, where ordering of the principal stresses has been undertaken resulting in a primary plane as shown in Figure 3.5, a stress return may be required to either line L_{61} or L_{36}. In these cases, $\boldsymbol{r}^l (= \boldsymbol{r}_g^l$ for associated flow) for L_{61} is given by $(\boldsymbol{a}_6 \times \boldsymbol{a}_1)$ and for L_{36} is $(\boldsymbol{a}_3 \times \boldsymbol{a}_6)$. Evaluation of Equation 3.19 results in:

$$t = \tfrac{1}{3}(\sigma_1^B + \sigma_2^B + \sigma_3^B) + \tfrac{2}{3}s_u \tag{3.20}$$

Using Equation 3.18, the stress return for the possible lines is:

$$\boldsymbol{\sigma}^C = t\boldsymbol{r}^l + \boldsymbol{\sigma}^l = \begin{bmatrix} \frac{1}{3}(\sigma_1^B + \sigma_2^B + \sigma_3^B) + \frac{2}{3}s_u \\ \frac{1}{3}(\sigma_1^B + \sigma_2^B + \sigma_3^B) + \frac{2}{3}s_u \\ \frac{1}{3}(\sigma_1^B + \sigma_2^B + \sigma_3^B) + \frac{2}{3}s_u \end{bmatrix} + \boldsymbol{\sigma}^l \text{ where } \quad \begin{matrix} L_{61}\text{: } \boldsymbol{\sigma}^l = [-2s_u \quad 0 \quad 0]^T \\ L_{36}\text{: } \boldsymbol{\sigma}^l = [0 \quad 0 \quad -2s_u]^T \end{matrix} \tag{3.21}$$

As demonstrated by Hazell (2008), it is convenient to manipulate the above into the form of Equation 3.10 as $\boldsymbol{\sigma}^C = \boldsymbol{\sigma}^B - \Delta\boldsymbol{\sigma}^p$:

$$L_{61}\text{: } \boldsymbol{\sigma}^C = \begin{bmatrix} \sigma_1^B \\ \sigma_2^B \\ \sigma_3^B \end{bmatrix} - \begin{bmatrix} \frac{1}{3} & \frac{1}{3} \\ -\frac{2}{3} & \frac{1}{3} \\ \frac{1}{3} & -\frac{2}{3} \end{bmatrix} \begin{bmatrix} f_6 \\ f_1 \end{bmatrix} \qquad L_{36}\text{: } \boldsymbol{\sigma}^C = \begin{bmatrix} \sigma_1^B \\ \sigma_2^B \\ \sigma_3^B \end{bmatrix} - \begin{bmatrix} -\frac{1}{3} & \frac{2}{3} \\ \frac{2}{3} & -\frac{1}{3} \\ -\frac{1}{3} & -\frac{1}{3} \end{bmatrix} \begin{bmatrix} f_3 \\ f_6 \end{bmatrix} \tag{3.22}$$

The elasto-plastic constitutive matrix on a line $\boldsymbol{D}_l^{ep}$ is derived in Clausen et al. (2007) and can be described by

$$\boldsymbol{D}_l^{ep} = \boldsymbol{G} + \widehat{\boldsymbol{D}}_l^{ep}, \qquad \boldsymbol{G} = \frac{E}{2(1+\nu)} \begin{bmatrix} \boldsymbol{0}_{3\times3} & \boldsymbol{0}_{3\times3} \\ \boldsymbol{0}_{3\times3} & \boldsymbol{I}_{3\times3} \end{bmatrix} \tag{3.23}$$

where **G** is the shear stiffness and $\widehat{\boldsymbol{D}}_l^{ep}$ is a 6 x 6 matrix that contains the elements related to normal stresses

$$\widehat{\boldsymbol{D}}_l^{ep} = \frac{\boldsymbol{r}^l (\boldsymbol{r}_g^l)^T}{(\boldsymbol{r}^l)^T \boldsymbol{D}^{-1} \boldsymbol{r}_g^l} \tag{3.24}$$

Again, for the case of associated flow $\boldsymbol{r}^l = \boldsymbol{r}_g^l$.

3.1.3.5 Determining the type of stress return required

A concept of stress regions introduced by Clausen et al. (2006) is used to determine the type of stress return required for a given elastic trial stress $\boldsymbol{\sigma}^B$. Each plane or line on the yield surface has a region of principal stress space associated with it. When a given trial stress is located with a particular stress region it is returned to the corresponding line or plane (or point for yield surfaces with an apex). The orientation of the boundary between the regions for a plane S_i and its edge L_{ij} is defined by the direction $\boldsymbol{r}_i^P$ of the plastic corrector for the plane, and the direction of the line $\boldsymbol{r}_{ij}^l$. The normal n_{i-ij}^T to the boundary plane is given by the cross product $\boldsymbol{r}_i^P \times \boldsymbol{r}_{ij}^l$, so the equation of the boundary line plane is

$$p_{i-ij}(\boldsymbol{\sigma}) = n_{i-ij}^T\left(\boldsymbol{\sigma} - \boldsymbol{\sigma}^l\right) = \left(\boldsymbol{r}_i^P \times \boldsymbol{r}_{ij}^l\right)^T\left(\boldsymbol{\sigma} - \boldsymbol{\sigma}^l\right) = 0 \tag{3.25}$$

The stress region boundaries for Tresca relevant for the ordering of the principal stresses are shown in Figure 3.6. As conditions of associated flow are adopted, the boundaries of the stress region associated with plane S_6 are a pair of perpendicular planes passing through the lines at the edge of the face.

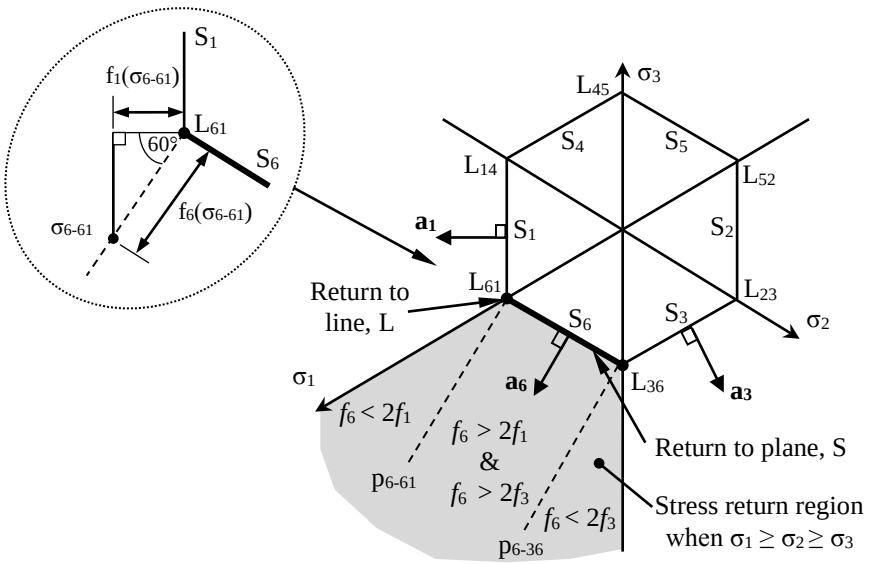

Figure 3.6: Boundaries for stress regions associated with returns to plane S_6 and lines L_{61} and L_{36} (after Hazell, 2008)

The geometry of the Tresca yield surface means that simple relationships exist between the values of the yield functions on the stress region boundaries (Hazell, 2008). For example, the inset in Figure 3.6 shows a point $\sigma_{6\text{-}61}$ in principal stress space that lies on the boundary $p_{6\text{-}61}$. At any point on this plane $f_6 = 2f_1$ so it acts to separate the principal stress space into half with $f_6 > 2f_1$ and the other with $f_6 < 2f_1$. Similar relationships can be derived for the other boundary planes. The resulting inequalities relevant to the primary plane and associated lines are shown in Figure 3.6. By using these inequalities the stress region for an elastic trial stress can be determined from the values of the yield functions at that stress point.

A state variable was included in the UMAT to allow the stress regions being returned from to be plotted for visual inspection.

3.1.3.6 Consistent constitutive matrix

In global iterations the convergence will be slow if $\boldsymbol{D}^{ep}$ is used, as the stress and strain increments are finite rather than infinitesimal (Clausen et al., 2007). Clausen et al. (2007) describe the following relation between changes in finite stress and strain increments:

$$d\Delta\boldsymbol{\sigma} = \boldsymbol{D}^{epc} d\Delta\boldsymbol{\varepsilon} \tag{3.26}$$

in which $\boldsymbol{D}^{epc}$ is referred to as the consistent constitutive matrix which is consistent with the Newton iteration scheme, preserving the quadratic rate of convergence. It is shown in Clausen et al. (2007) that $\boldsymbol{D}^{epc}$ can be determined as per Equation 3.27 in which $\boldsymbol{T}$ and $\boldsymbol{D}^{c}$ are evaluated at $\boldsymbol{\sigma}^{C}$.

$$\boldsymbol{D}^{ep} = \boldsymbol{D}^{c} - \frac{\boldsymbol{D}^{c}\frac{\partial g}{\partial \sigma}\left(\frac{\partial f}{\partial \sigma}\right)^{T}\boldsymbol{D}^{c}}{\left(\frac{\partial f}{\partial \sigma}\right)^{T}\boldsymbol{D}^{c}\frac{\partial g}{\partial \sigma}} \tag{3.27}$$

$$\boldsymbol{T} = \left(\boldsymbol{I} + \Delta\lambda \boldsymbol{D}\frac{\partial^2 g}{\partial \boldsymbol{\sigma}^2}\bigg|_{C}\right)^{-1} \text{ and } \boldsymbol{D}^{c} = \boldsymbol{T}\,\boldsymbol{D}$$

For linear criteria it has been shown that the consistent constitutive matrix, $\boldsymbol{D}^{epc}$ can be calculated in a simpler manner at the stress predictor point, $\boldsymbol{\sigma}^{B}$ (Equation 3.28). Matrix inversion is avoided by this approach.

$$\boldsymbol{D}^{epc} = \boldsymbol{T}\,\boldsymbol{D}^{ep}$$
$$\boldsymbol{T} = \boldsymbol{I} - \Delta\lambda \boldsymbol{D} \left.\frac{\partial^2 g}{\partial \boldsymbol{\sigma}^2}\right|_{B} \tag{3.28}$$

In principal stress space $\Delta\lambda \boldsymbol{D} \frac{\partial^2 g}{\partial \boldsymbol{\sigma}^2}$ can be formed by geometrical arguments to take the form

$$\Delta\lambda \boldsymbol{D} \frac{\partial^2 g}{\partial \boldsymbol{\sigma}^2} = \begin{bmatrix} 0 & & & & & \\ & 0 & & & & \\ & & 0 & & & \\ & & & \frac{\Delta\sigma_1^p - \Delta\sigma_2^p}{\sigma_1 - \sigma_2} & & \\ & & & & \frac{\Delta\sigma_1^p - \Delta\sigma_3^p}{\sigma_1 - \sigma_3} & \\ & & & & & \frac{\Delta\sigma_1^p - \Delta\sigma_2^p}{\sigma_2 - \sigma_3} \end{bmatrix} \tag{3.29}$$

When the prediction stress is returned to L_{36} then $\left(\Delta\lambda \boldsymbol{D} \frac{\partial^2 g}{\partial \boldsymbol{\sigma}^2}\right)_{4,4} = 0$ and for the case of a stress return to L_{61} then $\left(\Delta\lambda \boldsymbol{D} \frac{\partial^2 g}{\partial \boldsymbol{\sigma}^2}\right)_{6,6} = 0$.

3.1.3.7 Transformation

To implement the return algorithm as has been described, the stresses received as inputs to the material subroutine must be transformed to principal stress space and then eventually restored to the original coordinate system. As the stress return preserves the principal stress directions the updated stress can readily be transformed back into the original coordinate system. The eigenvectors associated with the three principal stresses were determined using the Abaqus utility routine SPRIND. These form a coordinate transformation tensor $\boldsymbol{L}$:

$$\boldsymbol{L} = \begin{bmatrix} l_1 & m_1 & n_1 \\ l_2 & m_2 & n_2 \\ l_3 & m_3 & n_3 \end{bmatrix} \tag{3.30}$$

The stress in original Cartesian space $\boldsymbol{\sigma}$ is transformed to or from principal stress space to $\boldsymbol{\sigma}'$ as per the following:

$$\boldsymbol{\sigma}' = \boldsymbol{R}\boldsymbol{\sigma} \;\; or \;\; \boldsymbol{\sigma} = \boldsymbol{R}^{-1}\boldsymbol{\sigma}' \tag{3.31}$$

where $\boldsymbol{R}$ is the transformation matrix

$$\boldsymbol{R} = \begin{bmatrix} l_1^2 & m_1^2 & n_1^2 & 2l_1m_1 & 2l_1n_1 & 2m_1n_1 \\ l_2^2 & m_2^2 & n_2^2 & 2l_2m_2 & 2l_2n_2 & 2m_2n_2 \\ l_3^2 & m_3^2 & n_3^2 & 2l_3m_3 & 2l_3n_3 & 2m_3n_3 \\ l_1l_2 & m_1m_2 & n_1n_2 & l_1m_2 + l_2m_1 & l_1n_2 + l_2n_1 & m_1n_2 + m_2n_1 \\ l_1l_3 & m_1m_3 & n_1n_3 & l_1m_3 + l_3m_1 & l_1n_3 + l_2n_3 & m_1n_3 + m_2n_3 \\ l_2l_3 & m_2m_3 & n_2n_3 & l_2m_3 + l_3m_2 & l_2n_3 + l_3n_2 & m_2n_3 + m_3n_2 \end{bmatrix} \tag{3.32}$$

The elasto-plastic matrix $\boldsymbol{D^{ep}}$ is transformed according to

$$\boldsymbol{D}^{ep\prime} = \boldsymbol{R}\boldsymbol{D}^{ep}\boldsymbol{R}^{T} \;\; or \;\; \boldsymbol{D}^{ep} = \boldsymbol{R}^{-1}\boldsymbol{D}^{ep\prime}\boldsymbol{R}^{-T} \tag{3.33}$$

3.2 Validation of the Tresca UMAT

To verify the correct functioning of the UMAT several test case problems were analysed. These problems included:

1. Unconfined compression test of a three-dimensional (3D) soil block
2. Axisymmetric and 3D analysis of the vertical bearing capacity of a circular foundation
3. Vertical bearing capacity of a square foundation

3.2.1 Case 1: Unconfined compression test

The model used for the unconfined compression analysis of a soil block is shown in Figure 3.7. Symmetry was exploited by modelling only 1/8th of the soil block. Compression was applied by imposing a prescribed axial strain. A purely cohesive soil using the Tresca UMAT was modelled with an undrained shear strength, s_u = 1 kPa, Young's modulus E =1000 kPa and Poisson's ratio ν = 0.499. Two end conditions were considered: smooth platens and rough platens.

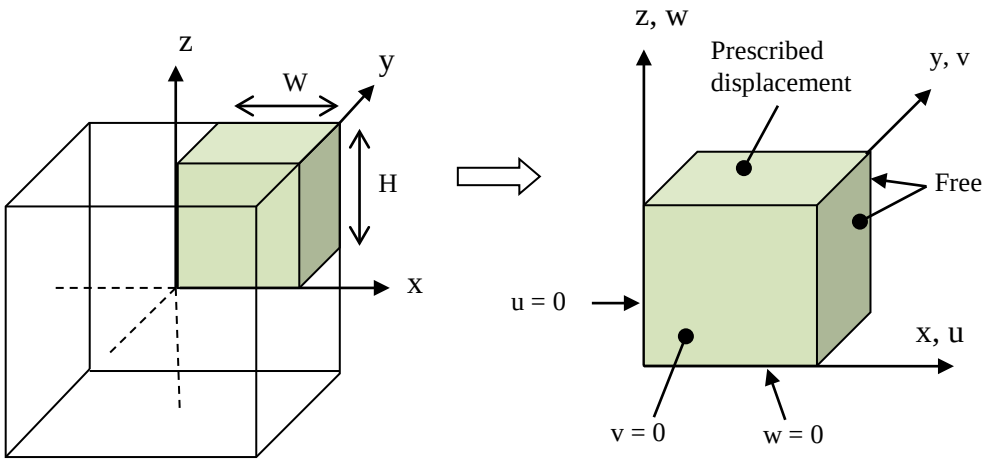

Figure 3.7: Geometry and boundary conditions for unconfined compression test

3.2.1.1 Smooth platens

A single hexahedral 8-noded linear element (C3D8) with a height to width ratio H:W = 1:1 was adopted to model the soil for an unconfined compression test between smooth rigid platens. An exact analytical solution ($p = 2s_u$) for the average bearing pressure p at collapse is available to validate the analysis results. The results are shown in Figure 3.8. Also included in the figure is the exact analytical solution for the soil parameters used. The UMAT results are seen to follow the correct linear elastic profile and exhibit perfectly plastic behaviour at the expected collapse load.

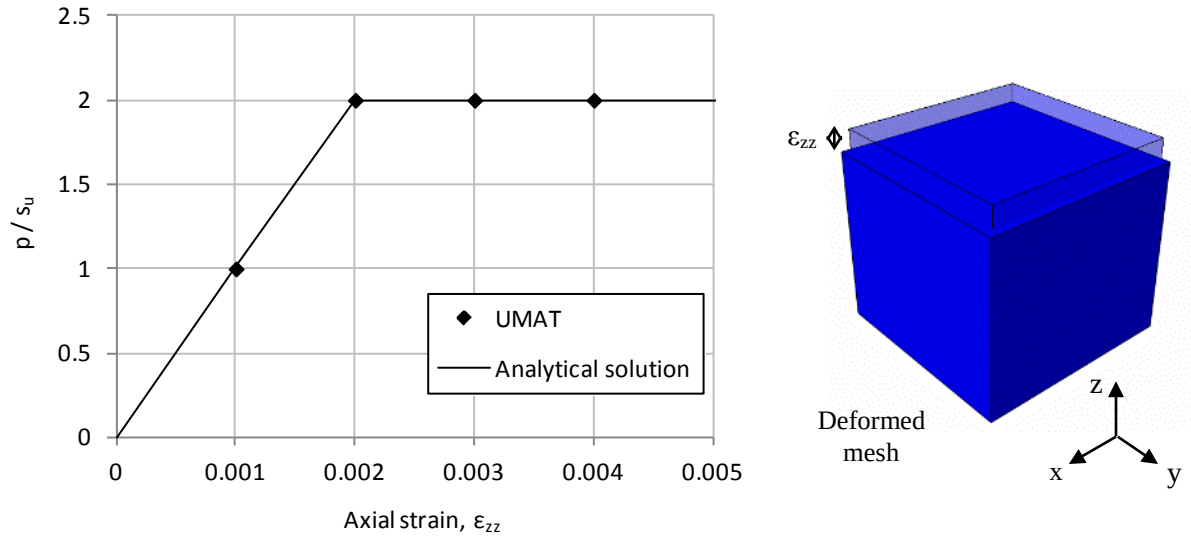

Figure 3.8: Comparison of UMAT and analytical results for unconfined compression test and deformed mesh at end of test

3.2.1.2 Rough platens

The unconfined compression test was repeated as per the arrangement in Figure 3.7 for the case where a rough interface between the soil and the rigid platens is assumed. Three different *H*:*W* ratios were investigated, namely 1:1, 1:2 and 2:1. The soil was modelled with 10-noded tetrahedral hybrid elements (C3D10H) as shown by the examples in Figure 3.9.

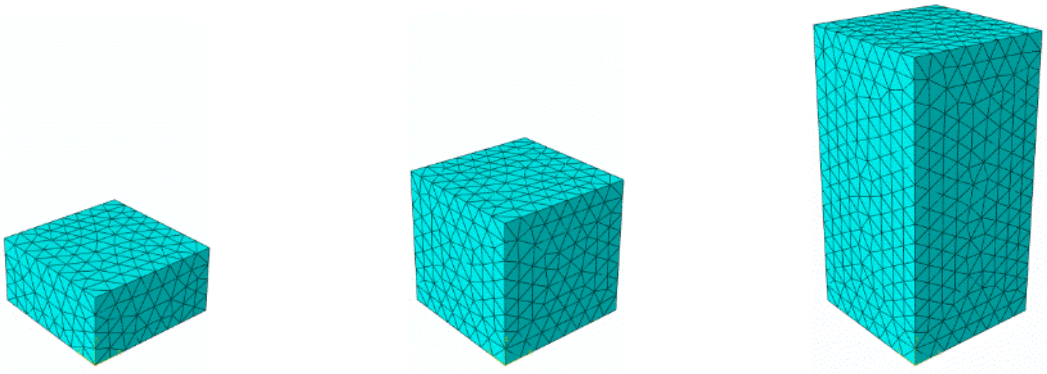

(a) 1:2 (b) 1: 1 (c) 2:1

Figure 3.9: Models for unconfined compression tests with varying *H*:*W* aspect ratios

The average bearing pressure *p* at failure was assessed by applying sufficient compressive strain to cause plastic yield. The results for the different aspect ratios are plotted in Figure 3.10 in which the number of elements was increased (manually, without adaptivity) to refine the solution. The final solution obtained for each case is listed in Table 3.1.

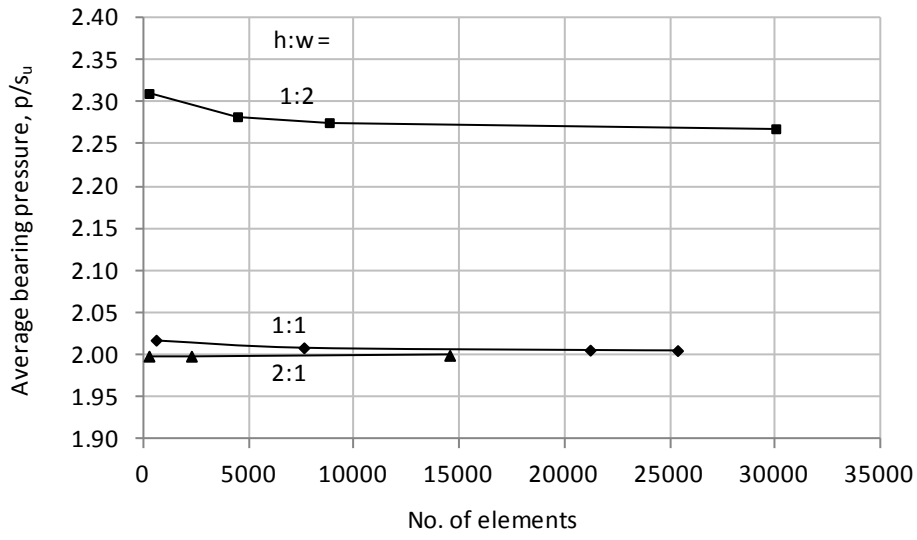

Figure 3.10: Unconfined compression test results with rough platens

Table 3.1: Abaqus results for rough unconfined compression test

Aspect ratio (*H*:*W*)	**No. of elements**	***p* / s_u**
2:1	14,523	2.000
1:1	25,349	2.006
1:2	30,015	2.268

The 2:1 aspect ratio test was seen not to be influenced by the rough platens as a value of p = 2 kPa was obtained. The 1:1 aspect ratio test however was found to experience end effects having an average bearing pressure of slightly above 2 kPa. For the 1:2 aspect ratio test, the analysis results for p/s_u can be compared with upper bound (2.305) and lower bound (2.230) solutions determined by Martin & Makrodimopoulos (2008) using finite element limit analysis. The results from the Abaqus UMAT analysis are compared with the upper and lower bounds in Figure 3.11 (a) with the mesh showing the plastic strains at failure in Figure 3.11 (b). The results from the UMAT analysis are seen to lie between the upper and lower bound solutions.

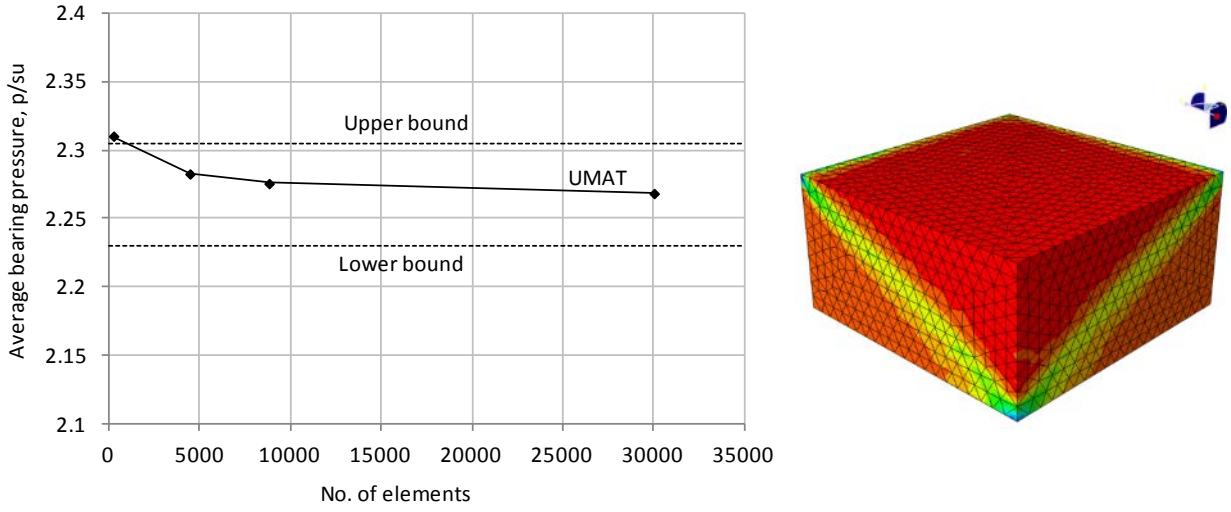

(a) UMAT results compared with upper & lower bound results from Martin & Makrodimopoulos (2008)

(b) Plastic strain at failure

Figure 3.11: Results of 1:2 unconfined compression test

3.2.2 Case 2: Bearing capacity of a circular foundation

The UMAT was used in an axisymmetric analysis to examine the bearing capacity of a rigid circular foundation under vertical loading. This also provides a useful validation case as exact solutions are available for both smooth and rough soil-foundation interfaces. The soil was modelled with 8-noded quadrilateral elements (CAX8) such as shown in Figure 3.3. An undrained shear strength s_u = 1 kPa, a Young's modulus E =1000 kPa and a Poisson's ratio v = 0.49 were used in modelling the soil. A rigid foundation of diameter D = 1 m was located at the soil surface and both smooth and rough interfaces were assessed.

The results were used to determine the corresponding bearing capacity factor N_c, which relates to the failure load V_{max} as given by Equation 2.5. For a rough interface, the exact value is N_c = 6.048, whilst for a smooth interface N_c = 5.689 (Table 2.2). The value of N_c was determined for an increasingly refined mesh as shown in Figure 3.12. The results using the UMAT are seen to approach the exact values. Corresponding results using the built-in Abaqus implementation of the Tresca criterion are also given in Figure 3.12. It is seen that these results are converging to a value that is under-predicting the bearing capacity. This is expected given the results seen earlier in Figure 3.3(a).

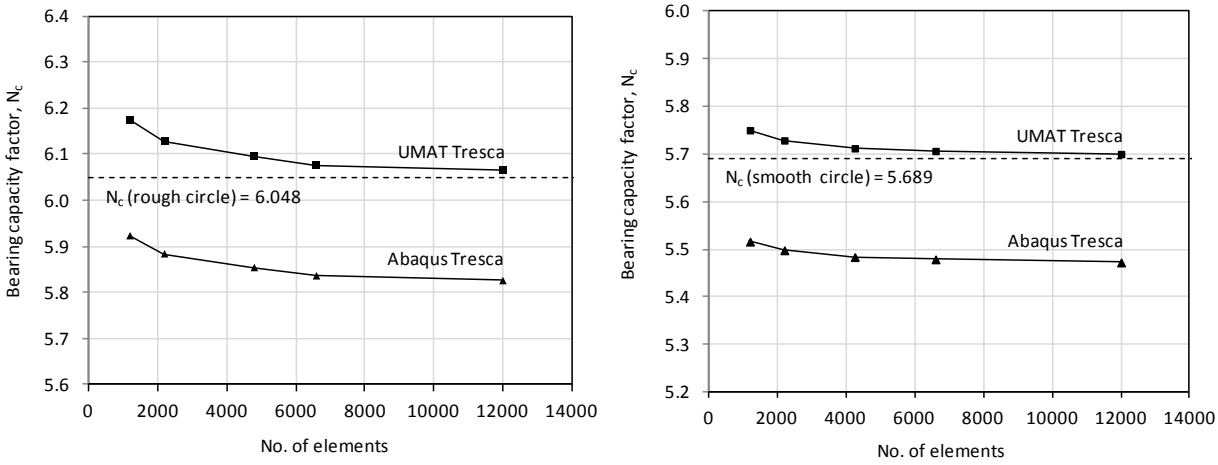

(a) Rough base (b) Smooth base

Figure 3.12: Bearing capacity analysis of a circular foundation

Gourvenec & Randolph (2003) suggest that large deformation of the elements local to the foundation may be a cause for the under-prediction of the built-in Abaqus implementation of the Tresca criterion. Since the results from the UMAT closely converge to the exact solution using an identical mesh, it is likely that element distortion may only play a small role in contributing to the analysis error.

3.2.3 Case 3: Bearing capacity of a square foundation

A further case examined was using the UMAT to calculate the bearing capacity of a rigid square foundation under vertical loading. The soil was modelled with 8-noded hexagonal elements (C3D8H) as shown in Figure 3.13(a) with the same soil properties as for the circular foundation analysis. A rigid footing of width B = 1 m located at the soil surface with a rough interface was used, and symmetry was exploited by modelling only ¼ of the problem.

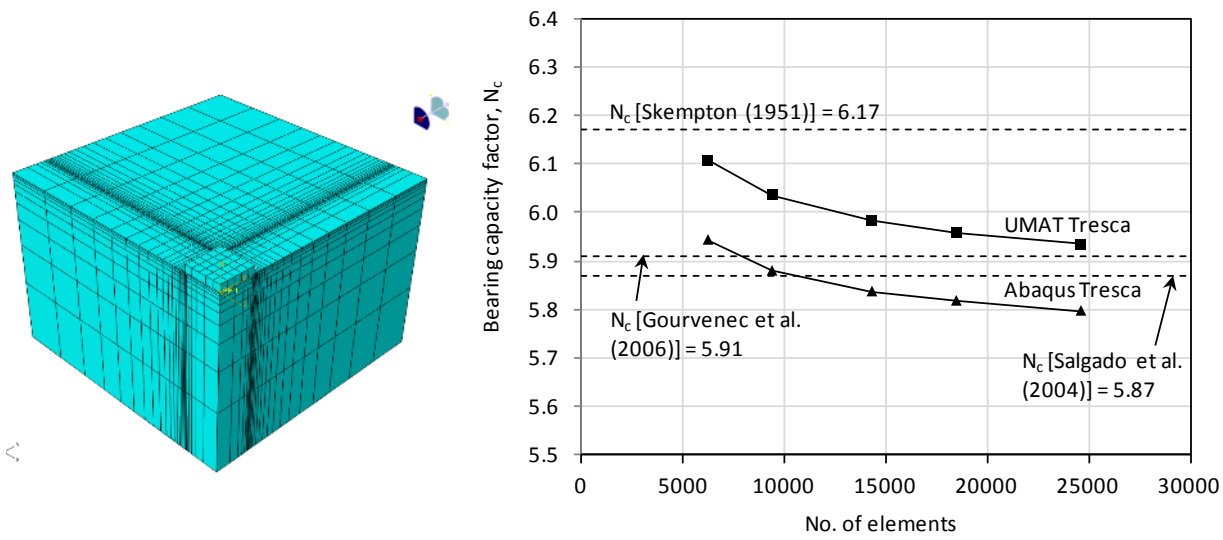

a) Finite element mesh example (18,496 elements)

b) Bearing capacity factor result

Figure 3.13: Bearing capacity analysis of a rough square foundation

The results were used to determine the bearing capacity factor N_c. An exact solution for a square foundation has not as yet been determined (as discussed in Section 2.2.2.1). The values of N_c determined using the UMAT for an increasingly refined mesh are shown in Figure 3.13(b). These are compared with solutions found in several other studies, taken from Table 2.4. The UMAT results are seen to approach a value of approximately N_c = 5.9. This

lies close to other recent solutions, although the result is sensitive to the nature of the mesh refinement used. Corresponding results using the built-in Abaqus implementation of the Tresca criterion are also given in Figure 3.13(b). It is seen that these results are converging towards a lower prediction of the bearing capacity.

3.3 Adaptive meshing scheme

3.3.1 Background

The manner in which the soil body is discretised into finite elements can be a source of error in FEA. For the analysis of shallow foundations, the size and distribution of the elements beneath and in the vicinity of the foundation will strongly influence the bearing capacity result obtained. For example it is important that the mesh is sufficiently refined at the corners or edges of shallow foundations as this is where large gradients in stresses and strains occur (Potts and Zdravkovic, 2001). This is shown for a circular foundation at failure in Figure 3.14, in which a rapid change in the direction of the displacement vectors occurs at the foundation edge. A higher concentration of smaller elements in this area enables more accurate modelling of this behaviour.

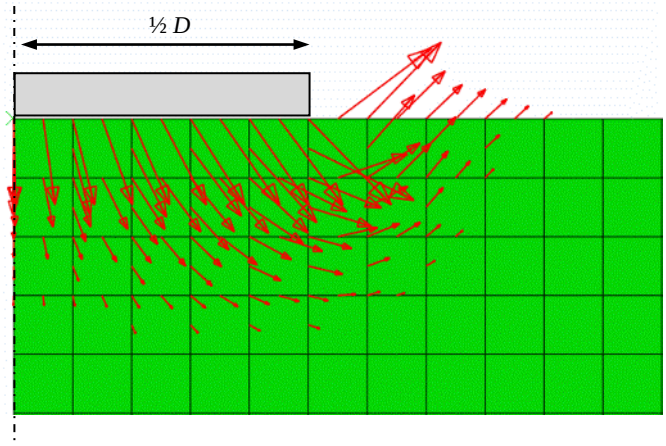

Figure 3.14: Displacement vectors for a circular foundation at failure

The solution obtained from the uniform mesh shown in Figure 3.14 would therefore be improved if the mesh was made up of finer elements. The refined elements outside of the

zone of soil displacement would however have minimal impact on improving the solution accuracy, and the extra computing power required for these elements would be for limited gain.

A more effective approach is to target the refinement of the mesh elements only in the areas where they make a significant contribution to the solution. This can be done by manually increasing the density of the discretisation in the critical areas, such as foundation edges and corners, or in the zone of the failure mechanism (if there is prior knowledge of this). The meshes shown in Figure 3.3(a) and Figure 3.13(a) were created manually using this approach. A process of trial and error mesh refinement may be required by the user until the point that additional refinement does not result in a significant adjustment to the solution. Gourvenec and Mana (2011) found that shallow foundation bearing capacity predicted by FEA was especially sensitive to mesh refinement using manual meshing for high soil strength heterogeneity and low embedment. These were cases where the failure mechanism was localised close to the foundation.

An alternative to manual discretisation is to use an adaptive finite element procedure which automatically adjusts the mesh (over the course of several iterations) in order to improve the solution to a specified accuracy. Adaptive meshing can offer the following advantages:

i) The user does not need to spend time or require experience to manually construct a tailored mesh that optimises running time and accuracy. Instead, an initial coarse mesh is set up by the user and then the discretisation is undertaken automatically allowing greater solution accuracy to be achieved. This means that no prior knowledge of the failure mechanism is required.

ii) The targeted mesh refinement restricts surplus elements, providing a more efficient use of computer power, and enabling faster analysis runtimes.

3.3.2 Adaptive meshing methods

A number of adaptive meshing methods for FEA have been developed. Whilst not used routinely, they have been adopted in geotechnical engineering as there are various important nonlinear problems where adaptivity can be used to improve the accuracy of numerical solutions (Zienkiewicz and Zhu, 1987, Zienkiewicz and Zhu, 1991, Zienkiewicz et al., 2005, Kardani et al., 2012). A common application has been for large deformation analysis, as adaptive finite element methods can be used to implement increment remeshing and overcome the problem of mesh distortion. Whilst this aspect is not relevant for the small deformation adaptive analysis considered in this thesis, small deformation analyses will benefit from improved accuracy of the finite element solution. Adaptive finite element methods that have been used include the following:

- *r – adaptive method*: refines the location of the nodes, but does not increase the overall number of nodes (Li et al., 2001).
- *h – adaptive method*: the number of nodes and elements is not constant and the element size can be reduced or increased to obtain a prescribed solution precision (Hu and Randolph, 1998, Kardani et al., 2012).
- *p – adaptive method*: the interpolation order of the elements is increased, such as from linear to quadratic shape functions (Zienkiewicz and Zhu, 1991).

In order to determine the areas of the mesh that are to be refined, an error estimation needs to be made to predict the error distribution of the solution in the current mesh. There are a number of different error estimation techniques used, including those based on the energy norm, the Green-Lagrange strain, and the plastic dissipation (Nazem et al., 2012). An alternative approach used by Martin (2011) for finite element limit analysis (FELA) of 2D problems determines the elements that need to be refined by considering the distribution of the maximum shear strain γ_{max} in an upper bound displacement field. The calculation

$\int \gamma_{\max} dA$ is made for all elements in the mesh and used to determine new target element areas. With successive mesh refinements the adaptivity strategy seeks to equalise this integral over all of the elements in the mesh.

After the error has been assessed, the new mesh is generated based on the refinement criterion. Small deformation problems have the advantage that a new analysis can be started from the beginning using the new mesh. For large deformation problems, the state variables have to be mapped from the old to the new mesh, and the analysis resumed at the next time increment.

3.3.3 Adaptive meshing strategy

A *h*-adaptive meshing scheme has been developed for 2D and 3D small deformation FEA. The scheme developed operates in conjunction with the Tresca UMAT to enable exact solutions for bearing capacity problems to be approached.

The refinement strategy adopted is based on the approach implemented by Martin (2011). An element is refined depending on whether the integral of the maximum plastic shear strain, $\int \gamma_{\max} dA$ (in 2D) or $\int \gamma_{\max} dV$ (in 3D) in the element is above or below the average across all elements being modelled in the soil body. The approach used to determine the new target element area A_i or volume V_i involves assessing the plastic shear strain factor D_i for each element i, which is given by

$$D_i = \gamma_{max_i} A_i \quad \text{(2D)}$$

$$\text{or} \qquad (3.34)$$

$$D_i = \gamma_{max_i} V_i \quad \text{(3D)}$$

The average plastic shear strain factor $\overline{D}$ across the total of n elements in the mesh is then determined

$$\overline{D} = \frac{1}{n} \sum_{i=1}^{n} \gamma_{max_i} A_i \quad \text{(2D)} \qquad (3.35)$$

or

$$\bar{D} = \frac{1}{n}\sum_{i=1}^{n} \gamma_{max_i} V_i \quad \text{(3D)}$$

The new target element area A_{new_i}or volume $V_{new_i}$is generated from the previous values as follows

$$A_{new_i} = \left(\frac{1}{\frac{D_i}{\bar{D}}}\right)^2 A_i \quad \text{(2D)}$$

or

$$V_{new_i} = \left(\frac{1}{\frac{D_i}{\bar{D}}}\right)^3 V_i \quad \text{(3D)} \tag{3.36}$$

with limits: $\alpha \leq \frac{D_i}{\bar{D}} \leq \beta$

Unstructured triangular meshes are used for 2D analysis and these are generated using the program Triangle (Shewchuk, 2002). Unstructured tetrahedral meshes are used for 3D analysis and these are generated using the program TetGen (Si, 2011). These programs use a Delaunay triangulation method for unstructed mesh generation. Using unstructured meshes allows elements to be highly concentrated in areas where they are needed. The minimum angles of the triangles or tetrahedra are maximised to ensure that good quality meshes are generated. Surrounding elements must also be refined to ensure that all nodes join to form triangles with no very acute angles.

The analysis of a problem is started with an initial coarse mesh and after several iterations the concentration of mesh refinement begins to reflect the intensity of γ_{max}. When the mesh is more highly refined, plastic regions can be identified by a dense concentration of mesh refinement, while regions experiencing minimal plastic strain have limited or no refinement. The plastic regions formed by the refined mesh can be used to infer the nature of the failure mechanism occurring.

3.3.4 Adaptive meshing procedure

A Python master script has been written to implement the steps of the adaptive mesh refinement process. The basic steps carried out are as follows:

1. The user inputs the maximum number of iterations to be performed and/or a minimum required solution difference between successive iterations in order to define when the analysis will stop.
2. The initial coarse mesh is generated in Triangle (2D) or TetGen (3D)
3. The Abaqus input file of the analysis problem is created with a Python subscript which incorporates the element and nodal information from the generated mesh.
4. The input file is analysed in Abaqus using the UMAT to define the Tresca constitutive model. The UMAT is also used to calculate and return the total accumulated plastic shear strain γ_{max} in each element at the end of the analysis.
5. At the completion of the Abaqus analysis a Python subscript records the iteration number, number of elements in the mesh, the failure load results and time taken to run the analysis to a text file. This enables the user to have a quick summary of the results after each iteration. A picture of the mesh is also saved to file. If either of the criteria specified in Step 1 is met then the procedure terminates. Otherwise Step 6 is performed.
6. A Python subscript recovers the γ_{max} data and the element area (2D) or element volume (3D) and derives the new target element area or volume as per Equation 3.36.
7. The target element area/volume information is fed to Triangle/TetGen and the next iteration of the mesh is generated. The process then returns to Step 3.

The sequence of steps carried out is shown in Figure 3.15. Initial analysis was undertaken using this procedure to investigate the i) accuracy and ii) efficiency of the scheme.

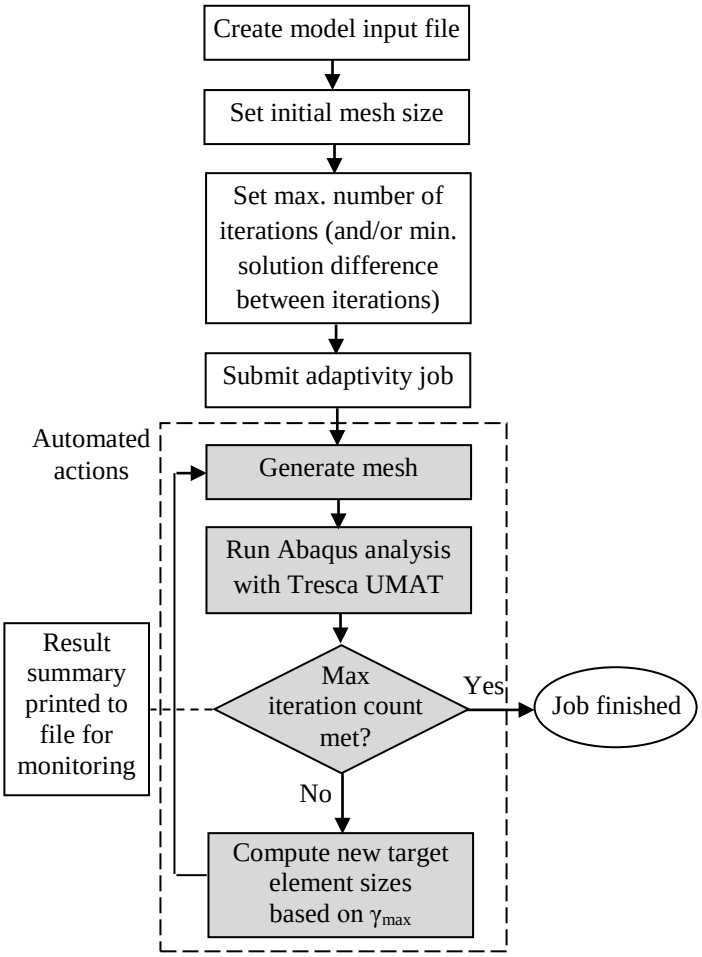

Figure 3.15: Adapative meshing scheme

3.4 Accuracy of the adaptive meshing scheme

Validation of the functionality of the adaptive mesh refinement scheme was undertaken by analysing circular and square foundations and comparing the results with exact or reported solutions. Results are presented for a both an axisymetric and a 3D model of a circular foundation, and for a 3D model of a square foundation.

3.4.1 Case 1: Circular footing – axisymmetric model

An axisymmetric model of a circular foundation was set up in Abaqus as shown in Figure 3.16. The soil was modelled as a Tresca material using the UMAT and having a homogeneous undrained shear strength of s_u = 1 kPa, an undrained Young's modulus E_u = 1000 kPa and undrained Poisson's ratio of ν = 0.499. Both rough and smooth foundation

interfaces were investigated with a uniform vertical displacement applied until failure. The mesh was composed of triangular quadratic hybrid elements (CAX6H) with an initial coarse mesh as shown in Figure 3.16. The mesh was subsequently refined using the adaptive mesh refinement scheme for a total of six iterations.

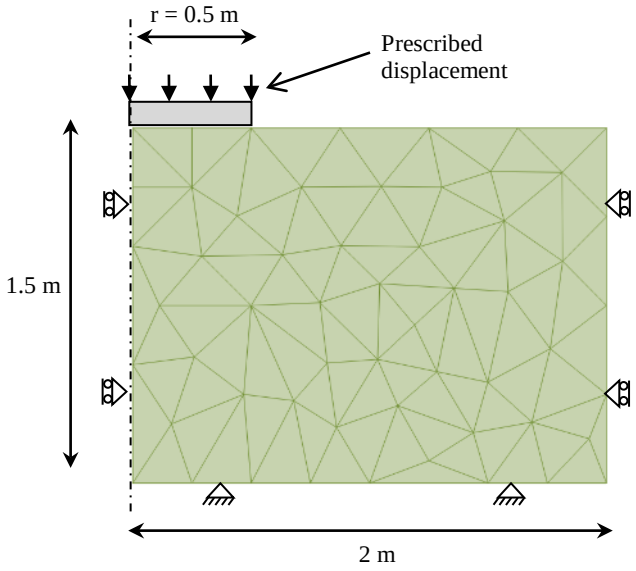

Figure 3.16: Axisymmetric model of circular footing with initial coarse mesh

The progression of adaptive mesh refinement for the analysis of a rough circular foundation is shown in Figure 3.17. The increasing concentration of the mesh in areas of plastic shear strain is evident with successive iterations and after 6 iterations the nature of the plastic regions can be clearly identified through inspection of the focused mesh (Figure 3.17 (d)). The bearing capacity factor N_c from the six iterations for both the smooth and rough circular foundations are shown in Figure 3.18. Also included is the exact solution for each case. After four iterations an answer close to the exact solution is achieved. Only smaller improvements occur with successive iterations.

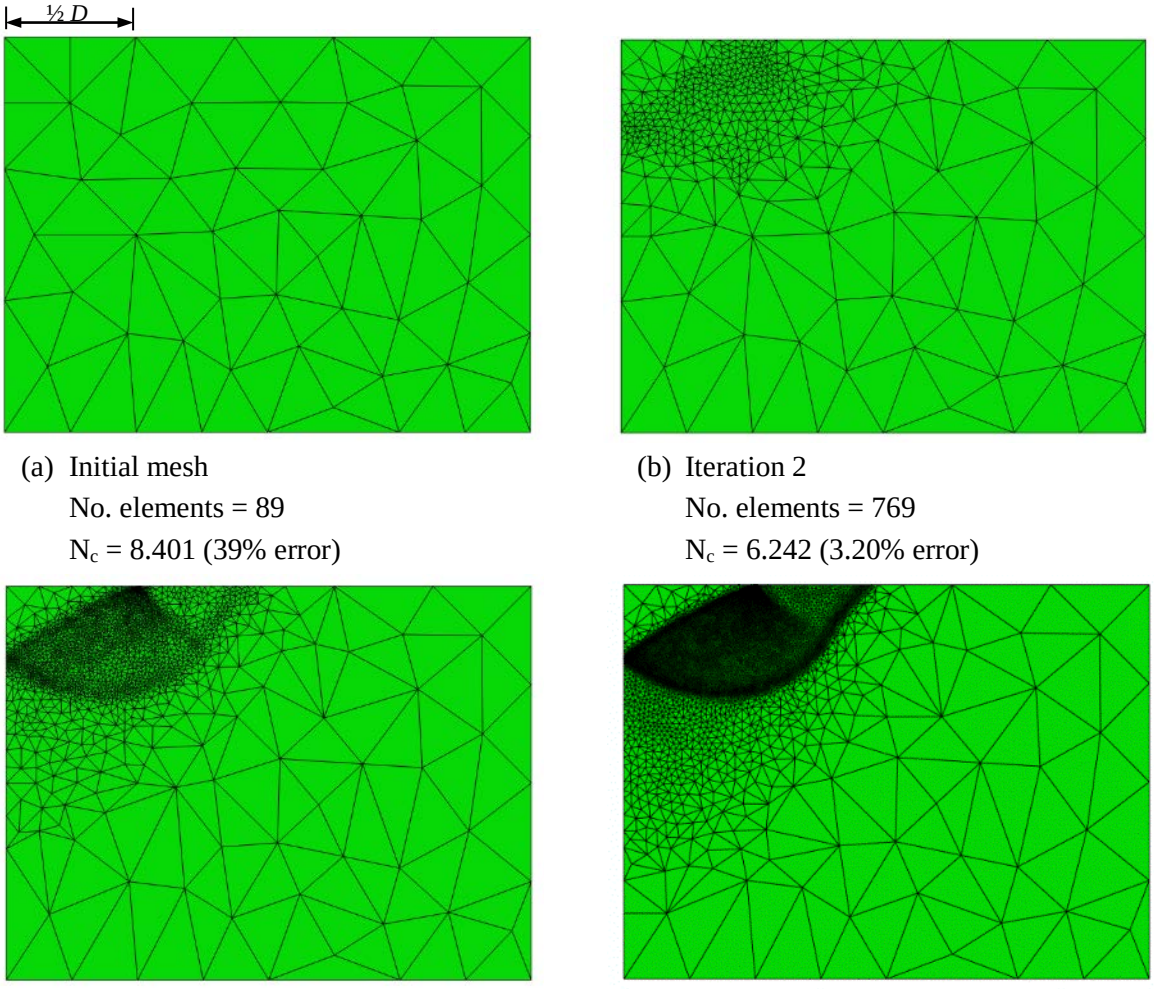

(a) Initial mesh
No. elements = 89
N_c = 8.401 (39% error)

(b) Iteration 2
No. elements = 769
N_c = 6.242 (3.20% error)

(c) Iteration 4
No. elements = 4,034
N_c = 6.068 (0.33% error)

(d) Iteration 6
No. elements = 15,718
N_c = 6.052 (0.07% error)

Figure 3.17: Automatic adaptive mesh refinement of a rough circular foundation

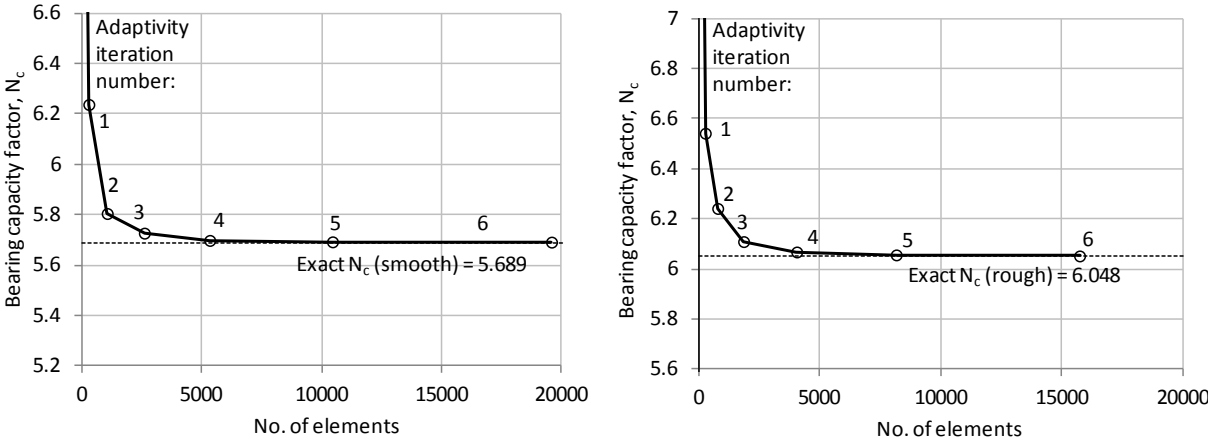

(a) Smooth (b) Rough

Figure 3.18: Circular foundation bearing capacity factor with increasing adaptive mesh refinement

Table 3.2 compares the results from the last (6th) iteration undertaken with the exact solutions determined by Martin (2004) using the method of characteristics. The results from the Abaqus analysis are very close to the exact solutions, having an error of less than 0.1%.

Table 3.2: Circular foundation bearing capacity results

Interface condition	**Bearing capacity factor, N_c**		**Abaqus % Error**
	Abaqus – this study	ABC (Martin, 2004)	
smooth	5.691	5.689	0.04
rough	6.052	6.048	0.07

The plastic regions as shown by the refined mesh for both the smooth and rough cases are provided in Figure 3.19, along with the equivalent slip-lines fields corresponding to the exact solutions from the software ABC (Martin, 2004). The plastic regions indicated by the refined Abaqus mesh are seen to compare well to those given by the slip-line solutions.

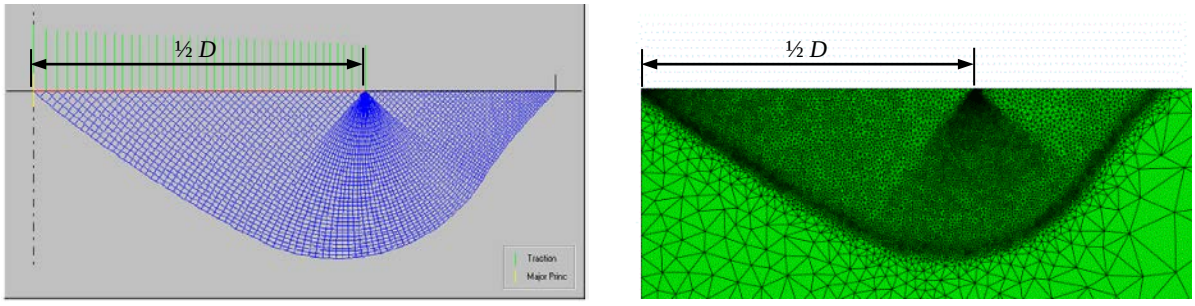

(a) Smooth interface: slip-line solution (left) and Abaqus mesh (right)

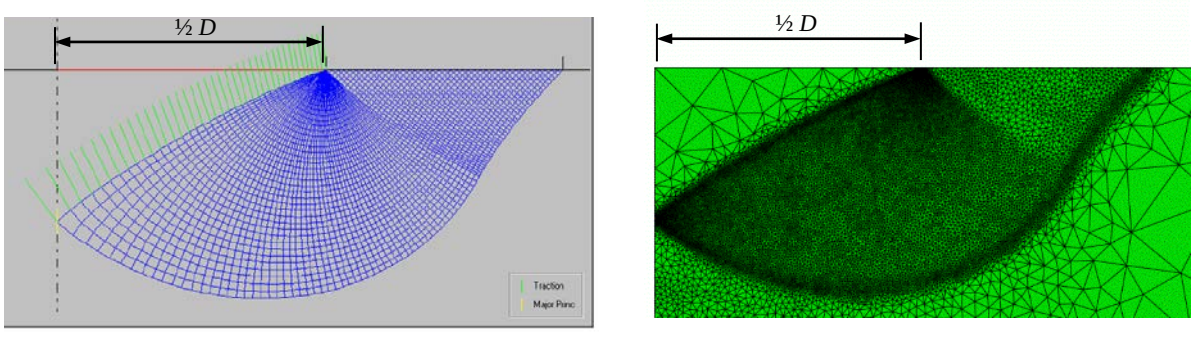

(b) Rough interface: slip-line solution (left) and Abaqus mesh (right)

Figure 3.19: Comparison of refined Abaqus mesh of a circular footing compared with slip-line solutions from Martin (2004)

3.4.2 Case 2: Circular footing – 3D model

A 3D model of a circular foundation was also analysed in Abaqus for the purpose of validating the adaptive mesh refinement in 3D. The circular foundation was constructed using 5 degree segments and symmetry was exploited such that only 1/8th of the foundation was modelled. The mesh was composed of tetrahedral quadratic hybrid elements (C3D10H) and the same soil properties as in the axisymmetric model were used. Both rough and smooth foundation interfaces were investigated with a prescribed displacement applied until failure.

The results of the analysis are shown in Figure 3.20 and the bearing capacity factors obtained after 7 mesh refinement iterations are summarised in Table 3.3. Compared with the axisymmetric analysis, the 3D circular models needed more mesh refinement iterations to obtain equivalent accuracy to the axisymmetric analysis. This was due to the more intensive element requirement for 3D modelling. Despite this, the final error in both cases was still found to be less than 0.3% for both extremes of roughness.

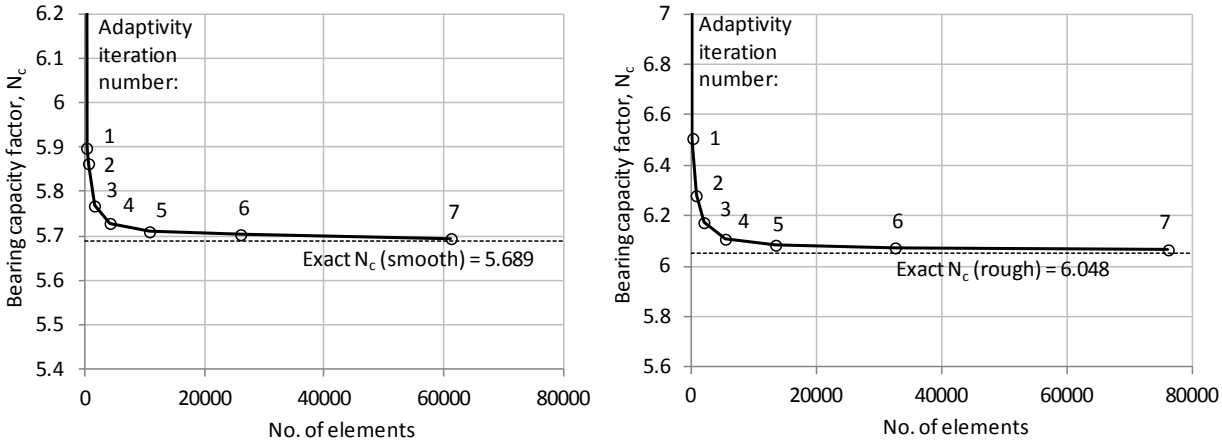

(a) Smooth (b) Rough

Figure 3.20: 3D circular foundation bearing capacity factor with increasing adaptive mesh refinement

Table 3.3: 3D circular footing bearing capacity results

Interface condition	**Bearing capacity factor, N_c**		**Abaqus % Error**
	Abaqus – this study	ABC (Martin, 2004)	
smooth	5.694	5.689	0.10
rough	6.065	6.048	0.28

Andersen and Clausen (2009) also modelled the case of a rough circular foundation (with symmetry such that only 1/24th was modelled) using a non approximated implementation of Tresca but no adaptive meshing scheme. In this analysis they achieved a result that was 7% above the exact solution. Taiebat and Carter (2009) cite this as evidence that the application of a more accurate flow rule in a finite element analyses fails to result in a better prediction. However, the results shown in Table 3.3 indicate that when used in conjunction with an adaptive meshing scheme, adopting an accurate flow rule can result in very accurate predictions.

The plastic regions as shown by the refined mesh for both the smooth and rough cases at the 7th iteration are provided in Figure 3.21. The plastic regions are not as sharply defined as the axisymmetric analysis since equivalent refinement would require an excessively large mesh which becomes onerous for computing time. It is still evident however that Prandtl- and Hill-type mechanisms as seen in the axisymmetric analysis also occur in the 3D analysis.

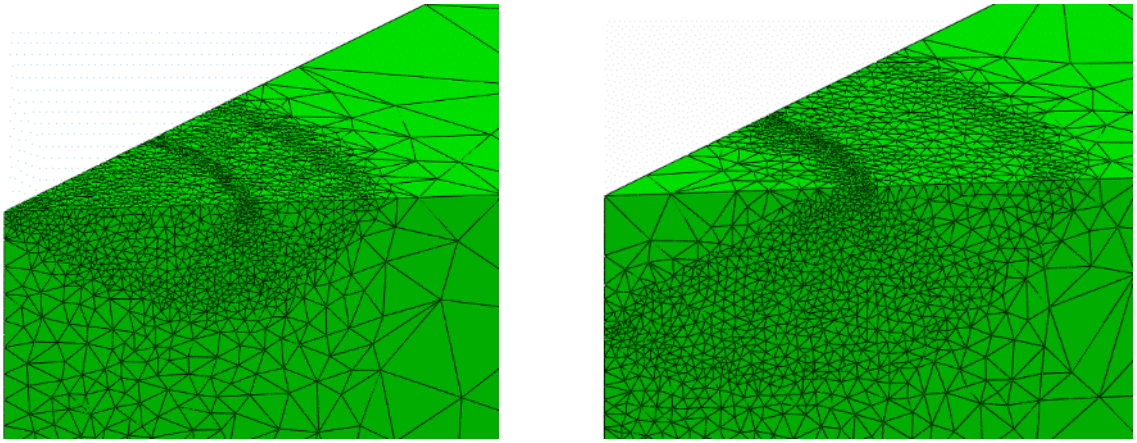

(a) Smooth (b) Rough

Figure 3.21: 3D circular foundation refined mesh

Figure 3.22 shows the refined mesh with displacement magnitude contours for the rough circular foundation. The deformed mesh is shown for the section view (Figure 3.22(b)). In combination with the displacement contours, the deformed mesh helps the nature of the failure mechanism to be inferred.

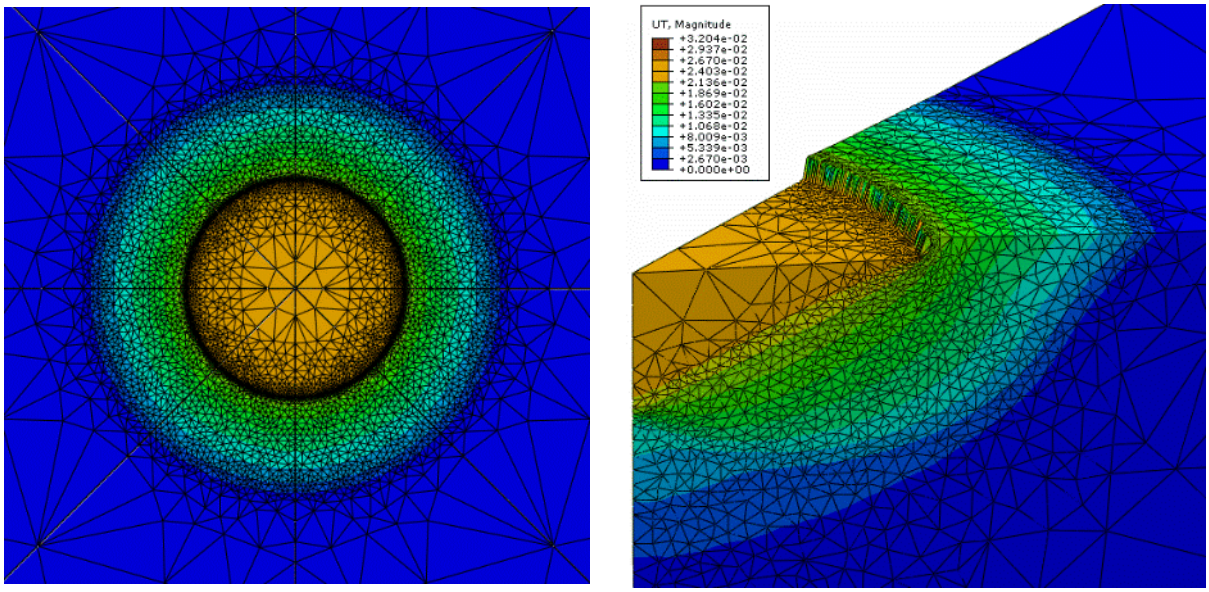

(a) Plan view (b) Section view with deformed mesh

Figure 3.22: 3D rough circular foundation refined mesh with displacement contours

3.4.3 Case 3: Square footing – 3D model

The bearing capacity of a square foundation was analysed to further assess the effectiveness of the adaptive meshing scheme for 3D modelling. Having confidence in modelling a square foundation was of particular importance in this thesis. This is because analysis of a square geometry is used extensively for the purpose of investigating perforated foundations (see Chapters 4 & 5).

Symmetry was used such that only 1/8th of the foundation was modelled as shown in Figure 3.23. The Tresca UMAT was used to model the soil having a homogeneous undrained shear strength of s_u = 1 kPa, an undrained Young's modulus E_u = 1000 kPa and undrained Poisson's ratio of ν = 0.499. Both rough and smooth foundation interfaces were investigated with a prescribed displacement applied until failure. The mesh was composed of tetrahedral quadratic hybrid elements (C3D10H) with an initial mesh as shown in Figure 3.23. The mesh was subsequently refined using the adaptive mesh refinement scheme for a total of ten iterations.

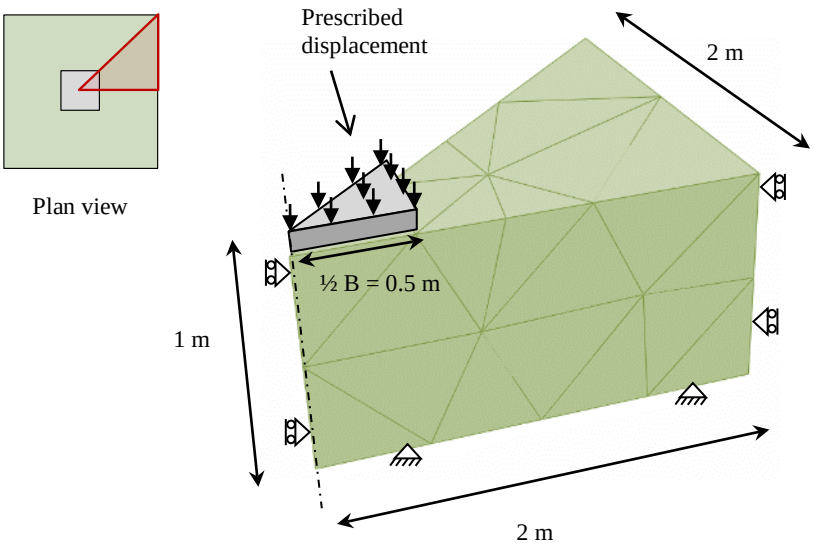

Figure 3.23: 3D model of a square foundation with initial coarse mesh

3.4.3.1 Smooth square

The bearing capacity factor results from the ten mesh iterations undertaken for a smooth square are shown in Figure 3.24. A bearing capacity factor of N_c = 5.442 was obtained on the final iteration, and this is compared with values from other studies in Figure 3.24. It is seen that the result from this study is at the lower end of other results reported in the literature, and significantly lower than the N_c = 6.17 which is commonly adopted in design codes based on empirical work by Skempton (1951).

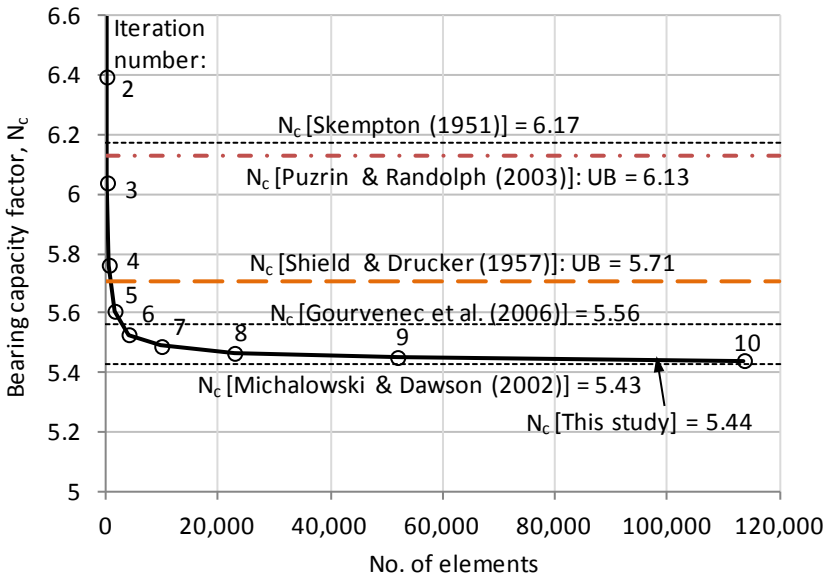

Figure 3.24: Bearing capacity factors for smooth square foundations

The failure mechanism from the smooth square footing analysed in this study as indicated by the refined mesh and displacement magnitude contours is shown in Figure 3.25. The mechanism tapers in at each corner of the square and has four planes of symmetry, including two diagonal planes.

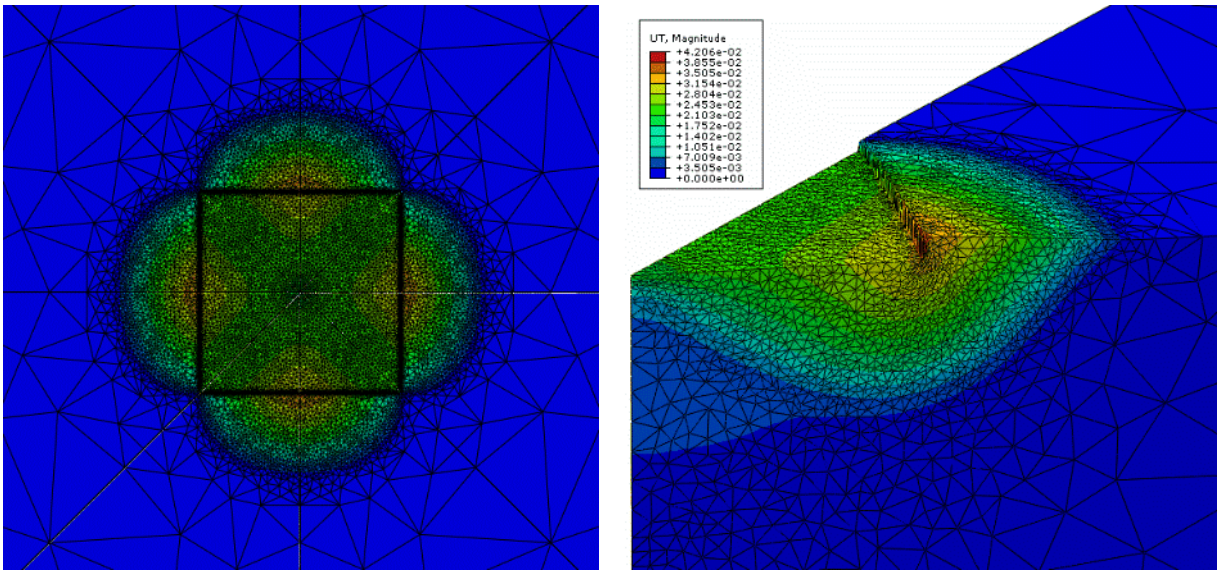

(a) Plan view (b) Section view with deformed mesh

Figure 3.25: Displacement magnitude contours of a smooth square foundation at failure

The following observations are made when comparing the results with those from previous studies:

- Displacement contours for a smooth square footing at failure from by Gourvenec et al. (2006) using Abaqus were shown in Figure 2.9(b). This result did not show the same tapering of the displacement profile at the corners as seen in Figure 3.25. The Abaqus analysis in this case used a coarser manually generated mesh and the Abaqus built-in approximation to the Tresca plastic potential function. This may provide an explanation for the difference.
- The contours of velocity magnitude at the soil surface from the finite difference analysis undertaken by Michalowski & Dawson (2002) are more similar to the displacement profile obtained in this study (see Figure 2.9(a)). The deformation field in Michalowski & Dawson (2002) also exhibited four planes of symmetry, with two

being diagonal. In their analysis a result of N_c = 5.43 was obtained, which is only slightly lower than the result in this study. The mesh used in the Michalowski & Dawson (2002) analysis however was very coarse and there was no concentration of elements around the foundation.

- Upper bound limit analysis of this problem was undertaken by Puzrin & Randolph (2003). N_c = 6.13 was obtained, which was higher than that found for a circular foundation in their study. A better upper bound value of 5.71 was obtained from limit analysis by Shield & Drucker (1953) which was based on deformation consisting of four plane strain regions.

3.4.3.2 Rough square

Results from the ten mesh refinement iterations undertaken for a rough square are shown in Figure 3.26. A bearing capacity factor of N_c = 5.762 was obtained on the final iteration analysed. As with the case of the smooth foundation, the result from this study is at the lower end of other results reported in the literature. It is significantly lower than the typical design code value of N_c = 6.17, which does not distinguish between rough and smooth interfaces.

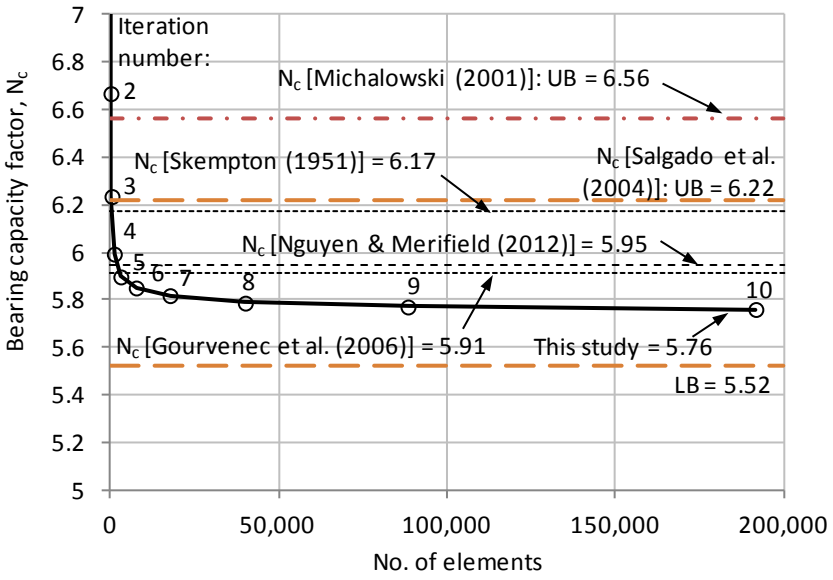

Figure 3.26: Bearing capacity factors for rough square foundations

The failure mechanism occurring for the rough square footing as indicated by the refined mesh and displacement magnitude contours is shown in Figure 3.27. The mechanism shape in plan is seen to be similar to that from the smooth footing, also having four planes of symmetry. However compared with the smooth footing the rough mechanism is wider and deeper. This would be expected due to the rough interface inducing a Prandtl-type mechanism as opposed to the Hill-type mechansism observed with the smooth interface.

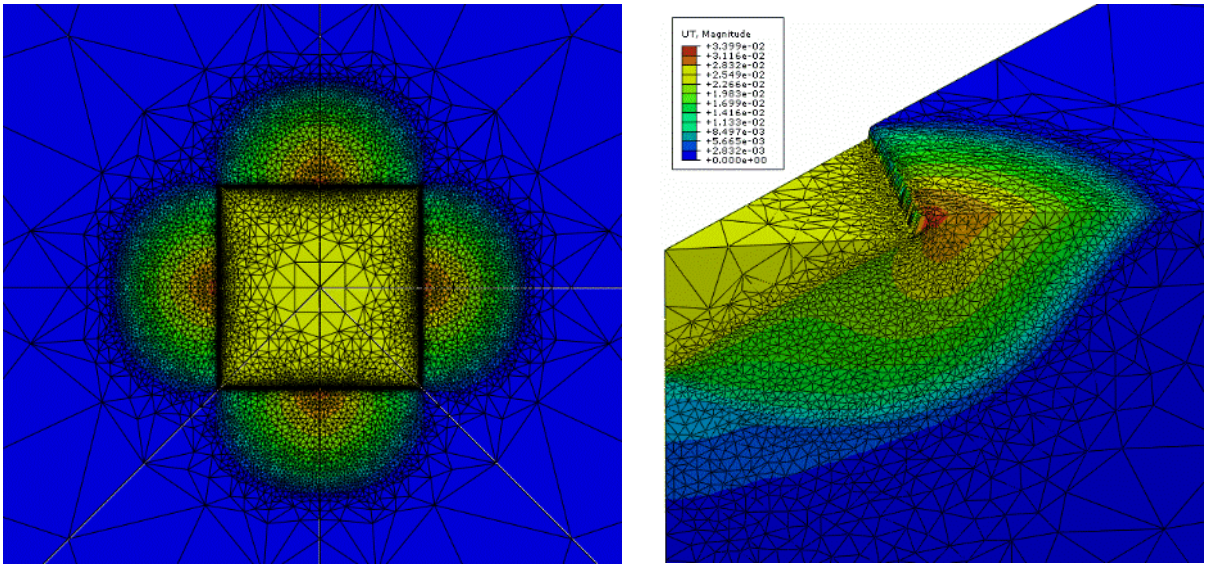

(a) Plan view (b) Section view with deformed mesh

Figure 3.27: Displacement magnitude contours of a rough square footing at failure

When comparing the results with previous studies the following observations are made:

- The N_c = 5.762 result from this study was found to lie between the lower and upper bound values of N_c = 5.523 and N_c = 6.221 determined from finite element limit analysis (FELA) by Salgado et al. (2004). This was also found to be the case when footings of lower aspect ratio (B/L) were analysed and the results compared with the bounded values given by Salgado et al. (2004) (Figure 3.28).
- The displacement contours from the Abaqus study by Gourvenec et al. (2006) shown in Figure 2.11 do not taper toward the corners of the square as seen in Figure 3.27. Another Abaqus study by Nguyen and Merifield (2012) achieved a similar N_c result to

Gourvenec et al. (2006). The analysis in that study also had a less refined mesh than in this study, and used the in-built approximated plastic potential function. A plan view of displacement contours for the footing at failure was not provided so no mechanism comparison can be made.

- Different types of mechanisms were trialled in the limit analysis undertaken by Michalowski (2001). A multi-block mechanism was found to produce a better upper bound solution than a continuous mechanism (Table 2.4). The least upper bound estimate of the failure load occurred for the mechanism with no symmetry with respect to the diagonal planes. This finding is in contrast to the mechanism seen from the Abaqus analysis in this study.

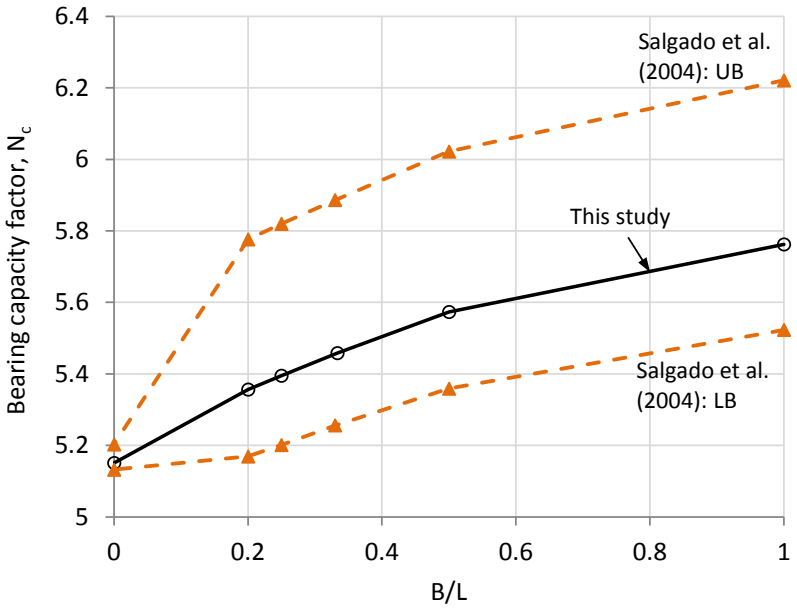

Figure 3.28: Bearing capacity factor variation with footing aspect ratio (*B*/*L*)

3.5 Efficiency of the adaptive meshing scheme

The previous section has shown that accurate solutions can be achieved by using the adaptive meshing scheme. Another consideration is the efficiency of the meshing scheme in terms of the computing time required to obtain a certain accuracy level. A study has been carried out to assess calculation times required using adaptive meshing compared with non-adaptive

meshing. In the case of non-adaptive meshing, discretisation is undertaken using both i) uniform meshing and ii) manually refined meshing.

An axisymmetric circular foundation and a 3D square foundation were examined for the study. A constant element size was used to make up the uniform meshes. The manually refined meshes were constructed by concentrating elements around the foundation edge and in the estimated area of the failure mechanism (using prior knowledge of this). The total CPU time as given in the Abaqus .dat file was recorded for each job to compare analysis efficiency across the different mesh types. The CPU times of all iterations were combined to give the total calculation time for an adaptive mesh solution. The individual job time was used for the uniform and manual meshes. All analyses used the Tresca UMAT such that the Tresca model was correctly implemented.

3.5.1 Axisymmetric analysis efficiency comparison

The same axisymmetric model of a rough circular foundation as described in Section 3.4.1 was used to undertake the comparison analysis. Uniform and manual meshes were set up to compare with the adaptive mesh results shown in Figure 3.18(b). The meshes were created to roughly match the number of elements used in the four adaptive mesh cases, containing approximately 760, 1,900, 4,000 and 8,100 elements. The meshes used for the case of approximately 4,000 elements for each mesh type are shown Figure 3.29.

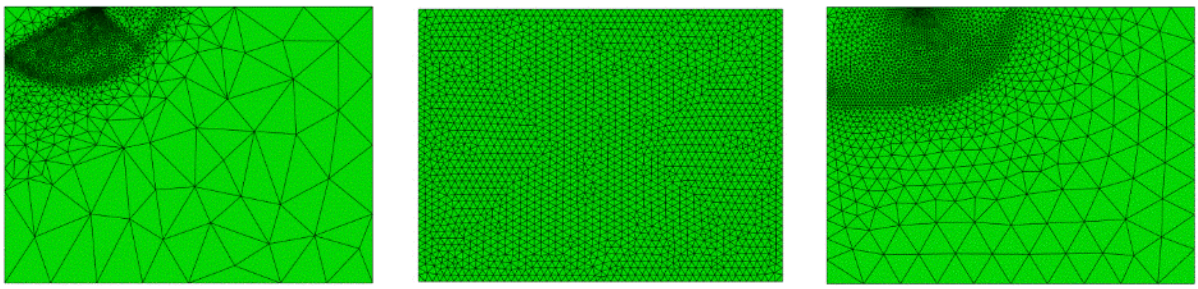

(a) Adaptive mesh 4,034 elements

(b) Uniform mesh 4,031 elements

(c) Manual mesh 4,033 elements

Figure 3.29: Comparison of mesh types for a rough circular foundation

The bearing capacity results with respect to the number of elements and calculation times are shown in Figure 3.30. The results are given in terms of the percentage error from the exact solution for a rough circular foundation (N_c = 6.048). The uniform mesh had significantly less accuracy than the adaptive mesh with a comparable number of elements. The adaptive mesh gave slightly more accurate results than the manual mesh, although in general the accuracy of a manually refined mesh will of course be sensitive to the discretisation implemented by the user. The results in Figure 3.30(b) show that if an error of less than about 3% is sought then the adaptive meshing will result in the fastest calculation time and so is most efficient. If an error of greater than about 3% is satisfactory, then the manual meshing is most efficient. However the manual meshing approach requires time to design the mesh, and this may often involve undertaking several exploratory analyses to decide upon the mesh to be used.

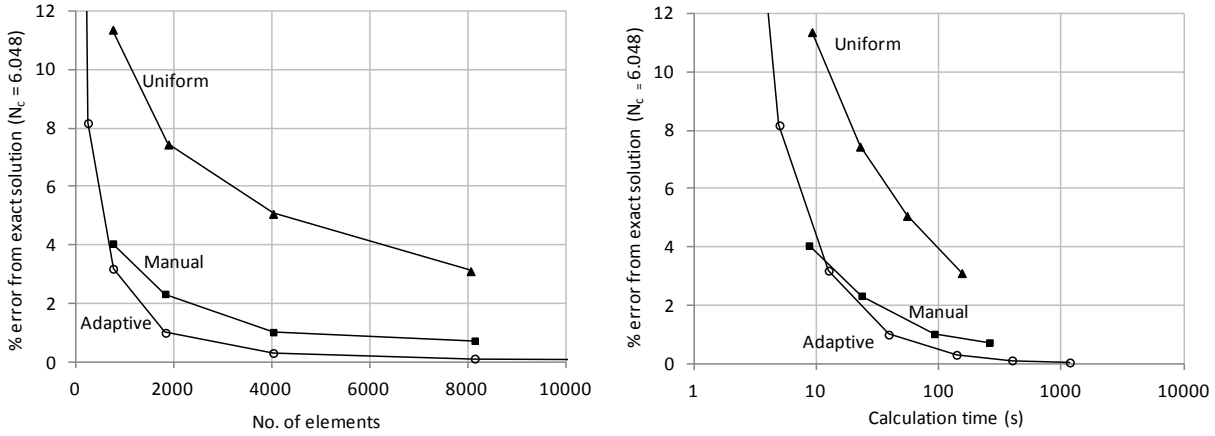

(a) Number of elements (b) Calculation time

Figure 3.30: Bearing capacity results for different mesh types – rough circular foundation

3.5.2 3D analysis efficiency comparison

The mesh comparison process was repeated for the 3D analysis of a rough square foundation as per the case described in Section 3.4.3.2. Uniform and manual meshes were set up to compare the bearing capacity results with the adaptive mesh results shown in Figure 3.26. Five meshes containing approximately 500, 1,100, 3,000, 7,700 and 17,700 elements were set

up for each of the uniform and manual mesh types. The meshes used for the case of approximately 7,700 elements for each mesh type are shown Figure 3.31.

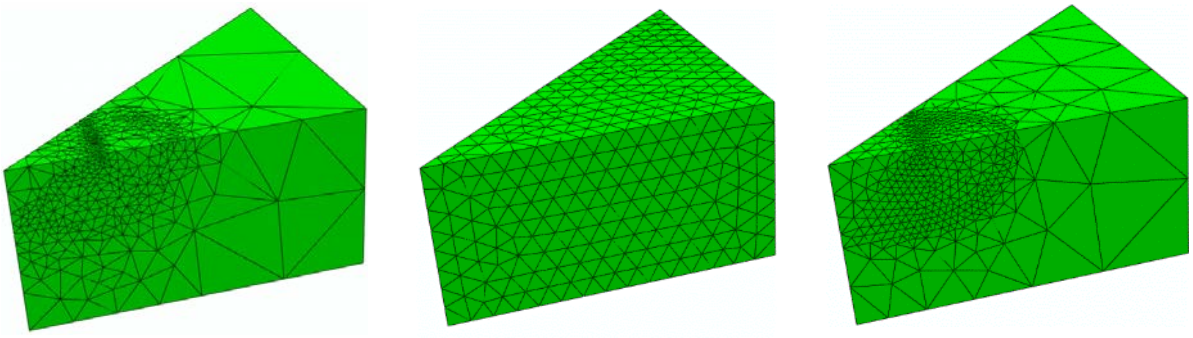

(a) Adaptive mesh 7,647 elements

(b) Uniform mesh 7,879 elements

(c) Manual mesh 7,714 elements

Figure 3.31: Comparison of mesh types for a rough square foundation

The bearing capacity results from the analyses with the different mesh types are shown in Figure 3.32. The results are given in terms of the percentage error from the final adaptive solution found for a rough square foundation (N_c = 5.762). The adaptive meshes gave slightly more accurate results than the manual meshes, and significantly more accuracy than the uniform meshes.

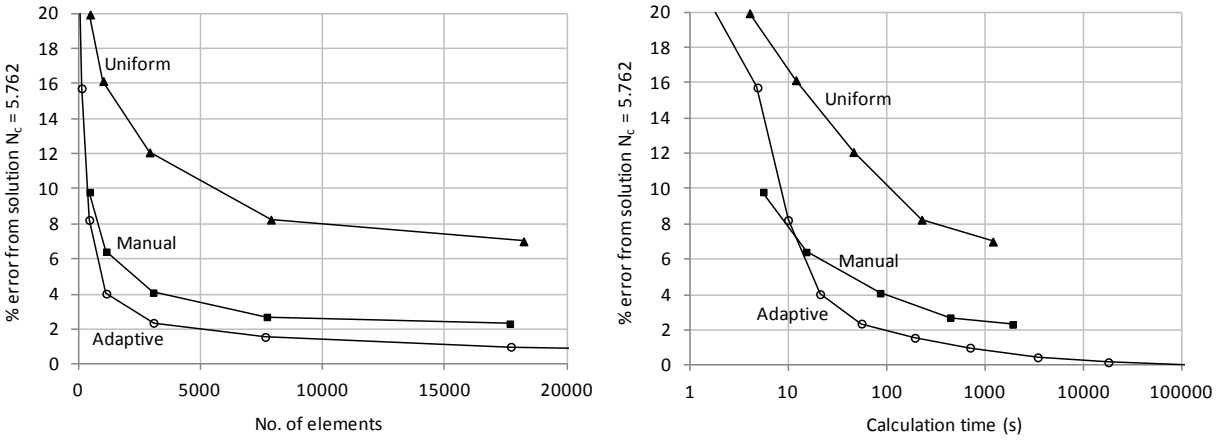

(a) Number of elements

(b) Calculation time

Figure 3.32: Bearing capacity results for different mesh types – rough square foundation

The results in Figure 3.32(b) show that adaptive meshing is most efficient if an error of less than about 7% is sought. If an error greater than 7% is satisfactory is satisfactory then manual meshing is most efficient in terms of calculation time. Again this disregards the design time for the manual mesh. The adaptive approach has the advantage of convenience as meshing is automated.

3.6 Summary and conclusions

A UMAT subroutine has been described comprising a stress return algorithm that implements the Tresca yield criterion without any approximation of the yield or plastic potential surfaces. Results obtained with the UMAT were found to closely match known bearing capacity solutions, whereas other approaches involving surface approximations provided an under-prediction of the solutions in both axisymmetric and 3D problems.

To reduce the error in the assessment of foundation bearing capacity in FEA associated with discretisation of the soil, an adaptive mesh refinement scheme has been implemented. This automatically refines the mesh based on the concentration of plastic shear strain. The adaptive mesh refinement also enables the layout of the plastic regions making up the failure mechanism to be visualised through inspection of the refined mesh.

It has been shown through validation analysis of circular foundation bearing capacity that the combination of the Tresca UMAT and the adaptive meshing scheme allows Abaqus FEA solutions to converge towards the exact solution as the mesh is refined. The procedure was used to investigate the bearing capacity of a square foundation for which a wide range of bearing capacity factors N_c have previously been proposed. Part of the hindrance in solving this problem is uncertainty surrounding the nature of the failure mechanism occurring. Examination of the refined mesh indicated the critical mechanism to contain four planes of symmetry, including two diagonal planes. Square foundation bearing capacity factors of N_c = 5.44 (smooth interface) and N_c = 5.76 (rough interface) were determined. These are generally

lower than values found in previous studies, and particularly compared with the value of N_c = 6.17 commonly adopted in design codes.

The required calculation time when using adaptive meshing compared to manual meshing was assessed. Adaptive meshing was more efficient in 2D analysis for obtaining an error less than about 3%, or in 3D analysis if an error less than about 7% was sought. This assessment disregards the time needed to design the manual mesh, which may require a process of trial and error by the user. This design time is not required for the adaptive meshing scheme as the meshing process is automated.

Chapter 4. Vertical bearing capacity of perforated foundations

This chapter examines the bearing capacity of perforated foundations on undrained soil when subject to vertical loading. Although the offshore environment often imposes significant horizontal and moment loading, it is important to firstly understand the behaviour of perforated foundations for the case of purely vertical loading. Combined loading is considered subsequently in Chapter 5.

Both ring and square annular footings with a range of perforation ratios have been analysed using the finite element software Abaqus. Undrained Tresca soil has been modelled using the user material subroutine (UMAT) and the adaptive mesh refinement procedure described in Chapter 3. Foundations with both smooth and rough interfaces have been modelled on soil with uniform and linearly increasing undrained shear strength profiles. A varying degree of foundation embedment has been examined for the case of a rough interface, which is considered to be representative of a skirted foundation. The results have been used to derive a design method for the bearing capacity of ring and square annular foundations under vertical loading. Finally, as the analyses concentrate on a single perforation, consideration is given to the impact of multiple perforations on capacity.

4.1 Analysis approach

The geometric properties of the ring and square annular foundations analysed are summarised in Figure 4.1. The ring foundation has an outer radius r_o and an inner radius r_i, with the difference being defined as the effective width of the foundation, B^*. The square annular foundation has an outside width B and an effective width B^*. Boundary conditions are used to implicitly model a rigid foundation.

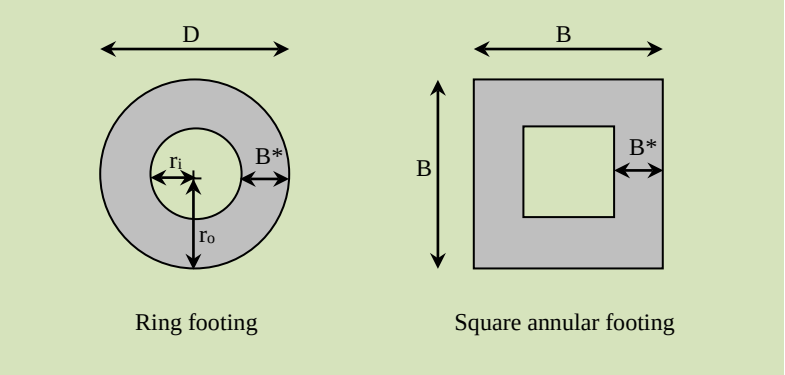

Figure 4.1: Geometry of ring and square annular foundations

The perforation ratio *R* for each foundation type can be defined by the following:

a) Ring foundation:

$$R = \frac{r_i^2}{r_o^2} \tag{4.1}$$

b) Square annular foundation:

$$R = \frac{(B - 2B^*)^2}{B^2}$$

Both foundations on the soil surface and at a range of embedded depths *d* were analysed as shown in Figure 4.2. The vertical capacity of solid and skirted foundations in uniform soil has been shown to be the same (Yun and Bransby, 2007) and so only solid embedded foundations have been modelled to cover both cases. However, when soil strength increases with depth the capacity of skirted foundations at shallower embedment depths (*d*/*B* < 0.3) can be lower than a solid foundation (Mana et al., 2013). In these cases the results presented may be unconservative for skirted foundations.

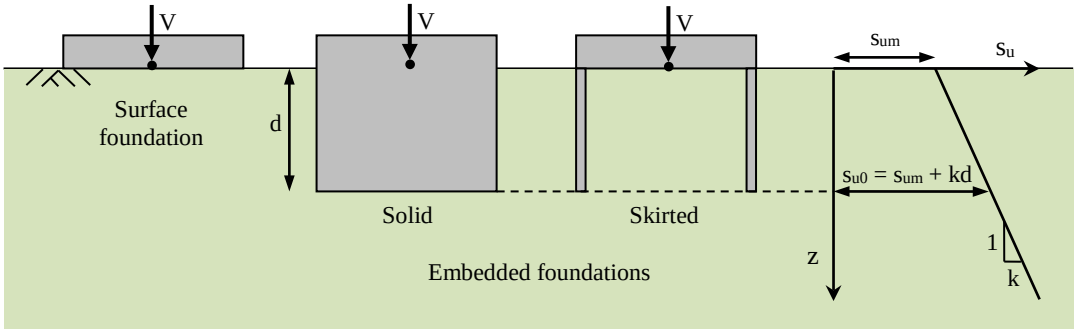

Figure 4.2: Surface and embedded foundations with variation of undrained strength with depth

Smooth and rough foundation-soil interfaces have been considered. Weightless ($\gamma = 0$), isotropic soils with both homogeneous and heterogeneous undrained soil strength profiles were adopted. For heterogeneous soil the shear strength varied linearly, with k defining the rate of strength increase as given by Equation 2.3. Undrained Tresca soil has been modelled using the user material subroutine (UMAT) and the adaptive mesh refinement procedure described in Chapter 3. The value of k is set as an input to the UMAT to describe the soil strength gradient (Figure 4.2).

A vertical load V has been applied via a prescribed vertical displacement until the failure load V_{max} is reached. Results for both the surface and embedded footings have been presented in terms of the bearing capacity factor N_c, which relates to V_{max} as follows:

$$N_c = \frac{V_{max}}{As_{um}} \tag{4.2}$$

where A denotes the foundation contact area (see Figure 1.2). The following cases have been analysed and the results presented in this chapter:

1) Ring foundations:
    i. Surface – rough interface
    ii. Surface – smooth interface
    iii. Embedded – rough base, smooth sides
2) Square annular foundations:
    i. Surface – rough interface
    ii. Surface – smooth interface
    iii. Embedded – rough base, smooth sides
3) Square foundations with multiple perforations:
    i. Surface – rough interface

Only a rough base interface has been modelled for the case of the embedded foundations. This was intended to simulate skirted offshore foundations in which a soil-soil

interface exists at skirt tip level. Curves have been fitted to the analysis results and an expression has been proposed for use in design.

4.2 Ring foundations

An axisymmetric finite element model was set up for the ring foundations as shown in Figure 4.3. The outside radius r_o of the footing was maintained at 0.5 m. The internal radius r_i was varied to investigate different perforation ratios R as defined in Equation 4.1. The values analysed were R = 0, 0.01, 0.04, 0.16, 0.36, 0.64, 0.81 and 0.90 (i.e. r_i/r_o = 0, 0.1, 0.2, 0.4, 0.6, 0.8, 0.9 and 0.95). The soil was modelled with the undrained shear strength at the surface s_{um} = 1 kPa; varying soil strength heterogeneity defined by the dimensionless quantity kD/s_{um} = 0 (homogeneous), 1, 2, 5; an undrained stiffness modulus E_u = 1000 kPa; and undrained Poisson's ratio of v = 0.499. The mesh was composed of triangular quadratic hybrid elements (CAX6H) with an initial coarse mesh as shown in Figure 4.3. The mesh was subsequently refined using the adaptive mesh refinement scheme and several iterations were undertaken until the failure load converged to within 0.1% of the previous solution.

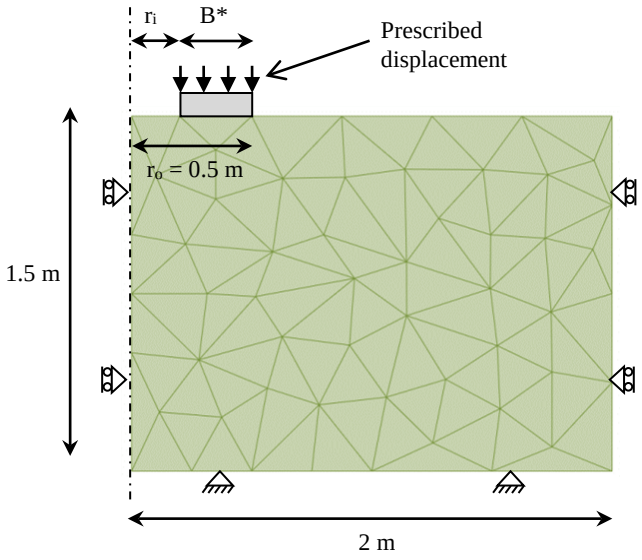

Figure 4.3: Ring foundation finite element model arrangement (foundation for illustration)

4.2.1 Surface foundation – rough interface

4.2.1.1 Circular foundation

Rough circular foundations (having a perforation ratio $R = 0$) were initially analysed for each strength profile, as exact solutions are available for comparison. The case of $kD/s_{um} = 0$ has already been examined in detail in Section 3.4.1. The bearing capacity factors N_c for each strength profile are shown in Table 4.1. The Abaqus results are compared with exact solutions from the program ABC using the method of characteristics (Martin, 2004), which themselves have been validated against previous studies by Salecon and Matar (1982), Houlsby and Wroth (1983) and Tani and Craig (1995). Table 4.1 shows that the Abaqus results closely match those from ABC, all having a difference of no more than 0.1%.

Table 4.1: Comparison of N_c for rough circular foundations

kD/s_{um}	**Bearing capacity factor, N_c**		**Abaqus analysis summary**		
	ABC (Martin, 2004)	Abaqus (this study)	Error (%)	No. of iterations	Final element count
0	6.048	6.051	0.07	6	15,718
1	6.946	6.950	0.05	6	20,632
2	7.626	7.632	0.07	6	23,586
5	9.232	9.241	0.10	6	28,299

The results are plotted in Figure 4.4 along with the values calculated using the classical approach given by Equation 2.6 (with $d_{ca} = i_{ca} = 0$) from the design code DNV (1992). The DNV (1992) results are seen to agree well with the numerical results.

The nature of the plastic regions for each case analysed is shown by way of the refined Abaqus meshes in Figure 4.5. Failure occurs through a Prandtl-type mechanism, which is expected due to the rough foundation-soil interface. The mechanism becomes more localised to the foundation base as the soil strength gradient increases. With increasing strength gradient the mechanism appears to approach the shape of a Hill type mechanism.

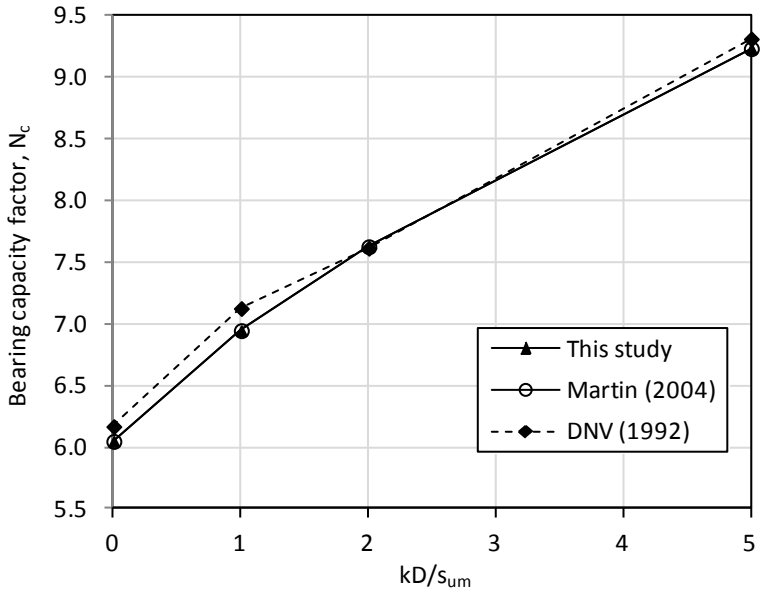

Figure 4.4: Rough circular foundation capacity results with increasing soil strength

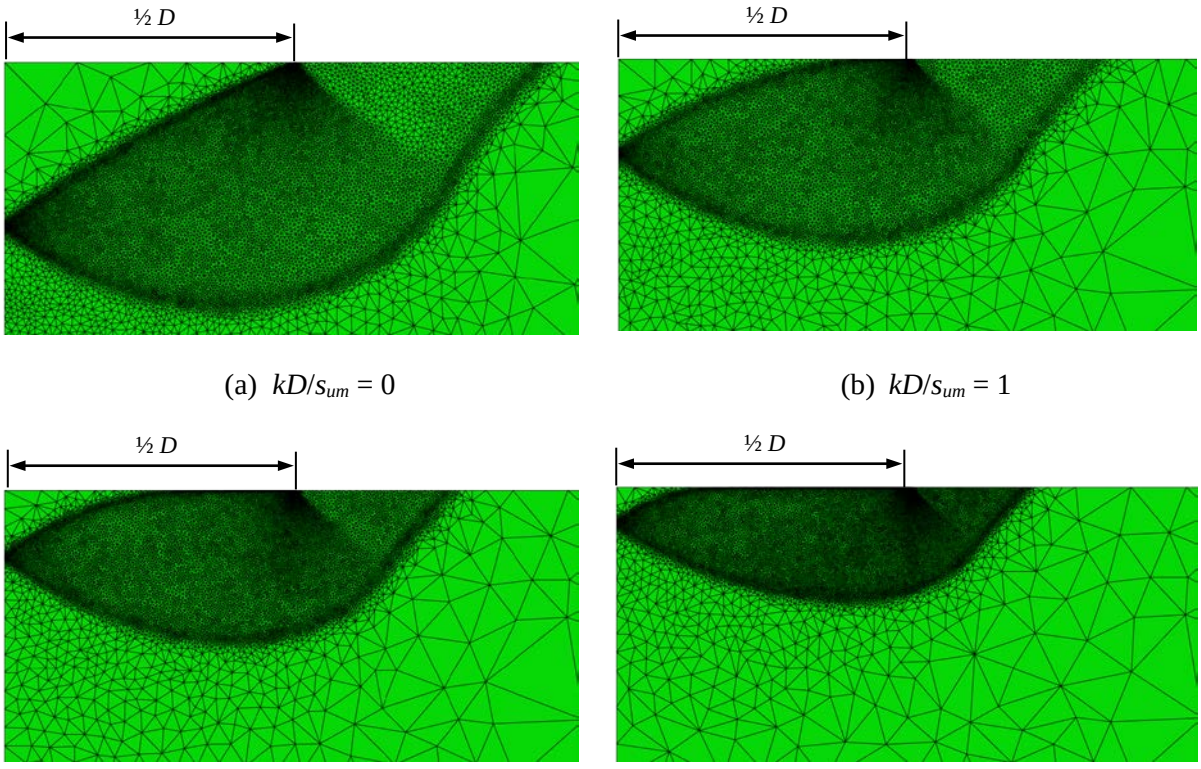

(a) $kD/s_{um} = 0$ (b) $kD/s_{um} = 1$

(c) $kD/s_{um} = 2$ (d) $kD/s_{um} = 5$

Figure 4.5: Refined mesh of rough circular foundation plastic regions

4.2.1.2 Ring foundation

The vertical load-displacement results for the rough ring foundations on homogeneous soil are given in Figure 4.6. A perfectly plastic response is seen at failure of the foundation. The load at this point is the ultimate vertical load, V_{max}. The vertical displacement required to mobilise the maximum load decreases as the perforation ratio increases. The bearing capacity factor N_c is determined from this maximum load as per Equation 4.2. The corresponding N_c values for the maximum loads for each foundation are plotted in Figure 4.7. As the perforation ratio increases the value of N_c decreases from N_c = 6.05 for a rough circle and approaches the value of N_c = 5.14 for a strip. The exception to this is at the smallest perforation in which soil arching occurs, resulting in a slight increase in N_c. The peak value in Figure 4.7 at this point is N_c = 6.10 occurring at R = 0.01.

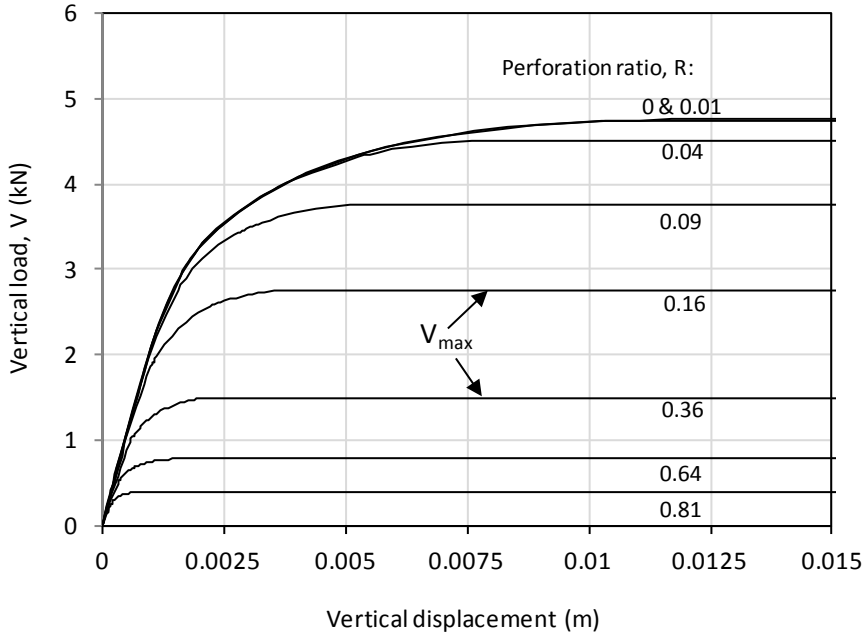

Figure 4.6: Load-displacement curves for rough ring foundations on homogeneous soil

The variation of the plastic regions as the perforation ratio increases is also shown in Figure 4.7. The mechanisms inferred from the plastic regions can be categorised into four types:

i) Full mechanism, (Prandtl-type) for a solid circle (Figure 4.7(a))

ii) 'Superfooting' mechanism, where arching occurs at very small *R* (Figure 4.7(b))

iii) Intermediate mechanism, in which there is interaction with the axis of symmetry (Figure 4.7(c - d))

iv) Isolated mechanism, when *R* becomes large enough such that interaction ceases (Figure 4.7(e - h)).

An isolated mechanism is seen to initiate between *R* = 0.16 and *R* = 0.36. At *R* = 0.9 it is seen that the Prandtl mechanism is not yet completely symmetrical. This provides a possible reason why the N_c value is not closer to that of a strip at this point.

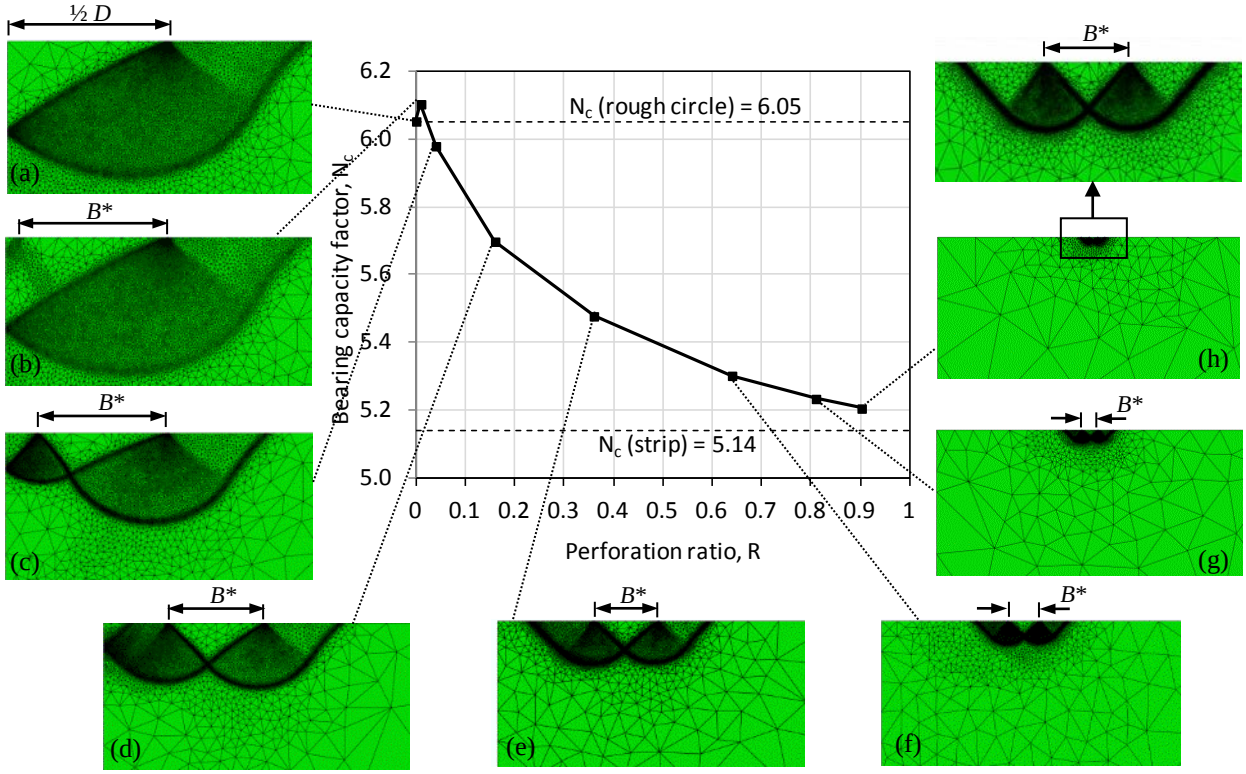

Figure 4.7: Bearing capacity for rough ring foundations on homogeneous soil

The results for a rough ring foundation with increasing soil strength heterogeneity are given in Figure 4.8. The N_c values at *R* = 0 represent the solid circular foundation results given in Table 4.1. A similar trend as occurred for homogeneous soil is observed. The N_c

value starts at the capacity of a solid circle and tends towards N_c = 5.14 as the perforation ratio approaches unity. This is because the effective heterogeneity ratio, kB^*/s_{um}, is reducing. The arching mechanism that occurred in homogeneous soil diminishes with increasing soil strength heterogeneity. Another impact of the strength gradient is that an isolated failure mechanism starts to occur at a lower perforation ratio R. This is shown in Figure 4.9, where at R = 0.16 the case of kD/s_{um} = 5 has an isolated mechanism whilst an interaction mechanism remains for kD/s_{um} = 0.

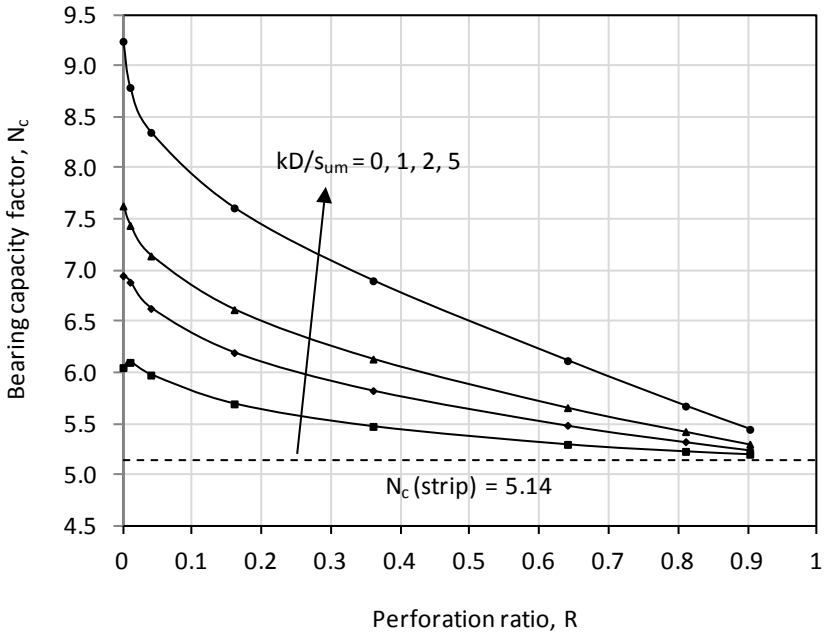

Figure 4.8: Bearing capacity factors for rough ring foundations

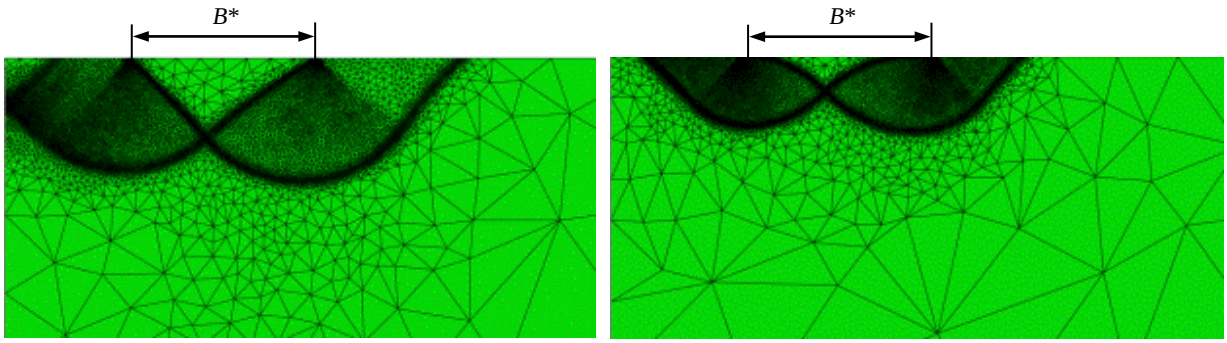

(a) kD/s_{um} = 0 (b) kD/s_{um} = 5

Figure 4.9: Refined mesh of rough circular foundations, R = 0.16

4.2.1.3 Comparison with previous results

The ring foundation results for homogeneous soil (k = 0) are compared in Figure 4.10 with those obtained by Galloway (2004) also using Abaqus, with fine but non-adaptive meshing. The results from this study are shown for the case when the UMAT and adaptive meshing were used, and the case when they were not. The result from Galloway (2004) at R = 0 under-predicts the exact value. As R increases the results remain under those predicted by this study until about R = 0.64 when they become higher. This disparity is expected to be due to the analysis by Galloway (2004) being performed using the built-in Abaqus Tresca material (which uses a Tresca-Mises plastic potential function) and with a less refined mesh. However the overall trend is similar.

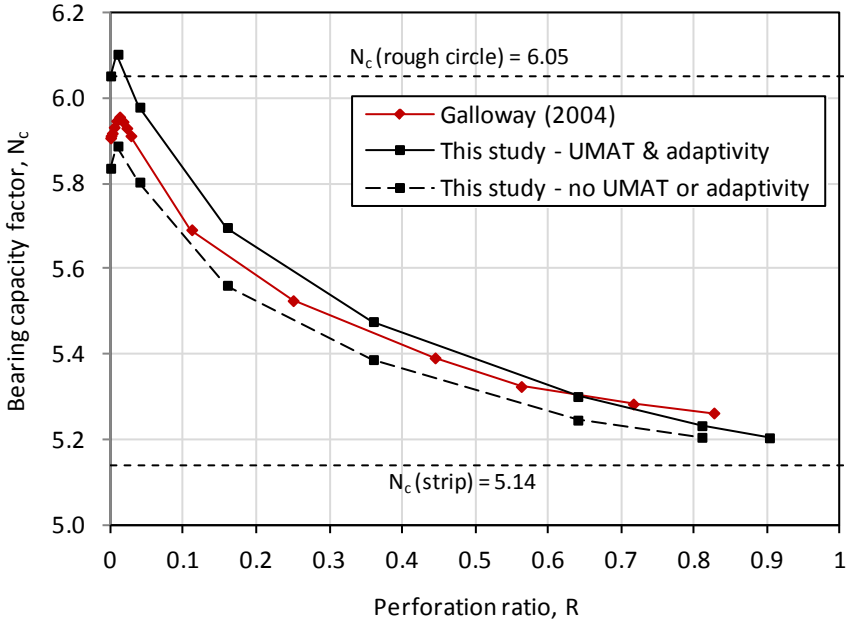

Figure 4.10: Comparison of results for rough ring foundation on homogeneous soil

4.2.2 Surface foundation – smooth interface

4.2.2.1 Circular foundation

Smooth circular foundations were initially analysed for each strength profile and the results compared against available exact solutions. The case of kD/s_{um} = 0 has been examined in

detail in Section 3.4.1. The bearing capacity factors N_c for each strength profile are shown in Table 4.2. The Abaqus results are compared with exact solutions from the program ABC using the method of characteristics (Martin, 2004), which themselves have been validated against previous studies by Houlsby and Wroth (1983), Martin (1994) and Tani and Craig (1995). It is seen in Table 4.2 that the Abaqus results closely match those from ABC, all having a difference of 0.04%.

Table 4.2: Comparison of N_c for smooth circular foundations

kD/s_{um}	**Bearing capacity factor, N_c**		**Abaqus result summary**		
	ABC (Martin, 2004)	Abaqus (this study)	Error (%)	No. of iterations	Final element count
0	5.689	5.691	0.04	6	19,577
1	6.246	6.248	0.04	6	15,794
2	6.723	6.726	0.04	6	15,199
5	7.937	7.940	0.04	6	15,640

The results are plotted in Figure 4.11 along with the values given by the design code DNV (1992) using Equation 2.6. It is seen that the DNV (1992) values overestimate capacity for $kD/s_{um} < 2$ but at higher values compare well with the results of this study and Martin (2004).

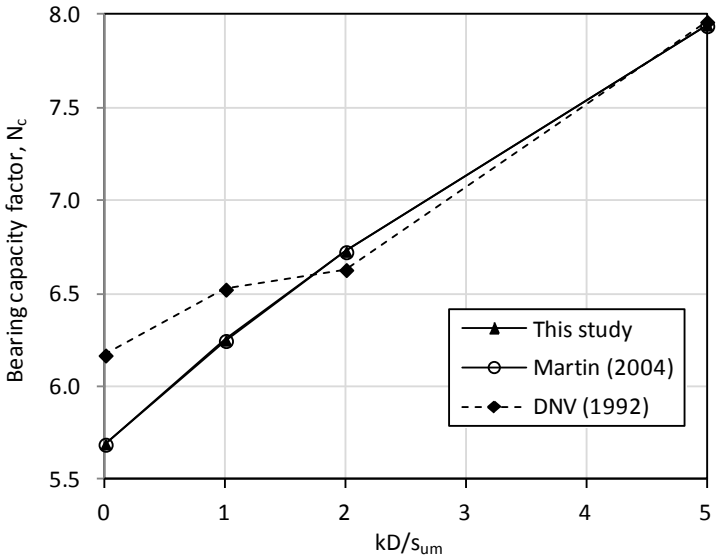

Figure 4.11: Smooth circular foundation capacity results with increasing soil strength

The nature of the plastic regions for each case analysed is shown by way of the refined meshes in Figure 4.12. Failure occurs by a Hill-type mechanism, which is expected due to the smooth foundation-soil interface. The mechanism becomes more localised to the foundation base as the soil strength gradient increases.

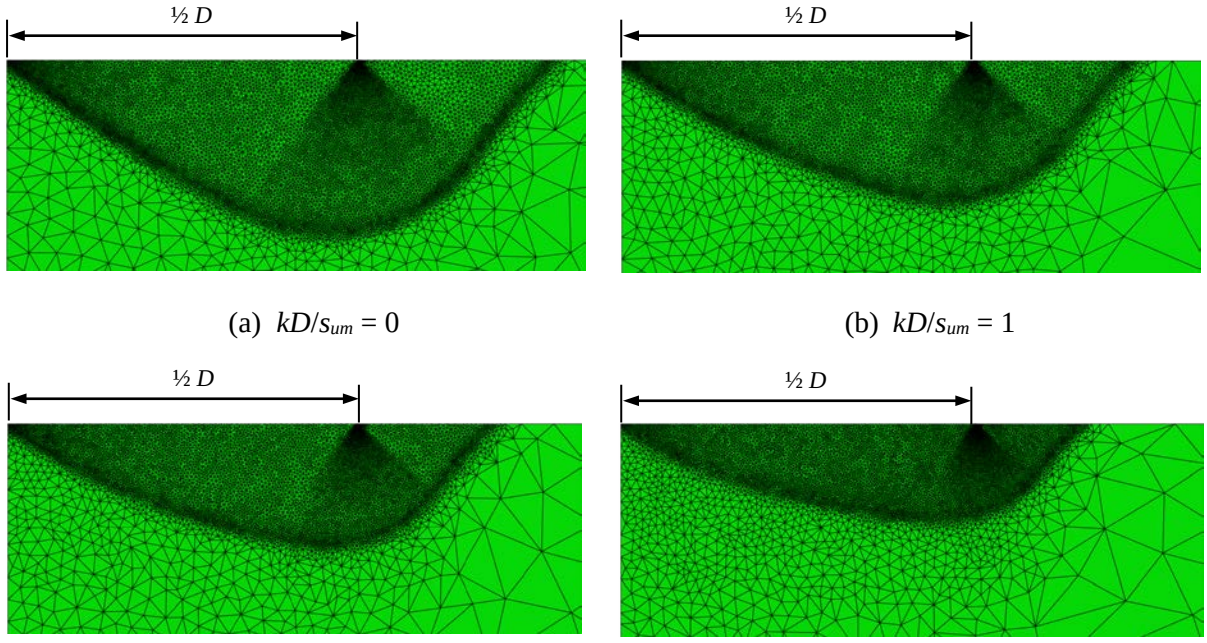

(a) $kD/s_{um} = 0$ (b) $kD/s_{um} = 1$

(c) $kD/s_{um} = 2$ (d) $kD/s_{um} = 5$

Figure 4.12: Refined meshes showing circular foundation plastic regions

4.2.2.2 Ring foundation

The results from the analysis of smooth ring foundations on homogeneous soil are given in Figure 4.13. As was seen with the rough ring, the value of N_c tends towards the expected 5.14 for a strip as the perforation ratio R increases. However no noticeable 'superfooting' effect is observed, as N_c drops immediately with the introduction of a perforation. The same variation in failure mechanism types occurs as with a rough ring, except there is no arching mechanism. The onset of an isolated mechanism occurs earlier than a rough ring. It is present by $R = 0.16$ as can be seen in Figure 4.13.

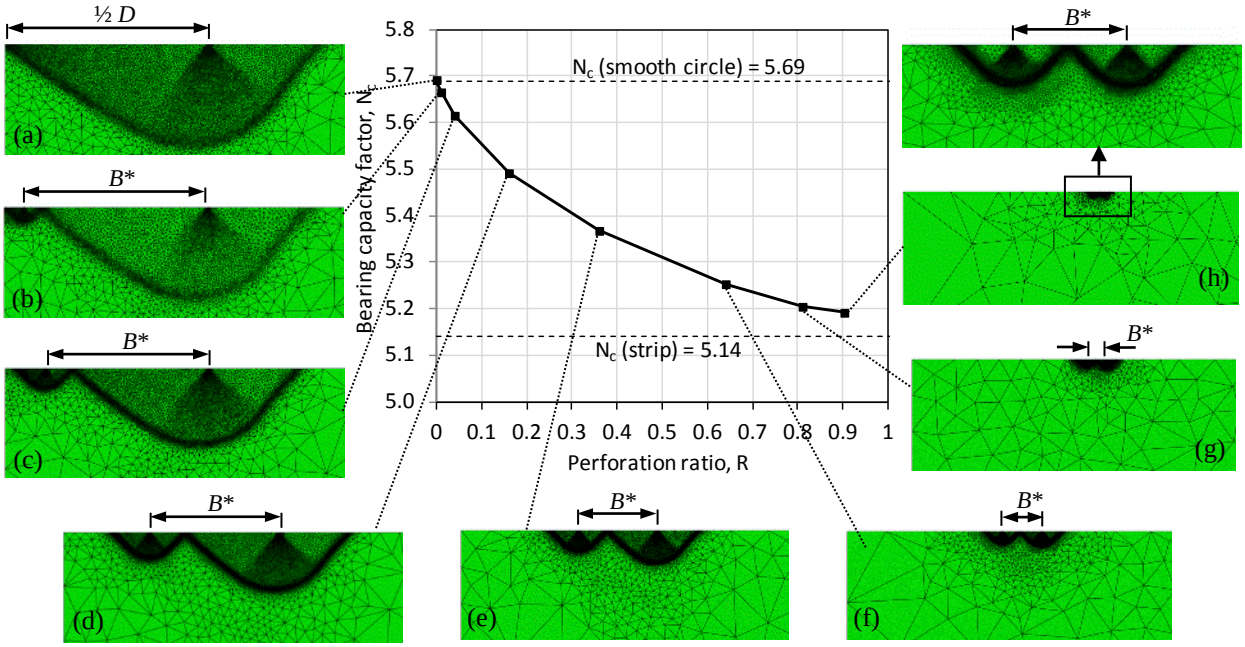

Figure 4.13: Bearing capacity for a smooth ring foundations on homogeneous soil

The results for a smooth ring foundation with increasing soil strength heterogeneity are given in Figure 4.14. The N_c values at R = 0 represent the solid circular foundation results given in Table 4.2. A similar trend is observed as occurred for homogeneous soil. The N_c value starts at the capacity of a solid circle and tends towards N_c = 5.14 as the perforation ratio increases.

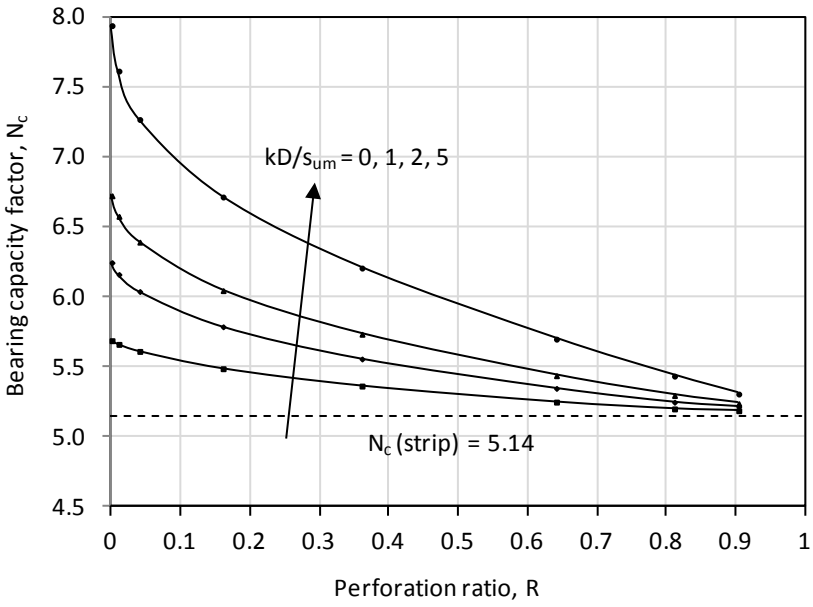

Figure 4.14: Bearing capacity factors for smooth ring foundations

4.2.2.3 Comparison with previous results

The ring foundation results for homogeneous soil (k = 0) are compared in Figure 4.15 with those obtained by Galloway (2004). The results from this study are shown for the case when i) the UMAT and adaptive meshing were used and ii) when they were not. Analysis in the study by Galloway (2004) was undertaken using Abaqus. Galloway (2004) compared his results with predictions from the program 'Mudnut' and those obtained using the ABC software, with modifications made to accommodate ring foundations.

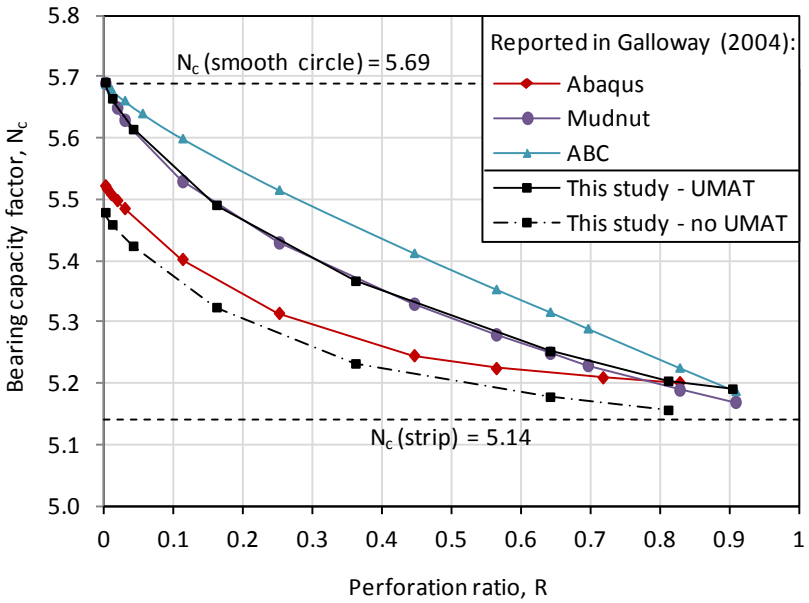

Figure 4.15: Comparison of results for smooth ring foundation on homogeneous soil

The Abaqus result from Galloway (2004) at R = 0 under-predicts the exact value for a circular foundation. As R increases the results continue to be lower than those predicted from this study with the UMAT, except at approximately R = 0.8 when they converge. This difference is expected due to the Abaqus analysis by Galloway (2004) using the built-in Abaqus Tresca model. The convergence of the results as R increases may be because of the under prediction due to the Tresca model offsetting an over-prediction from the lower degree of mesh refinement in the analysis by Galloway (2004).

The Mudnut results presented in Galloway (2004) are seen to provide a good match with those from this study (Figure 4.15). The Mudnut results are generated based on the

superposition of the pressure distribution of two cases as shown in Figure 4.16 (Galloway, 2004). The first case considers a solid circular foundation where the pressure distribution, taken as a multiple of s_u, ranges from a minimum value at the edge to a maximum value at the centre. The value at the edge is equal to 5.14 (the value for a strip footing), while the maximum value at the centre is such that the average pressure distribution on the footing is 5.69 (the value of a smooth circular footing). The second case considers the pressure distribution on an infinite footing with a central hole. The pressure at the edge of the hole is 5.14, and increases to a maximum as infinity is approached.

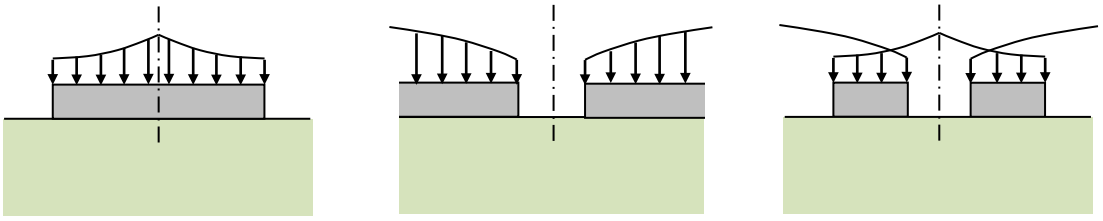

Figure 4.16: Ring foundation pressure distribution adopted by Mudnut (after Galloway, 2004)

There is some divergence in the results from Mudnut and this study at high perforation ratios which could be due to the increased mesh refinement effort required in Abaqus for smaller foundation geometry. Comparing the results produced using the modified ABC, it is seen that they provide a higher estimate of bearing capacity, but these solutions are not rigorous plasticity solutions except when $R = 0$.

4.2.3 Embedded foundation

To model an embedded ring foundation an axisymmetric finite element model was set up as shown in Figure 4.17. As was the case for the surface foundation, the outside radius r_o was maintained at 0.5 m whilst the internal radius r_i was varied to investigate different perforation ratios R. The soil was modelled with the undrained shear strength at the surface s_{u0} = 1 kPa, an undrained stiffness modulus E_u/s_u = 5000 and an undrained Poisson's ratio of ν = 0.499. A

foundation was modelled by imposing a rough foundation base and smooth side walls (having zero interface adhesion), which were chosen as being representative of a skirted foundation. Embedment depths of d/D = 0.1, 0.2, 0.3 and 0.5 were examined as well as d/D = 1 for the case of R = 0. The mesh was composed of triangular quadratic hybrid elements (CAX6H) with an initial coarse mesh as shown in Figure 4.17. The mesh was subsequently refined using the adaptive meshing scheme for several iterations until the failure load converged to within 1% of the previous solution.

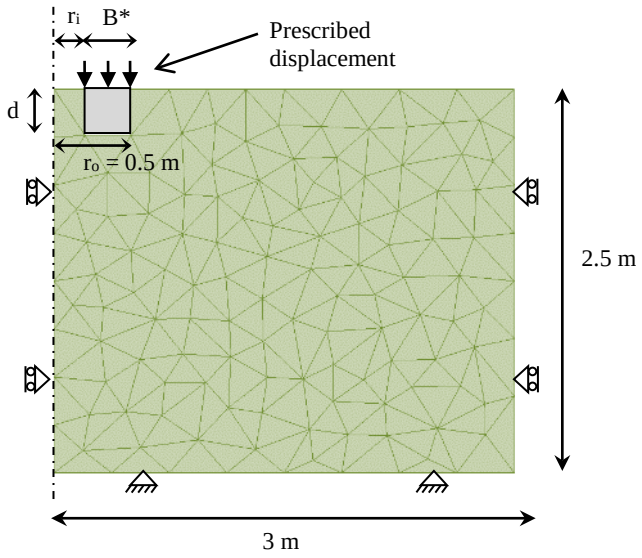

Figure 4.17: Embedded ring foundation model arrangement (foundation for illustration)

4.2.3.1 Circular foundation

An embedded circular foundation was initially analysed to allow comparison with results from previous studies (Salgado et al., 2004, Edwards et al., 2005, Gourvenec and Mana, 2011). Results are compared in Figure 4.18 for kD/s_{u0} = 0 and for kD/s_{u0} = 5, where s_{u0} is taken at embedment level. Good agreement is obtained with the results from the other studies. The prediction given by DNV (1992) using Equation 2.6 with the depth factor given by Equation 2.8 is included in Figure 4.18. It does not show good agreement and is seen to underestimate the increase in foundation capacity with embedment.

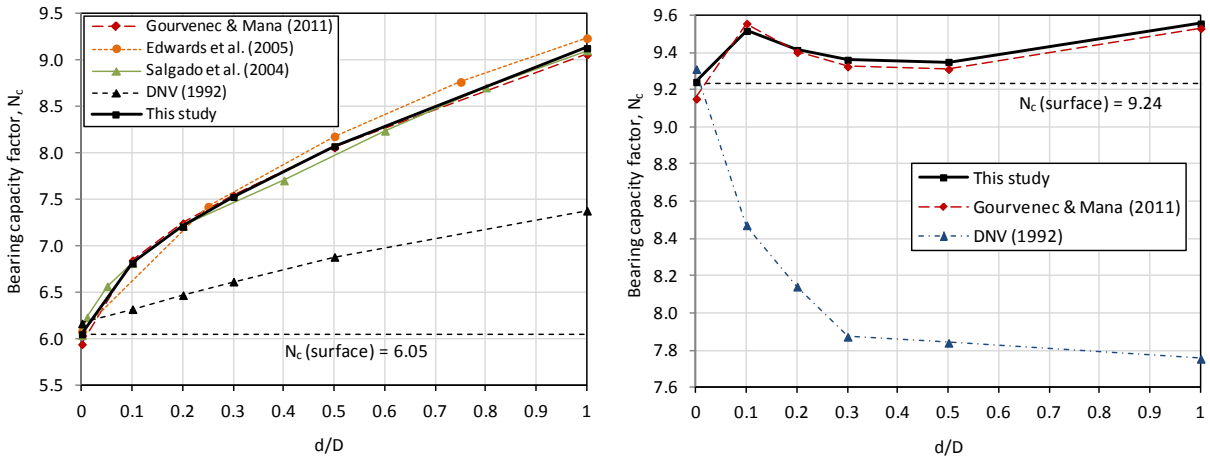

(a) $kD/s_{u0} = 0$ (b) $kD/s_{u0} = 5$

Figure 4.18: Bearing capacity factors for embedded circular foundations (rough base, smooth sides)

Examples of the plastic regions occurring for embedded circular foundations are shown in Figure 4.19. These are for embedment depths of $d/D = 0.2$ and 0.5 for the cases of $kD/s_{u0} = 0$ and for $kD/s_{u0} = 5$ as given in Figure 4.18. The failure mechanism extends from the base of the foundation to the surface of the soil as is expected. The mechanism decreases in size as the soil strength increases.

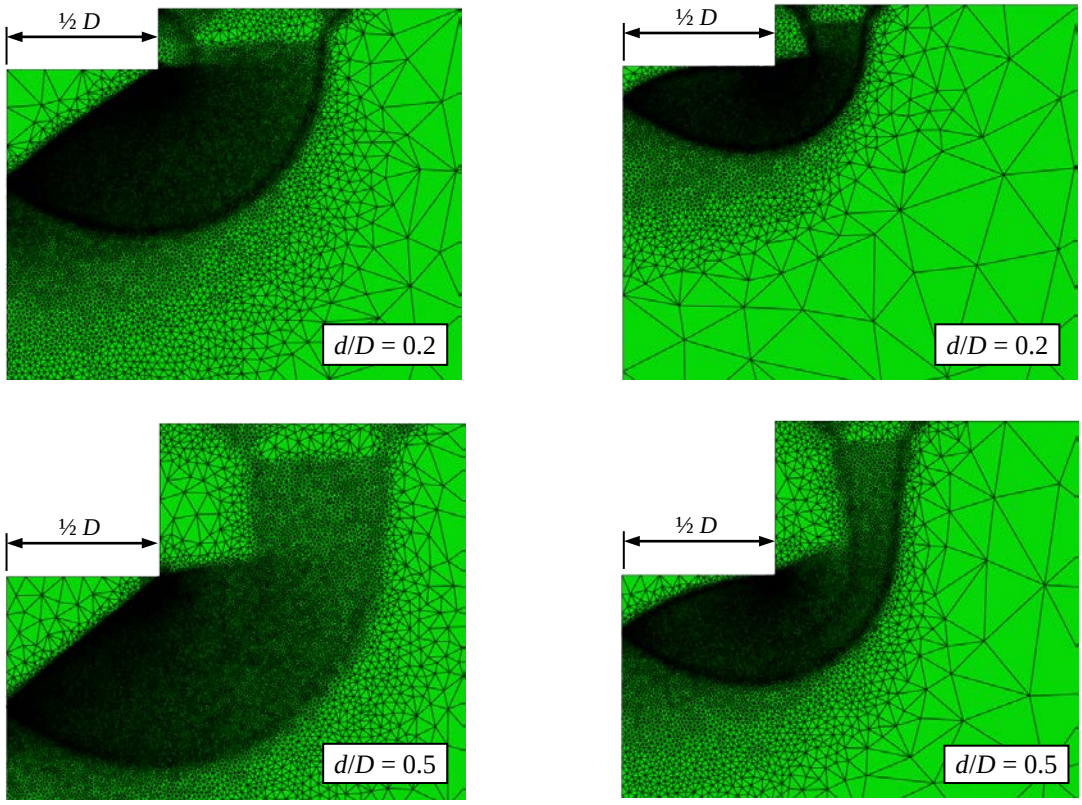

(a) $kD/s_{u0} = 0$ (b) $kD/s_{u0} = 5$

Figure 4.19: Plastic regions for embedded circular foundations

4.2.3.2 Ring foundation

The results from the analyses of embedded ring foundations are given in Figure 4.20. Embedment depths of d/D = 0, 0.1, 0.2, 0.3 and 0.5 were examined at different soil strengths where the dimensionless strength heterogeneity quantity kD/s_{um} was defined by using the soil strength at the surface s_{um}, rather than the strength at embedment depth level. Four different perforation ratios were assessed, being R = 0, 0.16, 0.36 and 0.64 which are considered to provide good coverage of the range of R that might be expected in the field. The bearing capacity factors N_c reduce with the introduction of a perforation. With increasing perforation the N_c values largely flatten out, albeit with a slight increase in N_c at higher R in some cases.

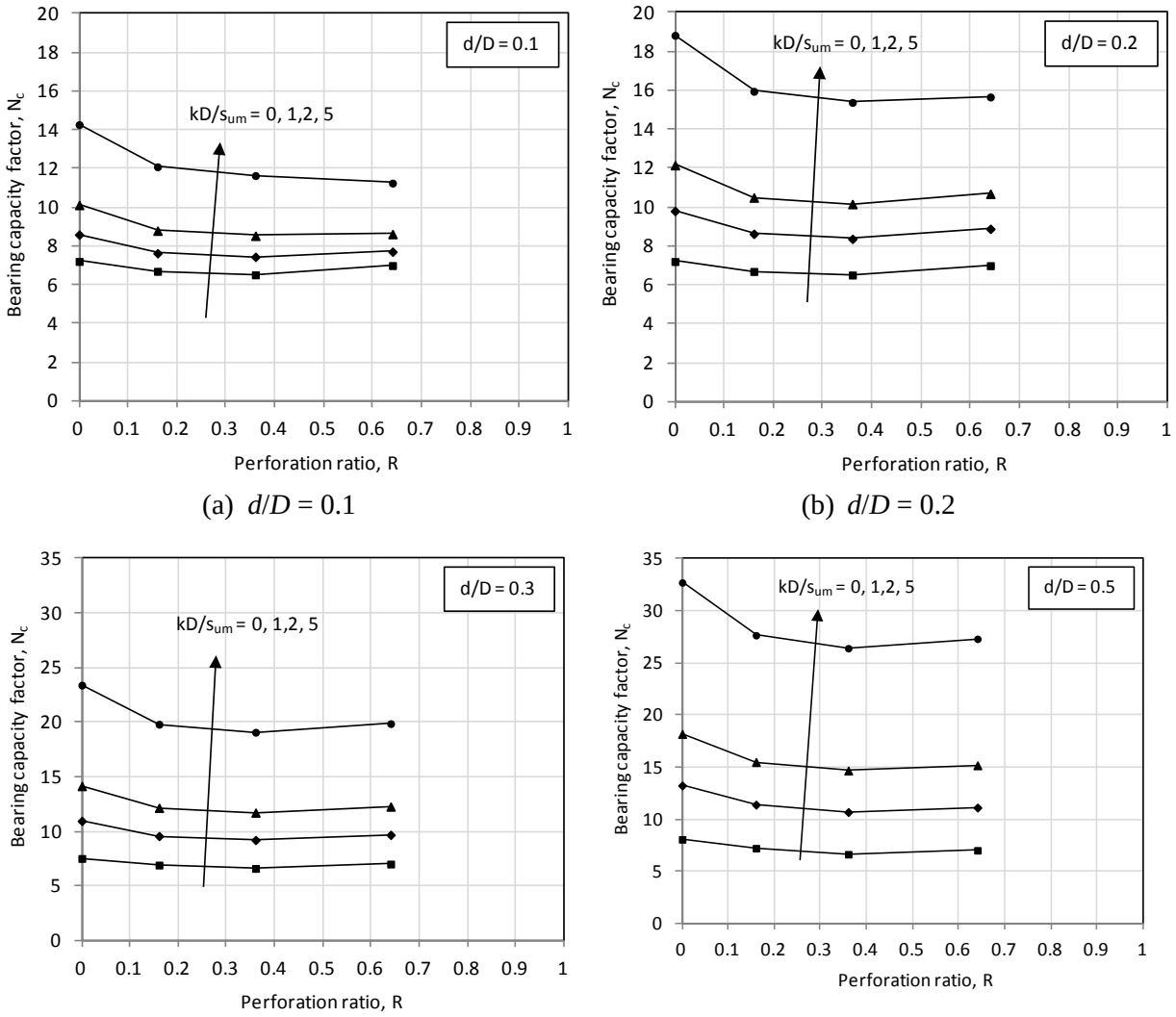

(a) d/D = 0.1 (b) d/D = 0.2

(c) d/D = 0.3 (d) d/D = 0.5

Figure 4.20: Bearing capacity factors for embedded ring foundations

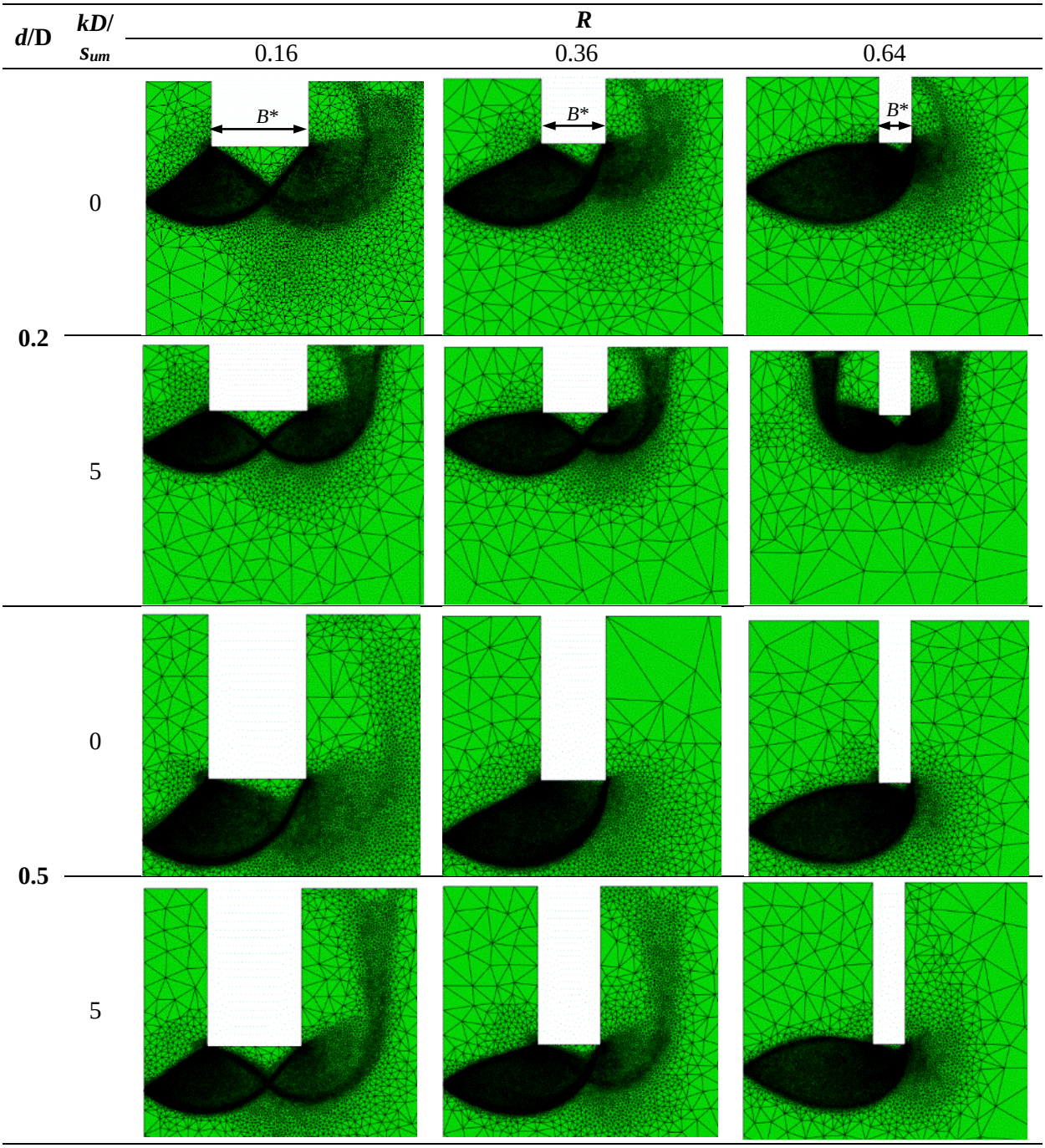

Figure 4.21: Failure mechanisms for embedded ring foundations

Examples of the failure mechanisms occurring for the embedded ring foundations are shown in Figure 4.21. Two different embedment ratios d/D = 0.2 and 0.5 and two strength gradients of kD/s_{um} = 0 and 5 have been presented. The nature of the mechanism varies as the perforation ratio R increases, as well as with the change in soil strength gradient and embedment depth. At d/D = 0.2 with homogeneous soil, the failure mechanism is seen to occur internally as R increases. This was not seen with surface foundations. With greater

strength heterogeneity however the mechanism remains either side of the ring. At a deeper embedment of d/D = 0.5 the failure mechanism is seen to remain internal, even with increasing strength heterogeneity. The internal failure mechanism results in the internal soil plug displacing upwards and little deformation occurs outside the ring.

4.3 Square annular foundations

A 3D finite element model was set up to analyse square annular foundations. Symmetry was used such that 1/8th of the foundation was modelled as shown in Figure 4.22. The outside width, B, of the footing was maintained at 1 m whilst the dimension B^* was varied to investigate different perforation ratios R. The perforation ratios analysed were R = 0.01, 0.04, 0.16, 0.36, and 0.64. The soil was modelled with an undrained shear strength at the surface s_{um} = 1 kPa; varying soil strength heterogeneity of kB/s_{um} = 0 (homogeneous), 1, 2, 5; an undrained stiffness modulus E_u/s_u = 5000; and undrained Poisson's ratio of v = 0.499. The mesh was composed of tetrahedral quadratic hybrid elements (C3D10H) with an initial coarse mesh refinement similar to that shown in Figure 4.22. The mesh was subsequently refined using the adaptive meshing scheme. Several iterations were undertaken until the failure load was within 1% of the previous solution.

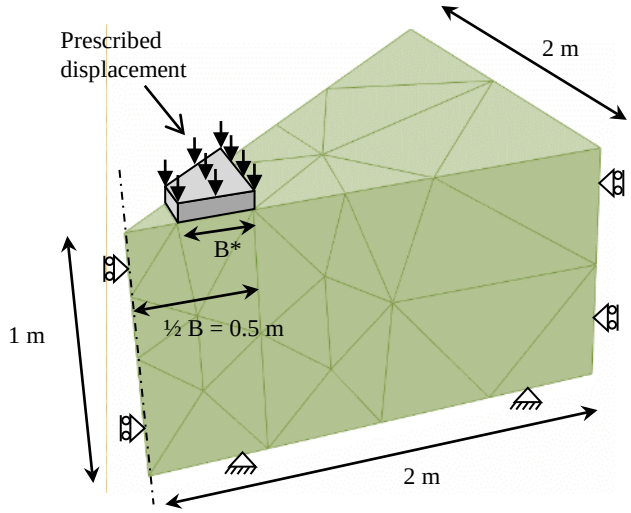

Figure 4.22: Square foundation model arrangement (foundation for illustration)

4.3.1 Surface foundation – rough interface

4.3.1.1 Square foundation

Rough square foundations (having a perforation ratio R = 0) were initially analysed for each of the soil strength profiles. The case of kB/s_{um} = 0 has been examined in detail in Section 3.4.3.2. The bearing capacity factors N_c for each strength profile are shown in Table 4.3. These are plotted in Figure 4.23 with the values using Equation 2.6 from the design code DNV (1992). Values from other studies for kB/s_{um} > 0 were not found for comparison. The DNV (1992) values overestimate the Abaqus predictions at all values of kB/s_{um}.

Table 4.3: N_c for rough square foundations with increasing soil strength

kB/s_{um}	Bearing capacity factor, N_c
0	5.762
1	6.663
2	7.359
5	9.022

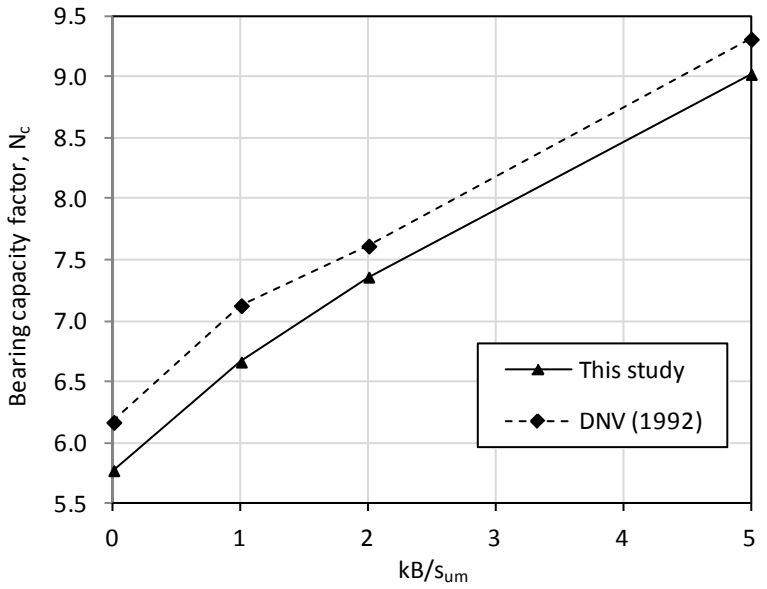

Figure 4.23: Rough square foundation capacity results with increasing soil strength

The nature of the failure mechanisms for each case analysed is shown by way of the refined mesh in Figure 4.24. The mechanism is not as sharply defined as the axisymmetric analysis

since equivalent refinement would require an excessively large mesh which becomes onerous for computing time. Failure occurs by a Prandtl-type mechanism, which is expected due to the rough foundation-soil interface. The mechanism is seen to become more localised to the foundation base as the soil strength gradient increases. With increasing strength gradient the mechanism appears to approach the shape of a Hill-type mechanism.

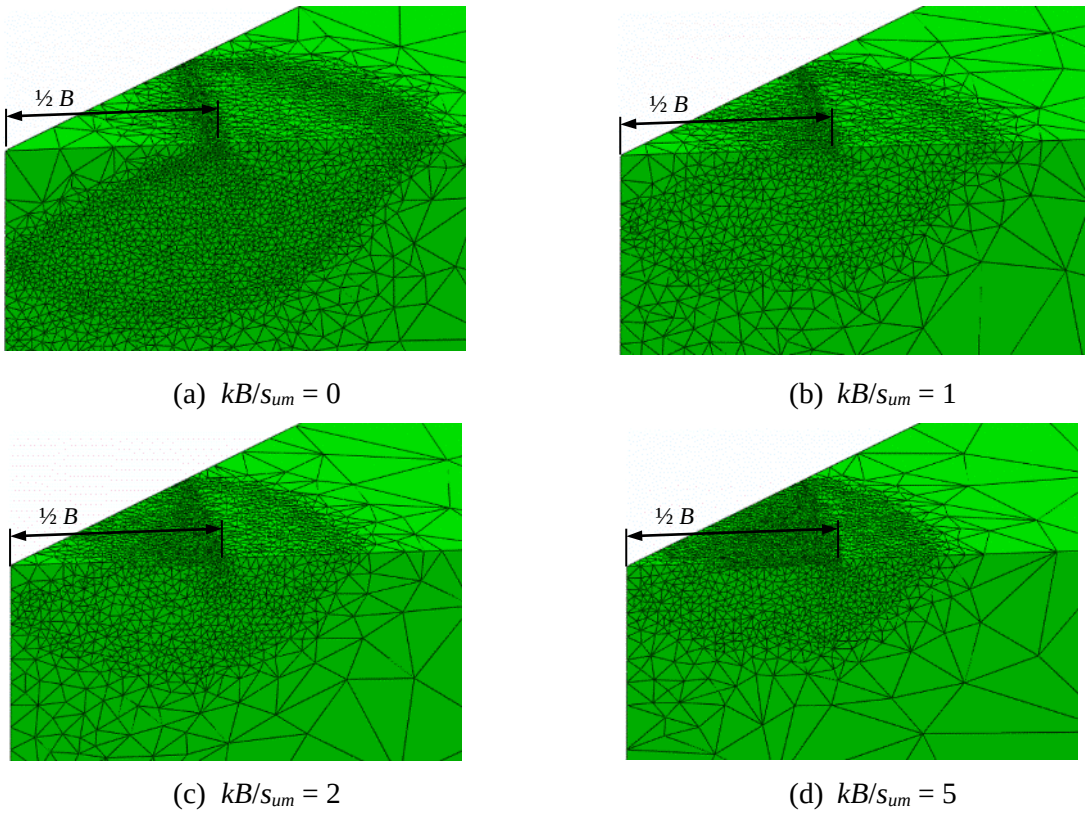

(a) $kB/s_{um} = 0$ (b) $kB/s_{um} = 1$

(c) $kB/s_{um} = 2$ (d) $kB/s_{um} = 5$

Figure 4.24: Refined meshes for rough square foundations

4.3.1.2 Square annular foundation

Results from the analyses of rough square annular foundations on homogeneous soil are given in Figure 4.25. In this figure results are included for the analysis cases of: i) standard Abaqus used with no Tresca UMAT or adaptive meshing, ii) UMAT is used with no adaptive meshing, and iii) both the UMAT and adaptive meshing are used. It is seen that the UMAT takes away the underestimation caused by the incorrect Tresca implementation, but the results do not exhibit the expected behaviour when manual meshing is used. This is

particularly the case as the perforation ratio *R* increases. With both the UMAT and adaptive meshing used, the results obtained are considered to be the best prediction of the solution.

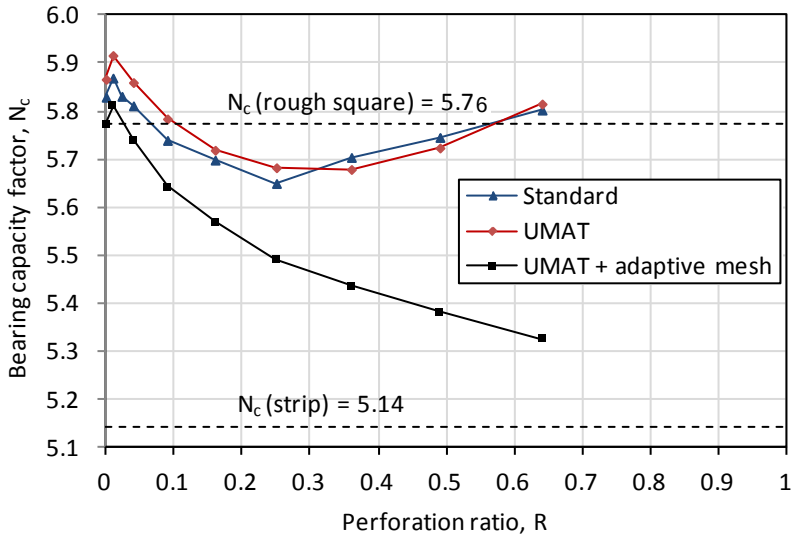

Figure 4.25: Bearing capacity factors for rough square annular foundations on homogeneous soil

The results for homogeneous soil are also given in Figure 4.26 with the corresponding plastic deformations (for 1/8th of the foundation). As the perforation ratio increases the value of N_c decreases from N_c = 5.76 for a rough square and approaches the value of N_c = 5.14 for a strip. The exception for this is at the smallest perforation in which soil arching occurs, resulting in a slight increase in N_c. The peak value in Figure 4.7 at this point is N_c = 5.81 occurring at R = 0.01. As with the rough ring foundation, the failure mechanisms occurring can be categorised into four types:

i) Full mechanism, (Prandtl-type) for a solid square (Figure 4.26(a))

ii) 'Superfooting' mechanism, where arching occurs at very small R (Figure 4.26(b))

iii) Intermediate mechanism, in which interaction occurs with the mechanism on the opposite side of the annulus (Figure 4.26(c - e))

iv) Isolated mechanism, where R becomes large enough such that interaction ceases (Figure 4.26(f - i)).

An isolated mechanism is seen to initiate at about R = 0.24. The difference between interacting and isolated failure mechanisms is shown in plan view in Figure 4.27.

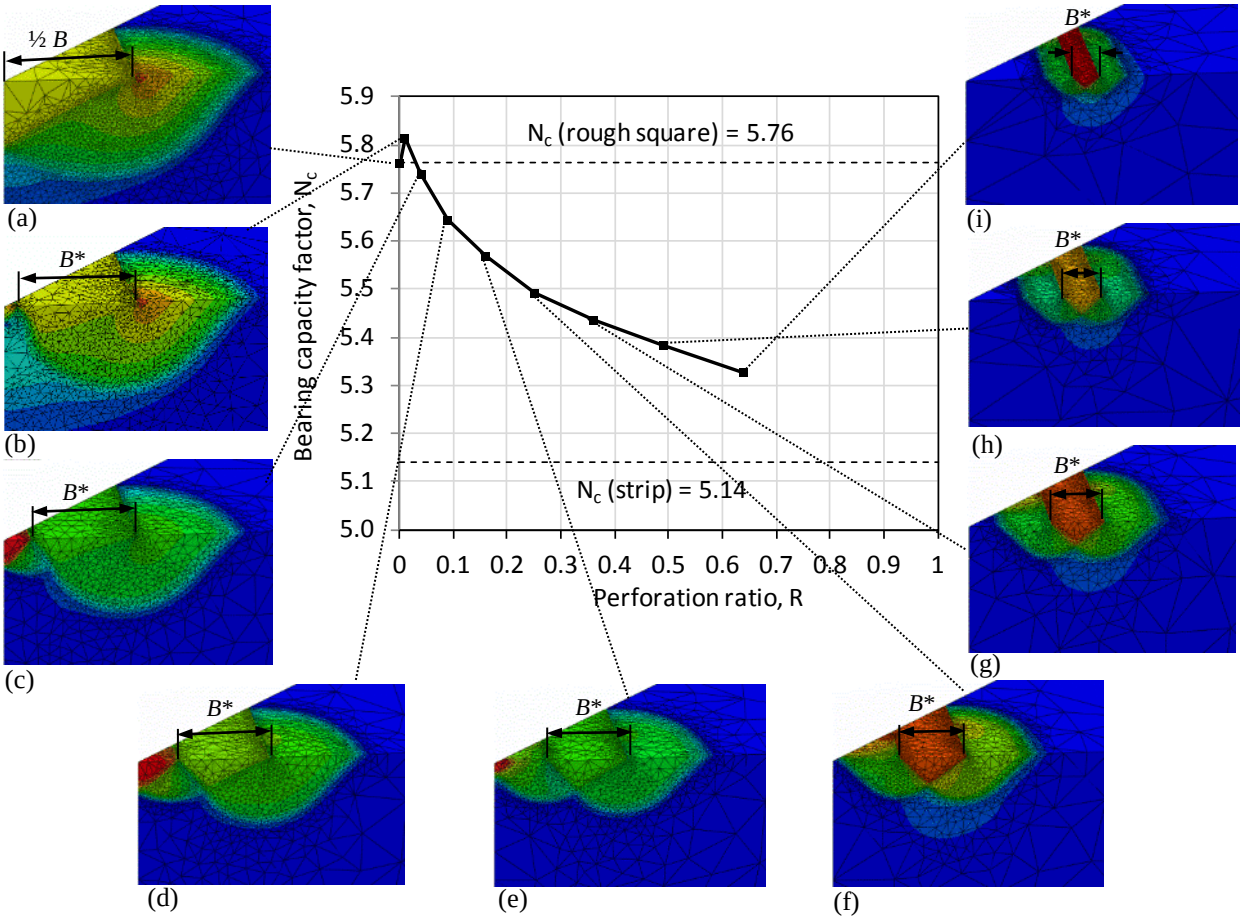

Figure 4.26: Bearing capacity for rough square annular foundations on homogeneous soil

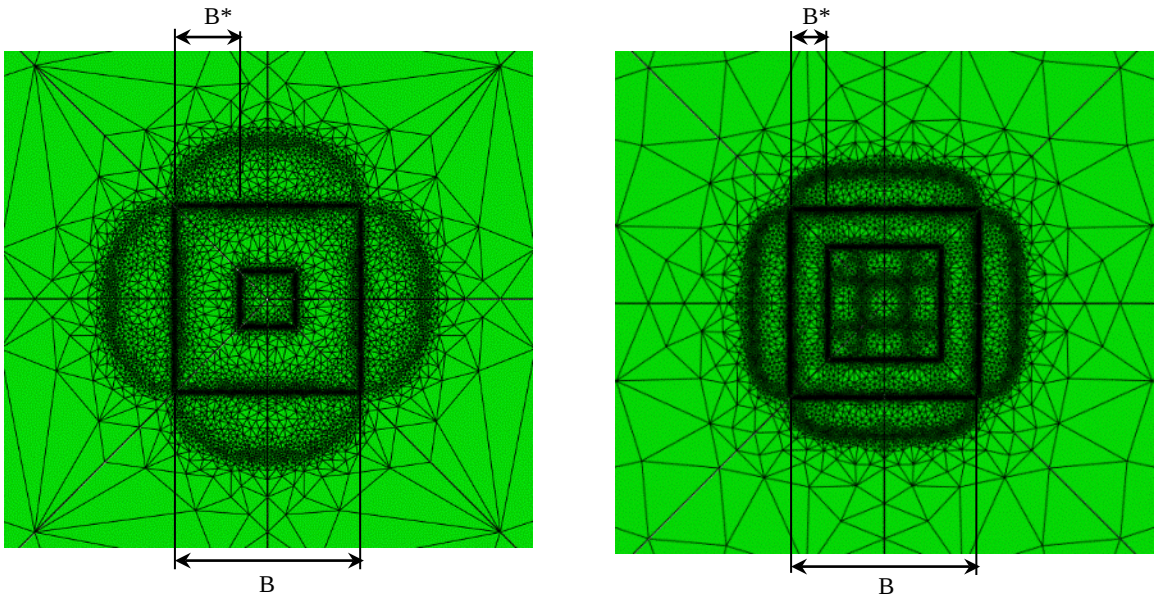

(a) R = 0.09 – interacting mechanism (b) R = 0.36 – isolated mechanism

Figure 4.27: Plan view of failure mechanisms for rough square annular foundations

The results for a rough square annular foundation with increasing soil strength heterogeneity are given in Figure 4.28. The N_c values at R = 0 represent the solid square foundation results as shown in Table 4.3. As the perforation ratio increases the N_c value for each strength profile decreases towards the value of N_c = 5.14 for a strip footing. This is because the effective heterogeneity ratio, kB^*/s_{um}, is reducing. The arching effect seen at low R for homogeneous soil does not occur for soil with linearly increasing strength.

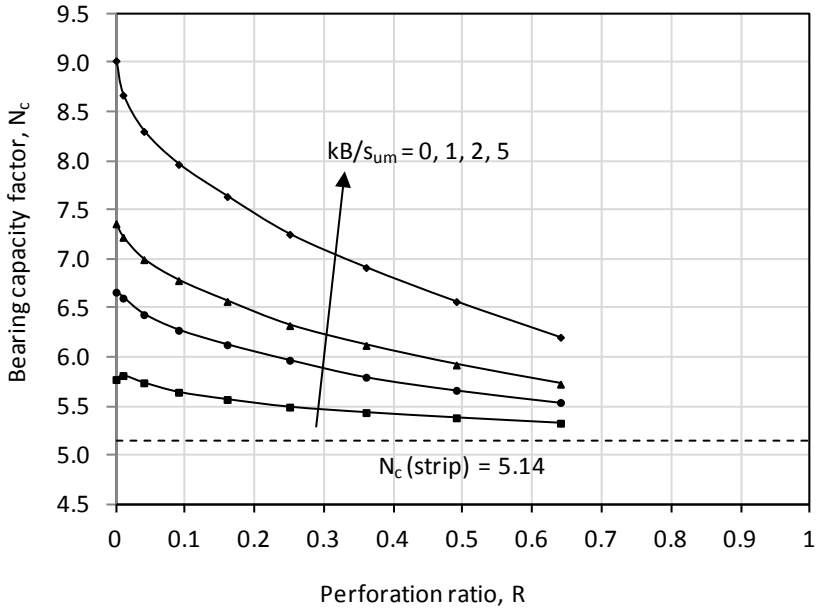

Figure 4.28: Bearing capacity factors for rough square annular foundations on heterogeneous soil

4.3.2 Surface foundation – smooth interface

4.3.2.1 Square foundation

Smooth square foundations were initially analysed for each strength profile. The case of kB/s_{um} = 0 has been examined in detail in Section 3.4.3.1. The bearing capacity factors N_c for each strength profile are shown in Table 4.4. Values for comparison for kB/s_{um} > 0 from any other studies were not found. These values in Table 4.4 are plotted in Figure 4.29 and are compared with those calculated using Equation 2.6 as given by the design code DNV (1992). It is seen that the DNV (1992) values overestimate the finite element predictions, particularly for kB/s_{um} < 2.

Table 4.4: Comparison of N_c for smooth square foundations (R = 0)

kB/s_{um}	**Bearing capacity factor, N_c**
0	5.442
1	6.033
2	6.513
5	7.724

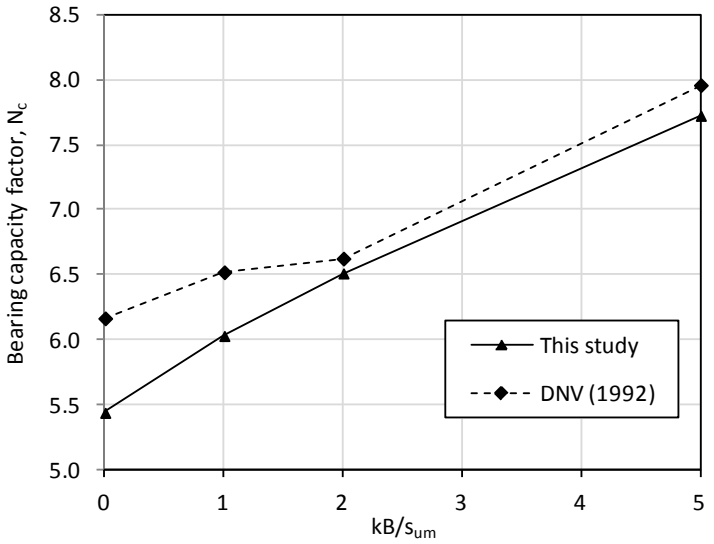

Figure 4.29: Smooth square foundation capacity results with increasing soil strength

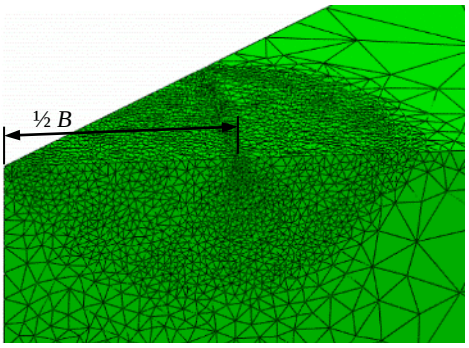

(a) kB/s_{um} = 0

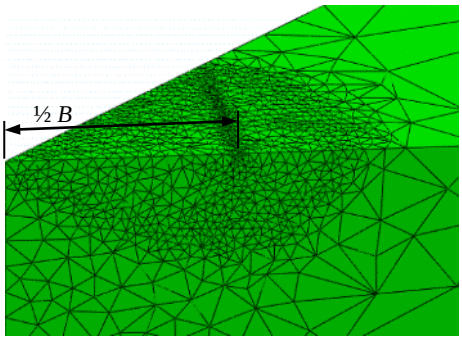

(b) kB/s_{um} = 1

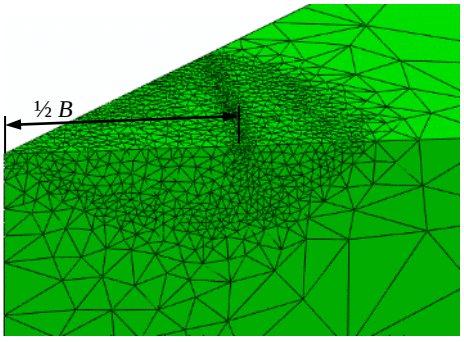

(c) kB/s_{um} = 2

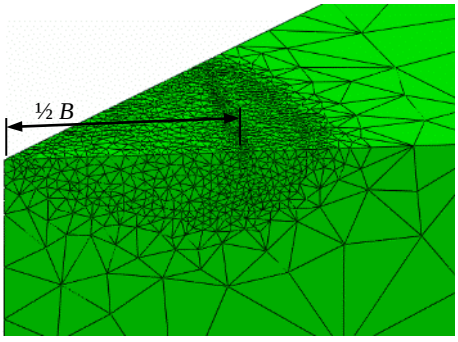

(d) kB/s_{um} = 5

Figure 4.30: Refined mesh of smooth square foundation failure mechanisms

Figure 4.30 shows the plastic regions from the refined mesh for each case analysed. These can be used to infer the nature of the failure mechanism. A Hill-type mechanism can be identified, which is expected due to the smooth foundation-soil interface. As has been generally observed, the mechanism becomes more localised to the foundation base as the soil strength gradient increases.

In Figure 4.31 the smooth square results for increasing soil strength heterogeneity, together with the rough square results, are compared with those originally plotted in Figure 2.12 for strip and circular foundations. The square foundation bearing capacity factors remain below that of a circular foundation as the soil strength increases. From about $kB/s_{um} = 1$ the bearing capacity factors of a strip foundation become greater than those of a square.

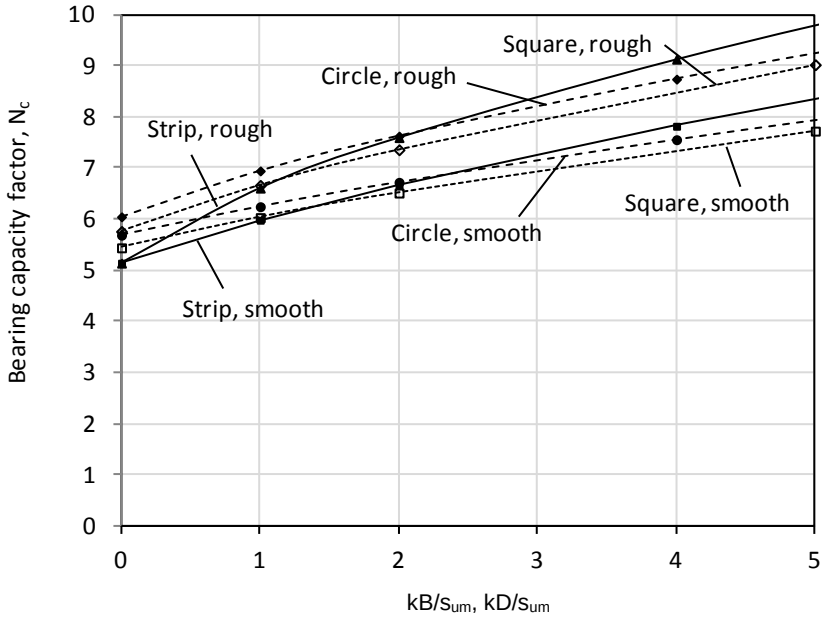

Figure 4.31: Smooth square foundation capacity results with increasing soil strength

4.3.2.2 Square annular foundation

The results from the analysis of smooth square annular foundations on homogeneous soil are given in Figure 4.32. As the perforation ratio increases the N_c value decreases. The N_c values at higher R are seen to slow in their approach towards the value of 5.14. This may be due to an under refinement of the mesh (i.e. more analysis iterations might have shown a lower

result rather than it necessarily being a feature of the capacity). No noticeable 'superfooting' effect was observed as the N_c value dropped immediately with the introduction of a perforation.

The variation in the plastic deformation occurring across the range of perforation ratios can be seen from the refinement of the meshes in Figure 4.32. By R = 0.09 the mechanism is no longer spanning from each side of the foundation. As R increases the mechanism continues to become more isolated around the local foundation section. Figure 4.33 shows the extra degree of localisation of the mechanism at R = 0.36 compared to R = 0.16. At R = 0.36 the majority of the failure is occurring in the soil on the outside of the foundation, with little occurring on the inside. This bias was also observed for the case of a smooth ring foundation.

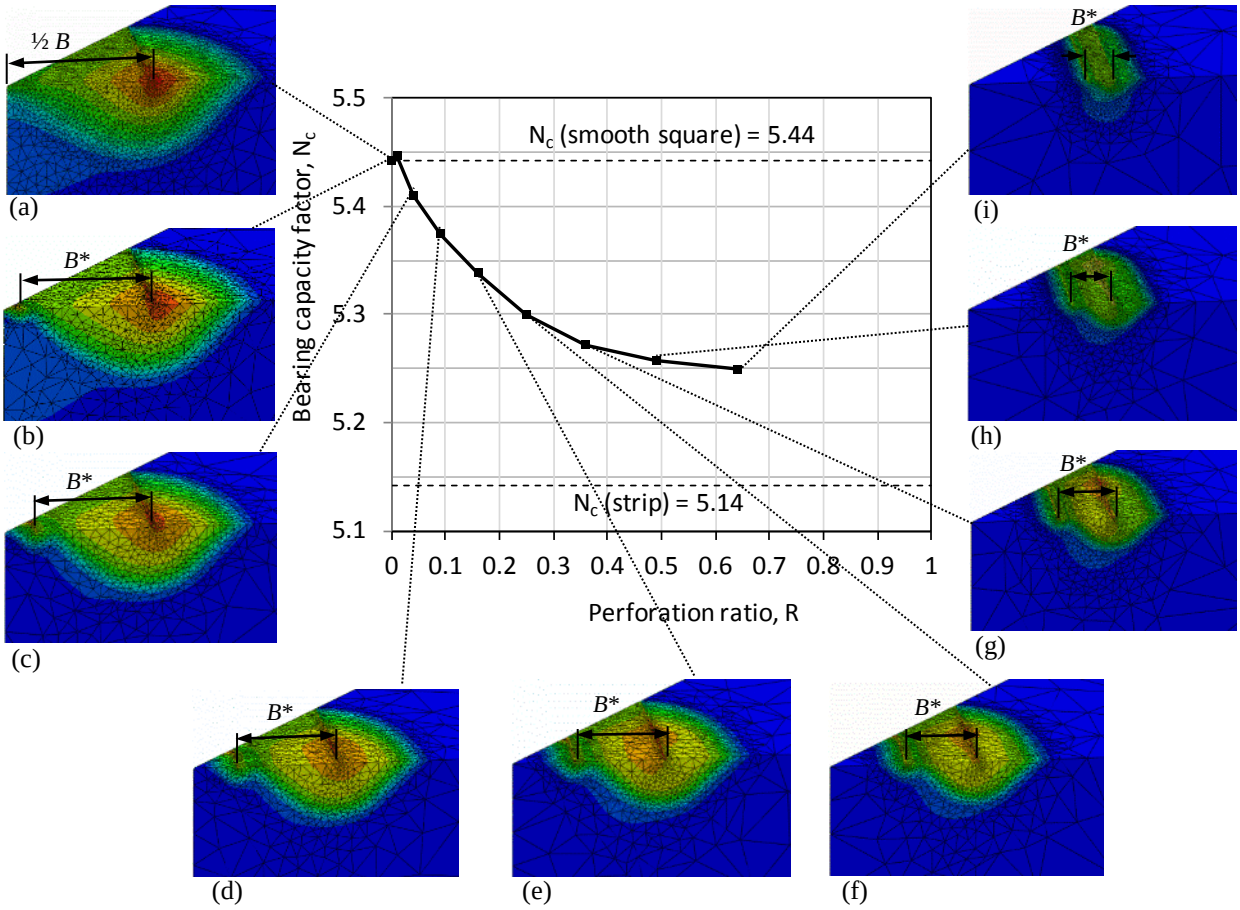

Figure 4.32: Failure mechanisms for smooth square annular foundations on homogeneous soil

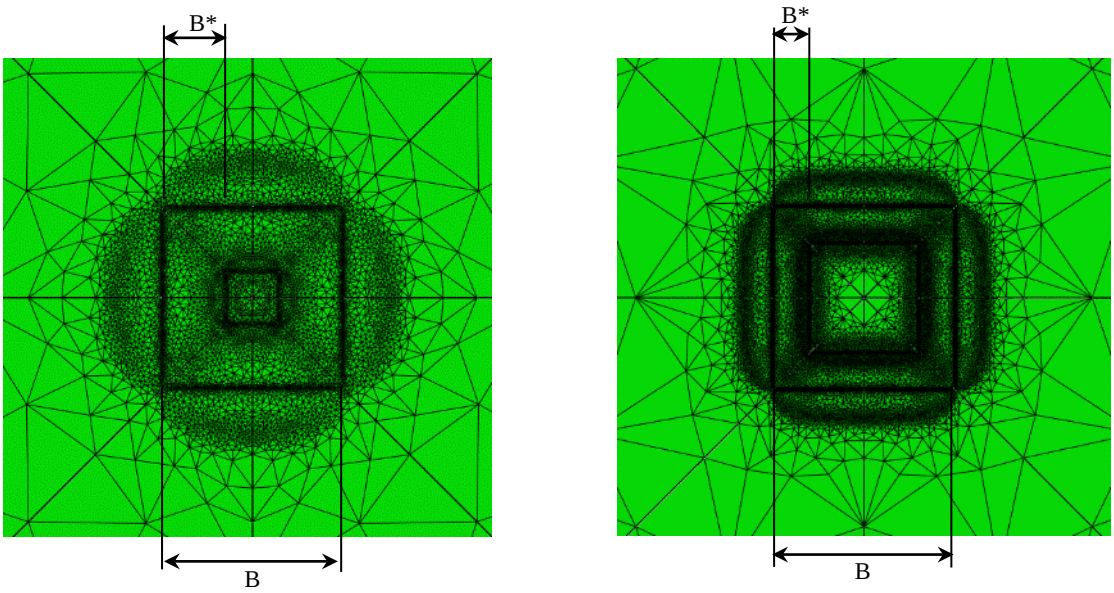

(a) R = 0.16 (b) R = 0.36

Figure 4.33: Plan view of failure mechanisms for smooth square annular foundations

The results for a smooth square foundation with increasing soil strength heterogeneity are given in Figure 4.34. The N_c values at R = 0 represent the solid square foundation results as shown in Table 4.4. As the perforation ratio increases the N_c values for each strength profile drop toward the expected value of N_c = 5.14 for a strip foundation. As previously mentioned, this is because the effective heterogeneity ratio, kB^*/s_{um}, is reducing.

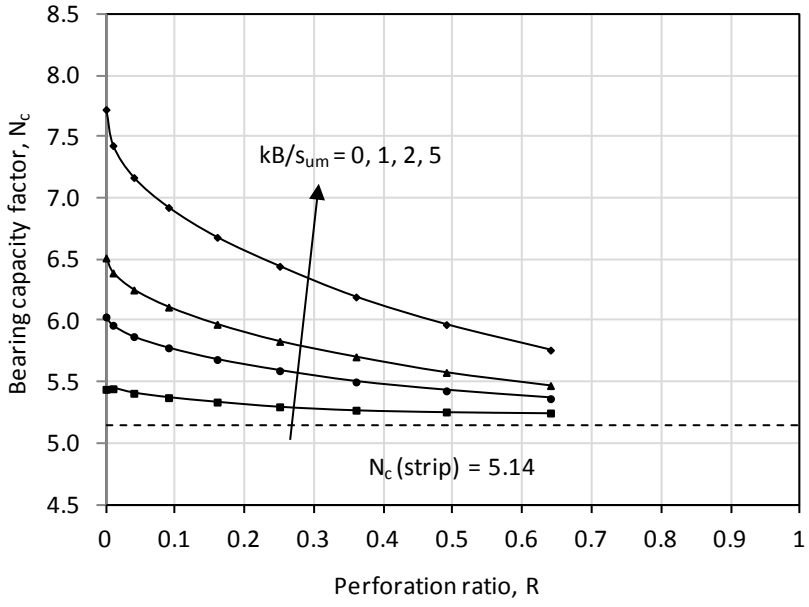

Figure 4.34: Bearing capacity results for smooth square annular foundations

4.3.3 Embedded foundation

Figure 4.35 shows a 3D finite element model that was set up to assess an embedded square foundation. The same model details as described for the surface foundation were adopted. Embedment depths of d/D = 0.1, 0.2, 0.3 and 0.5 were analysed, as well as d/D = 1 for the case of R = 0. A rough foundation base and smooth side walls (having zero interface adhesion) were modelled. The mesh was composed of triangular quadratic hybrid elements with an initial coarse mesh as shown in Figure 4.35. Mesh refinement was undertaken using the adaptive meshing scheme until a failure load within 1% of the previous solution was obtained.

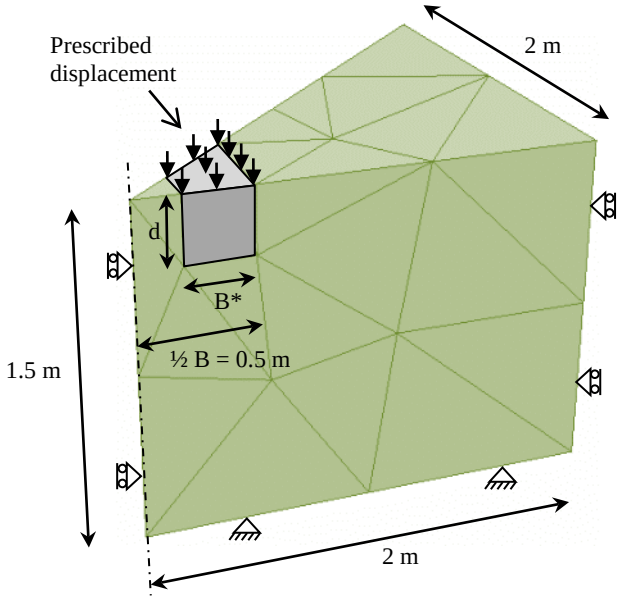

Figure 4.35: Square embedded foundation model arrangement (foundation for illustration purposes)

4.3.3.1 Square foundation

A rough square foundation (with smooth sides) on homogeneous soil at varying embedment depths was initially analysed. The results are plotted in Figure 4.36 and are compared with results from previous studies (Salgado et al., 2004, Nguyen and Merifield, 2012). The results from Nguyen and Merrifield (2012) were obtained using Abaqus. They lie close to upper bound results obtained by Salgado et al. (2004) using finite element limit analysis, and are higher than the Abaqus results from this study. This may be due to a coarser mesh being used

by Nguyen and Merrifield (2012) compared to this study. The results from this study were found to match well with the average of the lower and upper bounds from Salgado et al. (2004). The prediction given by DNV (1992) using Equation 2.6 with the depth factor given by Equation 2.8 is included in Figure 4.36. It is seen to significantly underestimate foundation capacity with embedment compared to the results from this study. Examples of the failure mechanisms occurring for the embedded square foundation results presented in Figure 4.36 are shown in Figure 4.37. These are for embedment depths of d/D = 0.1 and 0.3.

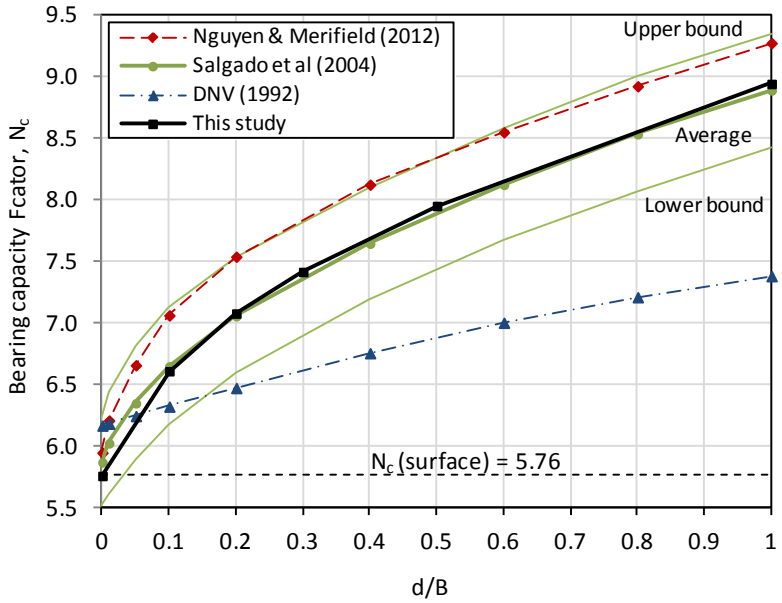

Figure 4.36: Bearing capacity factors for embedded rough square foundation

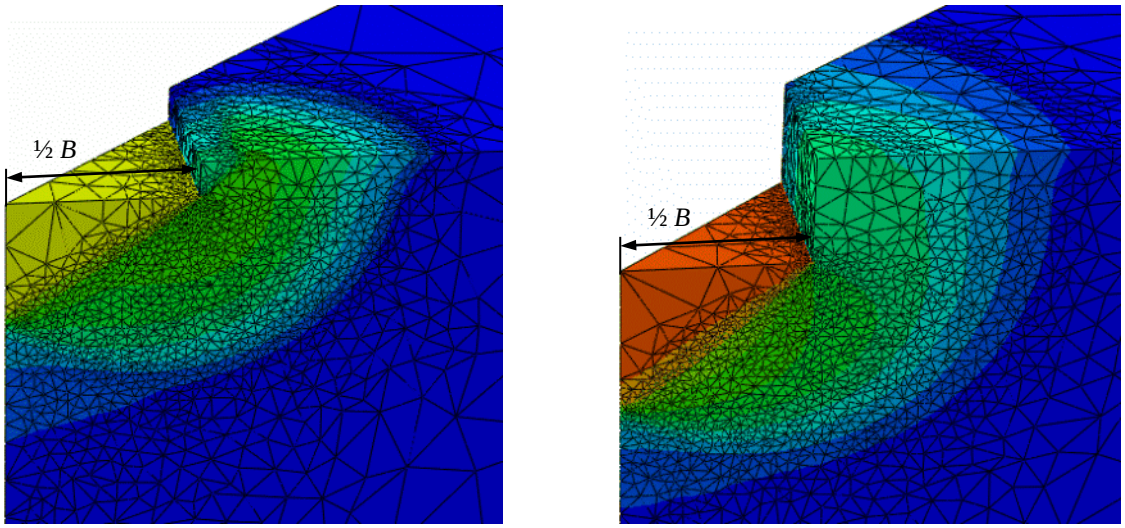

(a) d/B = 0.1 (b) d/B = 0.3

Figure 4.37: Embedded square foundations refined mesh and displacement contours

4.3.3.2 Square annular foundation

The square annular foundations embedment results are given in Figure 4.38. Different soil strength profiles were examined, where the dimensionless strength heterogeneity kB/s_{um} was defined by using the soil strength at the surface s_{um}. Four different perforation ratios were assessed, being R = 0, 0.16, 0.36 and 0.64. The bearing capacity factors N_c reduced with the introduction of a perforation, although a slight rise occurred once the perforation ratio had increased to R = 0.64.

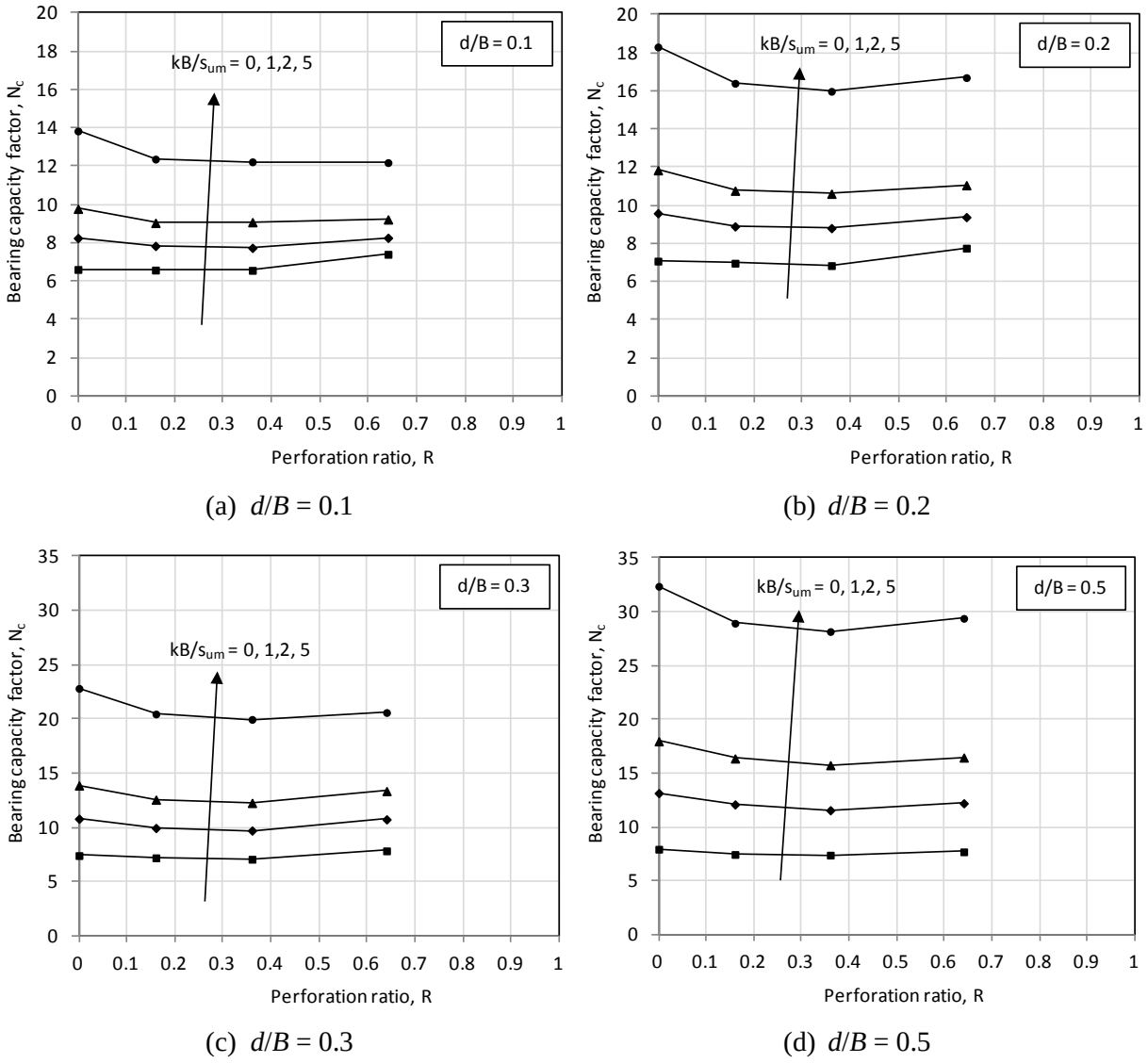

Figure 4.38: Bearing capacity factors for embedded square foundations

Examples of the different failure mechanisms occurring for embedded square annular foundations on homogeneous soil are shown in Figure 4.39. Three different embedment ratios d/B = 0.1, 0.3 and 0.5 have been presented. It seen that the nature of the mechanism varies as the embedment depth increases. At shallower embedment the failure mechanism favours the internal soil plug, with less soil deformation occurring externally to the foundation. As the foundation embedment increases to d/B = 0.5 the deformation is entirely directed to the centre of the foundation with no deformation occurring externally. With increased soil heterogeneity the deformation is more localised to the foundation base and is slower to occur completely in the central soil plug.

R	***d*/*B***		
	0.1	0.3	0.5
0.16	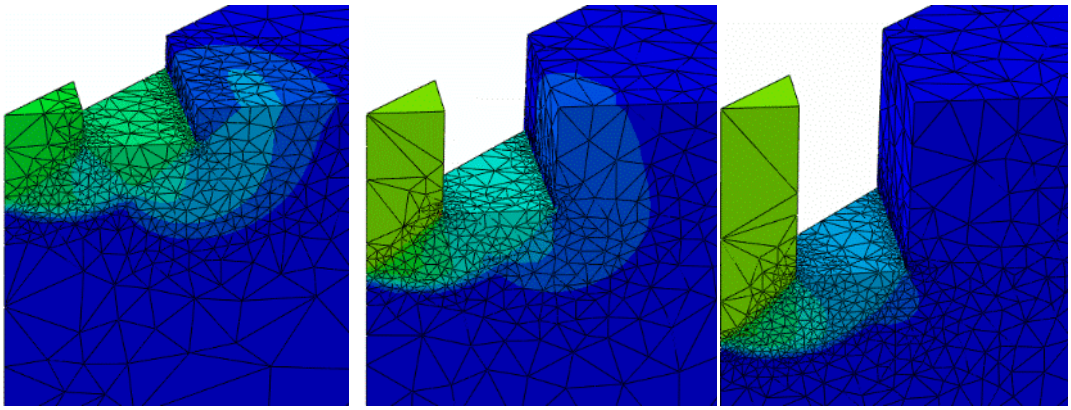		
0.36	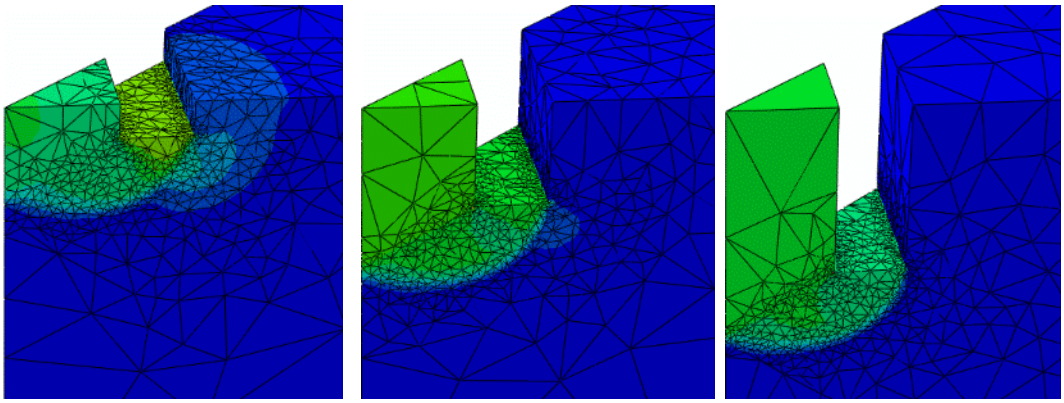		

Figure 4.39: Refined mesh with displacement magnitude contours for embedded square annular foundations on homogeneous soil

4.4 Design method for vertical loading of perforated foundations

A design method for the bearing capacity of ring and square annular foundations under vertical loading on heterogeneous soil is now proposed. The approach is based on curve fitting of the finite element results using the perforation ratio *R*.

4.4.1 Design expression

The ultimate undrained bearing capacity q_u of a ring or square annular foundation can be calculated as follows:

$$q_u = s_{um} N_c r_c d_c + \gamma d \tag{4.3}$$

where:

- $q_u = V_{max}/A$, where *A* is the foundation contact area (see Figure 1.2)
- N_c is the bearing capacity factor for a strip footing, such that $N_c = 2 + \pi = 5.14$
- The perforation ratio factor r_c is given by:

$$r_c = s_c + \sqrt{R}(1 - s_c) \tag{4.4}$$

  This expression was found to give the best fit across the range of FEA results (as shown later in Section 4.4.2).

- The perforation ratio *R* is given by Equation 1.1.
- The shape factor s_c for a given kD/s_{um} or kB/s_{um} can be determined from Figure 4.40.

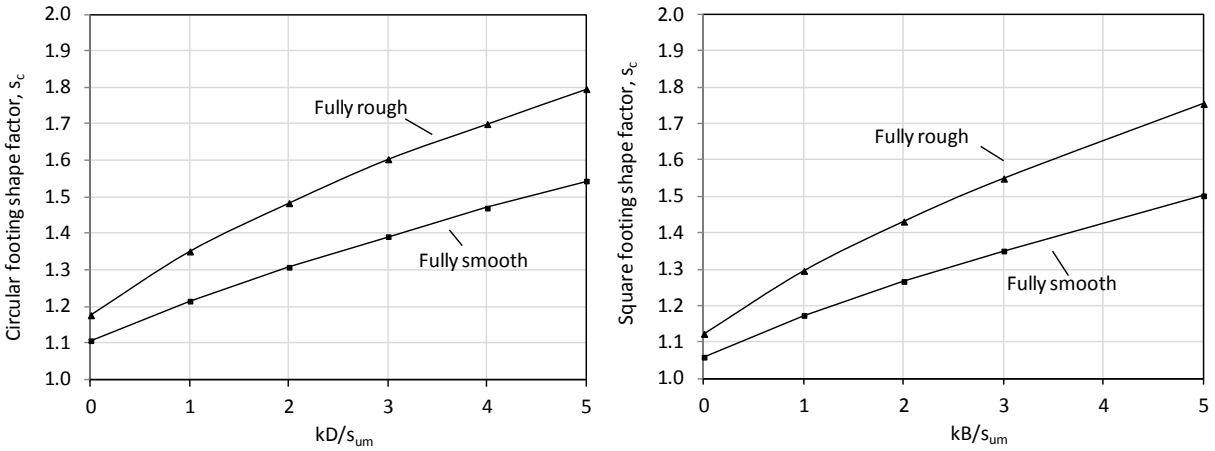

(a) Circular foundation (b) Square foundation

Figure 4.40: Shape factor, s_c

- The depth factor d_c for a given depth d, soil strength kD/s_{um} or $kB/s_{um,}$ and perforation ratio R can be estimated using Figure 4.41 for ring foundations or Figure 4.42 for square annular foundations. The depth factors have been determined for the case of a rough base and smooth sides. It can be seen that the depth factors increase slightly with increasing perforation ratio. For simplicity, the depth factors for a solid circle (Figure 4.41(a)) or for a solid square (Figure 4.42(b)) could be used for all values of perforation ratio R. This would be conservative, and the conservatism would increase with increasing perforation ratio R.
- The overburden contribution (if relevant) is given by γd where γ is the unit weight of the soil. If submerged the submerged soil unit weight should be used ($\gamma = \gamma'$).

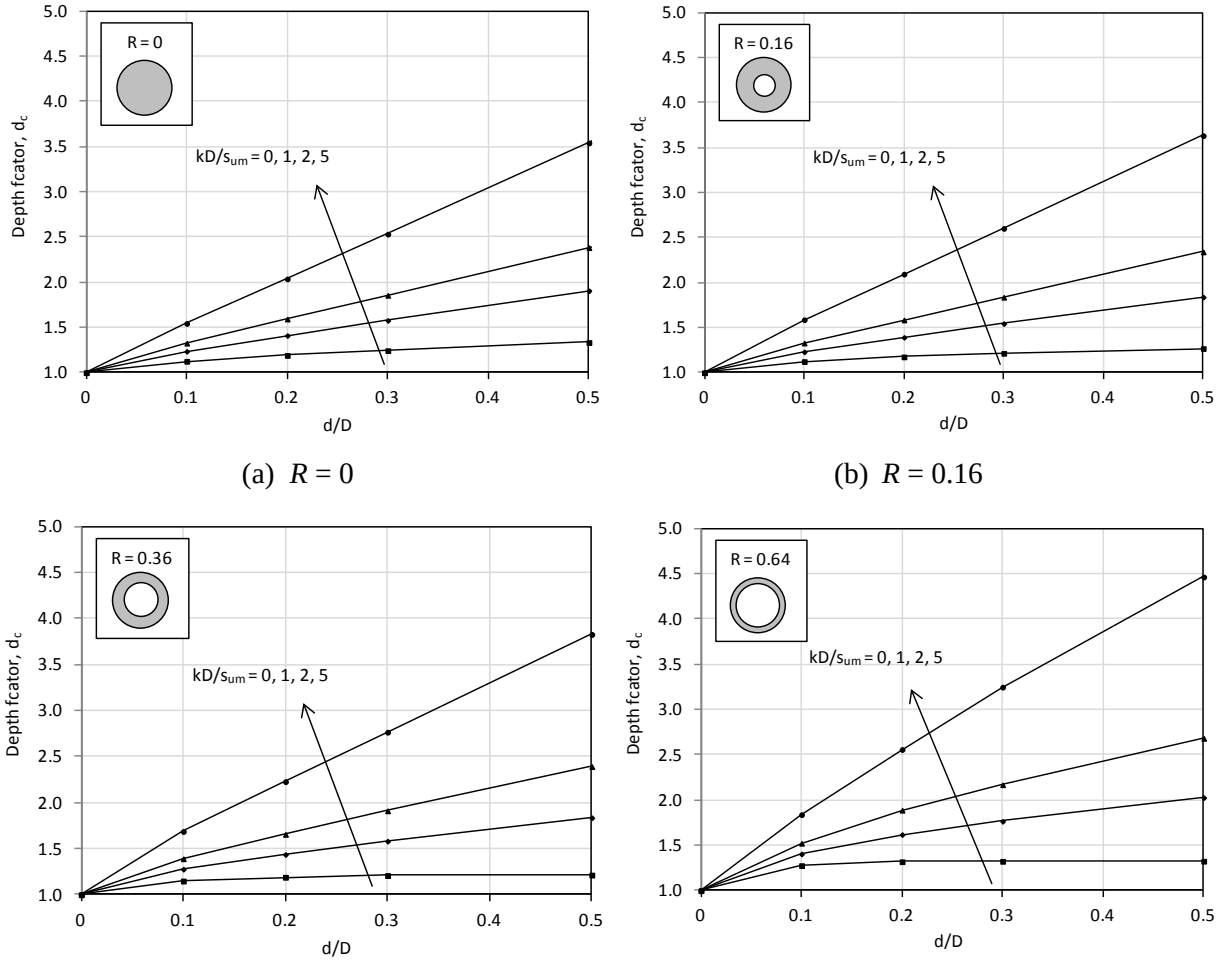

(a) $R = 0$ (b) $R = 0.16$

(c) $R = 0.36$ (d) $R = 0.64$

Figure 4.41: Depth factors, d_c for embedded ring foundations (rough base, smooth sides)

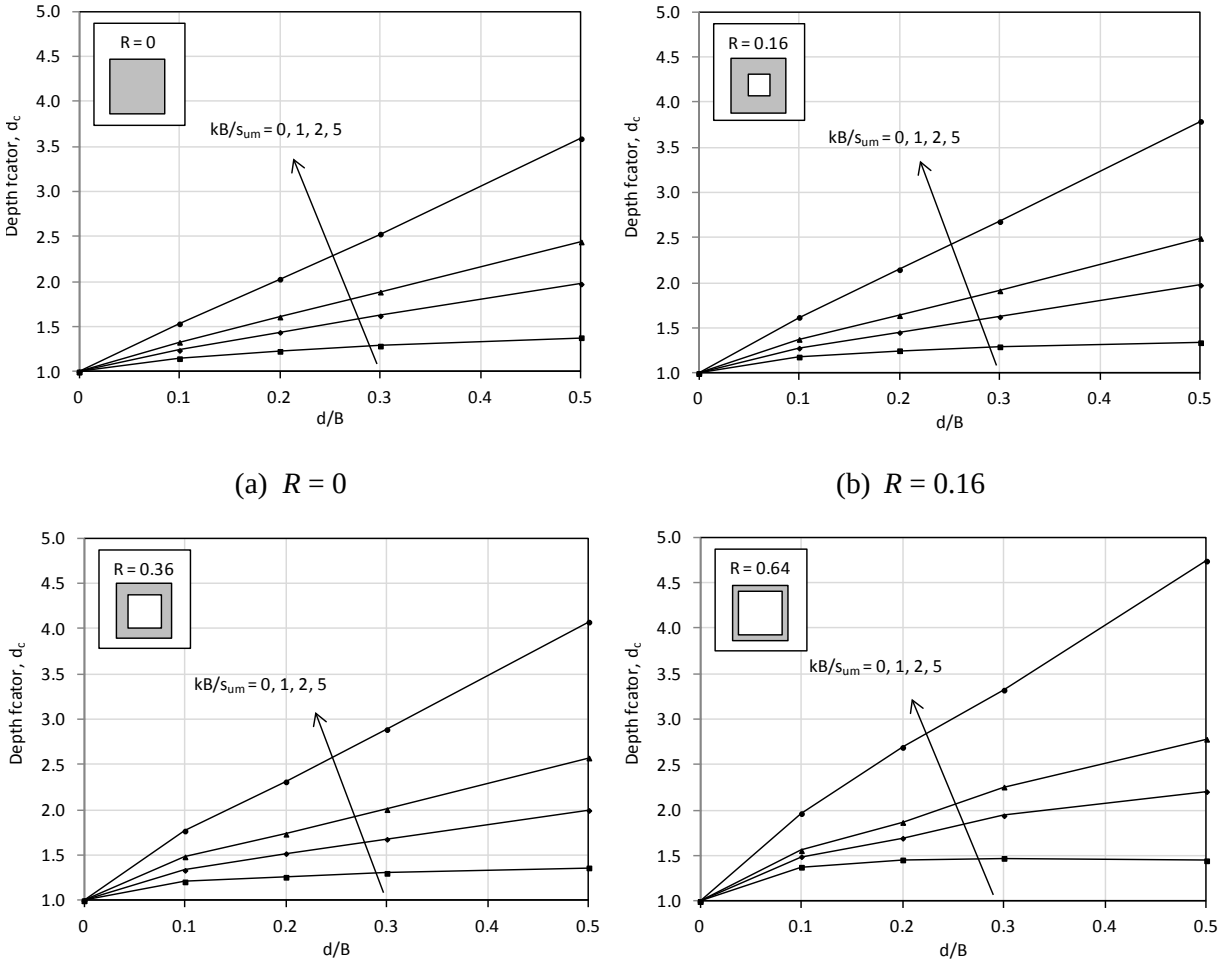

Figure 4.42: Depth factors, d_c for embedded square foundations (rough base, smooth sides)

4.4.2 Comparison of design expression with finite element results

The design expression given by Equation 4.3 is plotted against the FEA results in Figure 4.43. The results shown are for surface foundations, although a similar comparison would exist for embedded foundations since the depth factors are directly scaled from the surface foundation results. It is seen that the design expression provides a close fit to the FEA results. As such it is considered that Equation 4.3 could be used to provide a good estimate of the vertical bearing capacity of ring and square annular foundations.

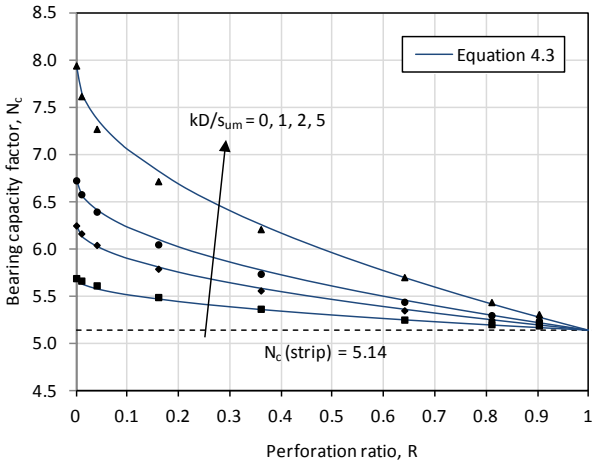

(i) Smooth

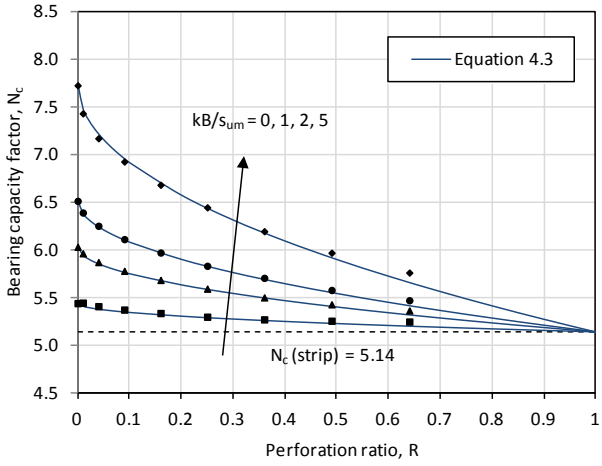

(i) Smooth

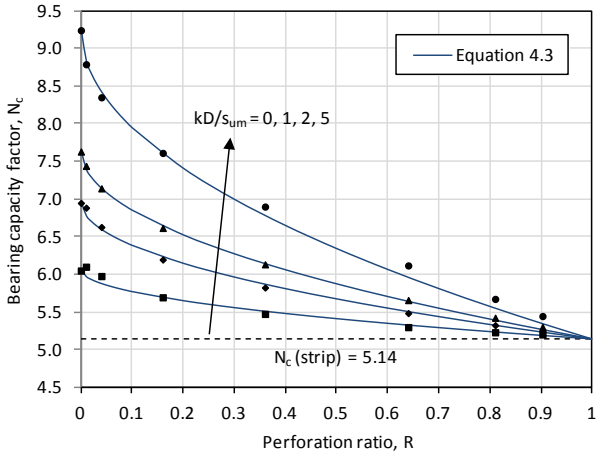

(ii) Rough

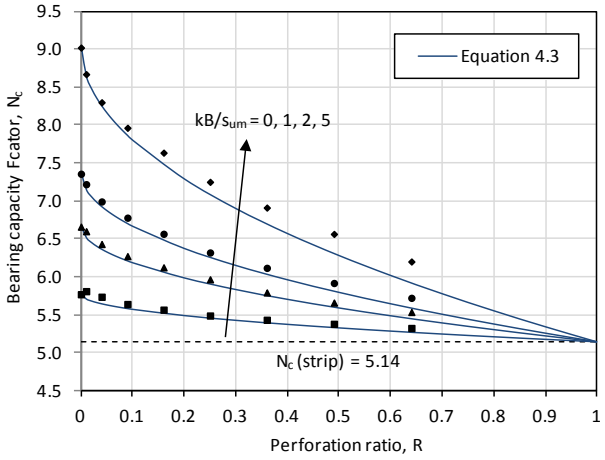

(ii) Rough

(a) Ring foundation (b) Square annular foundation

Figure 4.43: Comparison of design solution with finite element results

4.5 Effect of multiple perforations

This chapter so far has investigated the effect of perforations on bearing capacity by examining a single foundation perforation. The number perforations N_p in this case is $N_p = 1$. Foundations may also be designed to include multiple perforations (see for example Figure 2.23(a) where $N_p = 4$). As discussed in Section 2.3.1.1, foundations having the same perforation ratio R but a different number of perforations may not have the same capacity. This is because the effective width B^* reduces as the number of perforations increases. In heterogeneous soils a smaller width B^* can result in a shallower failure mechanism such that

the operative soil strength is reduced, and the effective strength gradient parameter kB^*/s_{u0} is also reduced.

To investigate the impact of increasing perforations, analysis was undertaken for the case of R = 0.16. Surface square foundations with the number of perforations of N_p = 4 and 9 were analysed as shown in Figure 4.44 and the results compared to N_p = 1 shown in Section 4.3.1.2. The foundations with N_p = 4 and 9 were modelled using the same model arrangement and soil properties as was used for the case of N_p = 1 (described in Section 4.3). A rough foundation interface was used and soil strength profiles of kB/s_{um} = 0, 2, and 5 were analysed.

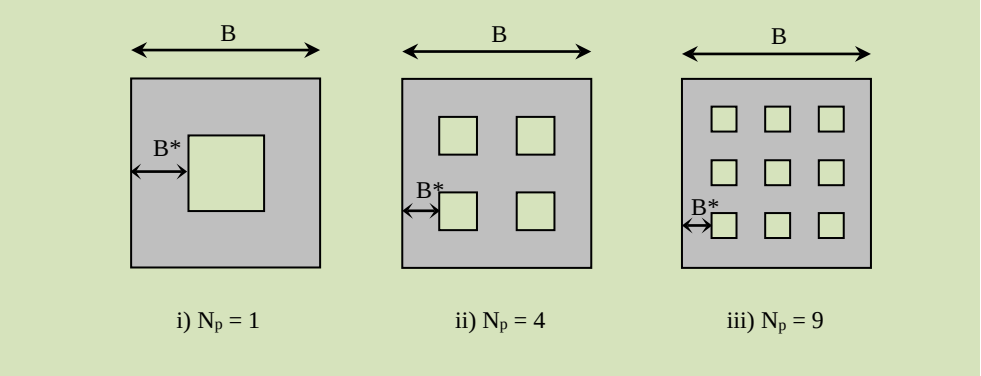

Figure 4.44: Foundations of increasing number of perforations N_p with R = 0.16

The vertical load-displacement results for each foundation type for the different soil strength profiles are given in Figure 4.45. The results are compared to the maximum vertical bearing load predicted by the design expression, Equation 4.3. For the homogeneous soil results in Figure 4.45(a), it is seen that the capacity slightly increases with increasing N_p. This is expected to be due to the meshes being less refined for higher N_p (and therefore lower B^*). This is because each analysis was undertaken for the same number of mesh iterations. More refinement is required as B^* becomes smaller, so the solutions for N_p = 4 and 9 will not be as accurate for the solution for N_p = 1.

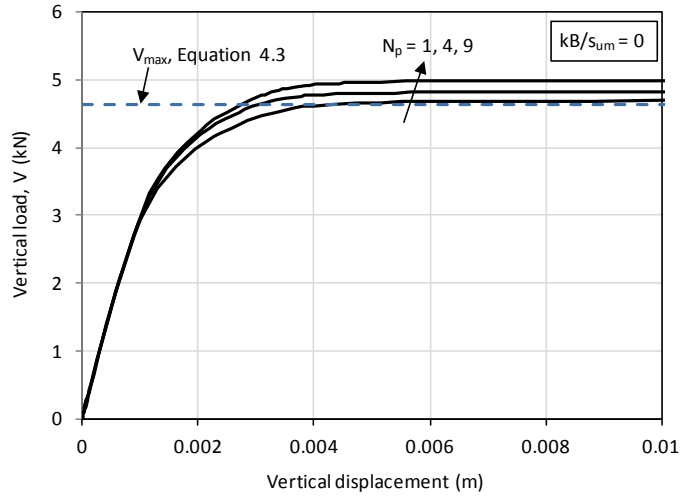

(a) $kB/s_{um} = 0$

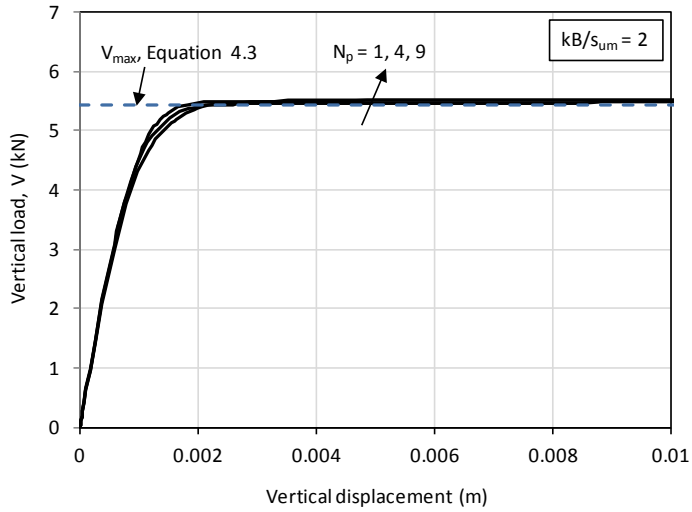

(b) $kB/s_{um} = 2$

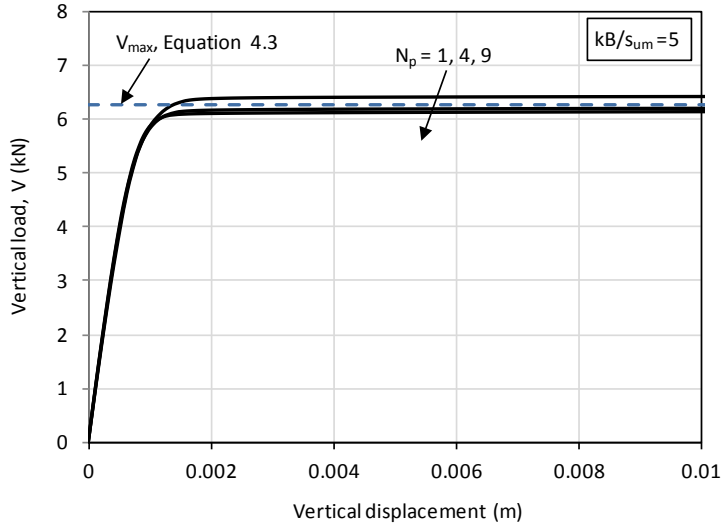

(c) $kB/s_{um} = 5$

Figure 4.45: Vertical load-displacement results with increasing perforation number N_p for $R = 0.16$

With soil heterogeneity introduced it is seen in Figure 4.45(b) that the difference in the solutions is less, indicating that capacity is reduced as B^* becomes smaller. At $kB/s_{um} = 5$ the capacity for $N_p = 4$ and 9 has fallen below that of $N_p = 1$. The results show that as soil strength heterogeneity increases the prediction using Equation 4.3 may over predict capacity where $N_p > 1$. Based on the results in Figure 4.45 however, and for the situation of $kB/s_{u0} \leq 5$ at least, the over prediction is expected to be minimal.

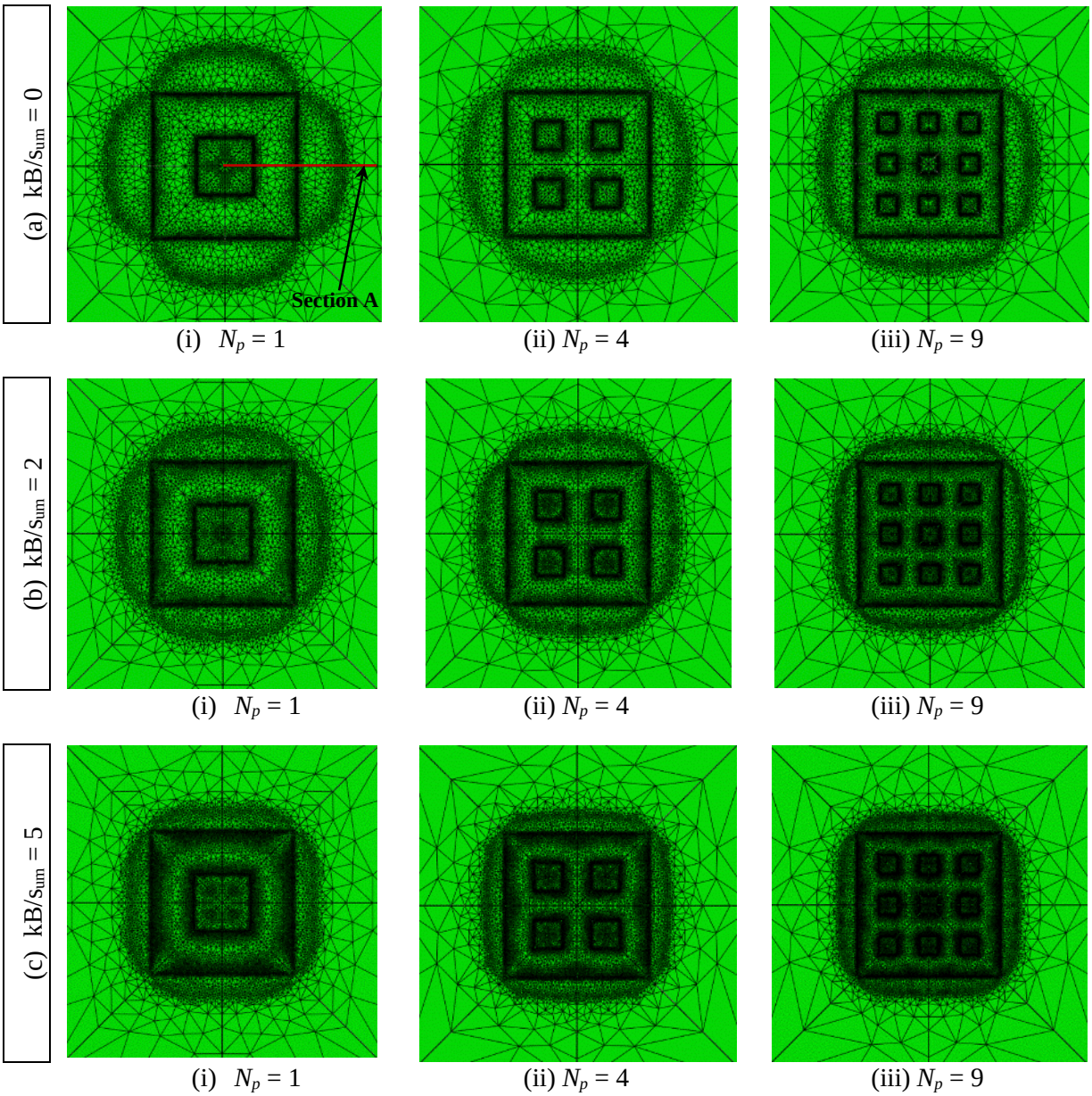

Figure 4.46: Plan view of plastic regions for foundations with $R = 0.16$

Figure 4.46 shows the plan view of the failure mechanisms for the various analyses. It is seen that as N_p increases the extent of the failure mechanism in plan reduces. The mechanism also becomes more localised as strength heterogeneity increases.

The depth of the failure mechanism at Section A (as indicated on Figure 4.46(a)(i)) for each analysis case is shown in Figure 4.47. This figure shows that as N_p increases (and B^* decreases) this acts to reduce the depth of the failure mechanism. As soil strength heterogeneity increases the failure mechanism depth also becomes shallower.

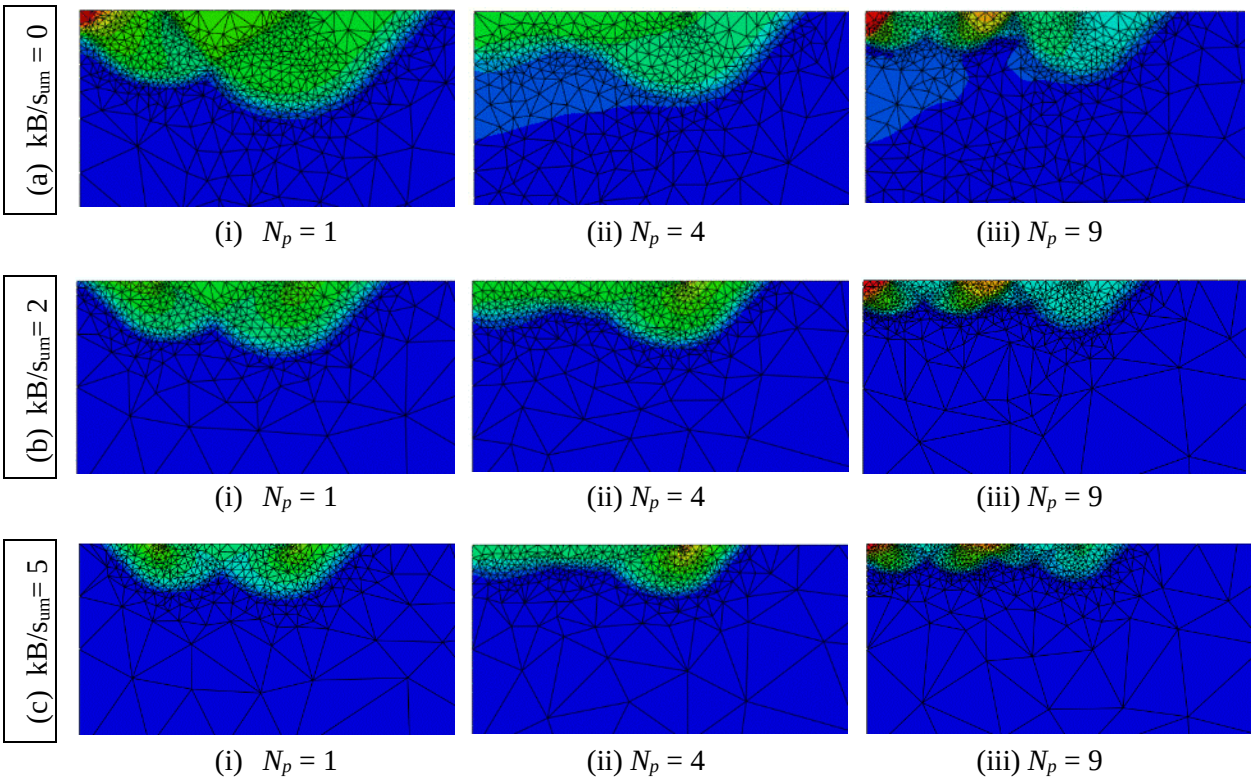

Figure 4.47: Section A (defined in Figure 4.45(a) (i)) view of failure mechanisms with displacement magnitude for foundations with R = 0.16

4.6 Conclusions

This chapter has presented finite element analyses of the vertical bearing capacity of ring and square annular foundations over a range of perforation ratios. Undrained Tresca soil has been modelled using the user material subroutine (UMAT) and the adaptive mesh refinement procedure from Chapter 3 to increase the accuracy of the solutions. Foundations with both

smooth and rough foundation-soil interfaces have been modelled on soil with uniform and linearly increasing undrained shear strength profiles.

It was found that as the perforation ratio R increased, the bearing capacity factor N_c decreased from N_c for a solid square or circular foundation and approach the value of N_c = 5.14 for a strip. This was the case for all levels of soil heterogeneity examined. Arching of the soil across the perforation occurred only at very small values of R ($R \leq 0.01$) and was only significant for homogeneous soil. The failure mechanism varied from an interacting mechanism spanning the full width of the foundation to a mechanism acting in isolation as the perforation ratio R increased. For rough foundations on homogeneous soil the isolated mechanism occurred at about R = 0.24 whilst for smooth foundations it occurred earlier at about R = 0.1. Isolated mechanisms were also seen to occur earlier with increased soil heterogeneity. As embedment increased the failure mechanism occurred into the internal soil plug with no soil deformation occurring externally to the foundation.

Curve fitting of the numerical results was used to derive an expression to estimate the capacity of ring and square annular foundations on undrained soil. This was done by introducing a perforation ratio factor r_c to adjust the shape factor to account for R. The expression was shown to provide a close fit to the numerical results and so is considered to be useful for estimating the capacity of these foundation types. The square annular foundation results (which had a single perforation, N_p = 1) were compared to analysis for the cases where N_p = 4 and 9. It was found that when the number of perforations was increased, similar capacity was achieved as for N_p = 1. For increasing soil heterogeneity the capacity for the multiple perforation foundations reduced below that for a single perforation, although the difference was small. As such, it was considered that the design expression based on N_p = 1 could be used to give a reasonable prediction for the capacity of foundations with multiple foundations, at least for cases where $kB/s_{u0} \leq 5$.

Chapter 5. Combined load capacity of perforated foundations

In Chapter 4 the bearing capacity of ring and square annular foundations were examined when subjected to purely vertical loads. In this chapter, conditions of combined vertical, horizontal and moment loading are considered. The bearing capacity under vertical and combined load has been investigated by undertaking centrifuge experiments. Tests were performed on clay and the perforated area of the foundation was varied from 0 – 64% of the total equivalent solid foundation area (R = 0 – 0.64). Both flat based and skirted foundations were tested.

The results of vertical and combined load centrifuge tests have been interpreted to examine the V:H:M failure envelope of the perforated foundations. The effect of the degree of perforation on the failure envelope of the ring and square annular foundations has been explored and comparison is made with results obtained from finite element analysis. The findings have been used to derive a design expression for the bearing capacity of perforated foundations under combined loading.

5.1 Analysis approach

The combined loading capacity of perforated foundations has been investigated by the following means:

i) Experimentally using centrifuge modelling

ii) Numerically with finite element analysis using Abaqus.

Ring and square annular foundations have been investigated experimentally with geometries as shown in Figure 5.1. The outer width B or diameter D was fixed at 5 m (prototype scale). This represents a typical foundation size for subsea infrastructure. The effective width B^* of

the square annular foundation was varied to investigate foundations with a perforation ratio *R* (as defined by Equation 4.1) of 0, 0.16, 0.36 and 0.64. A single perforation ratio of *R* = 0.36 was adopted for the ring foundation.

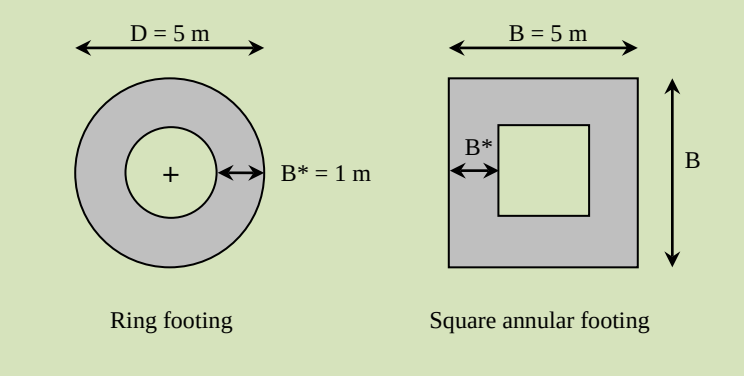

Figure 5.1: Geometry of ring and square annular foundations used in experiments (prototype scale)

The foundation geometries were tested as i) flat base surface foundation and ii) skirted foundations with skirts of length *d* = 1 m (Figure 5.2). This represents a skirt embedment ratio of *d*/*B* = 0.2, which is a typical skirt depth used for subsea and gravity base foundations. The undrained strength of the soil has been assumed to increase linearly with depth as described by Equation 2.3. The load reference point (LRP) for the vertical *V*, horizontal *H* and moment *M* loads has been taken to be located centrally at the base of the foundation as shown in Figure 5.2. This was chosen to be consistent with previous experimental and numerical studies (see for example Cassidy and Byrne (2001), Bransby and Yun (2009)).

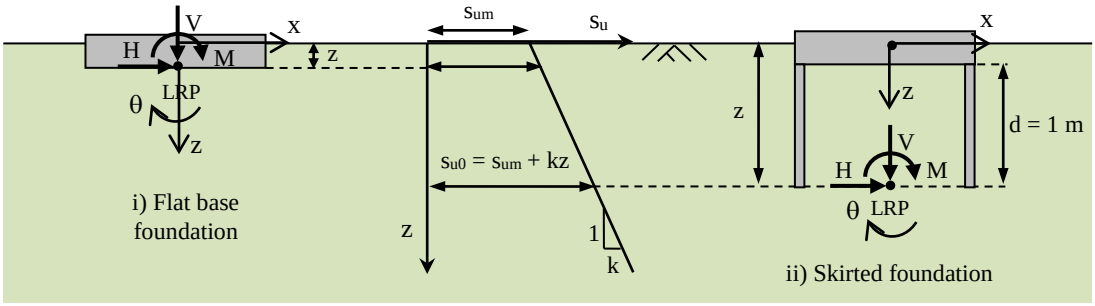

Figure 5.2: Sign convention adopted for flat base and skirted foundations

Details of the numerical analysis approach that has been adopted using Abaqas are described later in Section 5.6.

5.2 Experimental set up

Centrifuge modelling is a well established method for investigating geotechnical problems and has been used for the combined loading experiments. The principle of centrifuge modelling is to use a reduced scale model to recreate the stress conditions which would exist in a full-scale prototype. In centrifuge modelling the scale model and soil are subject to an acceleration equivalent to *ng* where *n* is a multiplier of earth's gravitational acceleration. The resulting relationships between the increased gravitational field and several common properties are listed in Table 5.1.

Table 5.1: Centrifuge scaling laws

Parameter	**Unit**	**Scaling Relationship** (model / prototype)
Gravity	m/s^2	n
Length	m	$1/n$
Density	kg/m^3	1
Mass	kg	$1/n^3$
Stress	kPa	1
Strain	-	1
Force	N	$1/n^2$
Moment	kNm	$1/n^3$
Time (consolidation effect)	s	$1/n^2$

5.2.1 UWA drum centrifuge

The experiments were performed in the drum centrifuge located at the University of Western Australia (UWA) (Figure 5.3(a)). The drum centrifuge has a diameter of 1.2 m and a maximum radial acceleration level of 485g. The soil sample is contained in an outer channel, which is 300 mm high and has a 200 mm radial depth (Figure 5.3(b)). The test sample length is 1.44 m long which allows for a significant number of testing sites per sample. A central actuator provides both vertical and radial motion. By using two concentrically driven shafts, relative motion between the outer channel and the central tool table can be achieved and

controlled. The central tool table can be stopped and raised out of the main testing area while the outside channel continues to rotate. The instrumented testing tools that are fixed to the actuator can thereby be modified or changed without affecting the acceleration level on the soil. A detailed description of the UWA drum centrifuge is given in Stewart (1998).

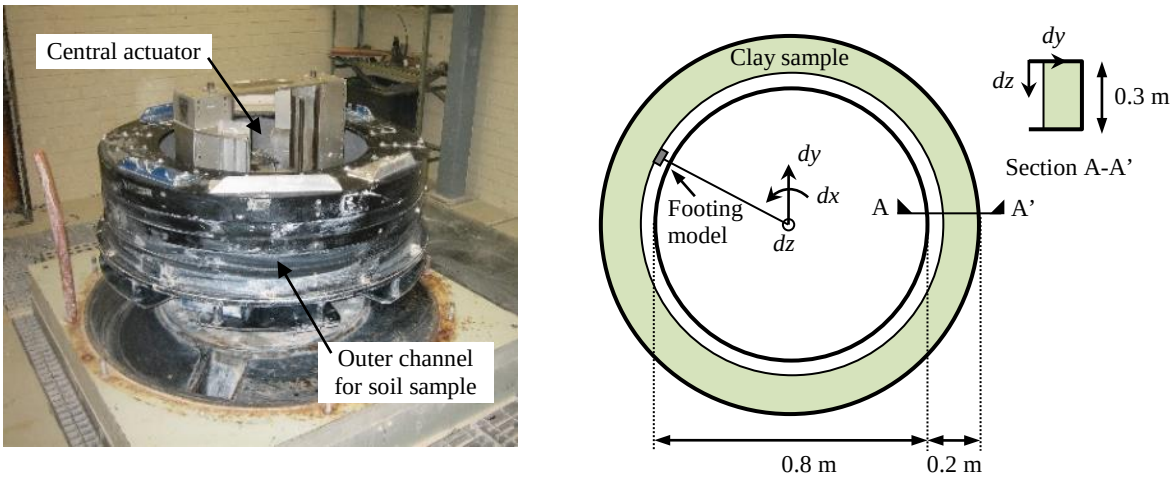

(a) Photograph of centrifuge

(b) Schematic section of centrifuge (after Gourvenec et al. (2008))

Figure 5.3: UWA drum centrifuge

5.2.2 Soil sample

5.2.2.1 Soil type

The soil type used for all centrifuge tests was a kaolin clay, which is commonly used in laboratory investigations. The properties of the kaolin clay used at UWA are given in Table 5.2.

Table 5.2: Kaolin clay properties (after Cassidy et al., (2004))

Property	Value
Liquid limit, LL	61%
Plastic limit, PL	27%
Plasticity index, PI	34%
Specific gravity, G_s	2.60
Internal friction angle, ϕ'	23°
Consolidation coefficient, c_v	2 m^2/yr
Submerged unit weight, γ'	6.82 kN/m^3

5.2.2.2 Sample preparation

The centrifuge tests were split into Test Series 1 and Test Series 2 which each had a different soil strength profile. A single overconsolidated kaolin clay sample was prepared to cover both test series. An overconsolidated sample was used as increased soil strength and stiffness was beneficial for the experimental method used. The sample preparation procedure adopted was as follows:

1. Mixing: Kaolin powder was mixed with water in a conventional barrel mixer for a period of 4 hours.
2. Placement in Drum: A layer of geofabric was placed for drainage at the base of the sample. The mixed kaolin slurry (approximately 260 kg) was slowly pumped into the channel whilst spinning at 20*g* in two stages. The first half of the slurry was pumped in initially and allowed to consolidate overnight at 200*g*. The acceleration was lowered back to 20*g* to lay the second half of the clay sample and returned to 200*g*.
3. Consolidation: The sample was consolidated at 200*g* for two days. The acceleration was then reduced to 100*g* giving an overconsolidation ratio (OCR) of 2. The sample was left to spin a further day before testing was commenced. The final height of the prepared sample was 167 mm.
4. Test Series 1: Tests for the first series were completed without disturbing material below 70 mm depth. At the completion of these tests the top 80 mm of the clay sample was scrapped away and the sample was left to spin at 100*g* for a day.
5. Test Series 2: The remaining sample was used for the Series 2 tests. The OCR for this sample ranged from about 16 at 1 m depth to 2 at 7 m depth.

5.2.2.3 Soil strength characterisation

A T-bar penetrometer was used to determine the undrained shear strength of the kaolin. The T-bar was 5 mm in diameter and 20 mm in length and attached to an instrumented shaft. T-

bar tests were carried out at 100g with a constant penetration rate of 1 mm/s to ensure undrained conditions. Tests were undertaken at regular intervals with 33 completed in total as listed in Table 5.3.

Table 5.3: T-bar test details

T-bar ID *Indicates cyclic T-bar	**Test Series**	**Soil profile**	**Position *dx*** (degrees)	**Position *dz*** (mm)
TB101	1	1-1	0	210
TB102a	1	1-1	65	210
TB102b	1	1-1	65	240
TB103	1	1-1	131	210
TB104	1	1-1	126	210
TB105	1	1-1	196	210
TB106	1	1-1	262	210
TB107	1	1-1	327	210
TB108	1	1-2	131	240
TB109	1	1-2	164	210
TB110	1	1-2	190	210
TB111	1	1-2	229	210
TB112	1	1-2	295	210
TB113	1	1-2	332	210
TB114	1	1-2	16	110
TB115	1	1-2	49	110
TB116	1	1-3	82	110
TB117	1	1-3	148	110
TB118	1	1-3	213	110
TB119	1	1-3	278	110
TB120*	1	1-3	344	110
TB201	2	2-1	189	150
TB202	2	2-1	243	150
TB203	2	2-1	297	150
TB204	2	2-1	333	150
TB205	2	2-1	135	150
TB206	2	2-1	153	150
TB207	2	2-1	171	150
TB208	2	2-1	9	150
TB209	2	2-1	63	150
TB210*	2	2-1	99	150
TB211	2	2-1	207	150
TB212	2	2-1	279	150
TB213	2	2-1	315	150

Undrained shear strength was derived using a T-bar bearing capacity factor $N_{T\text{-}bar}$ = 7.3. Whilst this is lower than the traditional T-bar bearing capacity factor of $N_{T\text{-}bar}$ = 10.5 (see for example Watson (1999)) the use of this factor leads to equivalence with the kaolin's simple shear undrained shear strength taken as s_u= 0.25 σ'_{v0} OCR$^{0.8}$ (Lehane et al., 2009).

The undrained shear strength profiles determined for each test series are shown in Figure 5.4 (at prototype scale). Unexpected centrifuge maintenance had to be undertaken during testing for Series 1 which required the centrifuge to be stopped for several periods. This had an impact on the soil strength profile. As a result the T-bar tests were grouped to form three strength profiles (1-1, 1-2 & 1-3). During Series 2 there were no unexpected stoppages and a single strength profile has been adopted (2-1). A linear best-fit line has been determined for each profile as shown in Figure 5.4. The equation for each best-fit line in terms of the undrained strength at the soil surface s_{um}, and the rate of strength increase with depth below the soil surface k are summarised in Table 5.4. The dimensionless parameter kB/s_{um} (or kD/s_{um}) is also shown for each case.

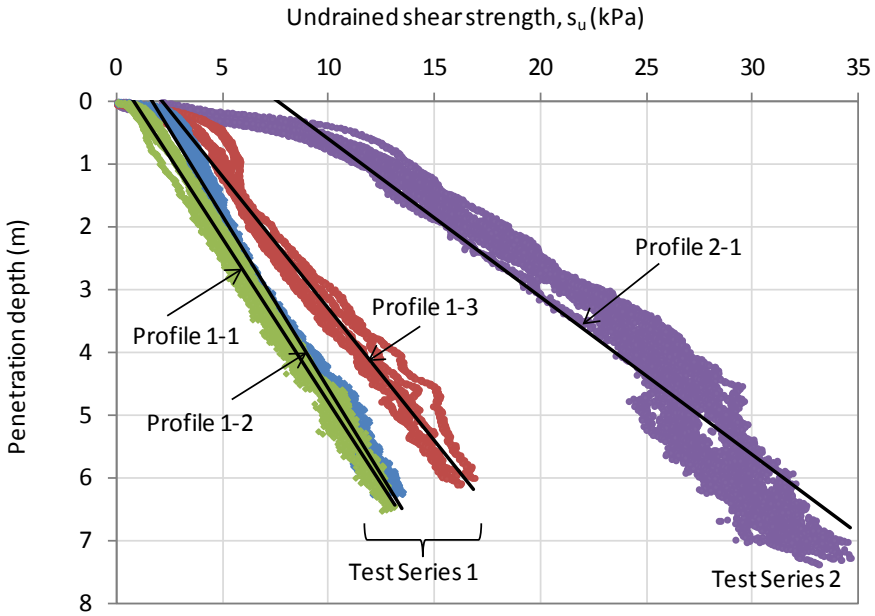

Figure 5.4: Undrained shear strength from T-bar results

Table 5.4: Soil strength profiles

Profile	s_{um}	k	$kB/_{sum}$, $kD/_{sum}$
1-1	0.84	1.90	11.3
1-2	1.76	1.80	5.1
1-3	2.40	2.31	4.8
2-1	8.85	3.64	2.1

A cyclic component was included in two of the T-bar tests to determine the remoulded strength of the clay. It involved cycles at displacement limits of ±1 m at a depth of about 2.5 m. Nine cycles were undertaken in TB120 and eleven cycles in TB210. The shear strength degradation, shown by the ratio of the shear strength during each penetration cycle to the initial penetration strength, is given in Figure 5.5. The friction or adhesion factor α used to assess skirt penetration resistance is often based on the remoulded strength. This is equal to the inverse of the sensitivity S_t (DNV, 2005). The degradation factor tended towards values between 0.3 and 0.35, indicating sensitivity of the clay to be between 2.5 and 3.5.

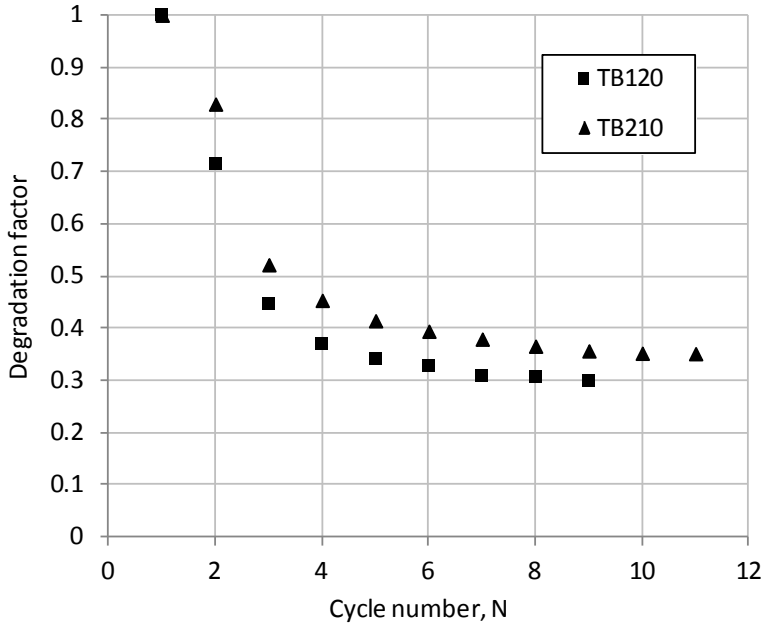

Figure 5.5: Shear strength degradation

5.2.3 Foundation models

Five different foundation geometries were fabricated for centrifuge testing. They included four square foundations with perforation ratios R = 0, 0.16, 0.36, 0.64 and a circular foundation with a perforation ratio R = 0.36. Each foundation type was tested with a flat plate base and with a skirted base, except for Type S4 in which only a flat base was tested. The bottom of the flat base foundations were roughened by sandblasting. The skirt length for all skirted foundations was d = 10 mm, giving d/B (or d/D) = 0.2. The skirt thickness was 0.6 mm. The model drawings are given in Figure 5.6 and the dimensions are listed in Table 5.5.

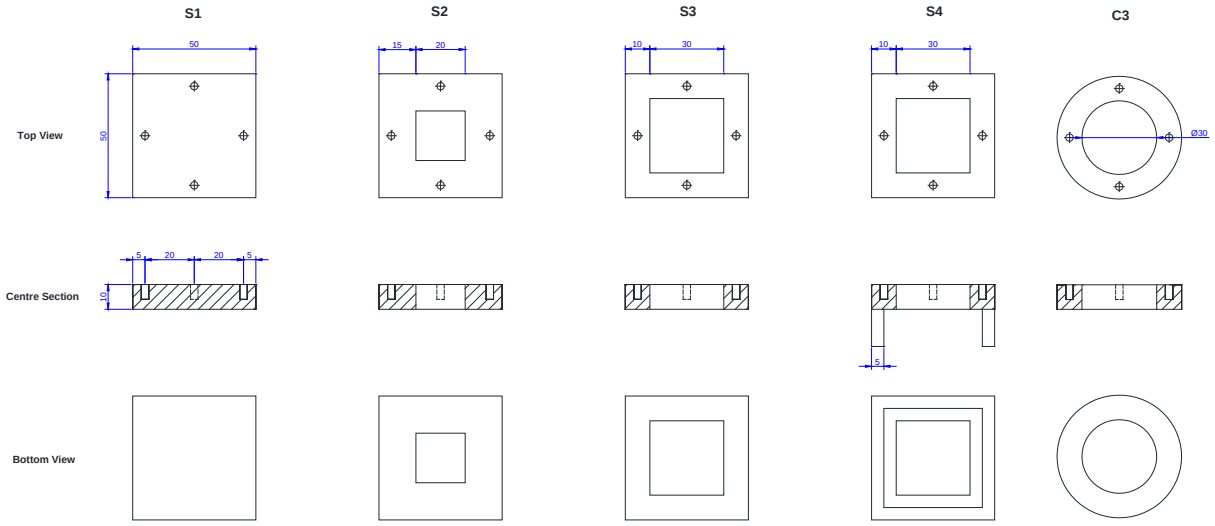

(a) Flat plate models

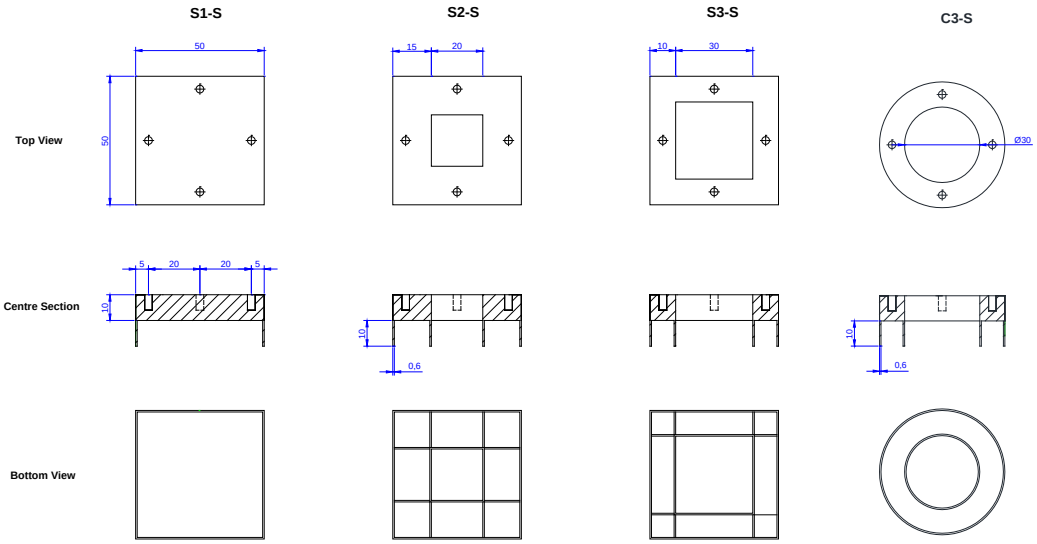

(b) Skirted models

Figure 5.6: Model foundation details

Table 5.5: Foundation model details

Model ID	**Base view**	**Total width, *B*** (mm)	**Perforation width, *P*** (mm)	**Effective strip width, *B**** (mm)	**Perfor-ation ratio, *R***	**Skirt length, *L*** (mm)
S1	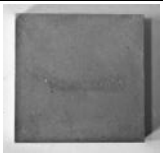	50	0	-	0	0
S1-S		50	0	-	0	10
S2	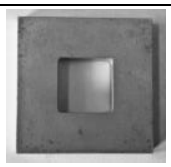	50	20	15	0.16	0
S2-S	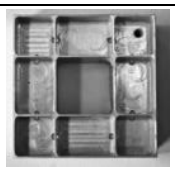	50	20	15	0.16	10
S3	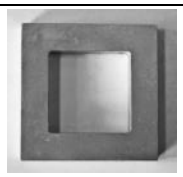	50	30	10	0.36	0
S3-S	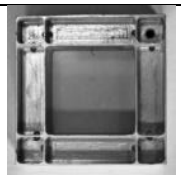	50	30	10	0.36	10
S4	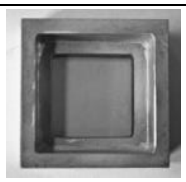	50	40	5	0.64	0
C3	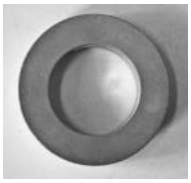	50 (*D*)	20	10	0.36	0
C3-S		50 (*D*)	20	10	0.36	10

A drainage hole that could be sealed was placed at the top base plate of each skirted foundation. Small drainage holes were also machined between skirts to allow all compartments to drain out of the main drainage hole. During installation the main drainage hole was left open to allow venting. The hole was then sealed prior to foundation loading. These details are shown in Figure 5.7.

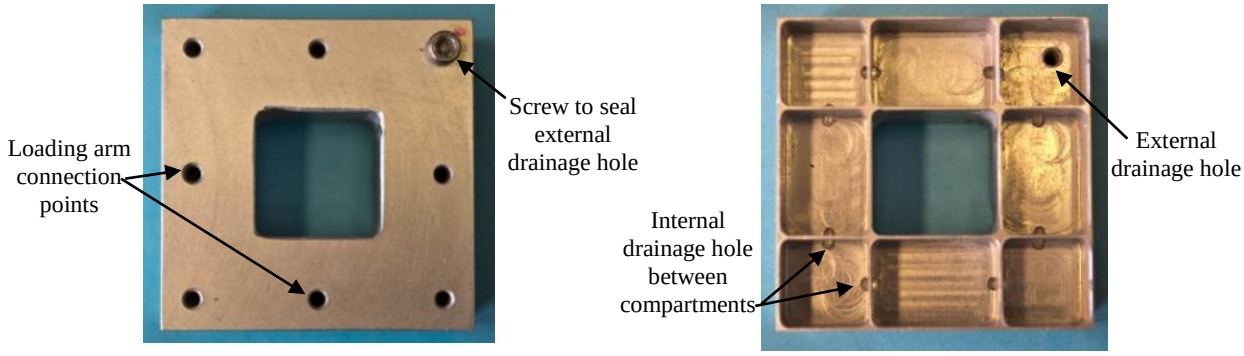

(a) Top of skirted foundation (b) Underside of skirted foundation

Figure 5.7: Skirted foundation drainage arrangement

5.2.4 Loading apparatus

The model foundations were connected to the drum centrifuge actuator via a loading arm. Two configurations of the load arm were used to allow different moment and horizontal load paths to be explored (Figure 5.8). These were:

i) Fixed: The loading arm could be fixed to the actuator such that the foundation could be displaced laterally. This allowed a load path in predominately the *V*:*H* load space to be followed (with minimal moment load).

ii) Hinged: Alternatively the loading arm could be attached to the actuator with a hinge to enable rotation of the foundation. By balancing the radial and vertical movement of the actuator, rotation about the reference point of the foundation could be possible. This allowed a load path in predominately the *V*:*M* load space to be followed (with minimal horizontal load). The accuracy of rotation occurring about the load reference point depends on the stiffness of the soil-foundation reaction.

The hinged loading arm arrangement was initially developed by Cassidy et al., (2004) for testing skirted and spudcan foundations in clay. A modification was made to the hinged arm for this set of experiments. An encoder was connected to measure the rotation of the hinge where previously a laser system had been used. The applied loads and bending moments are determined using strain gauges as shown in Figure 5.8. Foundation displacement was measured using a combination of the actuator's vertical and radial movements. Foundation rotation was determined using the encoder located at the shaft of the hinge leg.

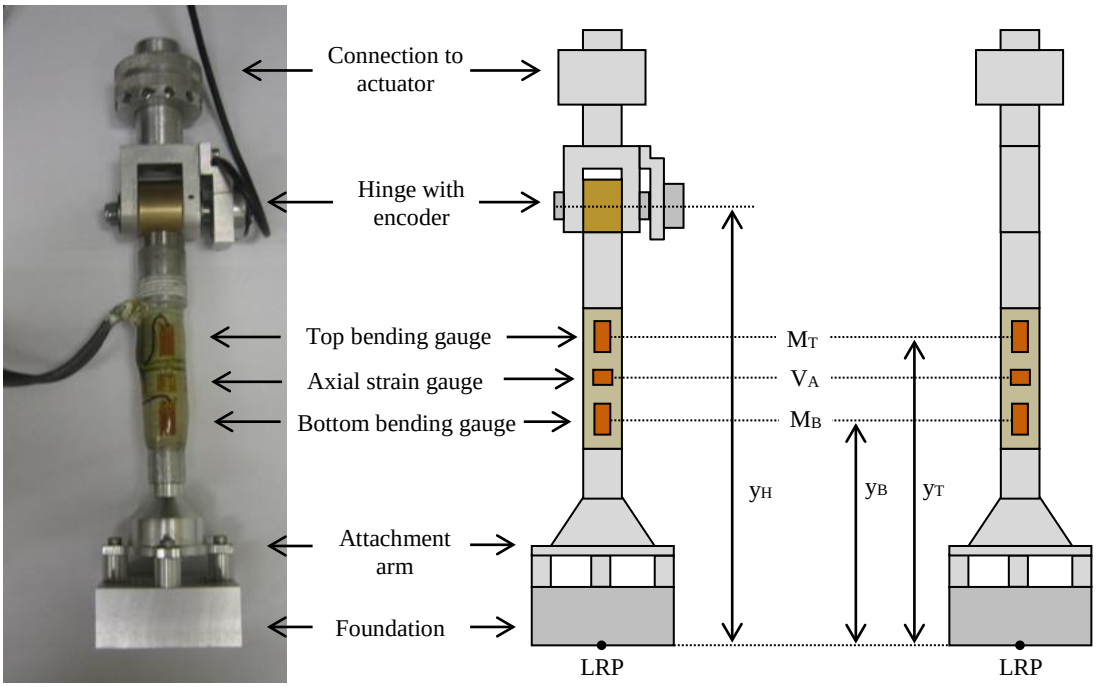

Figure 5.8: Loading arm arrangement

5.2.5 Load application and measurement

Combined loading was applied to the foundation primarily in an orthogonal direction (0 degrees), but also in an oblique direction (45 degrees). The sign convention adopted in each case is shown in Figure 5.9. The load reference point for each foundation model was taken at the base of the foundation. For the skirted foundations this was at skirt tip level. Testing was predominantly undertaken using displacement control. The radial actuator movement (*dy*)

was used to penetrate the foundation vertically and the vertical actuator movement (*dz*) was used to apply horizontal movement to the foundation (see Figure 5.3(b)). For the hinged arm increments of vertical and radial actuator movement were calculated to allow pure rotation about the foundation load reference point (i.e. assuming the reference point did not move).

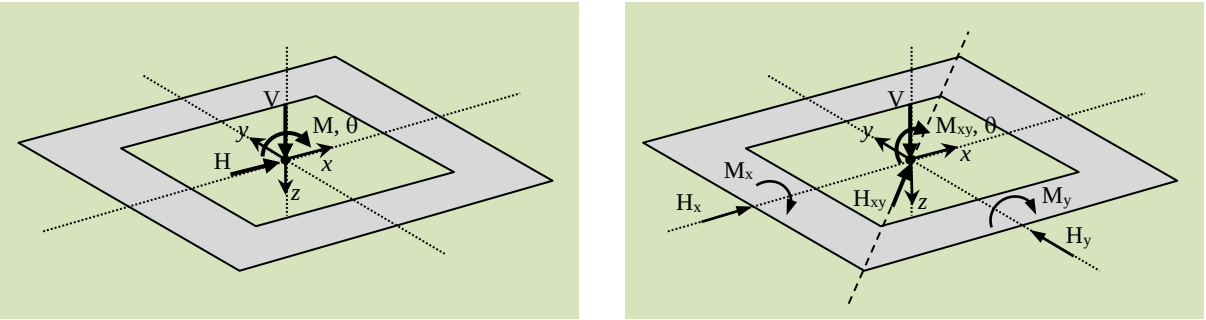

(a) Orthogonal loading (0 degrees) (b) Oblique loading (45 degrees)

Figure 5.9: Loading directions and sign convention

The vertical load at the load reference point (V_{LRP}) was taken to be the load measured by the axial strain gauge such that $V_{LRP} = V_A$. The horizontal load (H_{LRP}) and the moment (M_{LRP}) were interpreted using the top and bottom bending gauges (M_T & M_B) as follows

$$H_{LRP} = \frac{M_B - M_T}{y_B - y_T} \tag{5.1}$$

$$M_{LRP} = M_B + H_{LRP} y_B \tag{5.2}$$

The loads are adjusted to take into account the rotation of the footing. The final loads become

$$V = V_{LRP} \cos\theta + H_{LRP} \sin\theta \tag{5.3}$$

$$H = H_{LRP} \cos\theta - V_{LRP} \sin\theta \tag{5.4}$$

$$M = M_{LRP} \tag{5.5}$$

Similarly, the foundation displacement given by the actuator location is adjusted to account for hinge rotation:

$$z_{LRP} = z_{actuator} - y_{LRP}(1 - \cos\theta) \tag{5.6}$$

$$x_{LRP} = x_{actuator} - y_{LRP} \sin\theta \tag{5.7}$$

5.3 Testing methodology

The vertical and combined loading capacity of perforated foundations was explored with three types of tests:

1. Vertical loading tests
2. Swipe tests
3. Push-over tests

5.3.1 Vertical loading tests

A limited number of purely vertical loading tests were undertaken to help assess vertical bearing capacity. The test involved the following steps:

1. Installation of the foundation at a velocity of 0.1 mm/s to a penetration depth of 20 mm (except for model type S4 which was penetrated to 15 mm).
2. Extraction of the foundation at a velocity of 0.1 mm/s.

5.3.2 Swipe tests

Swipe tests were undertaken to investigate the failure envelope shape under combined loading. The tests involved loading the foundation vertically to a target penetration depth corresponding to a maximum vertical load V_0 (such that $V/V_0 = 1$). A swipe then involved translating (using the fixed arm) or rotating (using the hinged arm) the foundation while keeping the vertical penetration of the footing constant. Each loading arm tracks along a different section of the *V*:*H*:*M* failure envelope as described in Section 5.2.4.

A second type of swipe test was undertaken to examine foundation capacity under tension. In this case once the foundation was loaded to $V/V_0 = 1$, it is then unloaded to a point where $V/V_0 < 0$ before the swipe test was commenced. The two types of swipe tests undertaken are illustrated in Figure 5.10.

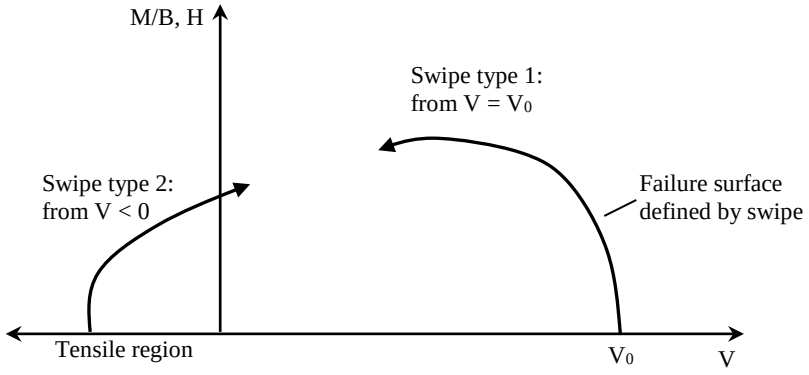

Figure 5.10: Description of swipe tests

Swipe tests were carried out at multiple embedment depths in the same location. This was done by ensuring sufficient penetration between swipe tests to re-join the virgin penetration line. The required penetration depth for this was determined by inspection of the initial test results. The fixed arm and hinged arm swipe tests involved the following steps:

i) Unskirted foundations:

1. The foundation is penetrated vertically at 0.1 mm/s to the target depth at which $V/V_0 = 1$.
2. The swipe test is undertaken at 0.1 mm/s.
3. After the swipe test is completed the loading arm is returned back to the centre line.
4. The foundation is penetrated to the next swipe position and the procedure is repeated for each further embedment depth required.

ii) Skirted foundations:

1. The foundation is penetrated vertically to about 10 mm (model) depth such that the base plate is in contact with the clay surface. This is undertaken in-flight with the vent hole open.
2. The centrifuge is ramped down and the vent screw is inserted to seal the skirted compartment/s. The sample is spun at 100g for 20 minutes.
3. The foundation is penetrated vertically to the depth established to be V_0.

4. The swipe test is undertaken at 0.1 mm/s
5. After the swipe tests the loading arm is returned back to the centre line
6. The foundation is penetrated to the next swipe position and the procedure is repeated for each further embedment depth required.

Type 2 swipe tests involved the same procedures except that after reaching V_0 the vertical load was dropped to a value of $V/V_0 < 0$ prior to the swipe test commencing.

5.3.3 Pushover tests

Pushover tests were undertaken using the hinged arm and involved applying a lateral load (or pushover load) until foundation failure. The tests were undertaken by initially applying a vertical load of approximately $V/V_0 = 0.3$, using V_0 as determined from swipe test results. The vertical load was held constant while the lateral monotonic pushover load was applied at hinge level until failure. In one of the tests a package of two-way displacement controlled cyclic loads were applied for 85 cycles prior to a post-cyclic monotonic pushover load.

5.3.4 Test drainage conditions

Testing was undertaken at a velocity of 0.1 mm/s to ensure undrained loading of the soil. The drainage conditions can be assessed using a normalised velocity V. This is a function of the foundation velocity v, the foundation diameter D, and the coefficient of consolidation c_v, as given by Equation 5.8 (Finnie and Randolph, 1994):

$$V = \frac{v.D}{c_v} \tag{5.8}$$

The coefficient of consolidation for kaolin can be taken as approximately $c_v = 1.5$ m^2/year, such that a normalised velocity of about $V = 105$ was achieved. For foundation loading to be essentially undrained a value of $V > 15$ is required (Schneider et al., 2008, Lehane et al., 2009), so a vertical penetration rate of 0.1 mm/s was satisfactory to ensure undrained conditions are present.

5.3.5 Test layout

The general test layout for Test Series 1 is shown in Figure 5.11. Two rows of tests were configured in order to maximise the test locations. The minimum edge to edge distance between tests was set to be about 2*B* to ensure no interference effects occurred between adjacent tests. The T-bar tests were generally undertaken prior to the foundation tests. A single central row of test locations was predominantly used in Test Series 2 as this allowed for a sufficient number of tests to be carried out.

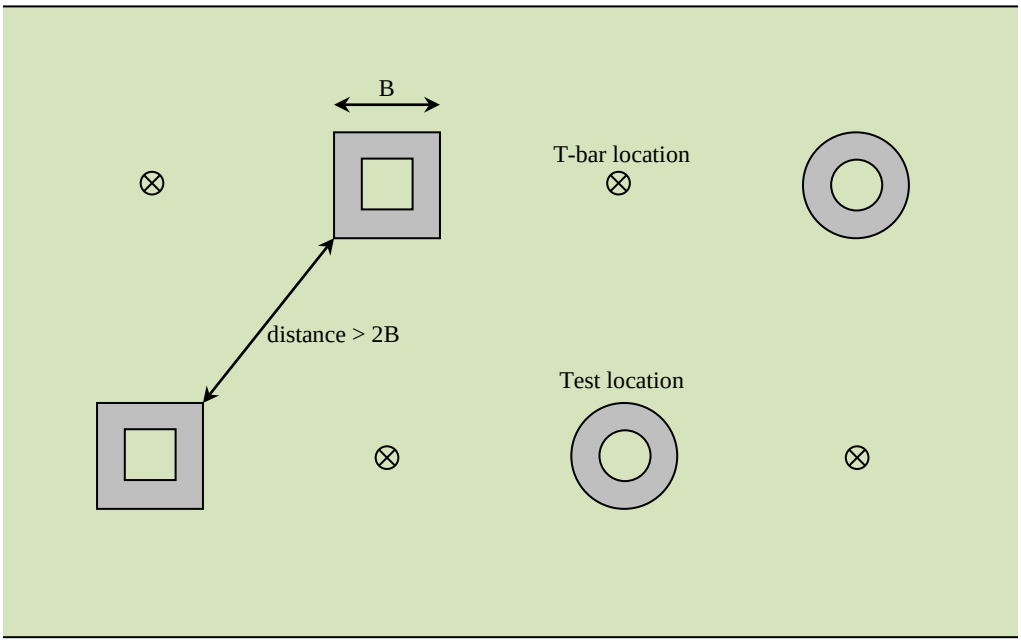

Figure 5.11: Example of test layout

5.3.6 Testing programme

Testing was undertaken in two series in which 48 individual tests were completed. At each swipe test location three sub-tests were undertaken at varying embedment depths. The two series are as follows:

- Test Series 1: top half of sample – 22 tests
- Test Series 2: bottom half of sample – 26 tests

A summary of the test details for Test Series 1 and Test Series 2 are given in Table 5.6 and Table 5.7 respectively.

Table 5.6: Test series 1

Model	Test ID	Soil profile	Test type	Loading arm	Load direction	Load start point
S1	T101	1-1	swipes	fixed	0°	$V/V_0 = 1$
	T122	1-3	swipes	fixed	0°	$V/V_0 \approx$ -0.1 – 0.2
	T105	1-2	swipes	hinge	0°	$V/V_0 = 1$
	T111	1-2	swipes	hinge	0°	$V/V_0 \approx$ -0.1 – 0.2
	T110	1-2	pushover - mono	hinge	0°	$V/V_0 \approx 0.6$ (constant)
S2	T102	1-1	swipes	fixed	0°	$V/V_0 = 1$
	T113	1-2	swipes	hinge	0°	$V/V_0 = 1$
S3	T103	1-1	swipes	fixed	0°	$V/V_0 = 1$
	T121	1-3	swipes	fixed	0°	$V/V_0 \approx$ -0.1 – 0.2
	T106	1-2	swipes	hinge	0°	$V/V_0 = 1$
	T120	1-3	swipes	hinge	0°	$V/V_0 \approx$ -0.1 – 0.2
	T119	1-3	pushover - mono	hinge	0°	$V/V_0 \approx 0.3$ (constant)
S4	T104	1-1	swipes	fixed	0°	$V/V_0 = 1$
	T114	1-2	swipes	hinge	0°	$V/V_0 = 1$
C3	T107	1-2	swipes	hinge	0°	$V/V_0 = 1$
S1-S	T115	1-2	swipes	hinge	0°	$V/V_0 = 1$
	T116	1-2	pushover - mono	hinge	0°	$V/V_0 \approx 0.3$ (constant)
S3-S	T117	1-2	swipes	hinge	0°	$V/V_0 = 1$
	T118	1-2	pushover - mono	hinge	0°	$V/V_0 \approx 0.3$ (constant)

Table 5.7: Test Series 2

Model	Test ID	Soil profile	Test type	Loading arm	Load direction	Load start point
S1	T219	2-1	swipes	hinge	0°	$V/V_0 = 1$
	T217	2-1	swipes	hinge	45°	$V/V_0 = 1$
	T220	2-1	swipes (un-vented)	hinge	0°	$V/V_0 = 1$
	T217a	2-1	vertical	hinge	-	-
S2	T221	2-1	vertical	hinge	-	-
S3	T218	2-1	swipes	hinge	0°	$V/V_0 = 1$
	T216	2-1	swipes	hinge	45°	$V/V_0 = 1$
	T216a	2-1	vertical	hinge	-	-
S4	T223	2-1	vertical	hinge	-	-
S1-S	T201	2-1	swipes	hinge	0°	$V/V_0 = 1$
	T202	2-1	pushover - mono	hinge	0°	$V/V_0 \approx 0.3$ (constant)
	T215	2-1	pushover - mono	hinge	45°	$V/V_0 \approx 0.3$ (constant)
	T224	2-1	vertical	hinge	-	-
S2-S	T203	2-1	swipes	hinge	0°	$V/V_0 = 1$
	T204	2-1	pushover - mono	hinge	0°	$V/V_0 \approx 0.3$ (constant)

Table 5.7: Test Series 2 (cont.)

Model	Test ID	Soil profile	Test type	Loading arm	Load direction	Load start point
S3-S	T209	2-1	swipes	hinge	0°	$V/V_0 = 1$
	T213	2-1	swipes	hinge	45°	$V/V_0 = 1$
	T211	2-1	swipes	hinge	0°	$V/V_0 \approx$ -0.2 – 0.1
	T207	2-1	swipes	fixed	0°	$V/V_0 = 1$
	T208	2-1	swipes	fixed	0°	$V/V_0 \approx$ -0.2 – 0.1
	T210	2-1	pushover - mono	hinge	0°	$V/V_0 \approx 0.3$ (constant)
	T214	2-1	pushover - mono	hinge	45°	$V/V_0 \approx 0.3$ (constant)
	T212	2-1	pushover - cyclic	hinge	0°	$V/V_0 \approx 0.3$ (constant)
C3	T203	2-1	vertical	hinge	-	-
C3-S	T205	2-1	swipes	hinge	0°	$V/V_0 = 1$
	T206	2-1	pushover - mono	hinge	0°	$V/V_0 \approx 0.3$ (constant)

5.4 Vertical loading results

The results of the vertical loading experiments are presented and are analysed in relation to the following aspects:

1. Vertical bearing capacity
2. Penetration resistance of skirted foundations
3. Pull-out capacity

All results are given in prototype units.

5.4.1 Vertical bearing capacity

A summary of the vertical loading tests used to assess the vertical bearing capacity of annular and ring foundations is given in Table 5.8. The results of the tests undertaken on soil profiles of kB/s_{um} = 2 & 5 are examined for both the surface foundation tests (d/B = 0) and the skirted foundation tests (d/B = 0.2).

Table 5.8: Vertical bearing capacity test summary

Case	Square annular		Ring	
	kB/s_{um}= 2 (Soil profile 2-1)	kB/s_{um} = 5 (Soil profile 1-2)	kD/s_{um} = 2 (Soil profile 2-1)	kD/s_{um} = 5 (Soil profile 1-2)
Surface (d/B = 0)	R = 0, 0.16, 0.36, 0.64	R = 0, 0.16, 0.36, 0.64	R = 0.36	R = 0.36
Skirted (d/B = 0.2)	R = 0, 0.16, 0.36	R = 0, 0.36	R = 0.36	-

5.4.1.1 Surface foundation results

The vertical load-displacement results for surface foundations with kB/s_{um}, kD/s_{um} = 2 & 5 are given in Figure 5.12. Once penetration is established there is a period of linear foundation load-displacement response prior to yielding of the soil. Past this strain hardening is seen in which the foundation is able to support increasing load but at an increased rate of penetration.

Given there is not a perfectly plastic response or clear peak capacity, identifying the bearing failure load is not straightforward. Several definitions for defining bearing failure in this situation have been proposed. Villalobos (2006) investigated a range of these methods when assessing bearing capacity of suction caisson results and found a method by Graham et al. (1982) to be effective. The approach by Graham et al. (1982) determines failure as the intersection of the two linear lines fitted to the experimental curve at either side of where yielding occurs. This criterion has been adopted as shown in Figure 5.12 in order to determine the initial bearing failure load V_0.

It is seen in Figure 5.12 that the failure load V_0 decreases with increasing perforation ratio R as is expected. The penetration depth required to mobilise V_0 is seen to generally decrease as R in increases. The mobilisation depth for kB/s_{um} = 2 decreased from approximately z/B = 0.05 for R = 0, to z/B = 0.04 at R = 0.64. For kB/s_{um} = 5, the mobilisation depth z/B ranged from approximately 0.02 to 0.015 as R increased from 0 to 0.64.

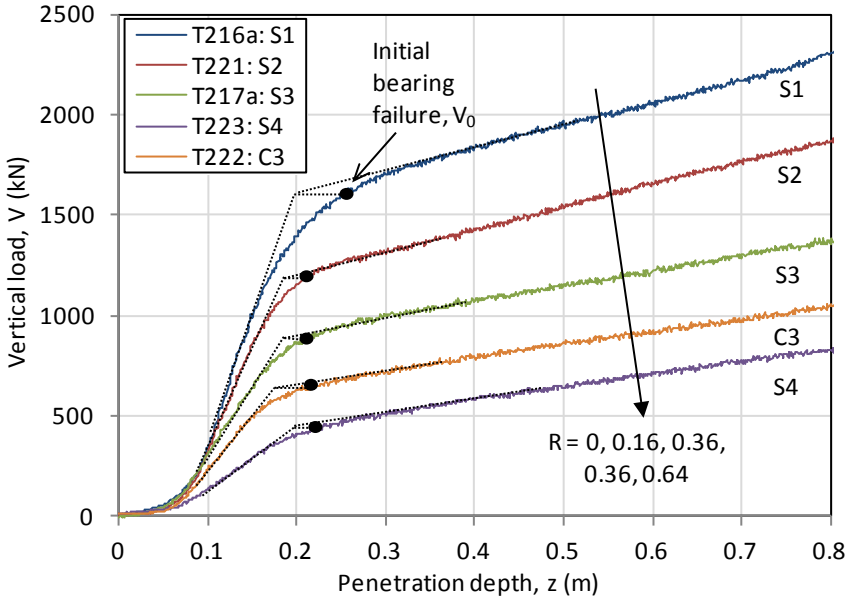

(a) $kB/_{sum}, kD/_{sum} \approx 2$

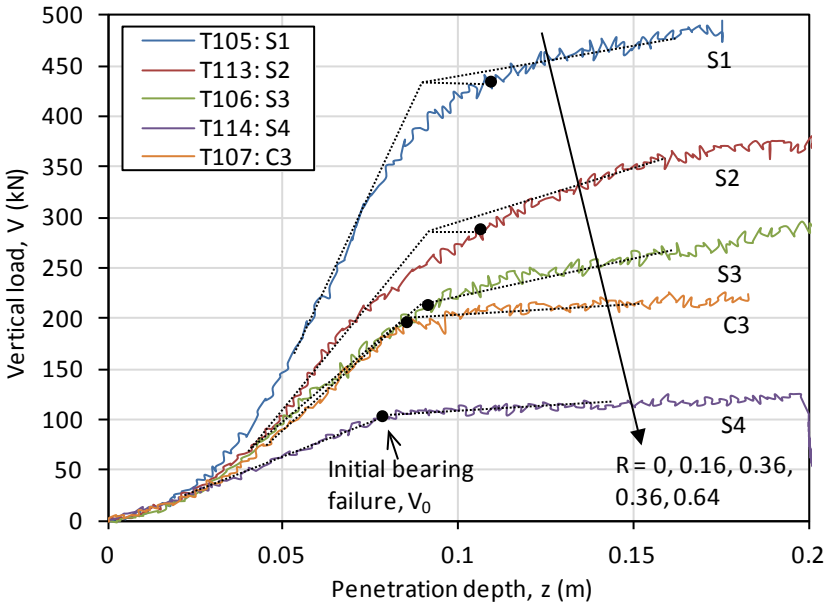

(b) $kB/_{sum}, kD/_{sum} \approx 5$

Figure 5.12: Surface foundation vertical load-displacement results

Figure 5.13 presents these results in terms of a bearing capacity factor at failure N_c, determined as follows:

$$N_c = \frac{V_0}{As_{um}} \tag{5.9}$$

The relevant value for the soil undrained shear strength at surface level s_{um} is selected from Table 5.4. The results from the numerical analysis described in Chapter 4 are also included in Figure 5.13. A reasonable match is seen, particularly for kB/s_{um}, kD/s_{um} = 2 rather than 5. The ring foundation at kD/s_{um} = 5 is significantly higher than the numerical result, which may be due to local variations in soil strength at the location of that test. It is noted that all the experimental N_c values are dependent on the accuracy of the s_{um} measurement used. The design solution proposed to predict vertical bearing capacity (Equation 4.3) provided a close estimation of capacity found by the centrifuge results in most cases, or otherwise was conservative.

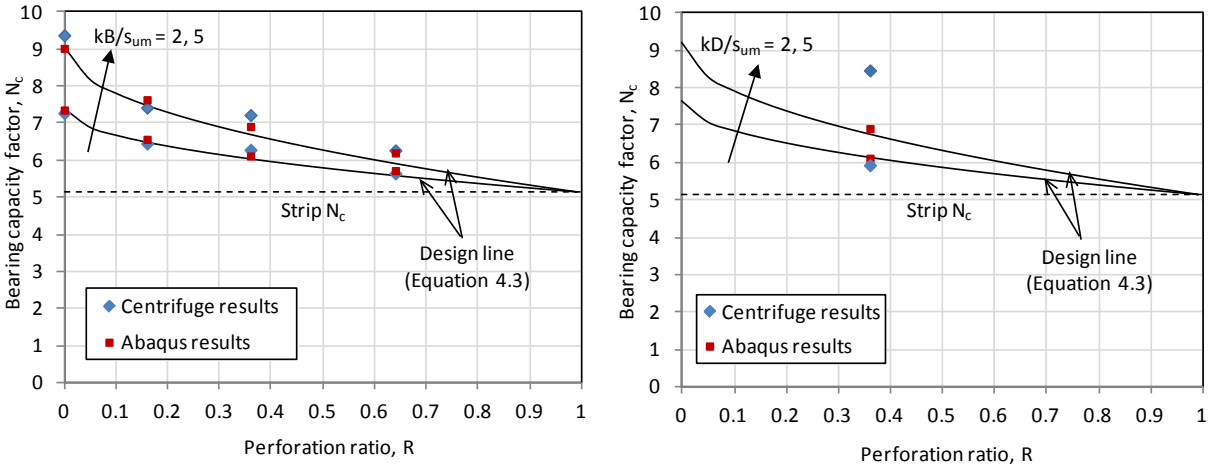

(a) Square annular (b) Ring

Figure 5.13: Comparison of surface foundation results

5.4.1.2 Skirted foundation results

The vertical load-displacement results for skirted foundations with kB/s_{um}, kD/s_{um} = 2 & 5 are given in Figure 5.14. The vertical load shows a steady increase as the skirts penetrate. There is a marked increase in vertical load when the soil plug starts to make contact with the foundation base plate. The contact occurs prior to full installation of the skirts as the internal soil plug heaves above the initial surface level because of the soil displaced by the skirts. At full skirt penetration there is a drop in vertical load as each test is temporarily stopped to

allow the vent hole to be sealed. After this the foundation is penetrated to failure, followed by a period of strain hardening with further penetration.

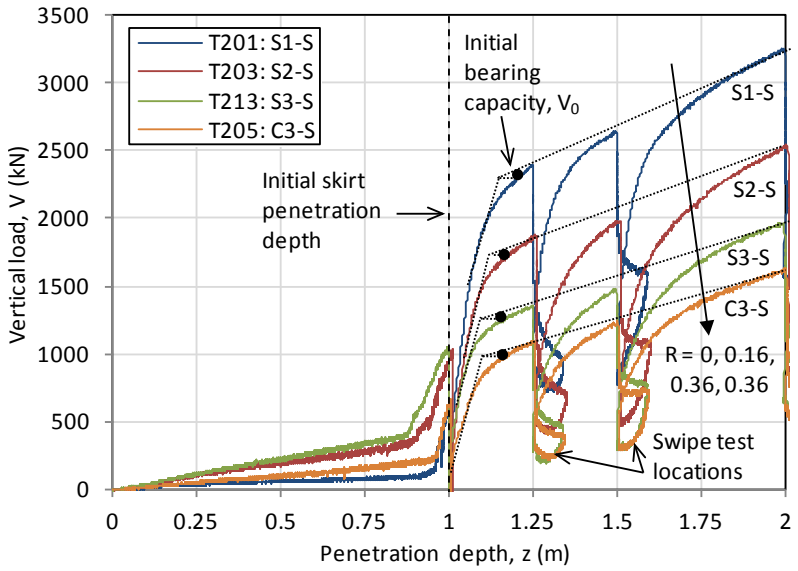

(a) $kB/_{sum}, kD/_{sum} \approx 2$

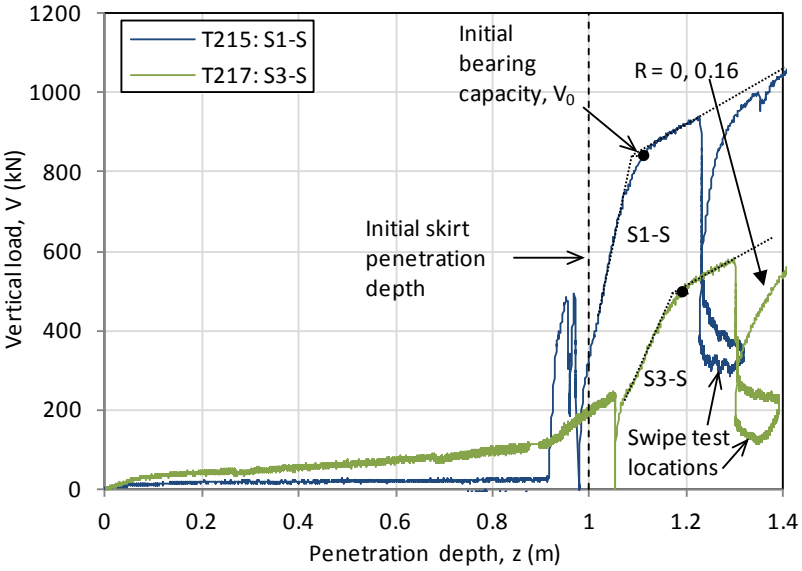

(b) $kB/_{sum} \approx 5$

Figure 5.14: Skirted foundation vertical load-displacement results

The initial bearing failure load V_0 for the skirted foundations has been determined in the same way as for surface foundations and is shown in Figure 5.14. The expected trend of failure load V_0 decreasing with increasing perforation ratio R is observed. The penetration depth required to mobilise V_0 for $kB/s_{um} = 2$ decreased from approximately $z/B = 0.04$ for $R =$

0 to z/B = 0.03 at R = 0.36. For kB/s_{um} = 5, the mobilisation depth for the cases tested of R = 0 and 0.16 occurred at approximately the same penetration of about z/B = 0.025.

Figure 5.15 presents the skirted foundation results in terms of the bearing capacity factor at failure N_c. The centrifuge results are compared with the Abaqus results as well as the corresponding design line given by Equation 4.3. A reasonable match is observed between the experimental and numerical results, although the numerical results generally over-predict the experimental capacity.

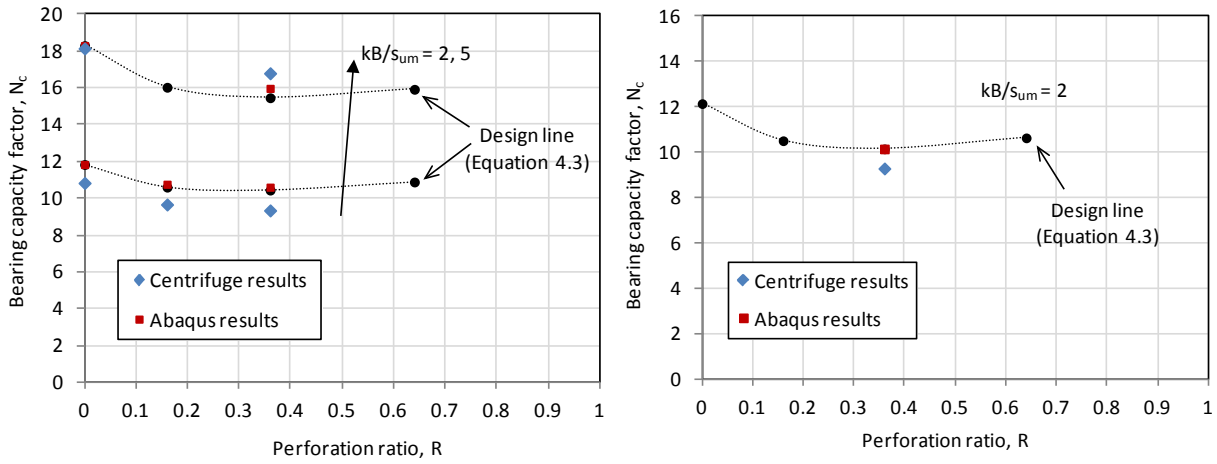

(a) Square annular (b) Ring

Figure 5.15: Comparison of skirted foundation results

5.4.1.3 Failure mechanisms

The nature of the failure mechanisms from the flat base foundation experiments as indicated by the deformed soil are shown for R = 0 and R = 0.36 in Figure 5.16 and Figure 5.17 respectively. Comparison is made with the soil deformation given by the Abaqus analysis inferred by the plastic regions shown by the refined mesh. It is seen that the extent and style of the soil deformation is similar between the experimental and numerical results. The deformation zone in the experimental results is seen to taper in at the foundation corner which is also observed in the Abaqus results. The extent of the deformation zone away from the foundation is reduced in R = 0.36 compared with R = 0. This is also seen to be the case in the Abaqus results.

(a) Centrifuge deformation

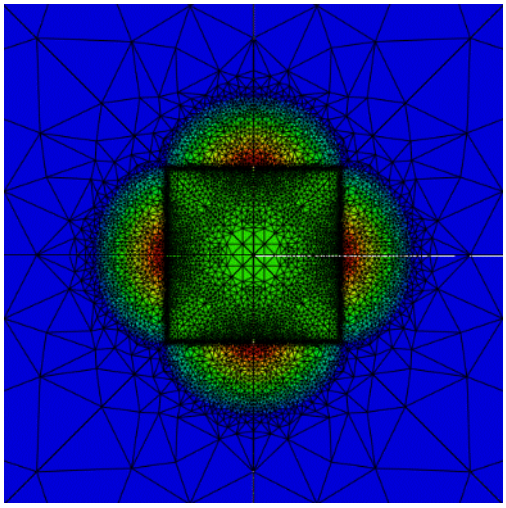

(b) Abaqus deformation

Figure 5.16: Soil deformation for square foundation (R = 0), kB/s_{um}= 2

(a) Centrifuge deformation

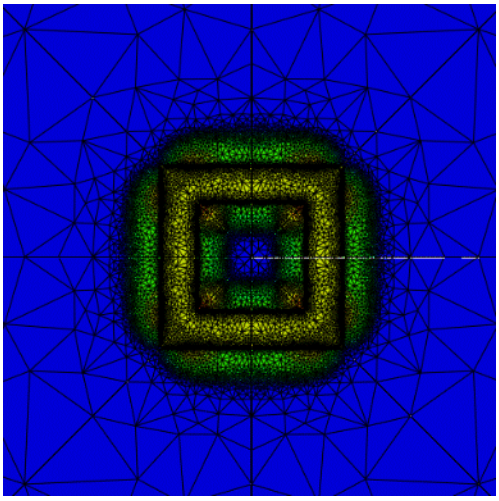

(b) Abaqus deformation

Figure 5.17: Soil deformation for square annular foundation (R = 0.36), kB/s_{um}= 2

5.4.2 Skirt penetration resistance

Quantifying the skirt penetration resistance that must be overcome to achieve installation of the foundation skirts is an important design consideration. An incorrect prediction of skirt resistance may mean the foundation cannot be installed to the required penetration depth.

As the skirt tips penetrate the clay, a zone of sheared soil develops along the skirt wall interface. Within this zone, the soil is assumed to be remoulded and mobilise shear stress on the skirts given by the product of an adhesion factor α and the in-situ soil undrained shear

strength s_u. End bearing resistance also occurs at the base of the skirts and this can be calculated using classical bearing capacity theory.

Skirt penetration resistance has been predicted for each of the skirted foundations tested and compared with the experimental results. Assumptions made in the calculations included:

1. An average soil strength profile from the T-bar results has been used as shown in Figure 5.18.
2. Adhesion factor $\alpha = 0.3$, based on the cyclic T-Bar results (see Figure 5.5).
3. End bearing factor $N_c = 9$, based on plane strain bearing capacity for deep foundations (DNV, 2005).

In the experiments the foundations were installed without the use of suction, which is often used in addition to self weight to achieve skirt installation. Previous research however has found that penetration resistance in clay is very similar for a skirted foundation that is installed with or without suction (Westgate et al., 2009).

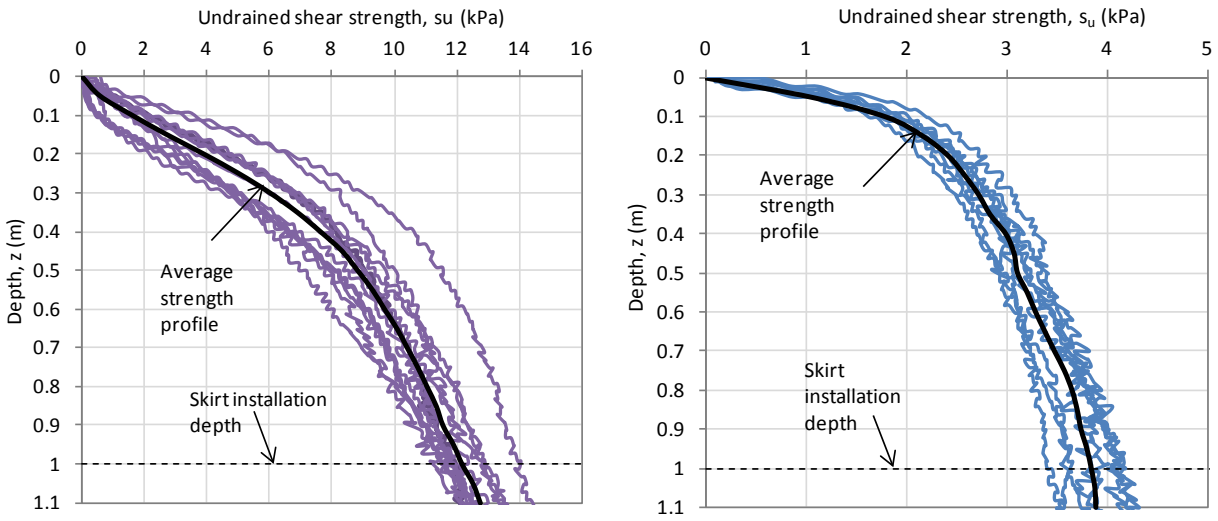

(a) $kB/_{sum}, kD/_{sum} \approx 2$ (b) $kB/_{sum}, kD/_{sum} \approx 5$

Figure 5.18: Soil strength profiles for skirt penetration resistance prediction

The skirt penetration predictions are compared with the experimental results in Figure 5.19. There is good agreement for the foundations where $R > 0$, but for the unperforated square geometry the penetration resistance is over predicted, particularly for $kB/s_{um} = 2$.

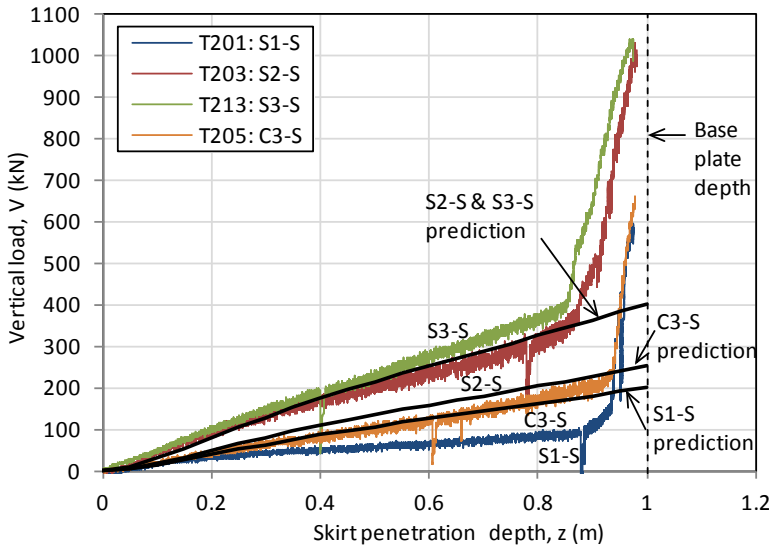

(a) $kB/_{sum}, kD/_{sum} \approx 2$

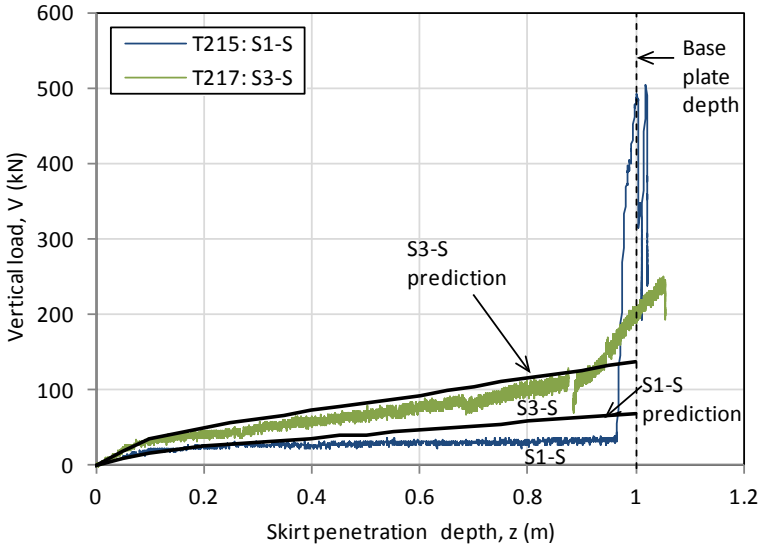

(b) $kB/_{sum} \approx 5$

Figure 5.19: Skirt penetration resistance

An important observation from the results is the impact of plug heave on penetration resistance. It is seen in Figure 5.19 that once the soil plug comes in contact with the base plate there is a significant increase in resistance. This could be onerous to overcome if full contact is sought, and may require alternative measures such as grouting to be considered. The resistance increase was seen to be greater for foundations with increasing *R* as a result of their increased skirt volume. The plug heave was seen to contact the base plate at a

penetration depth z/d = 0.85 for R = 0.36, and z/d = 0.9 for R = 0, where d is the skirt length. The value of z/d may be lower (i.e. contact occurs sooner) for skirted foundations installed with suction as more soil may be pulled inside the skirts contributing to greater plug heave (Westgate et al., 2009).

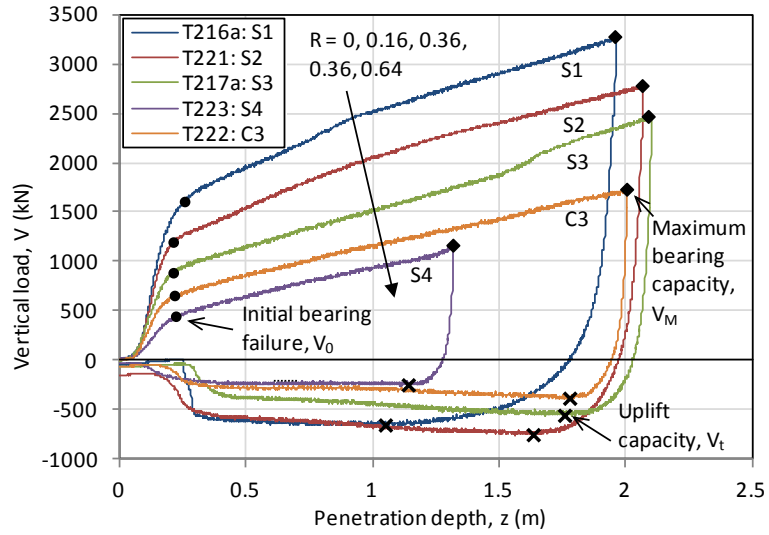

(a) Flat base

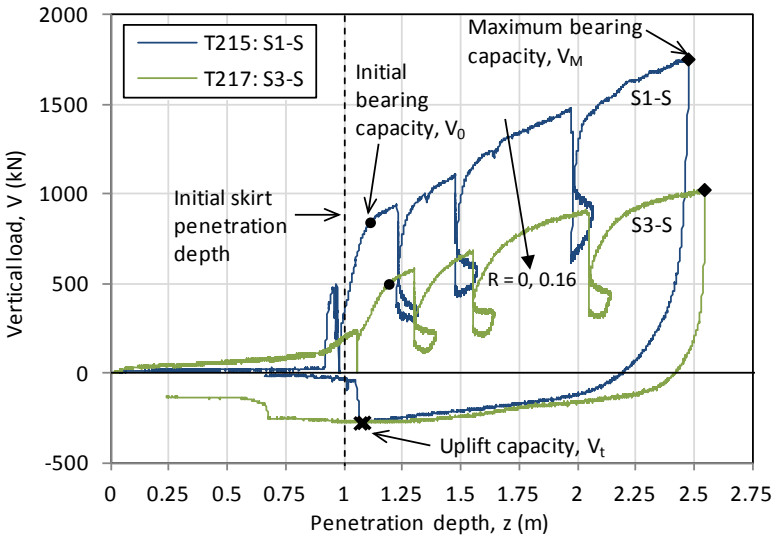

(b) Skirted

Figure 5.20: Foundation uplift capacity $kB/_{sum}$, $kD/_{sum} \approx 2$

5.4.3 Uplift capacity

The uplift resistance was measured during the extraction of the foundations to allow assessment of the foundation capacity. Once the vertical penetration or swipe tests were

completed the foundation was removed at the same rate as it was penetrated. The results for the penetration and extraction of the tests on the soil strength of kB/s_{um}, kD/s_{um} = 2 are shown in Figure 5.20. The maximum bearing load prior to extraction V_M, as well as the largest uplift load registered in tension V_t are indicated on the figure.

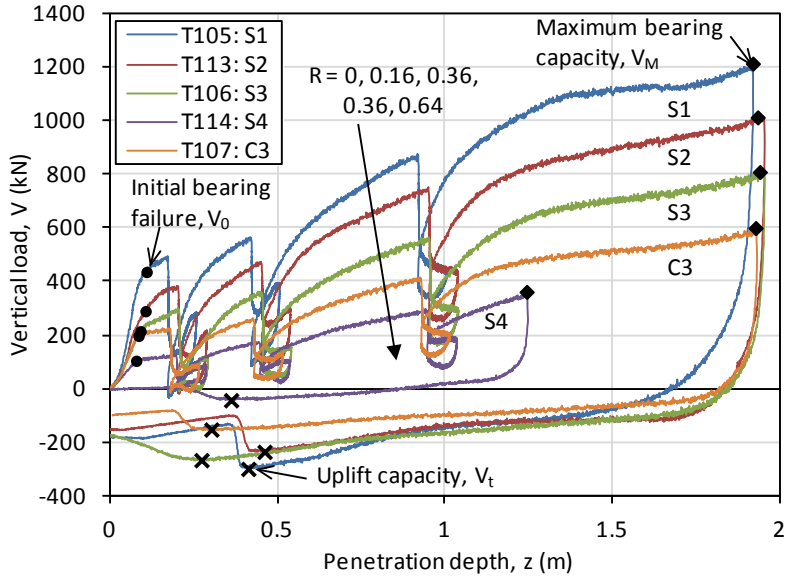

(a) Flat base

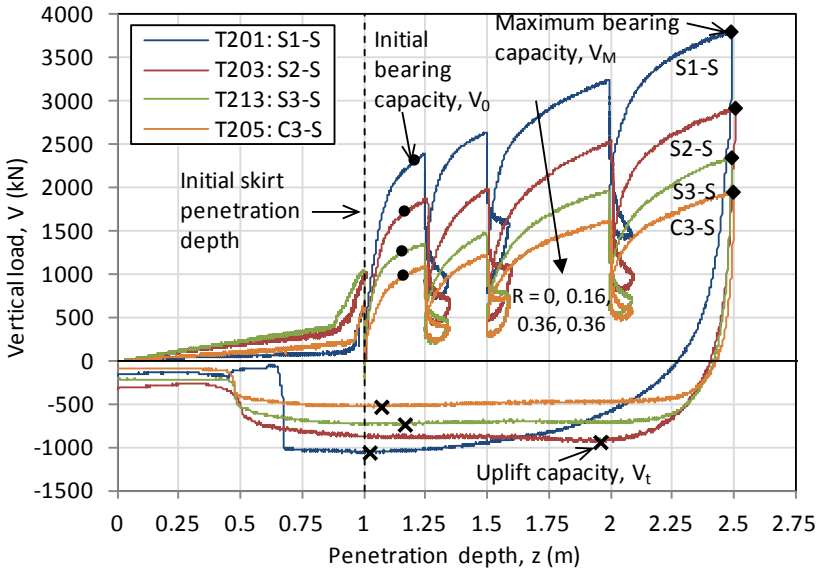

(b) Skirted

Figure 5.21: Foundation uplift capacity, $kB/_{sum}$, $kD/_{sum} \approx 5$

It is seen that the uplift capacity is lower than both the initial and maximum load capacity achieved during penetration. The same is noticed for the tests undertaken on soil having kB/s_{um} = 5 as shown in Figure 5.21. In all tests it is seen that the uplift resistance generally decreases with increasing R.

The results from Figure 5.20 and Figure 5.21 are summarised in Figure 5.22 in terms of the ratios $|V_t|/V_M$ and $|V_t|/V_0$. Both the ratios appear to increase from R = 0 until R = 0.36 and then decrease at R = 0.64. The average $|V_t|/V_M$ value is around 0.25 whilst for $|V_t|/V_0$ it is about 0.6. The skirted foundations are generally not seen to have higher ratios than the flat base foundations. This might have been expected as suction generated within the internal soil plug could be expected to increase uplift capacity. Theoretically, for fully undrained conditions uplift and compression capacity should be equal giving $|V_t|/V_0$ = 1. This might not have occurred in this case because:

1. Tests involving swipes where the foundation is translated or rotated may have gaps formed at the side of the foundation which could reduce the drainage path length.
2. The deformation of the soil caused by the large foundation embedment and swipe tests may have reduced the operational strength on extraction toward the remoulded strength of the clay.
3. The normalised velocity resulting in fully undrained behaviour for foundations in uplift has been found to be two orders of magnitude higher than foundations in compression (Lehane et al., 2008). The normalised velocity for the uplift tests in this study is about V = 105 (see Section 5.3.4) and so is an order below the magnitude suggested by these findings in order for fully undrained conditions to be achieved. A study on square and circular skirted foundations also embedded at h/D = 0.2 found that a normalised velocity of about V = 100 was sufficient for undrained conditions (Li et al., 2013). This study however did not have the complications of items 1 and 2.

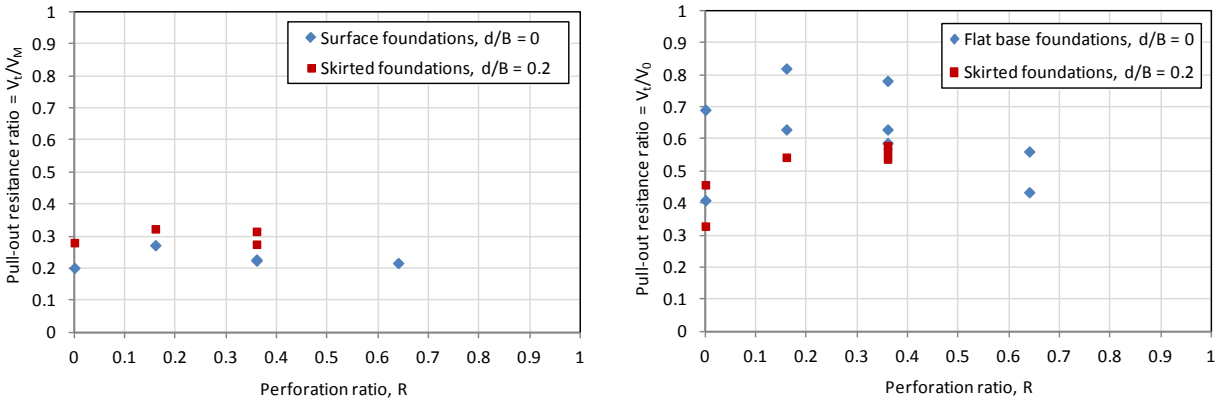

(a) $|V_t|/V_M$ (b) $|V_t|/V_0$

Figure 5.22: Foundation uplift ratios

In Figure 5.23 the uplift results are plotted in terms of an uplift bearing capacity factor, N_c. This has been calculated from the maximum uplift load V_t and the gross foundation area, A_0. It is seen that N_c is generally decreases as the perforation ratio increases. The uplift N_c values are lower than the equivalent values recorded during installation, which was also observed in perforated mudmat testing carried out by White et al. (2005).

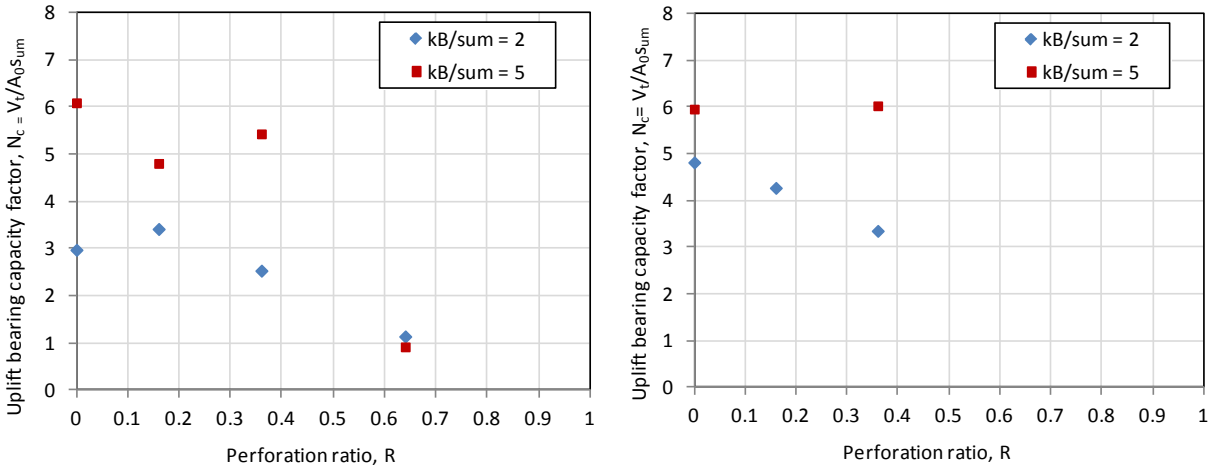

(a) Flat base foundations (b) Skirted foundations

Figure 5.23: Uplift bearing capacity factors

Figure 5.24 shows some examples of soil failure mechanisms after extraction of skirted ring and square annular foundations. The failure around the foundations and the depression

due to downward movement of the soil indicated that suction has been sustained and a reverse end bearing mechanism has been generated. This is instead of uplift resistance only being sustained by the friction mobilised at the inside and outside skirt-soil interfaces.

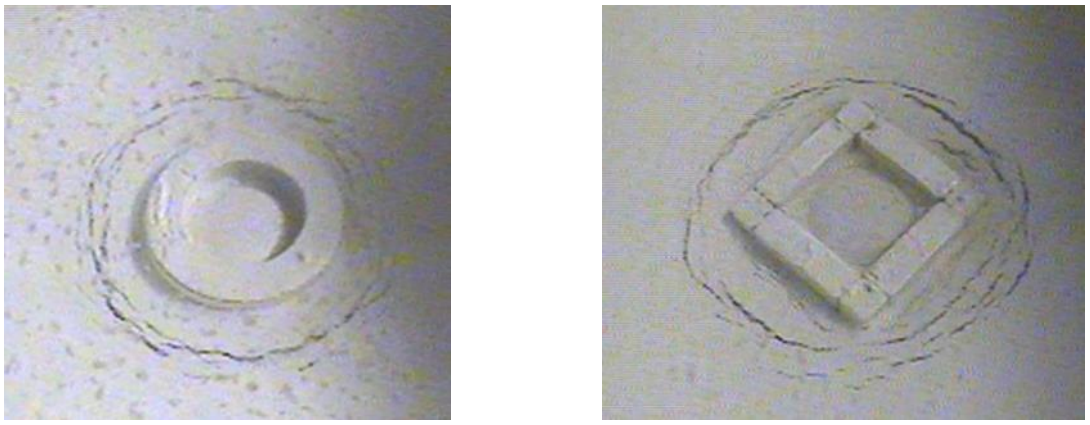

(a) Circle, $R = 0.36$ (b) Square, $R = 0.36$

Figure 5.24: Soil surface after foundation extraction with soil plug in-tact

On some occasions inspection of the foundation after extraction showed that the soil plug had remained trapped within the skirted compartments. This was not noticed for the case of the solid skirted square foundation ($R = 0$), which did not have internal skirts. This may explain why the uplift loads for the square skirted foundation in Figure 5.20(b) and Figure 5.21(b) show a more sharp breakaway point after which the uplift force drops to zero.

(a) Square, $R = 0.36$ (b) Square, $R = 0.16$

Figure 5.25: Skirted foundation base after testing

5.5 Combined loading results

The results of the combined loading experiments undertaken using i) swipe tests and ii) pushover tests are presented and are analysed in relation to the following aspects:

1. Impact of perforation ratio, R
2. Foundations embedment (flat base vs. skirted)
3. Foundations shape (annular vs. ring)
4. Loading direction (orthogonal vs. oblique)
5. Loading type (monotonic vs. cyclic)

5.5.1 Swipe test results

Swipe tests (as described in Section 5.3.2) were undertaken on flat base and skirted foundations using fixed and hinged loading arms. An example of the results for a swipe test (T101) using the fixed loading arm for a flat base foundation is shown in Figure 5.26. The foundation is penetrated to a point past initial failure to a vertical load $V_{0(1)}$. At this point the vertical displacement is fixed and the foundation is translated horizontally for the first swipe. The foundation is then penetrated to a vertical load $V_{0(2)}$ (during which the moment and horizontal load imposed from the previous swipe reduce back towards zero) and the second swipe test is completed. This process is repeated for a third swipe starting from a vertical load $V_{0(3)}$ before the foundation is penetrated to V_M and then extracted. During each swipe the horizontal load H and moment M are determined using the top and bottom bending gauges (M_T & M_B) as described in Section 5.2.5.

An example of the results for a swipe test (T201) using the hinged loading arm for a skirted foundation is shown in Figure 5.27. The foundation is initially installed until the skirts are fully penetrated. The test is then put on hold whilst the base plate venting hole is plugged to seal the compartments. The foundation is then penetrated to a point past initial failure to a vertical load $V_{0(1)}$. At this point the foundation is rotated for the first swipe. The rotation is

achieved by moving the actuator simultaneously in the *x* and *z* direction to follow an arc such that the rotation point is centred at the LRP. It is seen in Figure 5.27 that the *x* and *z* movement at the LRP is minimal which shows that good rotation is achieved about this point. This process is repeated for a further two swipes starting from a vertical load of $V_{0(2)}$ and $V_{0(3)}$. The foundation is then penetrated to V_M and finally is extracted. In each swipe the Horizontal load *H* and moment *M* are determined using the top and bottom bending gauges (M_T & M_B) as described in Section 5.2.5.

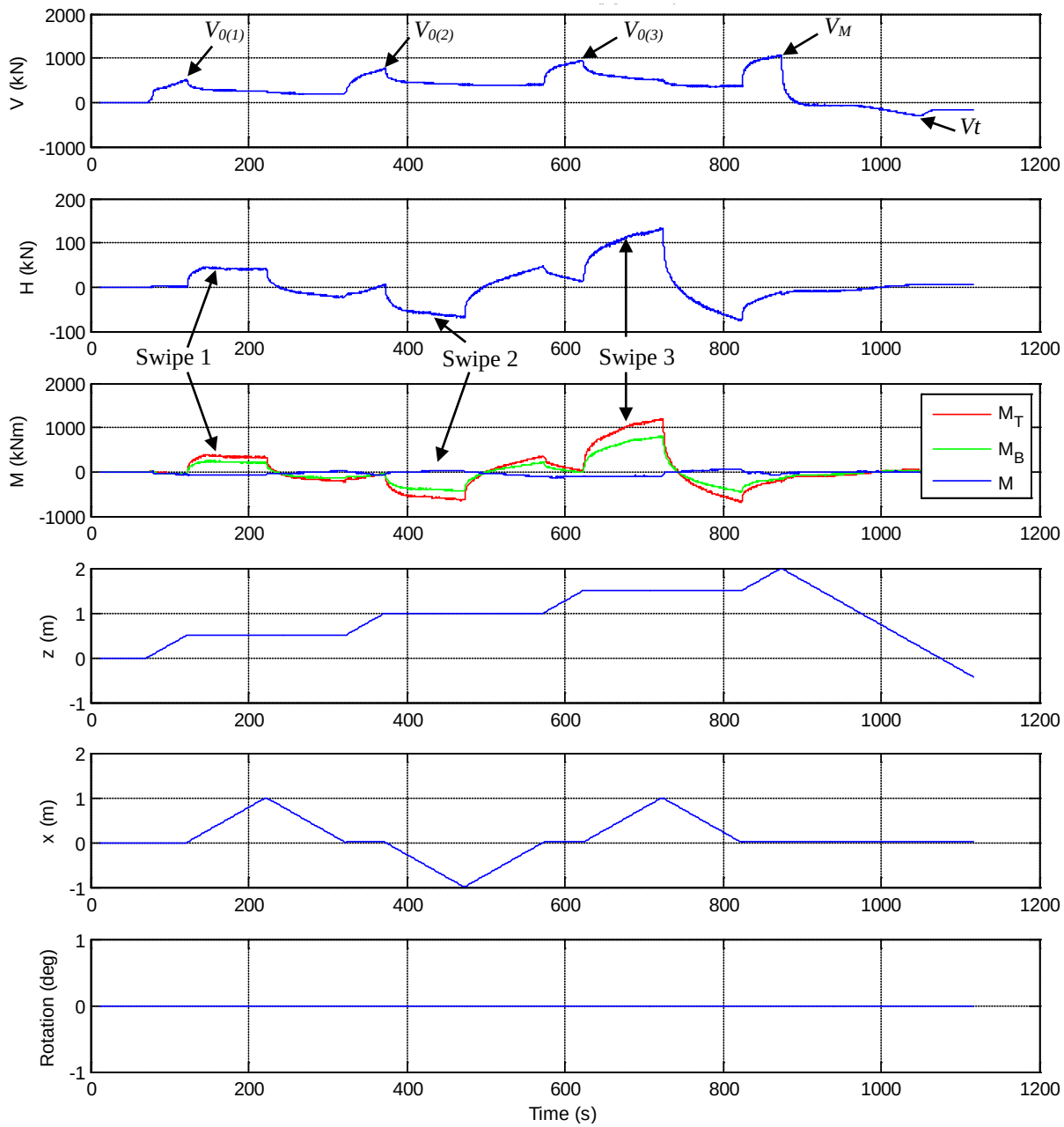

Figure 5.26: Fixed arms test results for T101: *R* = 0, flat base

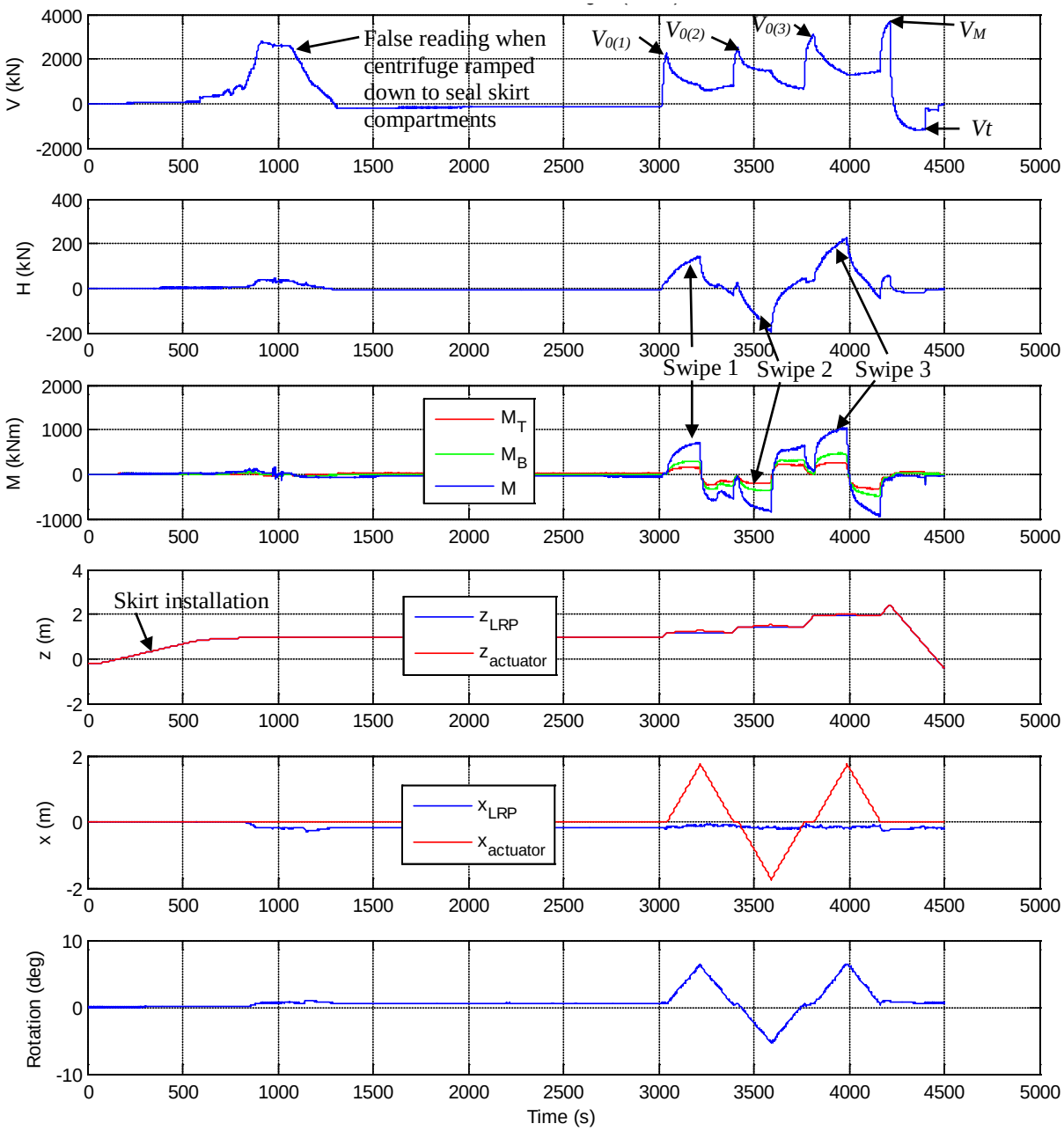

Figure 5.27: Fixed arms test results for T201: R = 0, skirted

5.5.1.1 Flat base foundations

The swipe tests for flat base foundations were undertaken at target embedment depths of z/B = 0.05, 0.1 & 0.2. The results for the unperforated square foundation (R = 0) from the fixed and hinged loading arms are given in Figure 5.28 and Figure 5.29 respectively. The measured loads have been normalised by the maximum vertical load prior to the swipe commencing,

V_0. The figures show results from the two types of swipes tests undertaken (Type 1 & 2) as illustrated previously in Figure 5.10.

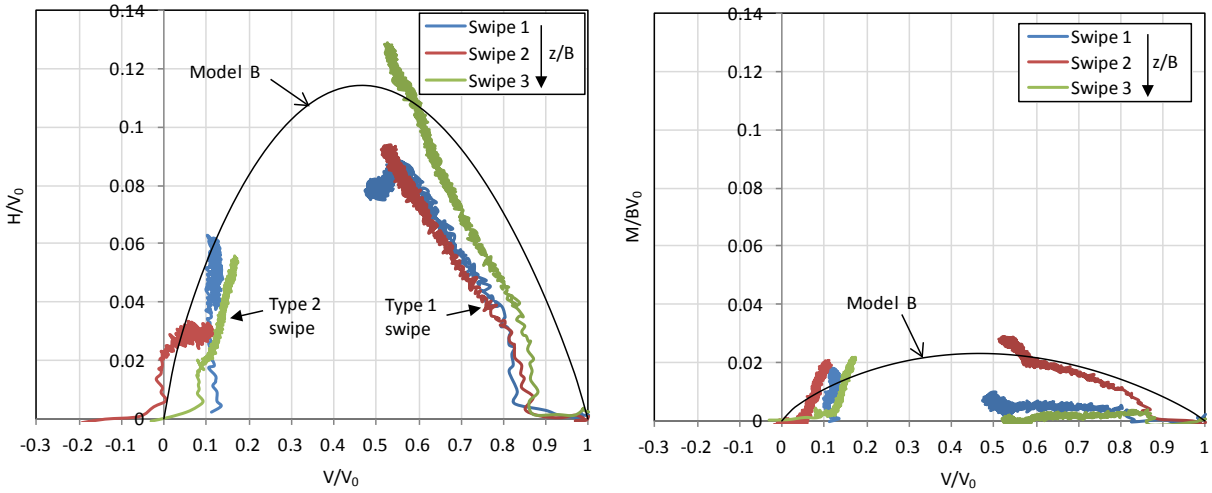

(a) *V*:*H* load space (b) *V*:*M* load space

Figure 5.28: Flat base foundation fixed arm results – $R = 0$

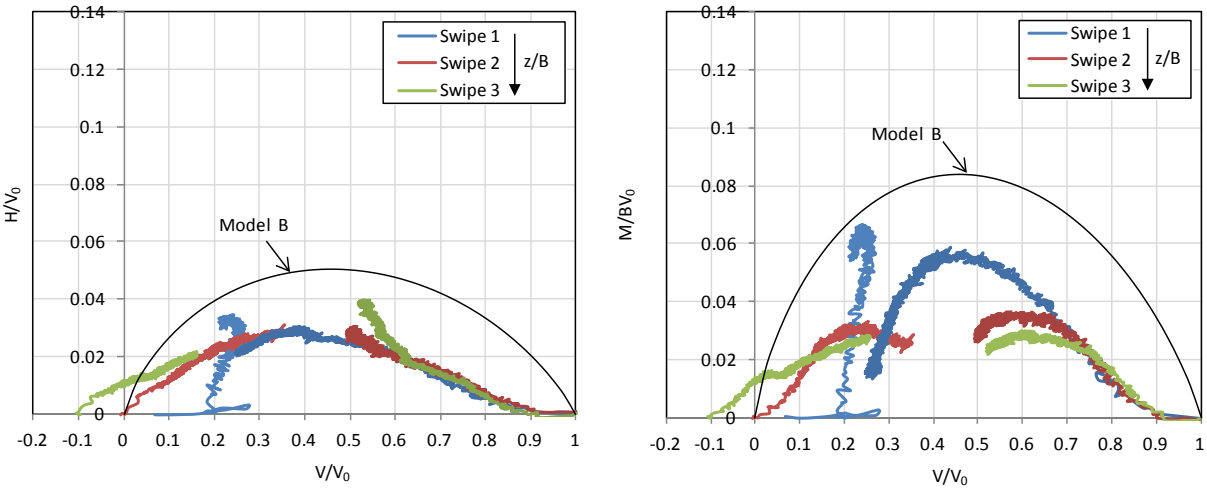

(a) *V*:*H* load space (b) *V* :*M* load space

Figure 5.29: Flat base foundation hinged arm results – $R = 0$

It is seen by the Type 2 swipe test results that minimal tension load was able to be sustained such that the majority of swipes were performed with $V > 0$. Given this, the failure envelope described by Model B for a solid circular foundation (see Equation 2.11) was plotted in the figures for comparison. Comparing the results with a failure envelope describing full tension capacity (such as Equation 2.14) would not be appropriate based on

the results obtained. Model B is seen to provide a reasonable approximation of the fixed arm results in Figure 5.28. The swipe results in Figure 5.29 for the hinged arm are significantly lower than those predicted by Model B. This is not expected, particularly as a square foundation is anticipated to have a higher moment capacity than a circular one (Figure 2.19). The low moment capacity may be due to the foundation swipe rotation not being completely about the load reference point.

The results for the fixed arm in H:V load space and the hinged arm in M:V load space are divided by As_{u0} and plotted as a dimensionless load in Figure 5.30. Results for the case of a square surface foundation using DNV (1992) (given by Equation 2.6) are also included. The experimental horizontal load results compare well with DNV (1992). A load close to the ultimate horizontal load is reached for the case where no passive resistance is assumed. The moment load results do not compare well, lying significantly lower than the DNV (1992) prediction.

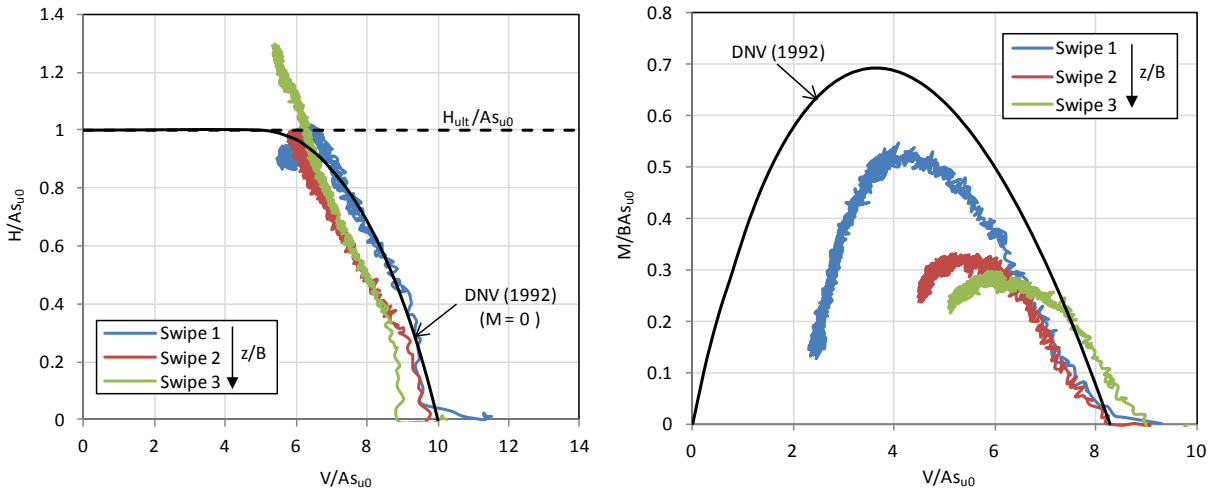

(a) Fixed arm – V:H (b) Hinged arm – V:M

Figure 5.30: Results normalised by As_{u0}, R = 0

The results for the square annular surface foundation with R = 0.36 from the fixed and hinged loading arms are given in Figure 5.30 and Figure 5.31 respectively. The Model B failure envelopes for a circular foundation are also included. A higher maximum H/V_0 and

M/BV_0 is achieved compared to the results of the unperforated square foundation (R = 0). The envelope traced out by the fixed arm swipes is larger than the Model B envelope. For the hinged arm the envelope is now of a similar size to the Model B envelope, although this was derived for a solid foundation with R = 0. As with the tests results for R = 0, minimal tension could be sustained with a maximum tension load of about V/V_0 = -0.1 being achieved.

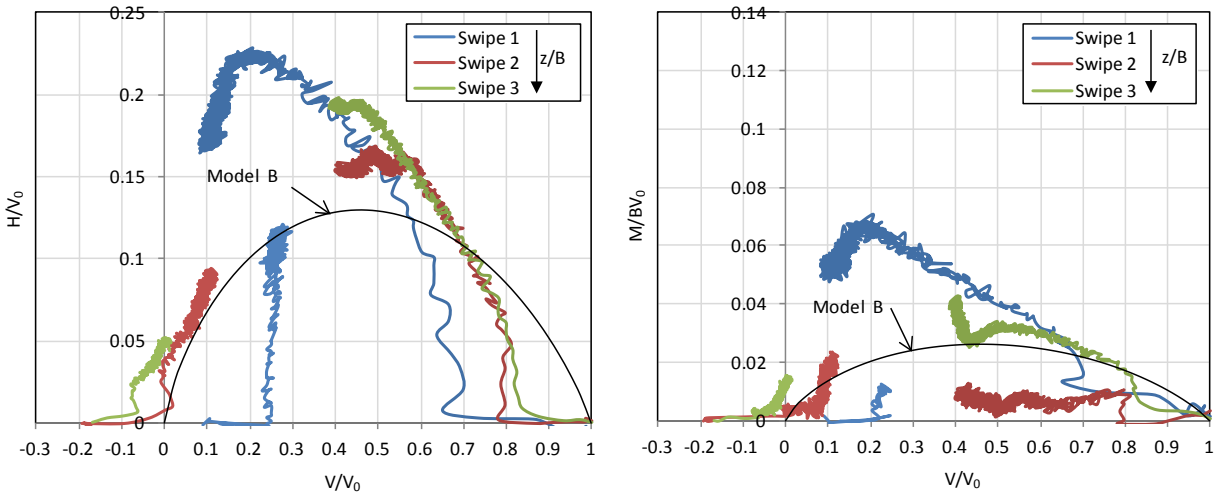

(a) *V*:*H* load space (b) *V*:*M* load space

Figure 5.31: Flat base foundation fixed arm results – R = 0.36

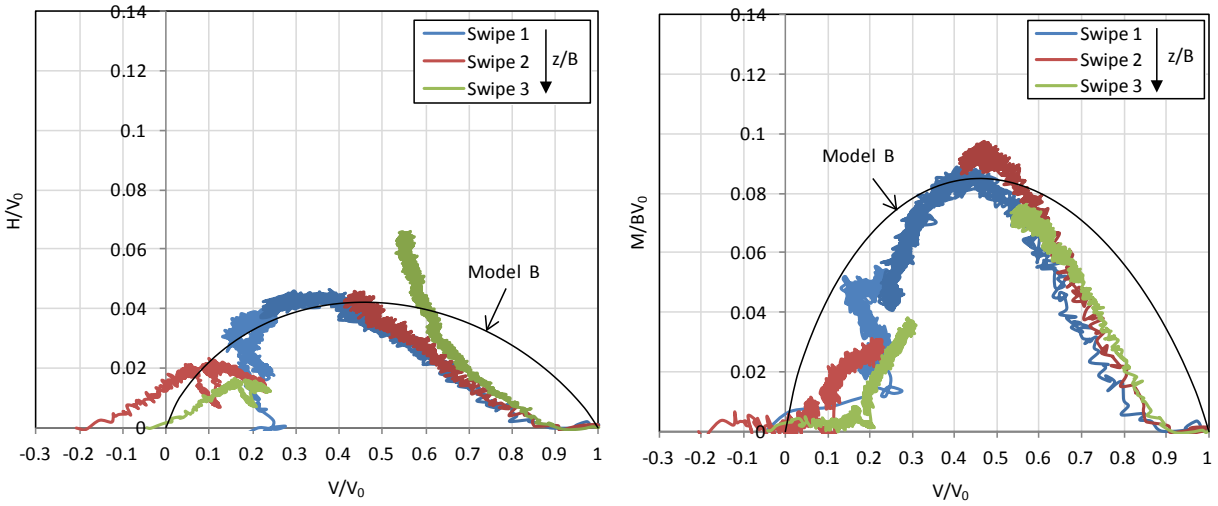

(a) *V*:*H* load space (b) *V*:*M* load space

Figure 5.32: Flat base foundation hinged arm results – R = 0.36

The results for R = 0.36 plotted as a dimensionless load are presented in Figure 5.33. The experimental horizontal load results are much higher compared to the DNV (1992) results for the case of a solid square in *V*:*H* load space. This suggests that the horizontal failure mechanism covers the whole base of the annular foundations rather than being localised around the strip width *B**. In this case it would be more appropriate to use the gross square foundation area rather than the contact foundation area to determine the horizontal sliding capacity. The moment load results in *V*:*H* load space show a higher normalised moment capacity compared to *R* = 0 (Figure 5.30). The results are now comparable to DNV (1992), although this calculation is for an unperforated square foundation.

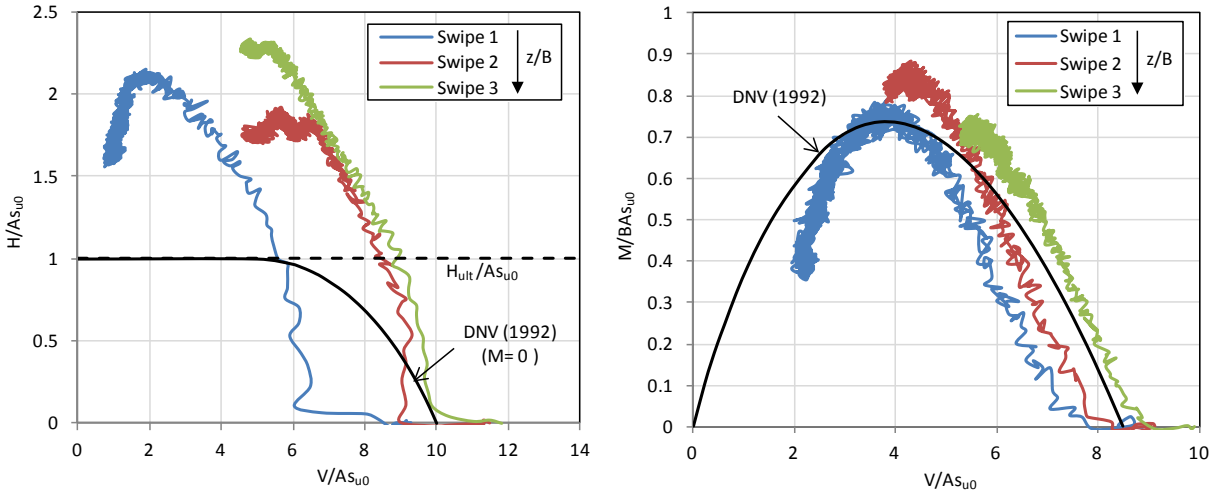

(a) Fixed arm – *V*:*H* (b) Hinged arm – *V*:*M*

Figure 5.33: Results normalised by As_{u0}, *R* = 0.36

The results for all of the foundations (*R* = 0, 0.16, 0.36 and 0.64) in *H*:*M* load space are shown in Figure 5.34. They are compared with the results from Model B at V/V_0 = 0.6. The load position at V/V_0 = 0.6 is marked on each swipe. The trend seen of the maximum H/V_0 increasing with perforation ratio *R* is evident in this figure. The maximum M/BV_0 is also seen to increase, except for *R* = 0.64 in which a decrease occurs.

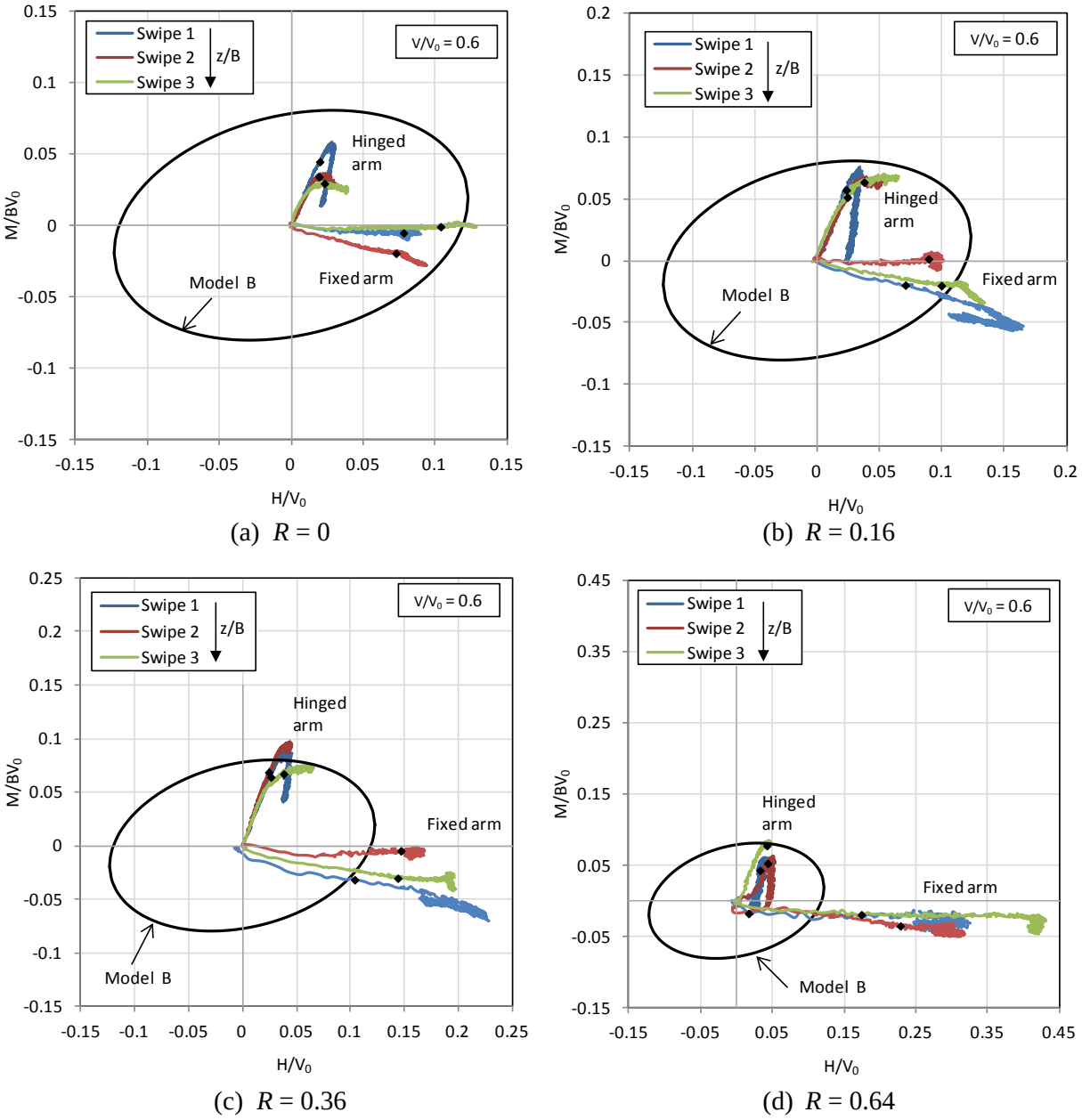

(a) $R = 0$ (b) $R = 0.16$

(c) $R = 0.36$ (d) $R = 0.64$

Figure 5.34: Flat base square annular results – *H*:*M* load space

5.5.1.2 Skirted foundations

The swipe tests for skirted foundations were undertaken at target embedment depths of z/B = 0.25, 0.3 & 0.4. The swipe test results for the skirted annular foundation with R = 0.36 from the fixed and hinged loading arms are given in Figure 5.35 and Figure 5.36 respectively. The swipes in both the *V*:*H* and *V*:*M* load spaces are larger than the size of the Model B envelopes. More tension can be sustained compared with the flat base foundation, with a value up to V/V_0 = -0.3 being achieved.

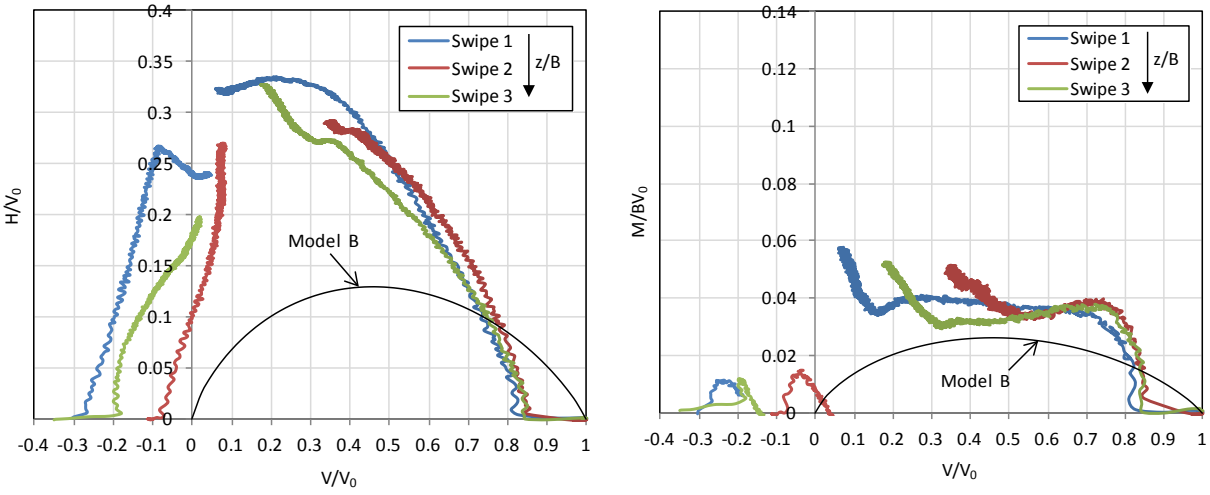

(a) *V*:*H* load space (b) *V*:*M* load space

Figure 5.35: Skirted foundation fixed arm results – R = 0.36

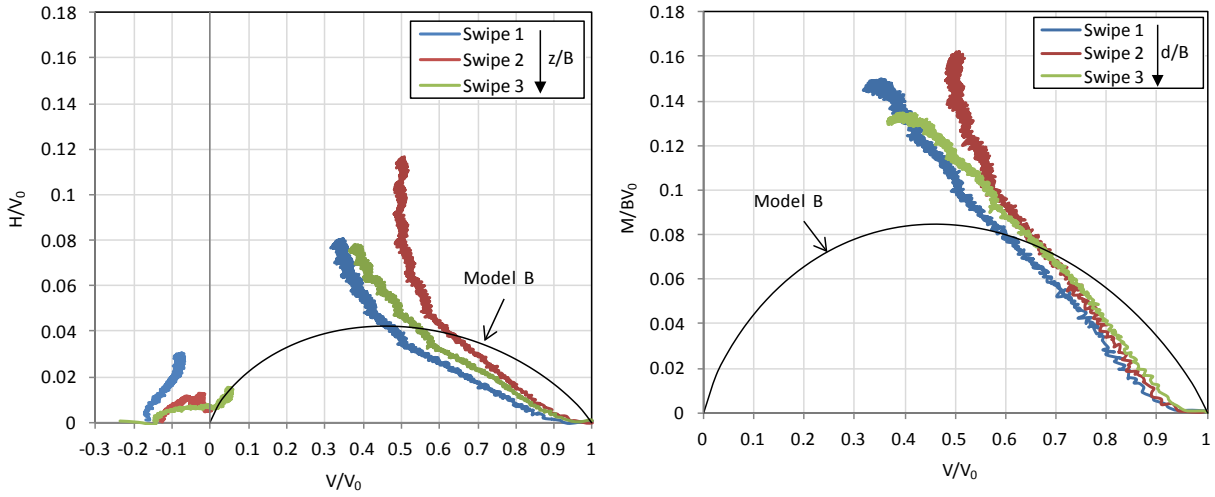

(a) *V*:*H* load space (b) *V*:*M* load space

Figure 5.36: Skirted foundation hinges arm results – R = 0.36

The results for each annular foundation with R = 0, 0.16 and 0.36 in *H*:*M* load space are given in Figure 5.37. They are compared with the results from Model B at V/V_0 = 0.6. The load position at V/V_0 = 0.6 is marked on each swipe. Fixed arm tests were not undertaken for R = 0 or 0.16. The solid square results (R = 0) lie within the Model B failure envelope. It would be expected that the experimental results should be closer to or greater than the Model B results. The trend seen of the maximum H/V_0 increasing with perforation ratio R is evident in this figure. The maximum M/BV_0 is also seen to increase. A skirted foundation was not tested for the case of R = 0.64.

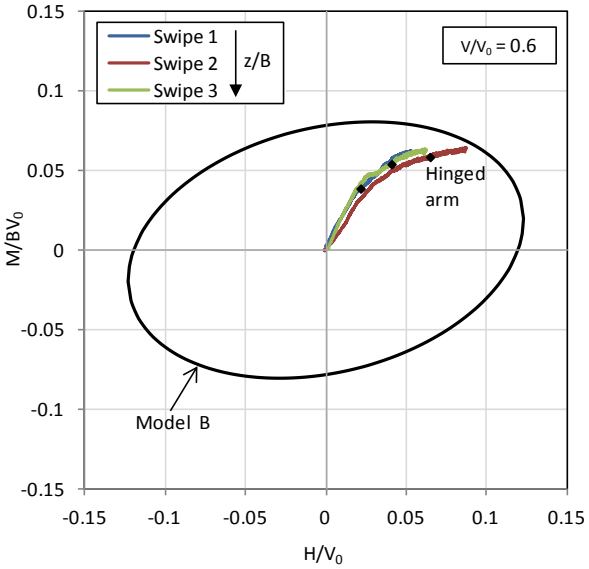

(a) $R = 0$

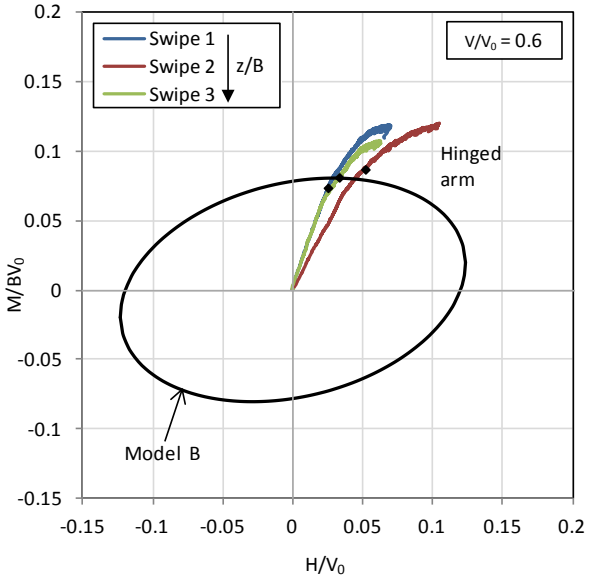

(b) $R = 0.16$

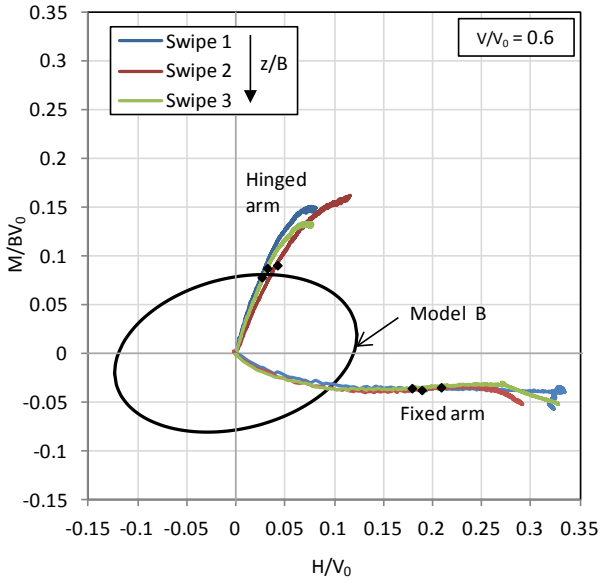

(c) $R = 0.36$

Figure 5.37: Skirted square annular foundation results – *H*:*M* load space

5.5.2 Pushover tests

Pushover tests (as described in Section 5.3.3) were undertaken on flat base and skirted foundations using the hinged loading arm. An example of the results for a skirted foundation pushover test (T210) is shown in Figure 5.38. The foundation is installed and the test paused whilst the base plate venting hole is plugged to seal the compartments. Under load control the foundation is loaded until $V/V_0 = 0.3$ is reached. The vertical load is maintained at this level while the actuator is moved horizontal to apply a pushover load to the foundation.

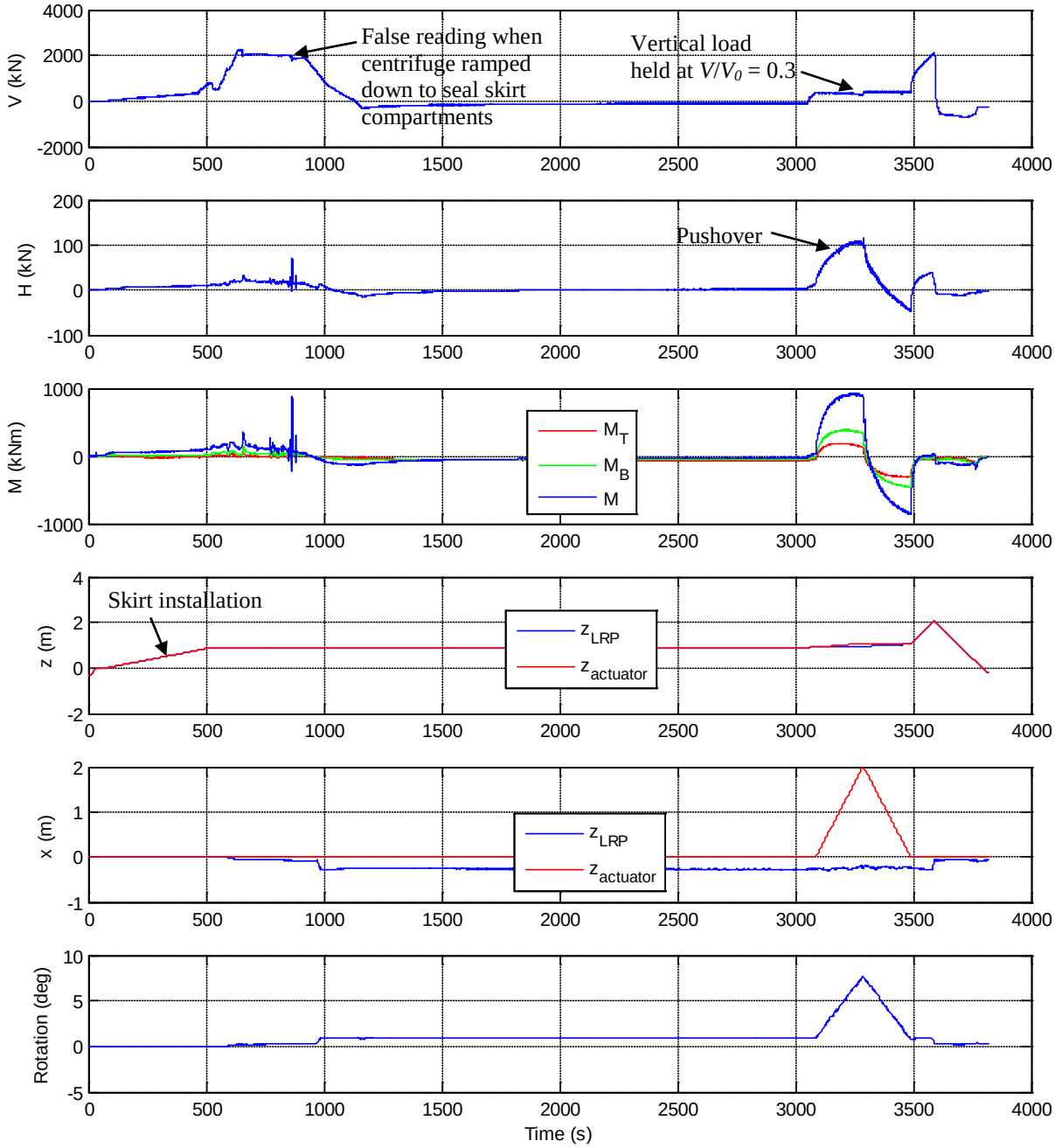

Figure 5.38: Pushover test results for T210: R = 0.36, skirted

The results are shown in more detail from the start of the pushover test in Figure 5.39. As the hinge arm is translated horizontally an increasing horizontal load and corresponding moment is applied to the foundation. At a rotation of about 5 degrees the maximum horizontal and moment loads are reached and the foundation is unable to sustain any further load. At this point the load control program is not able to maintain the vertical load at V/V_0 = 0.3 and the vertical load drops off.

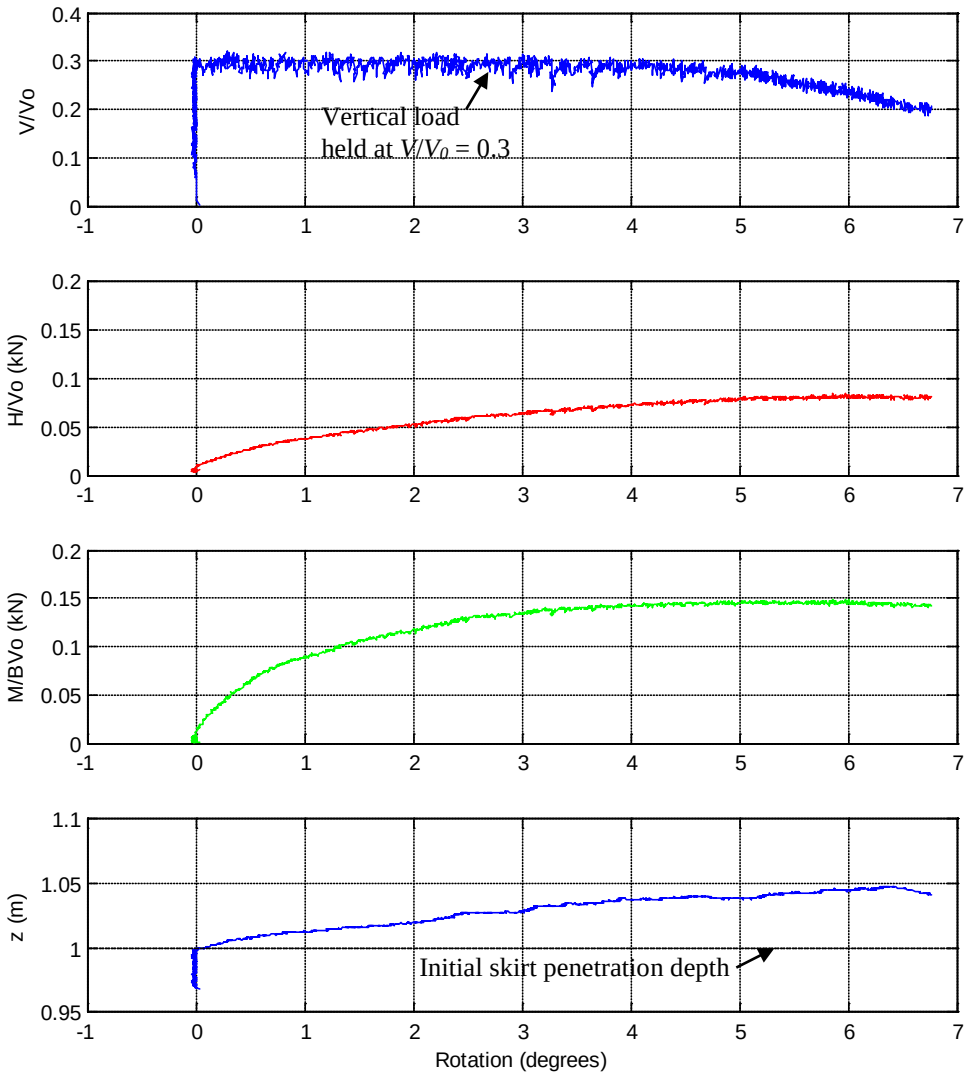

Figure 5.39: Pushover test for T210: R = 0.36, skirted

The pushover results for skirted foundations of R = 0, 0.16 and 0.36 in H:M load space are summarised in Figure 5.40. As the perforation ratio increases the foundations are able to support larger horizontal and moment load relative to their vertical capacity V_0. The corresponding point from the failure envelope as defined in the corresponding swipe test (for Swipe 1) is also plotted in this Figure. It is seen that pushover and swipe tests reach good agreement at the point of failure. This matches agreement observed numerically between swipe and probe tests as was shown in Figure 2.3, and as has been found in other numerical studies (Bransby and Randolph, 1998, Gourvenec and Randolph, 2003).

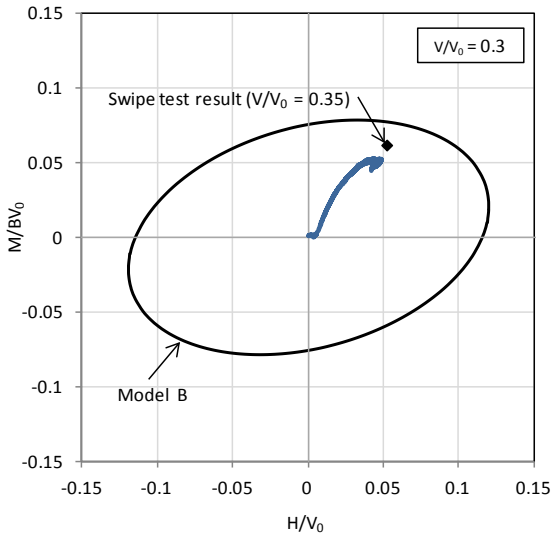

(a) $R = 0$

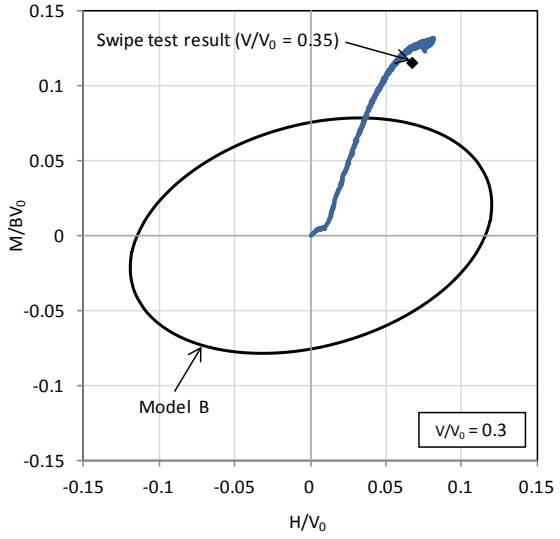

(b) $R = 0.16$

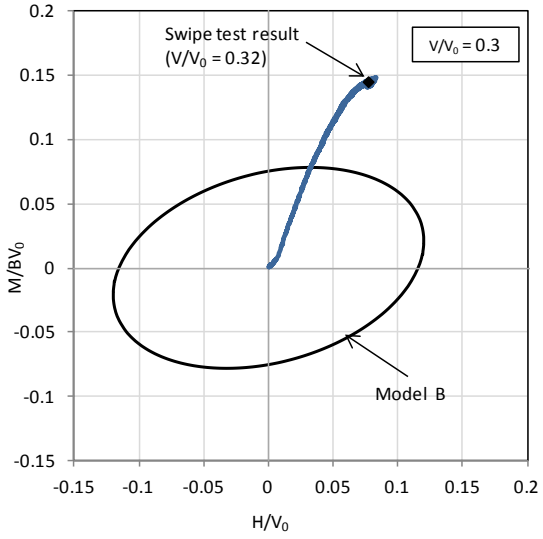

(c) $R = 0.36$

Figure 5.40: Skirted square annular foundation pushover results – *H*:*M* load space

5.5.3 Impact of perforation ratio

5.5.3.1 Maximum horizontal load capacity

The horizontal load results from the fixed arm tests for the flat base foundations are given in Figure 5.41. These show swipe tests results for the R = 0, 0.16, 0.36 and 0.64 foundations. As was observed previously, when the horizontal load is normalised by the maximum vertical load the normalised horizontal load increases with increasing R. The parameter h_0 can be used define the peak horizontal capacity in terms of the ratio of maximum horizontal load H_0

to maximum vertical load V_0 such that $h_0 = H_0/V_0$ (see Equation 2.11). The value of h_0 for each test is marked in Figure 5.41(b).

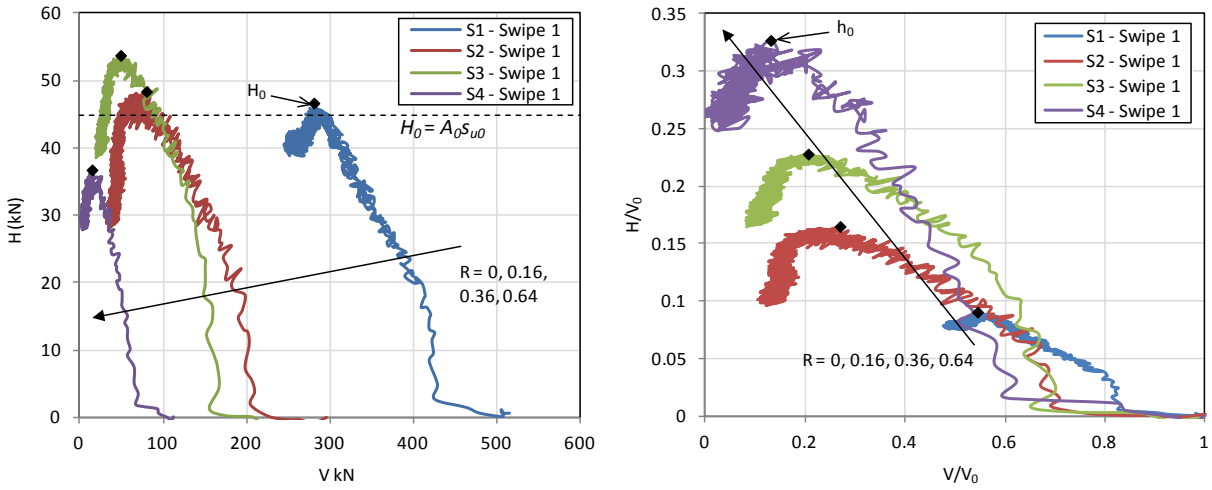

(a) Measured load (b) Normalised load

Figure 5.41: Comparisons of horizontal capacity for flat base foundations

Figure 5.41(a) shows that similar maximum horizontal load H_0 was achieved across the foundations of different perforation ratios. The values are close to $H_0 = A_0 s_{u0}$, where A_0 is the gross area of the foundation (as defined in Figure 1.2). This is the theoretical capacity due to sliding resistance across the gross base area. The additional load above the pure sliding resistance may be due to passive pressure resistance from the foundation embedment. If it is assumed that each foundation can achieve $H_0 = A_0 s_{u0}$ then it can be shown that:

$$h_0 = \frac{h_{0,R=0} s_c}{(1-R) r_c} \tag{5.10}$$

in which $h_{0,R=0}$ is the peak horizontal capacity for a solid foundation.

The variation of h_0 with R given by the flat base and skirted foundation experimental results are shown in Figure 5.42. Note that in each case h_o represents the average value from all three swipes in each test. Not all h_o values were for the situation where $M = 0$ and so may slightly under represent the pure peak horizontal capacity. The results show the increase in peak horizontal capacity as R increases. The values for the skirted foundation have a higher peak horizontal capacity than the flat base foundations. As fixed arm tests were not

undertaken on skirt foundations for R = 0 and 0.16, the values shown have been estimated from their respective hinged arm tests based on the average of $h_{0,fixed}/h_{0,hinged}$ found from the other tests.

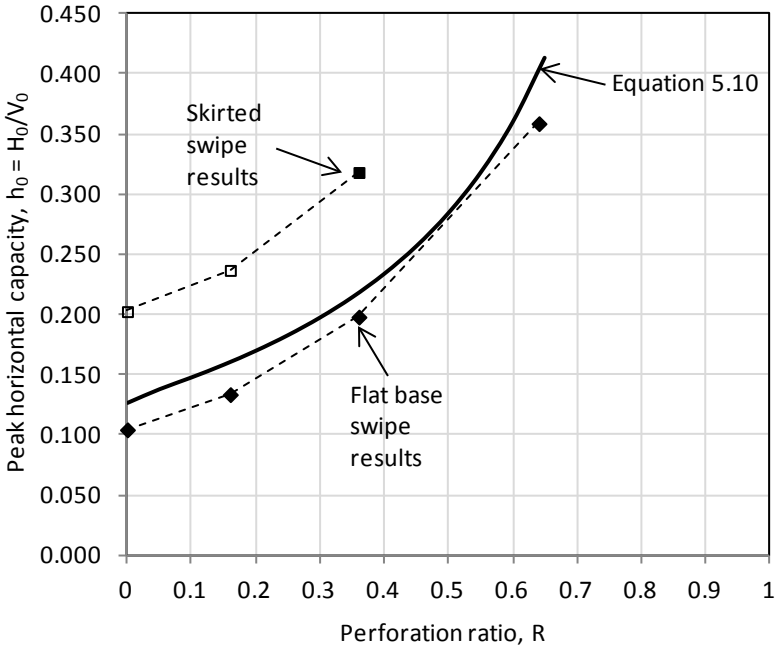

Figure 5.42: Variation in peak horizontal capacity, h_0

Equation 5.10 is plotted in Figure 5.42 in which $h_{0,R=0}$ = 0.127 has been adopted from Model B. A trend similar to the experimental results is seen. This relationship is not expected to be appropriate past R = 0.64, as even at this value the assumption that $H_0 = A_0 s_{u0}$ has not quite been met as shown in Figure 5.41(a).

5.5.3.2 Maximum moment load capacity

The moment load results from the hinged arm tests for the flat base foundations are given in Figure 5.43 for the flat base foundations and Figure 5.44 for the skirted foundations. They show results for the R = 0, 0.16, 0.36 foundations, as well as the R = 0.64 flat base foundation. As was observed previously, when the moment load is normalised by the maximum vertical load the normalised moment load increases with increasing R, except at R = 0.64 where it reduces.

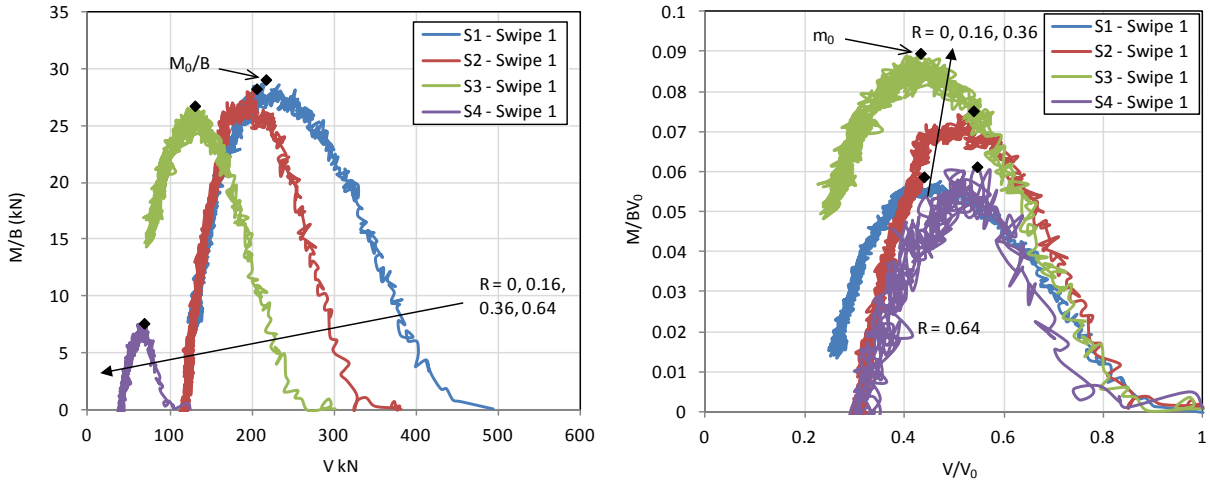

(a) Measured load (b) Normalised load

Figure 5.43: Comparison of moment capacity for flat base foundations

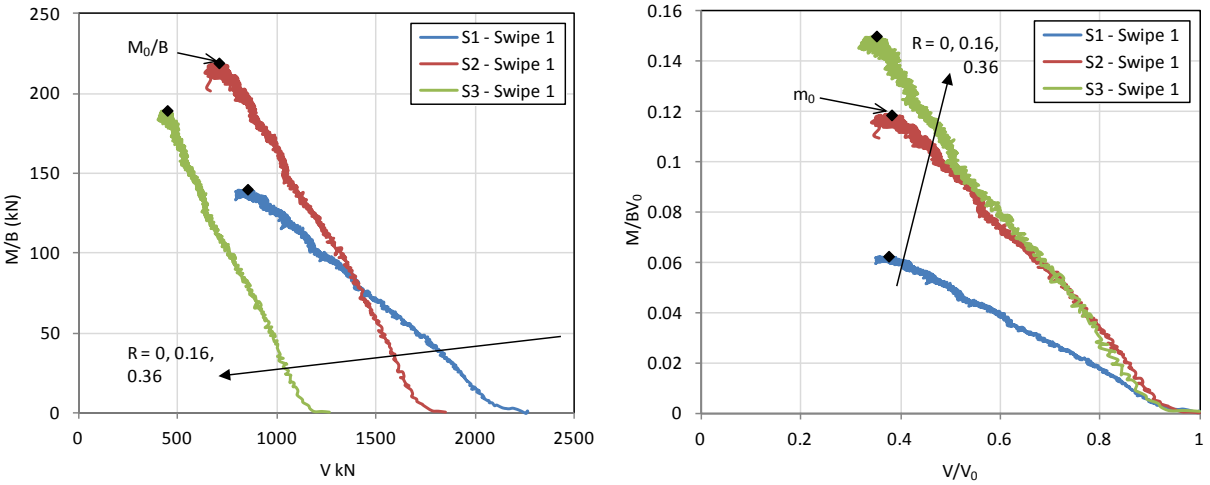

(a) Measured load (b) Normalised load

Figure 5.44: Comparison of moment capacity for skirted foundations

The parameter m_0 can be used define the peak moment capacity in terms of the ratio of maximum moment load M_0 to maximum vertical load V_0 such that $m_0 = M_0/BV_0$. The variation of m_0 with R is shown in Figure 5.45 for the flat base and skirted foundations. In each case m_o represents the average values from all three swipes in each test. It is noted that not all values were for the situation where $H = 0$ and so may slightly under represent the pure peak moment capacity. The results show the increase in peak moment capacity as R increases, except at $R = 0.64$ where it reduces. The value for the skirted foundation shows a

higher capacity than the flat base foundations. The results for the push-over tests are also plotted and are seen to provide a good match with the swipe m_0 results, especially for the skirted foundations.

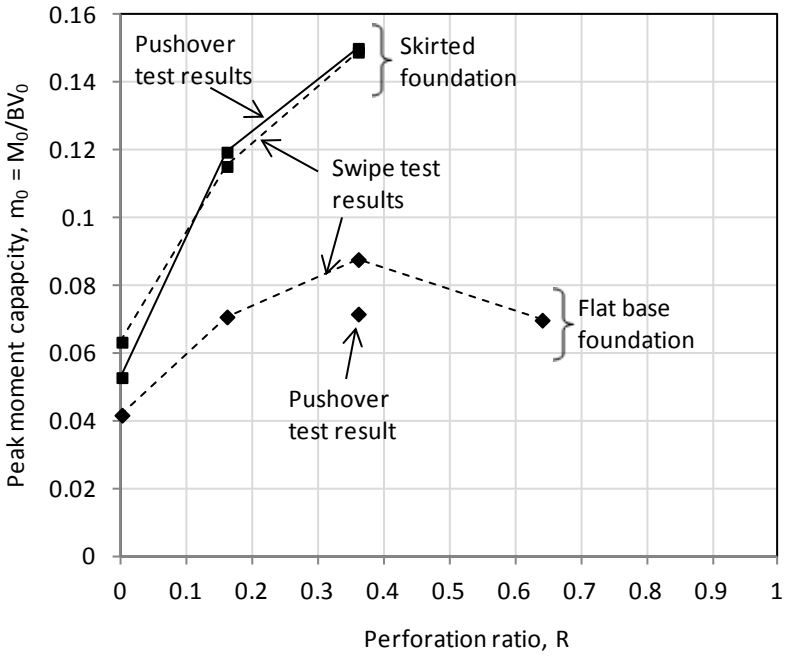

Figure 5.45: Variation in peak moment capacity, m_0

The value for the skirted R = 0 foundation may have been greater if it had of included internal skirts, as was the case with R = 0.16 and R = 0.36 (see Table 5.5). The value of m_0 is close to the case of a flat base foundation at lower embedment. The aspect ratio of the R = 0 skirted compartment was d/B = 0.2, being significantly lower than the other two skirted foundations. At d/B = 0.2 the failure mechanism may form inside the compartment as shown in Figure 2.22, reducing capacity compared to the case if internal skirts were included.

5.5.4 Impact of foundation shape

Tests were conducted on ring foundations with R = 0.36 in addition to square annular foundations of the same perforation ratio. The results for these two foundation types with skirts are compared in Figure 5.46 and Figure 5.47 for swipe and pushover tests respectively.

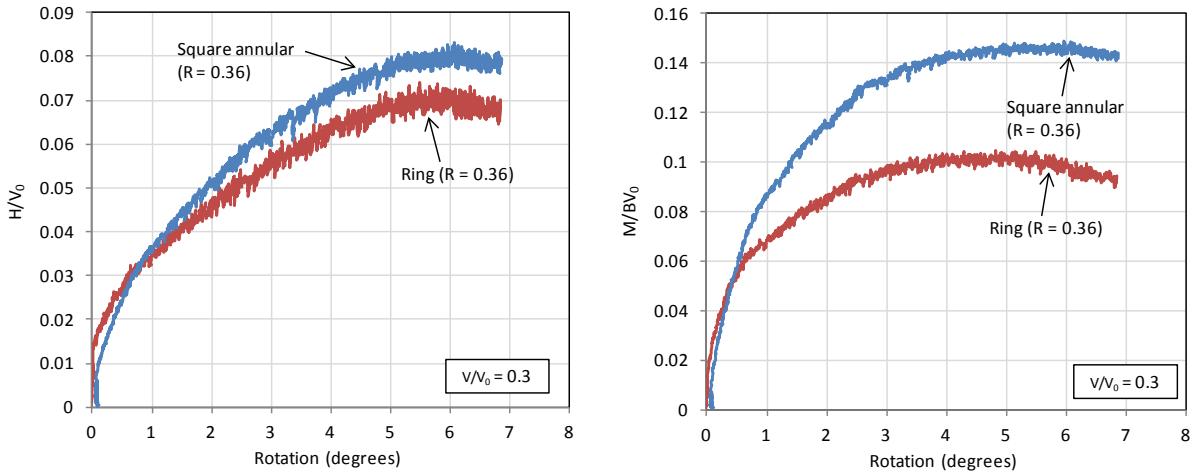

(a) *H*:*V* load space (b) *V*:*M* load space

Figure 5.46: Comparison between ring and annular foundation, R = 0.36 – pushover test

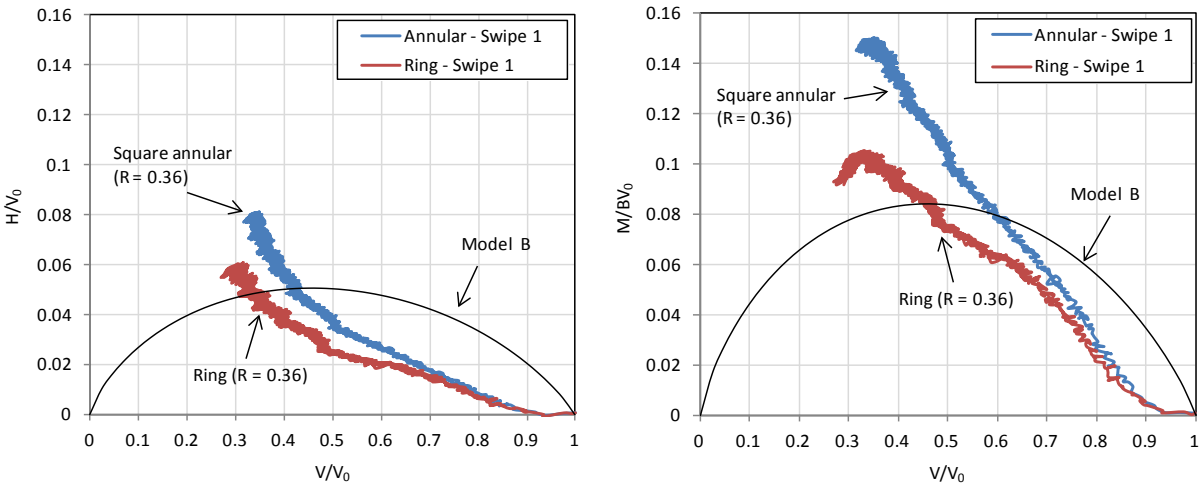

(a) *H*:*V* load space (b) *V*:*M* load space

Figure 5.47: Comparison between ring and annular foundation, R = 0.36 – swipe test

Good agreement is achieved between the swipe and pushover test failure loads as the load at V/V_0 = 0.3 (or closest point to this) are very close to the maximum pushover test loads. It is seen that the square annular foundation has greater combined loading capacity compared with the ring foundation. This is consistent with the finite element results of Gourvenec (2007b) which showed the combined load capacity of a square foundation (of R = 0) to be larger than that of a circular foundation (see Figure 2.19(a)).

5.5.5 Impact of load direction

Two different loading directions were tested as shown in Figure 5.9. The majority of tests were loaded at 0° heading, but a selection were modelled at 45° heading. A comparison between 0° and 45° pushover loading results using the hinged arm has been undertaken. Figure 5.48 compares the results for a square skirted foundation with no perforation (R = 0) while Figure 5.49 compares the results for a square annular skirted foundation with R = 0.36.

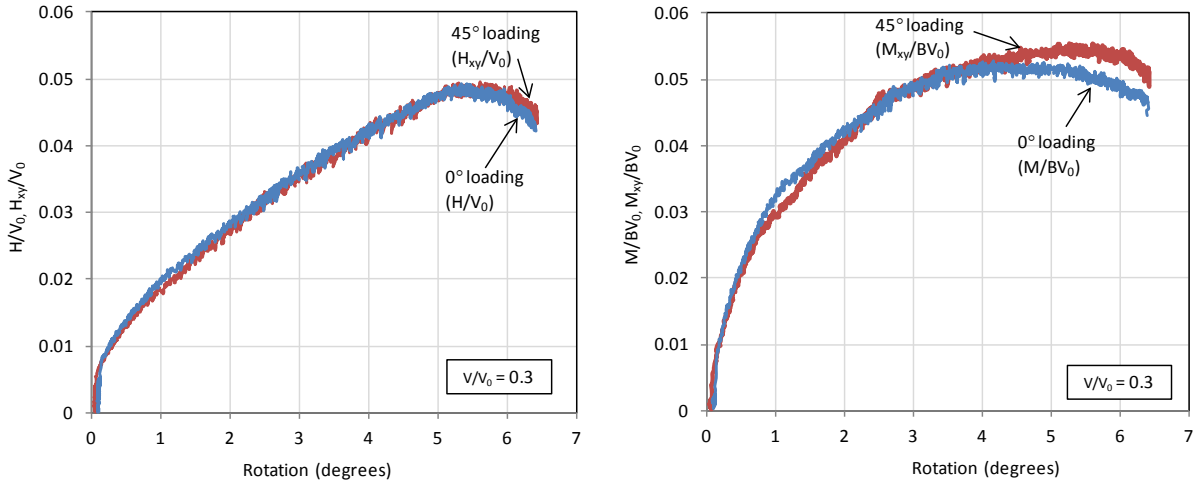

(a) Horizontal load (b) Moment load

Figure 5.48: Comparison of loading direction for a unperforated skirted foundation, R = 0

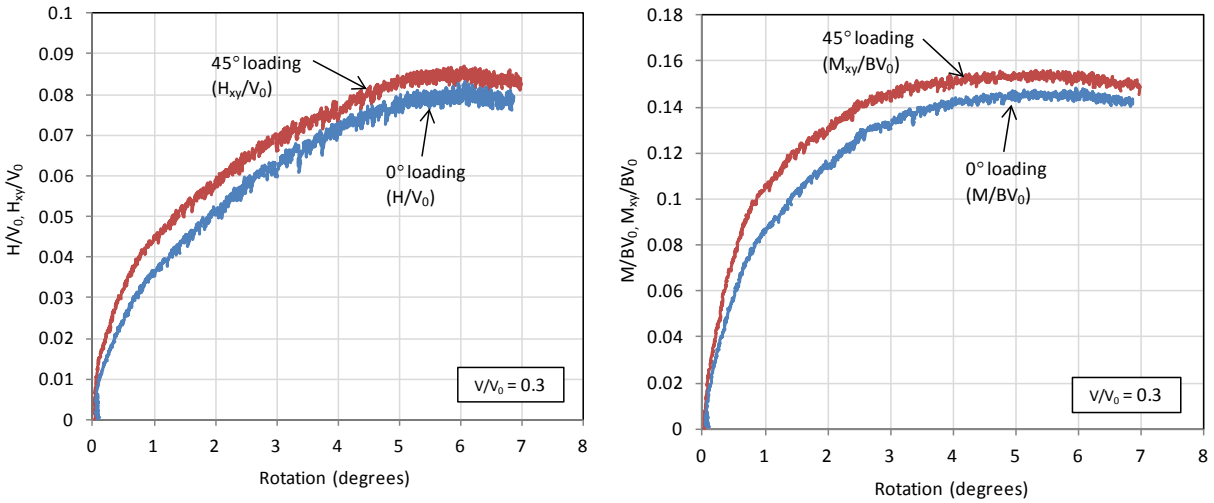

(a) Horizontal load (b) Moment load

Figure 5.49: Comparison of loading direction for a perforated skirted foundation, R = 0.36

The results show that a similar maximum magnitude of load was withstood by both the 0° and 45° loading directions. Slightly higher capacity was achieved for 45° loading, particularly for the perforated foundation, but overall the difference was minor. This may

have been due to the point of rotation being a similar distance from the neutral axis in each case. This indicates that for an estimation of bearing capacity, 3D loading conditions could be simplified into a 2D loading scenario and assessed using more straightforward plane strain calculations. The maximum horizontal load capacity $H_{0(2D)}$ or maximum moment load capacity $M_{0(2D)}$ determined under 2D loading conditions (Figure 5.9(a)) could be applied to a 3D loading scenario (Figure 5.9(b)), such that

$$H_{0(3D)} \approx H_{0(2D)}, \text{where } H_{0(3D)} = \sqrt{H_x^2 + H_y^2}$$
$$\text{or} \tag{5.11}$$
$$M_{0(3D)} \approx M_{0(2D)}, \text{where } M_{0(3D)} = \sqrt{M_x^2 + M_y^2}$$

5.5.6 Impact of cyclic loading

A cyclic loading test was undertaken on the skirted foundation with R = 0.36 and compared to the monotonic loading test results. Two-way cycling was applied via the hinged loading arm using displacement control, as load controlled cyclic loading could not be applied with the load control program used. For the duration of the test vertical load was held constant at V/V_0 = 0.3. The cyclic amplitude was chosen to apply a moment of approximately 60% of the ultimate monotonic moment capacity from the monotonic pushover test (as shown in Figure 5.39). This could be considered a reasonable design load case after application of applicable load and material factors (DNV, 2011). Cyclic testing was undertaken for N = 85 cycles. At the level of applied cyclic load this could conservatively represent the equivalent number of cycles for a 3 hour design storm, in which wave loading is assumed to progressively build over 1000 cycles (Hansteen, 1981). Waves generally occur with a period of around 10 - 15 seconds. Given the scaling laws associated with centrifuge testing, cycling was unable to be undertaken at this prototype frequency. This meant the pore pressure generation and dissipation may not have been representative of field conditions. After cycling the foundation was pushed monotonically to failure. The test results are shown in Figure 5.50.

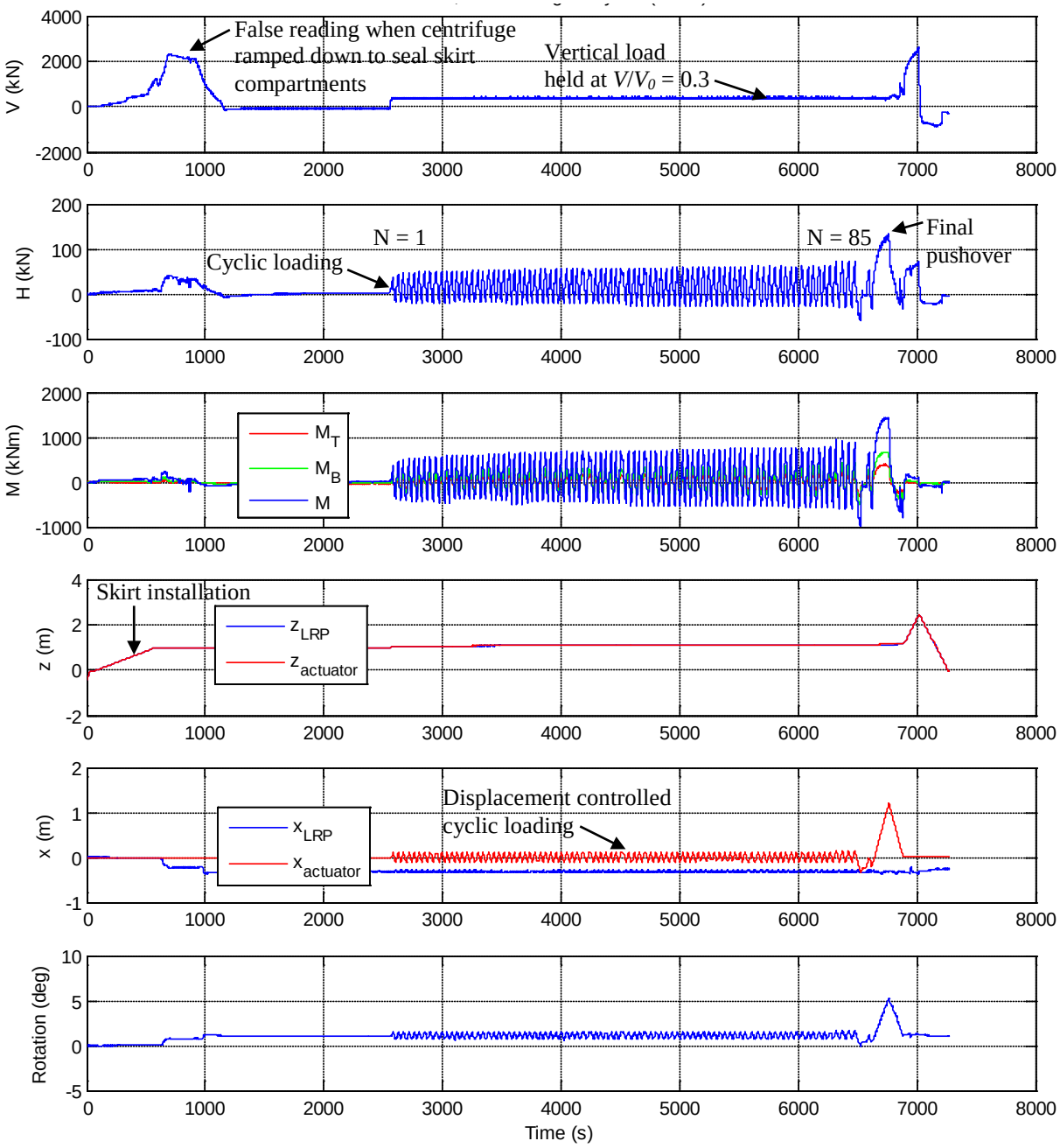

Figure 5.50: Cyclic loading test results for T212: R = 0.36, skirted

The results of the cyclic test are compared with monotonic loading results (both with R = 0.36) in Figure 5.51. The results have been shifted so that they both start from 0 degrees rotation to enable easier comparison. The two-way cycling is evident with rotations occurring at approximately ± 0.4 degrees for duration of approximately 80 cycles. Following this is a package of 5 cycles of increasingly larger amplitude is applied to reach the moment failure load found for the pure monotonic load test. After cycling the foundation was then loaded

monotonically until final failure. It is seen that the ultimate load reached by the post-cyclic monotonic test is significantly larger than the pure monotonic test (see also Figure 5.65). This may be as a result of consolidation taking place over the longer duration of the cyclic test compared with the monotonic test. It is notable that the final vertical settlement after the cyclic test is over twice that of the monotonic test.

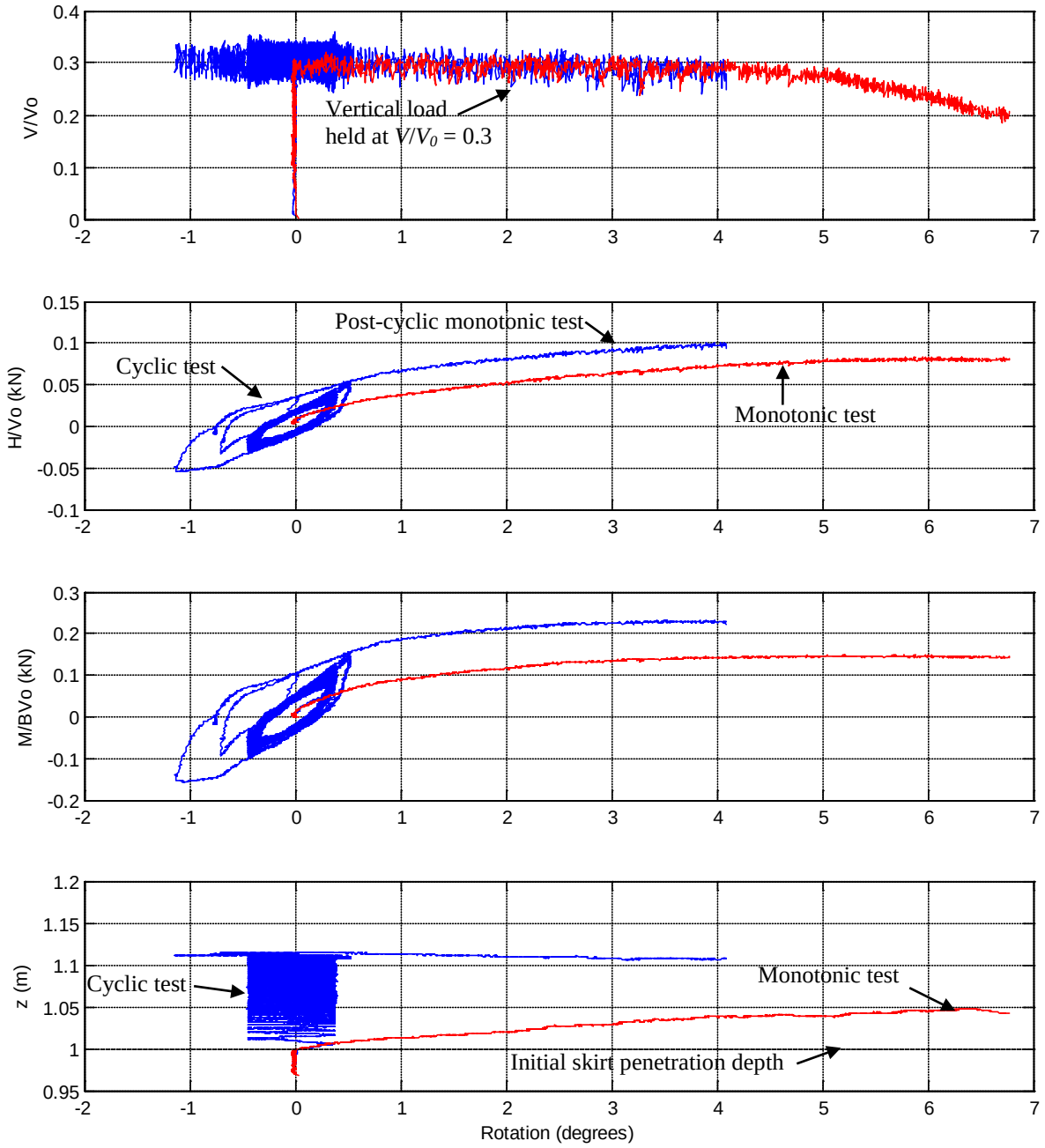

Figure 5.51: Comparison between cyclic and monotonic test results: R = 0.36, skirted

Figure 5.52 shows the progression of maximum and minimum horizontal and moment loading with the number of cycles. Also included is the maximum loads reached at failure from the pure monotonic test. It is seen that the monotonic failure loads are approached during the main package of cycles. With application of the final four larger cycles the maximum monotonic moment load is reached.

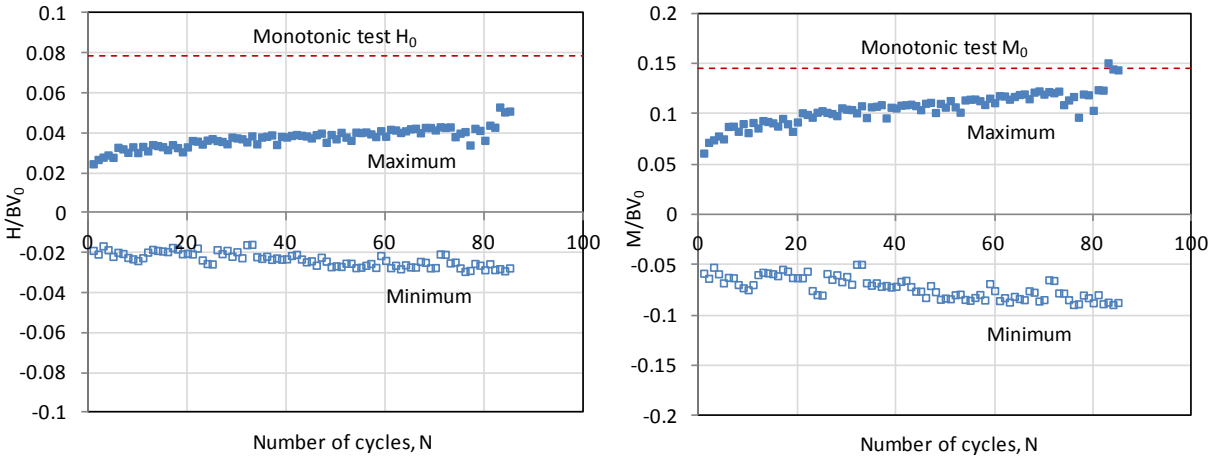

(a) Horizontal load (b) Moment load

Figure 5.52: Foundation loading during cyclic test, R = 0.36

Figure 5.53 shows the vertical displacement of the foundation during cycling. By 15 cycles the foundation displacement has passed the value reached in the purely monotonic test. After 85 cycles the foundation settlement is still increasing. Serviceability implications could arise if longer-term cycling of this magnitude cycling was to occur.

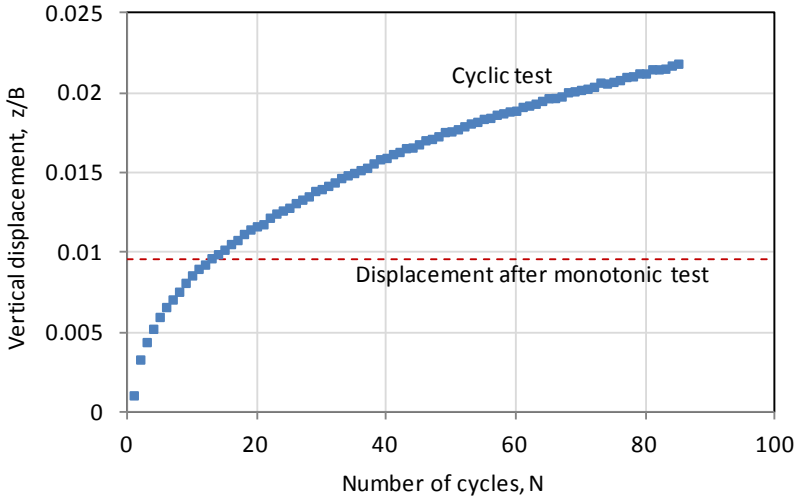

Figure 5.53: Foundation displacement during cyclic test, R = 0.36

5.6 Numerical modelling of combined load capacity

Numerical analysis of square annular foundations under combined loading was undertaken using the FEA method described in Chapter 3. A 3D finite element model was set up in which symmetry was exploited to model half the foundation as shown in Figure 5.54. The outside width, B of the foundation was maintained at 1 m, whilst the effective width B^* was varied to investigate different perforation ratios R. The perforation ratios analysed were R = 0, 0.16, 0.36, and 0.64. The soil was modelled using the Tresca UMAT with a uniform undrained shear strength of s_u = 1 kPa, an undrained Young's modulus E_u/s_u = 1000 and undrained Poisson's ratio of ν = 0.499. A fully rough base was assumed. Loading was applied using prescribed displacement probes. A full tension interface between the soil and foundation was present. The mesh was composed of tetrahedral quadratic hybrid elements with an initial mesh refinement similar to that shown in Figure 5.54. The mesh was subsequently refined using the adaptive meshing scheme. Six iterations were performed for each analysis case.

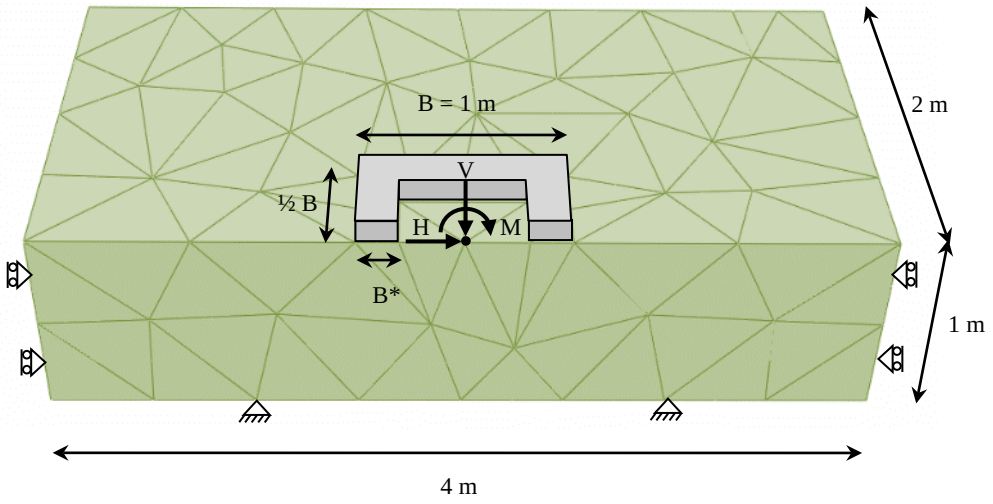

Figure 5.54: Square annular foundation model arrangement (foundation for illustration)

5.6.1 Square foundation

A square unperforated foundation (R = 0) was initially analysed in H:M load space and compared to the previous Abaqus analysis undertaken by Gourvenec (2007b) (see Figure 2.19(a)). The failure envelope was defined using displacements probes (as described previously in 2.1.2). The results are given in Figure 5.55 for the case of V/V_0 = 0.

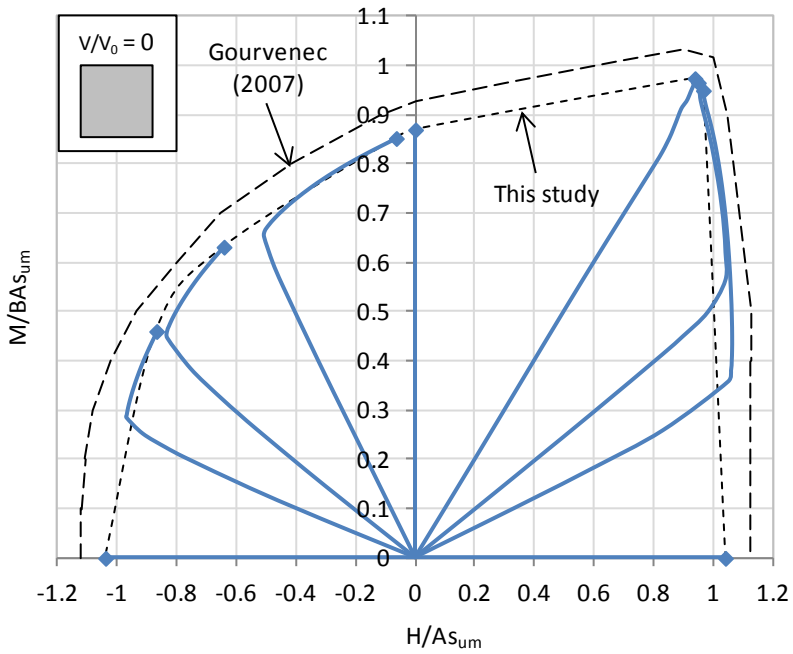

Figure 5.55: Failure envelope for V:H:M loading, square R = 0, V/V_0 = 0

The following observations are made regarding the results:

- The shape of the failure envelope is the same as that found by Gourvenec (2007b) with a positive eccentricity occurring, although the size of the envelope is seen to be smaller.
- At H = 0 a maximum moment value of M_0/BAs_{um} = 0.87 was obtained. This was lower than the value of M_0/BAs_{um} = 0.93 found by Gourvenec (2007b). The equivalent result for a circular foundation is M_0/BAs_{um} = 0.67 (Randolph and Puzrin, 2003), confirming that square foundations have greater moment capacity.
- At M = 0 the failure envelope slightly over-predicts the theoretical horizontal failure load of H_0/As_{u0} = 1. This however is known to occur for pure horizontal loading in finite element analysis where no interface elements are used.

The combined load capacity of a square foundation was also analysed for a vertical load of V/V_0 = 0.3 and the results are given in Figure 5.56. The size of the envelope is reduced from that in Figure 5.55 due to the addition of the vertical load. A comparison is made with Model B (for a circle) which does not allow any tension. Significantly less capacity is evident for the case of no tension.

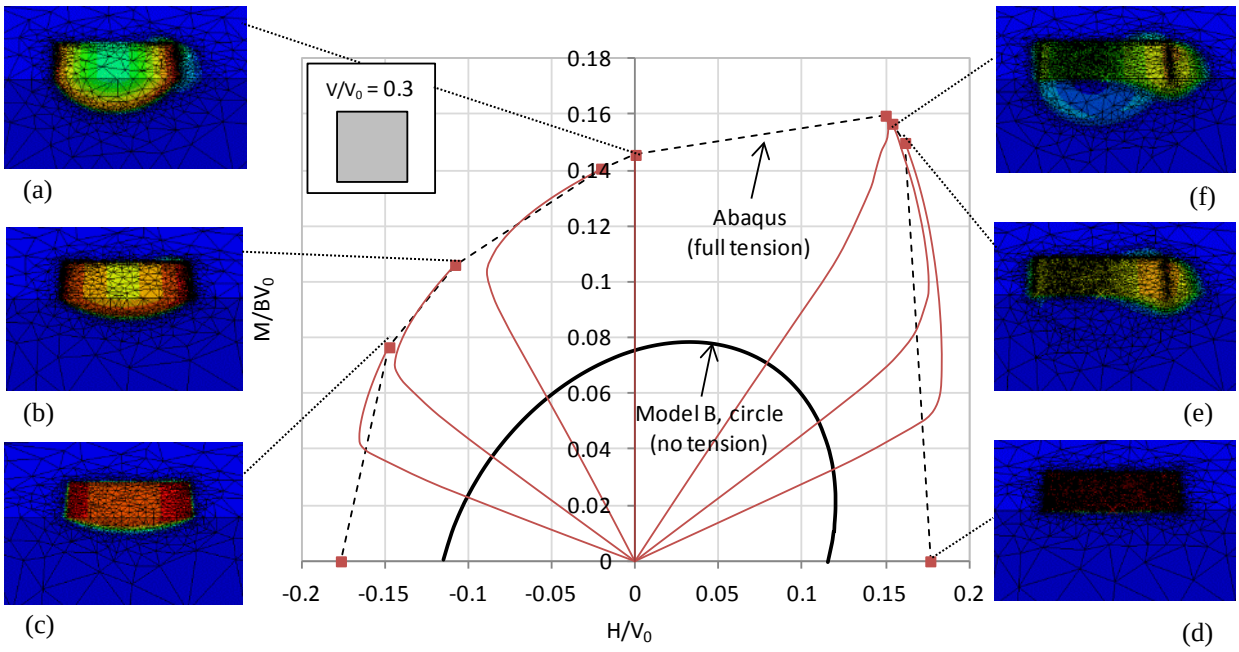

Figure 5.56: Failure envelope for *V*:*H*:*M* loading, square R = 0, V/V_0 = 0.3

The plastic regions and displacement magnitude contours shown in the refined meshes in Figure 5.56 can be used to infer failure mechanisms occurring for different load combinations. At M = 0 a horizontal sliding type mechanism occurs whilst at H = 0 a rotational scoop types mechanism is present. Different mechanisms are seen to occur when moment loading is in the same direction as the horizontal load (as per the sign convention in Figure 5.54) compared to when they are opposite. When they are in the opposite direction the capacity is reduced.

5.6.2 Square annular foundation

Results of the failure envelope for a square annular foundation with R = 0.36 at a vertical load of V/V_0 = 0.3 are given in Figure 5.57. The failure envelope has expanded compared to the

unperforated foundation failure envelope shown in Figure 5.56. The failure mechanisms for the case of R = 0.36 inferred from the mesh plastic regions are also shown in Figure 5.57, and can be compared against those for R = 0 in Figure 5.56. It is seen that the failure mechanism is more localised around the foundation for R = 0.36 when the moment and horizontal load are in the same direction (as indicated in Figure 5.54). When the loads are opposing, the plastic region joins across the foundation base. At H = 0 a full rotational mechanism across the foundation base also occurs.

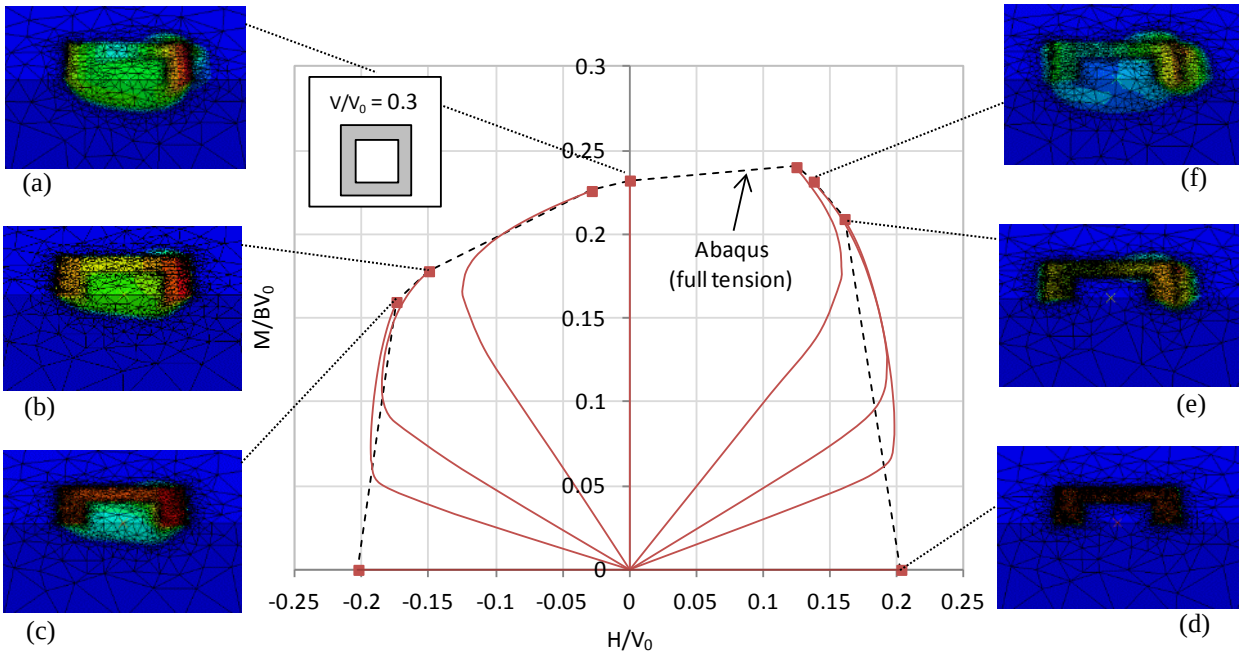

Figure 5.57: Failure envelope for V:H:M loading, square annular R = 0.36, V/V_0 = 0.3

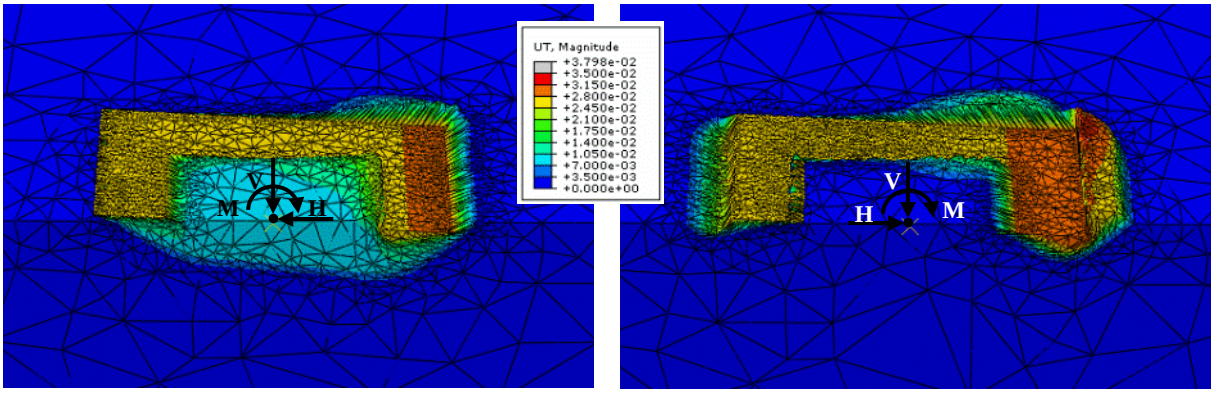

(a) Opposing horizontal and moment load (case given in Figure 5.58(c))

(b) Horizontal and moment load in same direction (case given in Figure 5.58(e))

Figure 5.58: Impact of load direction on failure mechanism ($|H/M|$ is the same for both cases)

Failure envelopes for the cases of R = 0, 0.16, 0.36 and 0.64 at a vertical load of V/V_0 = 0.3 are compared in Figure 5.59. As was found in the experiments, the size of the failure envelope is seen to increase for both horizontal and moment capacity with increasing perforation ratio R. As the perforation ratio increases the degree of eccentricity is seen to reduce, such that at R = 0.64 the envelope is close to being symmetrical.

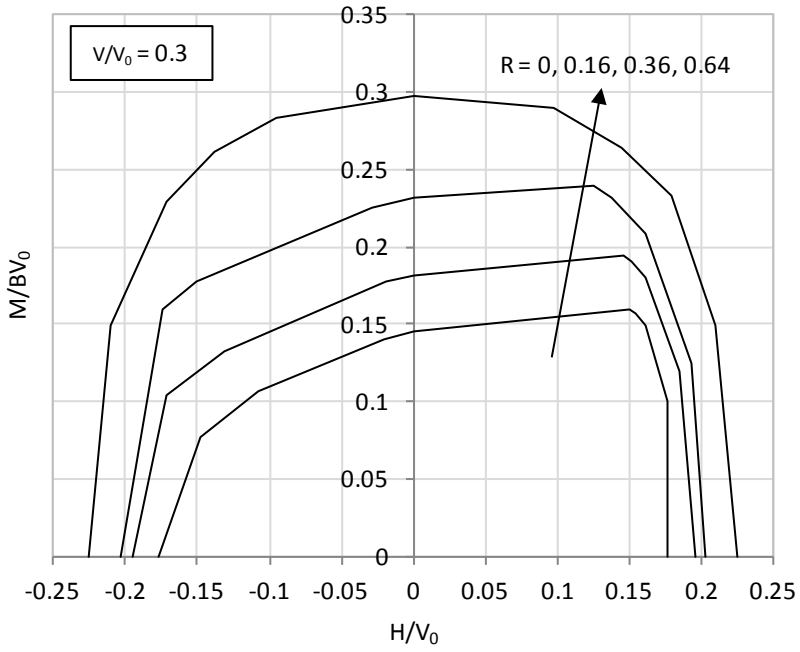

Figure 5.59: Square annular failure envelopes for R = 0, 0.16, 0.36, 0.64 at V/V_0 = 0.3

5.6.2.1 No tension interface condition

The above failure envelopes have been generated using a full tension interface condition. In the centrifuge experiments it was observed that limited or no tension was generated between the soil and the foundation. The adaptive meshing scheme in its current form does not incorporate interface elements or contact modelling to allow reduced or no tension cases. To get around this limitation, the effective width principle (see Figure 2.1) was used with the adaptive meshing scheme to model the case of no tension. This was undertaken by determining the effective area for a given load eccentricity and applying a vertical load until failure. The results using this approach for a square foundation are given in Figure 5.60. The analytical solution using the effective width principle (Meyerhof, 1953) for this case is also

plotted in Figure 5.60. The numerical results fit closely to this solution, with the peak lying slightly below the analytical peak value of $M/BV_0 = 0.125$.

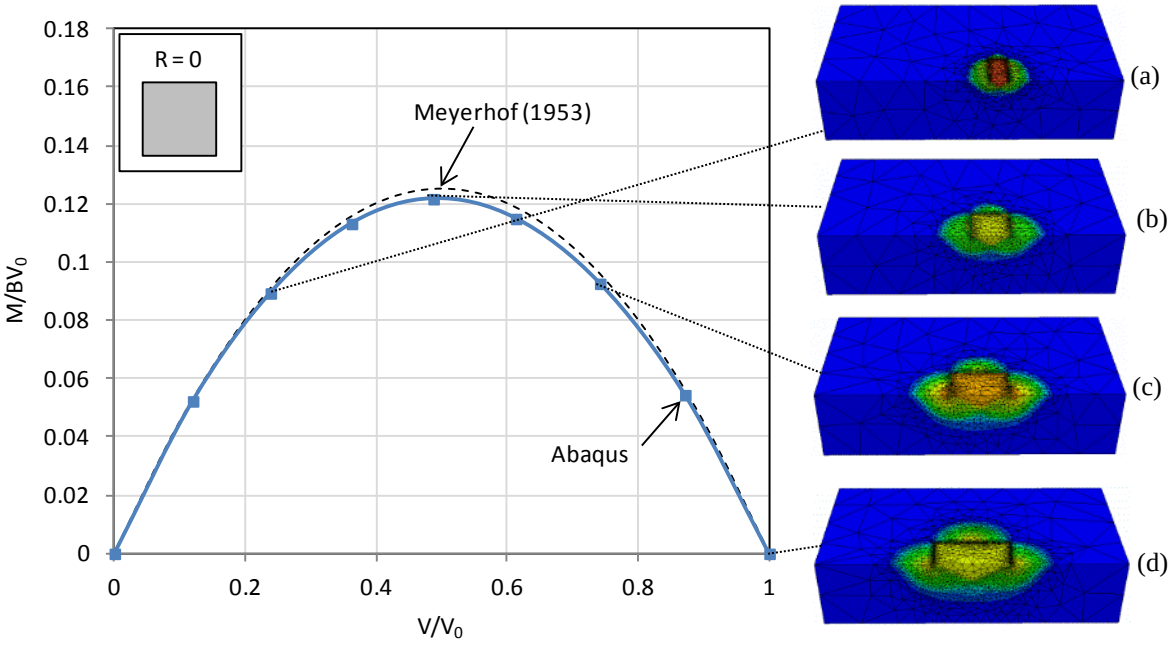

Figure 5.60: Failure envelope for *V*:*M* loading using the effective width rule, $R = 0$

Figure 5.61 shows the results for the case of $R = 0.36$. The peak value is slightly higher and occurs at a lower V/V_0 ratio compared with the results for $R = 0$.

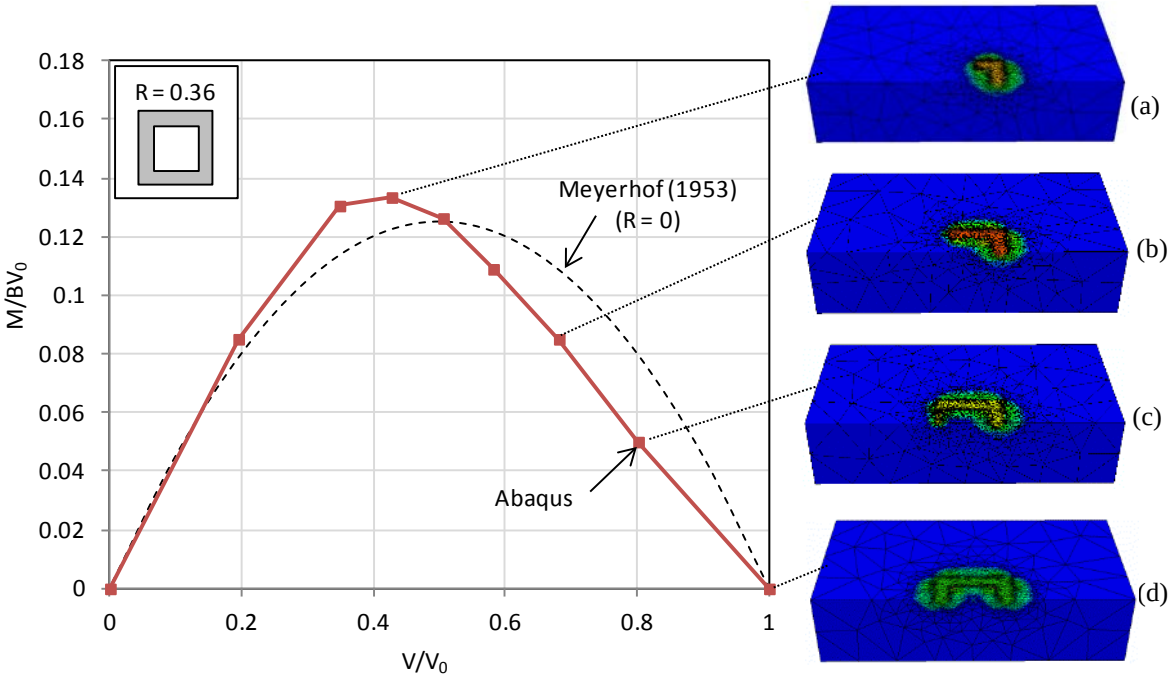

Figure 5.61: Failure envelope for *V*:*M* loading with zero-tension interface, $R = 0.36$

5.6.2.2 Peak horizontal capacity

The peak horizontal capacity h_o taken from the Abaqus results are given in Figure 5.62 and are compared with the flat base foundation experimental results. The Abaqus results show only a small increase in horizontal capacity as the perforation ratio increases. This is different to the marked increase that occurred in the experimental results. In the experiments, the foundations were slightly embedded such sliding resistance was mobilised across the gross foundation area, A_0. The foundations in Abaqus were modelled at the soil surface and resistance to sliding only occurred on the contact foundation area A (as indicated by the plastic regions in Figure 5.62). In this case the peak horizontal capacity h_o can be given by

$$h_0 = \frac{h_{0,R=0} s_c}{r_c} \tag{5.12}$$

and since $H_0 = As_{um}$, $h_{0,R=0}$ can be described by

$$h_{0,R=0} = \frac{1}{N_c s_c} \tag{5.13}$$

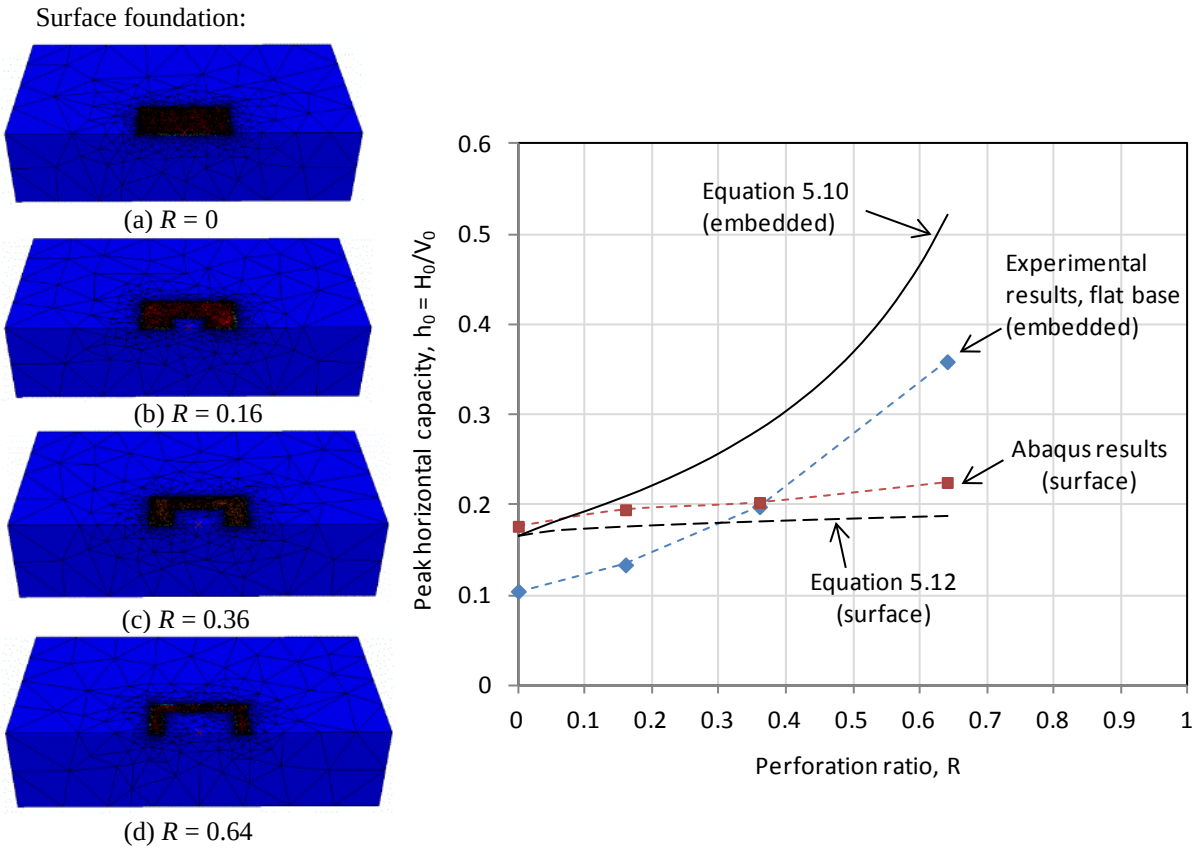

Figure 5.62: Square annular foundation peak horizontal capacity, h_0

Equation 5.12 is plotted in Figure 5.62 along with Equation 5.10 which assumes that sliding resistance is mobilised across the gross foundation area. In this case $h_{0,R=0}$ given by Equation 5.13 has been used in Equation 5.10 (rather than $h_{0,R=0}$ = 0.127 used in Figure 5.42). The Abaqus results compare well to Equation 5.12 for contact area sliding resistance. They are slightly higher which is expected as the Abaqus results overestimate sliding capacity when no interface elements are used. As seen previously in Figure 5.42, the experimental results follow the trend of Equation 5.10 for a gross sliding mechanism.

5.6.2.3 Peak moment capacity

Peak moment capacity was assessed for the cases of full and no interface tension:

i) *Full tension:* The Abaqus results for the peak moment capacity m_o with full interface tension are given in Figure 5.63. The skirted foundation experimental results are also included for comparison as they exhibited a partial degree of tensile capacity. The plastic regions shown by the refined meshes in Figure 5.63 indicate that with full tension up until at least R = 0.36 a full scoop mechanism is still occurring at failure. Using this observation, the peak moment capacity m_o could be described by the following

$$m_0 = \frac{m_{0,R=0}}{(1-R)N_c r_c} \quad (\text{for } R \leq 0.36) \tag{5.14}$$

In this case $m_{0,R=0}$ = 0.148 has been adopted, which uses the Abaqus result for pure moment loading as shown in Figure 5.55 (for a circular foundation the equivalent value would be $m_{0,R=0}$ = 0.141). It is seen that the Abaqus results compare well with Equation 5.14, and match the observation shown by the failure mechanism that by R = 0.64 a full scoop mechanism no longer occurs. Although the magnitude of the experimental m_0 values are less than that from Abaqus, the trend of the rate of moment increase falling after a certain degree of R is also observed. In the experiments this point had occurred by R = 0.36, whilst in the numerical results it occurred after R = 0.36.

ii) *No tension:* The Abaqus results for the peak moment capacity m_0 with no interface tension are shown in Figure 5.63. With increasing R it is seen that m_0 only slightly increases up until R = 0.36 is reached, after which there is a small decline. This trend matches that shown by the flat base foundation experimental results, although the experimental results were of lower magnitude. Based on the Abaqus results showing minimal change in the peak moment capacity m_0 as R increases, for a no tension interface it could be appropriate to use a constant m_0 as follows:

$$m_0 = m_{0,R=0} = 0.125 \tag{5.15}$$

This value represents the peak value given by the effective width principle (Meyerhof, 1953).

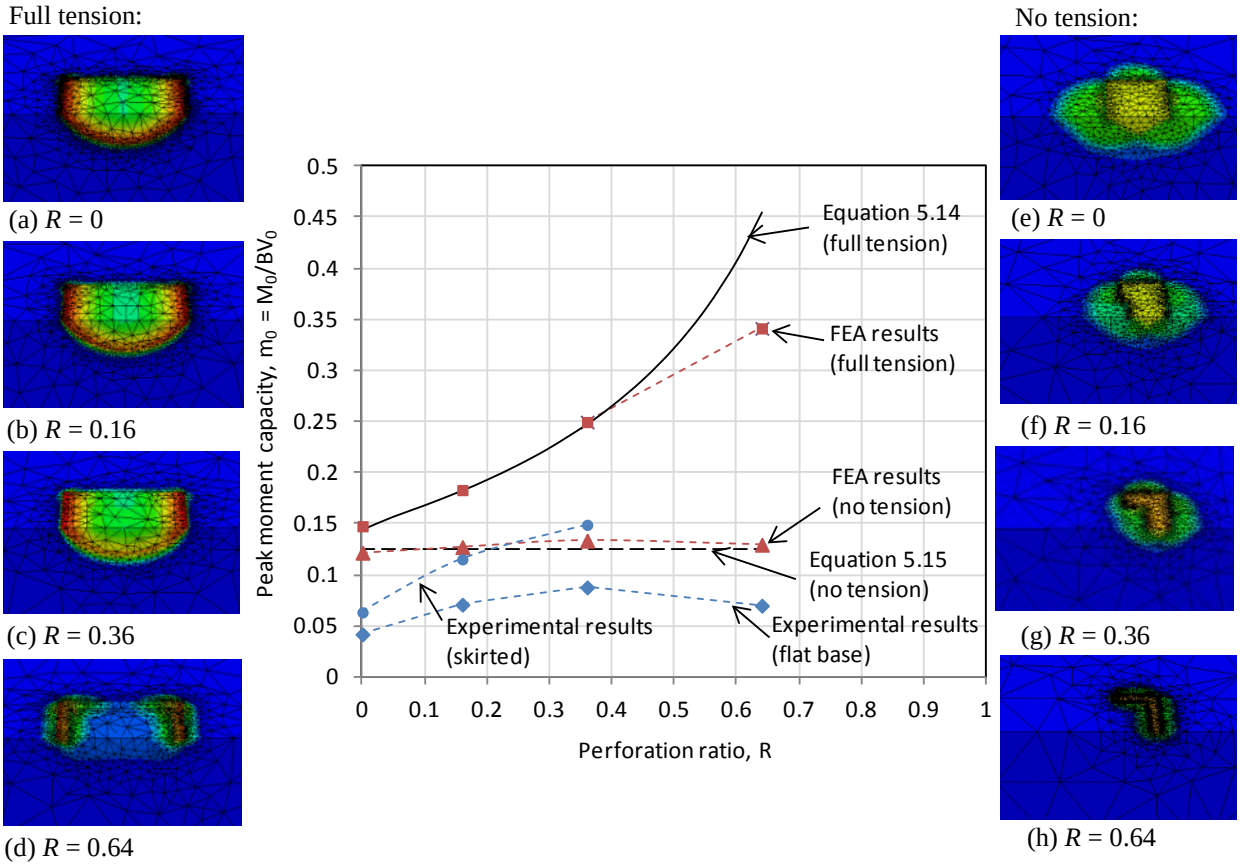

Figure 5.63: Square annular foundation peak moment capacity, m_0

5.7 Design method for combined loading

Based on the experimental and numerical results a method to estimate the combined load capacity of perforated foundations has been proposed. It has been developed by modifying the failure envelope expression given by Model B (Martin, 1994). The modifications involve:

i) Incorporating negative vertical load capacity V_t

ii) Adjusting the peak horizontal capacity h_o and the peak moment capacity m_o to account for the influence of the perforation ratio R

5.7.1 Design expression

The equation describing the failure envelope in dimensionless terms is as follows:

$$f = \left(\frac{H}{H_0}\right)^2 + \left(\frac{M}{M_0}\right)^2 - 2\bar{e}\frac{H}{H_0}\frac{M}{M_0} - \bar{\beta}^2\left(\frac{V}{V_0} - \frac{V_t}{V_0}\right)^{2\beta_1}\left(1 - \frac{V}{V_0}\right)^{2B_2} = 0 \tag{5.16}$$

where

$$\bar{e} = e_1 + e_2\left(\frac{V}{V_0}\right)\left(\frac{V}{V_0} - 1\right) \tag{5.17}$$

and

$$\bar{\beta} = \frac{(\beta_1 + \beta_2)^{(\beta_1+\beta_2)}}{{\beta_1}^{\beta_1}{\beta_2}^{\beta_2}\left(1 - \frac{V_t}{V_0}\right)^{(\beta_1+\beta_2)}} \tag{5.18}$$

where:

- The parameter values e_1 = 0.518, e_2 = 1.180, β_1 = 0.764 and β_2 = 0.882 are adopted based on Model B.
- $H_0 = h_0 V_0$, where h_0 can be estimated from Table 5.9.

Table 5.9: Peak horizontal capacity h_0 values (for $R \leq 0.64$)

Foundation case	$\boldsymbol{h_o}$	$\boldsymbol{h_{0,R=0}}$ (FEA / theoretical)	$\boldsymbol{h_{0,R=0}}$ (experimental)
Surface	$h_0 = \frac{h_{0,R=0}s_c}{r_c}$ (Eq 5.12)	$h_{0,R=0} = \frac{1}{N_c s_c}$ (Eq 5.10)	$h_{0,R=0}$ = 0.105
Embedded	$h_0 = \frac{h_{0,R=0}s_c}{(1-R)r_c}$ (Eq 5.10)	$h_{0,R=0} = \frac{1}{N_c s_c}$ (Eq 5.10)	$h_{0,R=0}$ = 0.127

- $M_0 = m_0 B V_0$, where m_0 can be estimated from Table 5.10.

Table 5.10: Peak moment capacity m_0 values (for $R \leq 0.64$)

Foundation case	$\boldsymbol{m_o}$	$\boldsymbol{h_{0,R=0}}$ (FEA / theoretical)	$\boldsymbol{h_{0,R=0}}$ (experimental)
Full tension	$m_0 = \frac{m_{0,R=0}}{(1-R)N_c r_c}$ (for $R \leq 0.36$) (Eq 5.14)	$m_{0,R=0}$ = 0.148	$m_{0,R=0}$ = 0.063 (skirted, partial tension)
No tension	$m_0 = m_{0,R=0}$ (Eq 5.15)	$m_{0,R=0}$ = 0.125	$h_{0,R=0}$ = 0.042 (flat base)

- The maximum vertical capacity V_0 can be determined using Equation 4.3.
- The ratio V_t/V_0 can be chosen based on the expected tension capacity of the foundation

Note that values of h_0 and m_0 are based on the numerical and experimental analysis of square and square annular foundations conducted within the scope of assessment undertaken in this study. Judgement or further investigation may be required for other foundation cases.

5.7.2 Comparison of design expression with experimental results

The failure envelope given by Equation 5.16 is plotted against the experimental results in Figure 5.64 for a skirted foundation with R = 0.36. As expected, the failure envelope provides gives a reasonable match with the experimental results. The Model B failure envelope for an unperforated circular foundation is also shown for reference. It is seen that the new failure envelope expression provides a more appropriate fit with the experimental results due to the incorporation of tension capacity, and the peak horizontal h_0 and moment m_0 capacities adjusted for the perforation ratio.

In Figure 5.65 the failure envelope given by Equation 5.16 is shown in H:M load space. In this plot all the relevant swipe and pushover test results have been presented. The cyclic test results and the post-cyclic pushover are also included. It is seen that in the H:M load space the design expression also provides a good match with the experimental results.

As the fit to derive the design expression was made with only a relatively limited amount of experimental results, further investigation could help improve the robustness of the design expression.

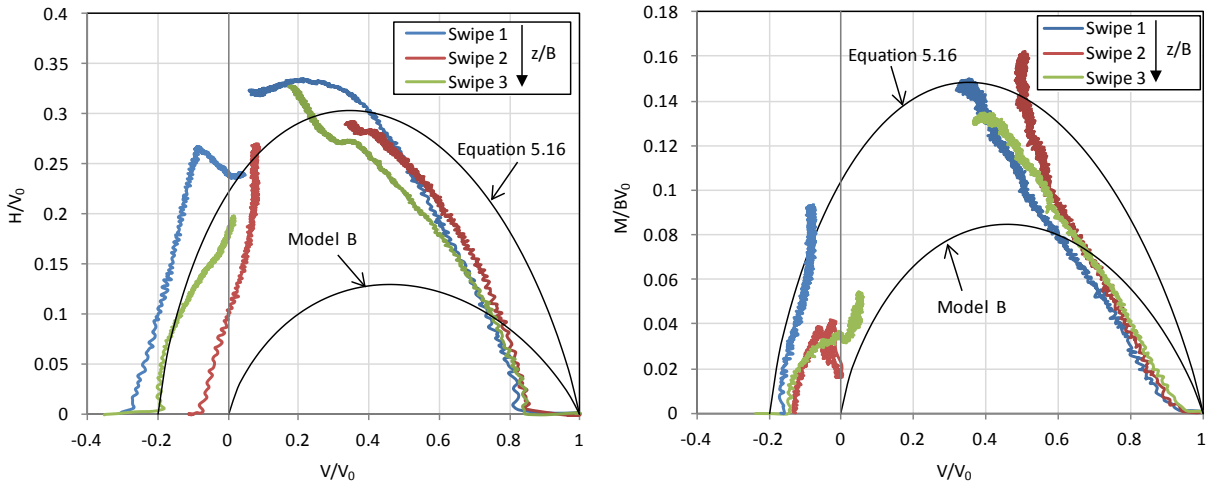

(a) *V*:*H* load space (b) *V*:*M* load space

Figure 5.64: Design expression failure envelopes compared with experimental results, R = 0.36 – skirted

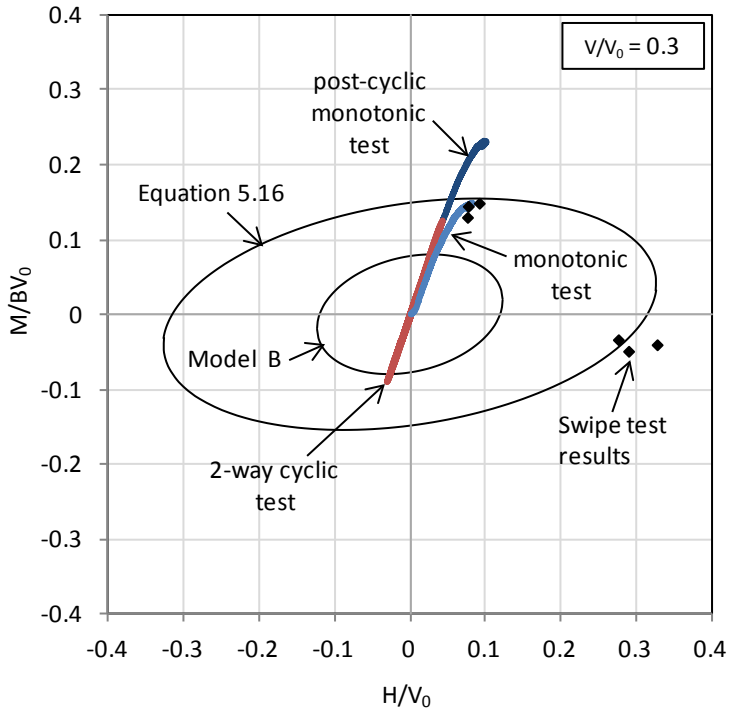

Figure 5.65: Design expression failure envelope compared with experimental results in *H*:*M* load space, R = 0.36 – skirted

5.7.3 Comparison of the design method with numerical results

In Figure 5.66 failure envelopes from the Abaqus results are compared with predictions given by Equation 5.16 for surface foundations with a full tension soil-foundation interface. A reasonable approximation is obtained using the failure envelope expression. The horizontal capacity is slightly less than the Abaqus results given Abaqus had a higher prediction of the peak horizontal capacity as shown in Figure 5.62. The failure expression is not seen to match as closely to the form of eccentricity as shown by the Abaqus results, although the match of the envelope shape is closer as the vertical load ratio V/V_0 moves towards 1 or -1 (see for example Figure 2.16).

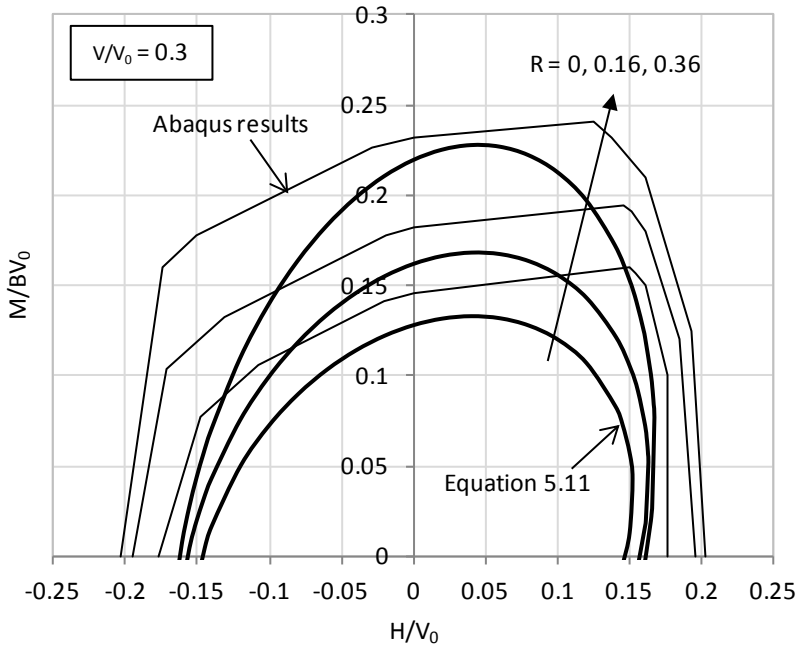

Figure 5.66: Design expression failure envelopes compared with FEA results for a square annular foundation

5.8 Conclusions

In this chapter, bearing capacity of square annular foundations under combined load has been investigated by undertaking centrifuge experiments. Tests were performed on clay and the perforated area of the foundation was varied from 0 – 64% of the total equivalent solid

foundation area (R = 0 – 0.64). Both flat based and skirted foundations were tested. In addition, tests were also conducted on a ring foundation of R = 0.36. Key points from the vertical loading, installation, and extraction tests were as follows:

- Vertical loading experiments showed that vertical bearing capacity decreased with increasing perforation ratio. The test results were compared with finite element analysis results and good agreement was obtained in most cases.
- The skirt penetration resistance measured during installation in general compared well with standard prediction methods. This was based on using N_c = 9 for end bearing and a side adhesion value of α = 0.3.
- The uplift capacity was less than 40% of the vertical capacity in compression. This may have been due to the extraction rate being too slow to maintain undrained conditions, as well as soil disturbance from the foundation penetration. The peak foundation pullout load decreased as the perforation ratio increased.

The key points from experimental and numerical combined loading results were:

- The normalised peak horizontal capacity ($h_0 = H_0/V_0$) found from experiments increased with increasing perforation ratio. This may have been as a result of a continuous sliding mechanism occurring across the gross base area of the perforated foundations which were slightly embedded. The surface foundation numerical results only mobilised sliding capacity on the contact area.
- The normalised peak moment capacity ($m_0 = M_0/BV_0$) increased with increasing perforation ratio, except the foundation with R = 0.64 where it reduced. This was particularly the case for when tension could be sustained. The experimental results suggested that only limited interface tension capacity in moment loading was achieved. The moment capacity for a solid square (R = 0) was found to be significantly lower than that expected theoretically.

- The ring foundation of R = 0.36 was found to have lower moment capacity than the square annular foundation of equivalent perforation ratio. This agrees with the comparison of capacity between unperforated square and circular foundations.
- Loading direction was also investigated and it was found that similar moment capacity was achieved for 0° and 45° degree loading directions. This indicated that it might be possible to simplify 3D loading conditions into a 2D loading scenario for which calculations would be more straightforward.
- Cyclic loading was found not to reduce the capacity below that of monotonic loading, although this came at a cost of significantly increased vertical displacement of the foundation.

Using the experimental and numerical results a new design expression for the V:H:M failure envelope for perforated foundations has been proposed (Equation 5.16). The expression is adapted from Model B for unperforated foundations. Tension capacity is accommodated and the peak horizontal (h_0) and moment (m_0) capacity inputs are based on the perforation ratio R. Parameters were assessed for different embedment and interface tension conditions such that the design expression gave a reasonable match with the experimental or numerical results. Further numerical and experimental investigation could help improve the robustness of the design expression.

Chapter 6. Vertical and combined load capacity of grillage foundations

Grillage foundations consist of a series of structurally connected strip footings, often vertical plates or steel beams. As was explained in Section 2.3.2, grillages can be a beneficial foundation option for subsea infrastructure. For example, compared with an equivalent solid mudmat foundation, grillages may have reduced material requirements and allow for easier handling offshore. Experiments have been undertaken using a six degree-of-freedom loading rig to investigate the capacity of grillage foundations. Combined vertical (V), horizontal (H) and moment (M) loading has been explored, such as that experienced in offshore conditions. Tests were performed on loose sand for both a single strip foundation and a collection of strips, representing a grillage, with a range of spacings. This chapter presents results from both vertical and combined loading tests, and these have been interpreted using V:H:M failure envelopes. Some comparisons are also made with results from finite element limit analysis using OxLim. The analysis results have been used to develop an expression for the V:H:M failure envelope of a grillage.

6.1 Analysis approach

The bearing capacity of grillage foundations have been investigated by the following means:

i) Experimentally at 1g using degree-of-freedom (6DOF)

ii) Numerically with finite element limit analysis (FELA) using OxLim

The geometry of the grillage foundations analysed is shown in Figure 6.1. Individual grilles of thickness t, height h and length L are arranged at centre-to-centre spacing s to give an overall grillage foundation width B. With penetration the grillage is embedded into the soil at depth d.

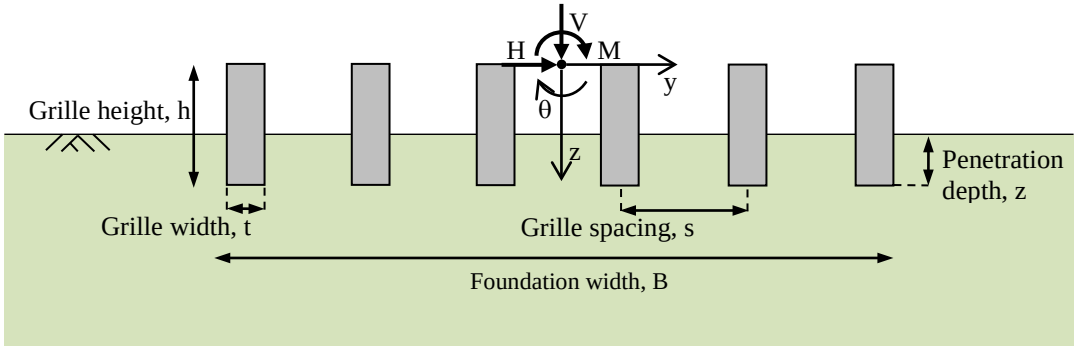

Figure 6.1: Schematic of grillage geometry

The tests were carried out on i) single strips and ii) a collection of six parallel strips, equally spaced to represent a section of a grillage foundation. For a grillage made up of N grilles, the perforation ratio R is given by

$$R = \frac{(N-1)(s-t)}{B} \tag{6.1}$$

where

$$B = Nt + (N-1)(s-t)$$

For a grillage in the field where N is large, the perforation ratio R can be simplified as

$$R = \frac{s-t}{s} \tag{6.2}$$

The experiments explored the bearing capacity of grillage foundations on loose sand subjected to combinations of vertical (V), horizontal (H) and moment (M) loading. The load reference point is taken to be the top centre position of the grillage as this was the closest position to the load reference point adopted by the control program (Figure 6.1).

The experimental results have been compared with predictions from analytical and plasticity-based methods proposed for grillages as summarised in Section 2.3.2 (Bransby et al., 2011, Bransby et al., 2012, Knappett et al., 2012). These methods do not include the effect of moment loading, so additional consideration has been given to assessing the impact of overturning moments on the bearing capacity. The experimental data have been compared with results from finite element limit analysis (FELA) performed using the program OxLim.

6.1.1 Experimental method

6.1.1.1 6 degree-of-freedom loading rig

Experimental testing was carried out under 1g conditions using a loading rig capable of applying 6 degree-of-freedom (6DOF) motions to a model foundation (Figure 6.2(a)). Centrifuge testing may not be suitable for this problem as the scaling required may result in the model grillage width and the sand grain size becoming too similar. The 6DOF loading rig consists of six actuators (Figure 6.2(b)), pinned at one end to a reaction frame and at the other end to the loading platform. The model foundation is attached to the loading platform via a load cell which is strain-gauged to enable all six load components to be measured.

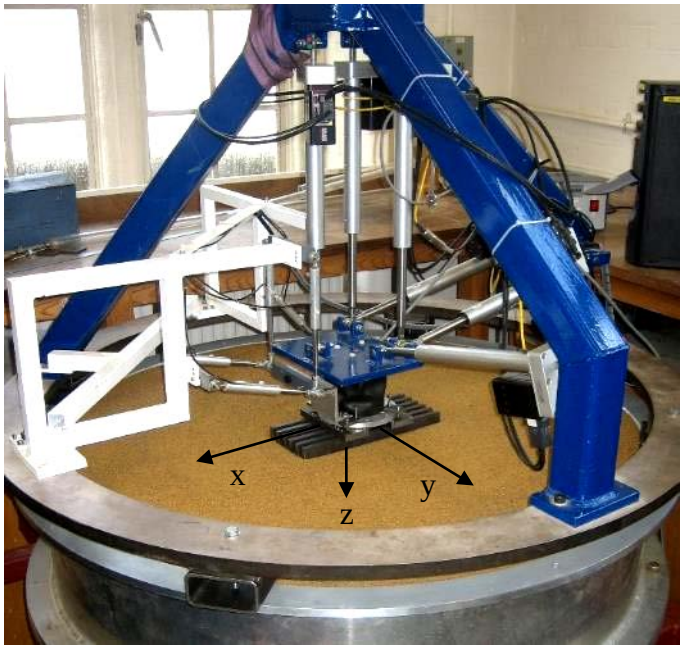

(a) Six DOF loading rig (with grillage attached)

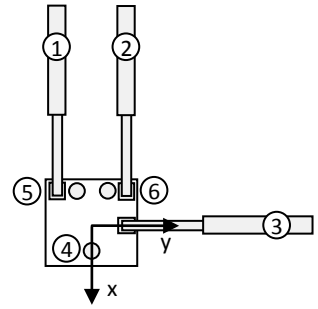

(b) System of six loading actuators

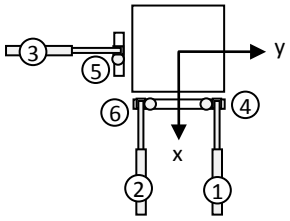

(c) System of six LVDTs

Figure 6.2: Experimental setup

A computer program controls the loading rig by determining the actuator displacements required for an incremental change in the platform position. The displacement path and the loads on the foundation are continuously recorded. The platform pose can be determined using the linear potentiometers within the actuators themselves. However, the resolution and the accuracy of these measurements may be compromised due to electrical noise as well as

flexibility in the loading rig. To counter this, a system of six high-resolution LVDTs is attached to the footing, but separated from the loading frame (Figure 6.2(c)). These LVDT readings are used by the control program to determine the pose of the platform, enabling accurate foundation movements to be imposed and recorded. A full description of the 6DOF loading rig can be found in Byrne & Houlsby (2005) and Bienen et al. (2006).

6.1.1.2 Experimental validation

A validation study was carried out in the first instance. A selection of tests were repeated from the study by Bienen et al. (2006). This process was to check repeatability and give confidence in using the rig to examine grillage capacity. The tests involved applying combined loading to a 150 mm diameter rough circular foundation on loose dry silica sand. Vertical penetration tests and tests exploring horizontal (H), moment (M) and torque (Q) capacity were repeated. The results from the tests undertaken are shown in Figure 6.3. They are compared with a vertical load-displacement hardening law and failure envelopes which were determined using a best fit with the test data from Bienen et al. (2006). A close match is obtained with the best fit data and provides confidence in using the 6 DOF loading rig for the grillage study.

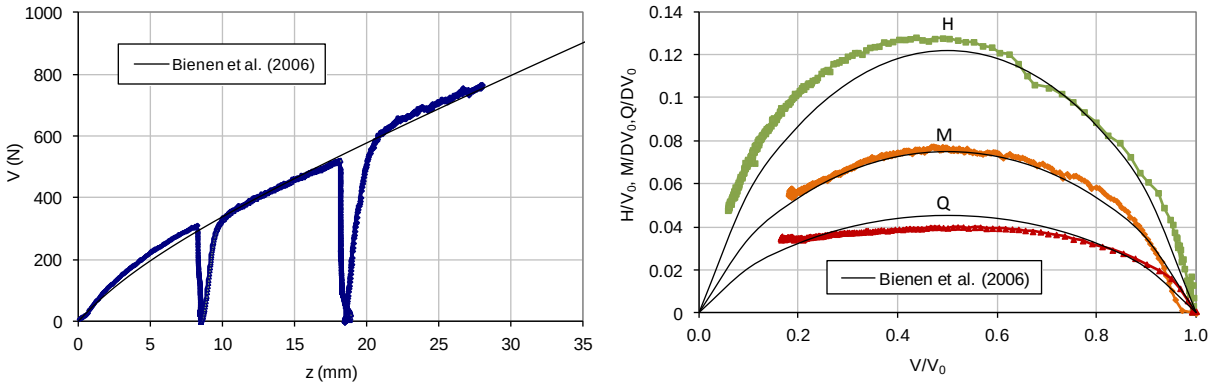

(a) Vertical penetration test (b) Swipe tests

Figure 6.3: Results from the 6 DOF loading rig for a circular foundation on loose sand compared to previous results from Bienen et al. (2006)

6.1.1.3 Model grillage foundations

The grillage foundations used in the experiments were constructed from steel plates, each having a width t = 9.5 mm, length L = 305 mm and height h = 50.5 mm. The underside of each grille was roughened by adhering sand to the base. The number of individual grilles, N, used in each grillage model was 6. These were connected together by two steel plates at the top to ensure a rigid foundation and parallel grilles. Four centre-to-centre grille spacings, s, were investigated so that the ratio s/t ranged from 1 to 3, corresponding to a perforation ratio R ranging from 0.36 to 0.63. This arrangement represents a full-scale grillage, though with a significantly reduced N and shorter length L. The grille width and spacing dimensions were selected to be in the range of the dimensions used in the field (see Section 2.3.2). In addition, some tests were undertaken on a single grille. A summary of each foundation configuration is given in Table 6.1.

Table 6.1: Model foundation details

Model ID	Illustration	*N*	*t* (mm)	*s* (mm)	*s/t*	R	B (mm)	L (mm)	h (mm)
S1-1		1	9.5	n/a	n/a	0	9.5	305	50.5
S6-1_0		6	9.5	9.5	1.0	0	57.0	305	50.5
S6-1_7		6	9.5	15.9	1.7	0.36	89.0	305	50.5
S6-2_3		6	9.5	22.2	2.3	0.53	120.5	305	50.5
S6-3_0		6	9.5	28.6	3.0	0.63	152.5	305	50.5

6.1.1.4 Soil properties

The experiments were undertaken on dry Leighton Buzzard 14/25 silica coarse grained sand having properties as given in Table 2. The average unit weight in all of the tests completed was 14.89 kN/m^3. This corresponds to very loose sand with a relative density of approximately 10%. These soil conditions represent the sand density likely to give the lowest capacity, such that accurate assessment of grillage capacity in these conditions would be most critical.

Table 6.2: Leighton Buzzard sand properties

Property	**Unit**	**Value**
Particle size D_{10}, D_{30}, D_{50}, D_{60}	mm	0.63, 0.70, 0.80, 0.85
Specific gravity, G_s	-	2.65
Coefficient of uniformity, C_u	-	1.3
Maximum dry density, γ_{max}	kN/m^3	17.58
Minimum dry density, γ_{min}	kN/m^3	14.65
Critical state friction angle, ϕ_{cs}	degrees	34.3

6.1.1.5 Testing procedure

For each test, sand was placed into a circular tank of diameter 1.1 m and height 0.25 m. The sample was prepared by careful layering of the sand with a small hand-scoop to achieve a consistent and low relative density. Each test started with the footing just above the soil surface. Vertical loading tests were completed at a penetration rate of 0.04 mm/s to a maximum penetration depth of 40 mm. In some tests the foundation was then extracted to estimate the interface friction on the plates. Combined loading was applied by first loading the footing vertically to the target penetration, then carrying out a swipe test. A swipe test involves translating or rotating the foundation while keeping the vertical displacement constant. It is used to determine the shape of the failure surface for the foundation at that embedment (see Section 2.1.2 for more details). The swipe tests were conducted at rates of

0.004 mm/s (horizontal) or 0.01°/s (moment) to ensure an adequate number of data points were recorded. An interval of at least 10 mm vertical penetration (determined by trial tests) was required between swipe tests to re-join the virgin penetration line, such that the previous test history was effectively erased. Table 6.3 gives details of the tests for which results have been presented in this chapter. In-plane *V*:*H*:*M* loading was applied, with the load reference point taken at the top of the grillage as shown in Figure 6.1.

Table 6.3: Experimental test details

Test ID	**Model**	**s/t**	**Average unit weight (kN/m^3)**	**Loading type**
S3-V	S1-1	n/a	14.80	Vertical
S4-V	S1-1	n/a	14.82	Vertical
S10-V	S6-1_7	1.7	14.87	Vertical
S8-V	S6-2_3	2.3	14.85	Vertical
S9-V	S6-3_0	3.0	14.86	Vertical
S11-V	S6-1_0	1	14.87	Vertical
S14-VHM	S6-1_0	1	14.89	Combined
S15-VHM	S6-1_0	1	14.90	Combined
S16-VHM	S6-1_7	1.7	14.90	Combined
S17-VHM	S6-1_7	1.7	14.90	Combined
S24-VMH	S6-1_7	1.7	14.95	Combined
S18-VHM	S6-2_3	2.3	14.91	Combined
S22-VMH	S6-2_3	2.3	14.94	Combined
S23-VMH	S6-2_3	2.3	14.94	Combined
S19-VHM	S6-3_0	3.0	14.92	Combined
S20-VMH	S6-3_0	3.0	14.94	Combined
S21-VMH	S6-3_0	3.0	14.95	Combined

At the end of each test the load and displacement data were retrieved from the control program for processing. Due to the grillage connection plate the chosen load reference point was 10 mm below the reference point adopted by the control program for the displacements applied and loads recorded. This meant that for the rotational swipe tests the action of the

swipe imposed additional horizontal and vertical displacement of the footing during the test. At maximum rotation this would equate to additional vertical and horizontal displacements of 0.01 mm and 0.5 mm respectively and so are considered to have minimal impact. The moments measured however were adjusted to account for the different reference points. A further consideration with the rotation swipe is that the load cell rotates along with the foundation. This means the vertical and horizontal loads are no longer measured as per the original coordinate system and so adjustments were made to account for this.

6.1.2 Numerical method

Numerical analysis was undertaken using the FELA program OxLim (Martin, 2011) to model some of the experimental tests. OxLim uses plasticity theory to generate both lower bound (LB) and upper bound (UB) collapse loads for plane strain problems. The lower bound solution requires a statically admissible stress field to be upheld and stresses associated with each element must satisfy equilibrium and not violate the yield criterion for the soil. OxLim applies these constraints to the boundaries and vertices of each element and uses external optimisation software to solve for the stress field giving the highest lower bound. For the upper bound (UB) solution, a kinematically admissible displacement field must be upheld. This requires that the strains associated with each element satisfy both compatibility conditions and the plastic flow rule. OxLim applies equivalent loads to the vertices of each element and generates constraints to enforce the plastic flow rule. The resulting solution requires equalising the internal and external work. The solution is then optimised to obtain the displacement field giving the lowest upper bound.

By employing an adaptive meshing technique, OxLim is able to refine these bounding solutions to a required precision in order to bracket the exact solution closely. The precision represents a percentage error of the solution, defined by: Err%= 100 x (UB – LB)/(LB + UB). The solution is taken as the average of the final collapse loads given by: Avg = (LB + UB)/2.

The OxLim analyses in this chapter were undertaken at specified grillage embedment depths, with the foundation 'wished in place'. Unless otherwise stated, the grilles were modelled with fully rough bases and sides with $\delta = 2/3\phi$, and were connected to act as a single rigid body. Sand with a friction angle $\phi'_{cs} = 34.3°$ and effective unit weight $\gamma' = 14.8$ kN/m^3 was analysed to be consistent with the experimental tests.

6.1.2.1 Numerical validation

The capacity of a single strip at different embedment depths in sand was investigated using OxLim to validate its use for the grillage study. A single strip model was set up in OxLim with width $B = 1$ m and $\phi = 30°$. The vertical capacity at different embedment depths z was examined over the range $0 \leq z/B \leq 2.5$. Bearing capacity increases with embedment, which is accounted for in classical bearing capacity equations by the superposition of surcharge and soil self weight through the N_q and N_γ components, and the use of depth factors (see Equation 6.4). However it is not theoretically correct to superimpose these two components, so the classical bearing capacity equation cannot be used as a benchmark for the OxLim results. Instead the results of other studies that explicitly accounted for embedment were used for comparison. A combined bearing capacity factor $N_{\gamma q}$ was defined which is related to the ultimate capacity q_u as follows

$$q_u = 0.5\gamma' B N_{\gamma q} \tag{6.3}$$

The OxLim results at different embedment depths are plotted in Figure 6.4 and represent the average of the upper bound and lower bound solutions, which were bracketed to an error of less than 1%. The results in terms of $N_{\gamma q}$ are compared with data from other studies of Lyamin et al. (2007) using finite element limit analysis and Salencon (2008) using the method of characteristics. The OxLim results provide a close fit with those from these other studies providing confidence in its use for analysing embedded strip foundations in sand.

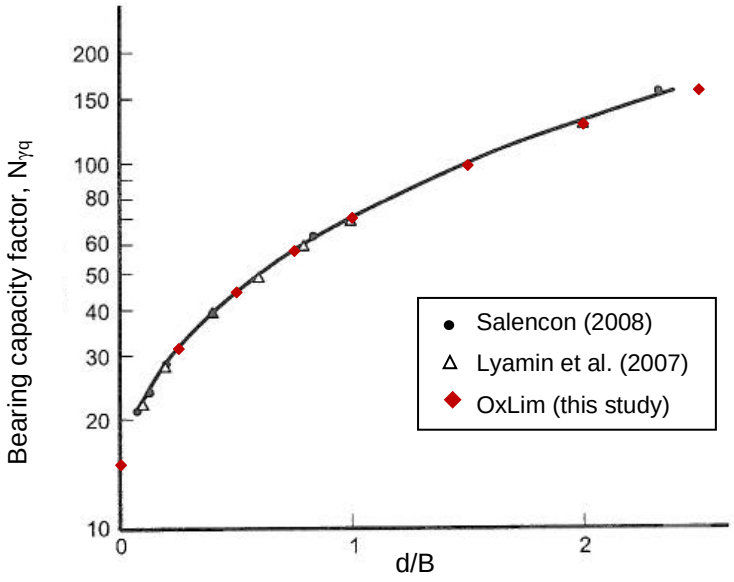

Figure 6.4: Comparison of OxLim results for an embedded strip foundation in sand ($\phi = 30°$) with previous studies

6.2 Single strip results

6.2.1 Vertical loading

The results of a vertical penetration test on a single grille foundation (Type S1-1) and six grille footing with no spacing (Type S6-1_0) are given in Figure 6.5. The tests are compared with the capacity calculated using a classical shallow foundation bearing capacity equation such as that given in DNV (1992), which could be used for a flat plate mudmat:

$$q_u = 0.5\gamma' B N_\gamma d_\gamma + \gamma' z N_q d_q \tag{6.4}$$

where $q_u = V/(BL)$, γ' is the soil effective unit weight, N_γ and N_q are bearing capacity factors, and d_γ and d_q are depth factors. A comparison is also made when treating the single grille as a pile using the method given by Equation 2.15. Figure 6.5 shows that the pile capacity equation provides a good match with the single strip data, whereas the shallow foundation equation under-predicts the results. This was also observed by Bransby et al. (2011).

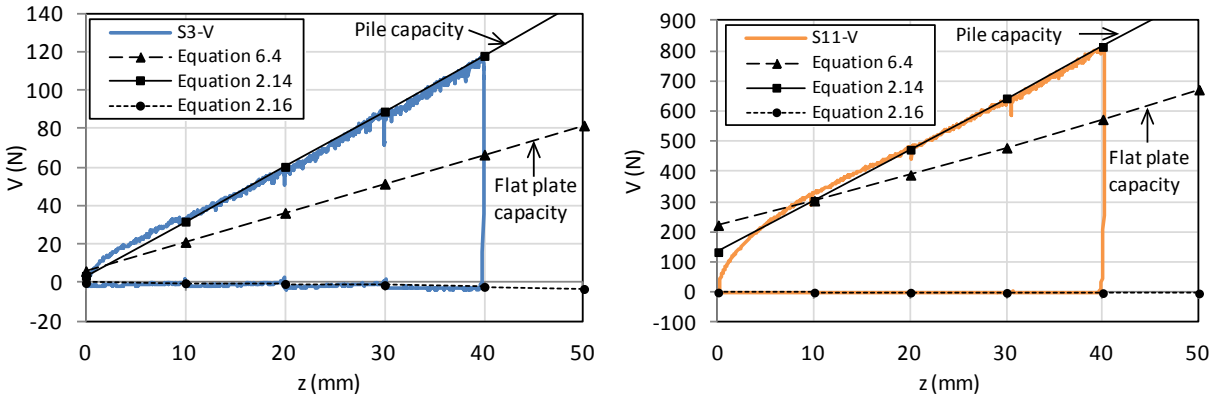

(a) Single strip (N = 1) (b) Single strip (N = 6, s/t = 1)

Figure 6.5: Results of single strip foundation tests during vertical penetration and extraction

The resistance was also measured during extraction of the single footings, allowing the side friction component of capacity to be assessed. The extraction data is shown in Figure 6.5 and is compared with the calculation of side friction using Equation 2.17. This calculation was made taking $K = 1.5K_0$ as done by Bransby et al. (2012) based on large displacement pile recommendations, and assuming $\delta = 2/3\phi$. This approach is seen to give a good match with the data in Figure 6.5. Based on measurements during extraction of the single grilles, the contribution of side friction to the total penetration resistance was minimal.

The single grille penetration results are compared in Figure 6.6 with those from OxLim, in which smooth, intermediate and fully rough side conditions were considered. The results are presented in terms of the combined bearing capacity factor $N_{\gamma q}$ defined in Equation 6.3. The OxLim results compare well with those from the experiment, slightly under-predicting the experimental results for the smooth side condition but matching for rough sides. Figure 6.7 shows, by way of the OxLim refined mesh, the extent of the plastic zone adjacent to the grille as it penetrates. At d/B = 2 this zone extends to approximately 8B from the grille edge, though it should be noted that OxLim uses an associated flow rule (dilation angle $\psi = \phi$) for modelling frictional soil.

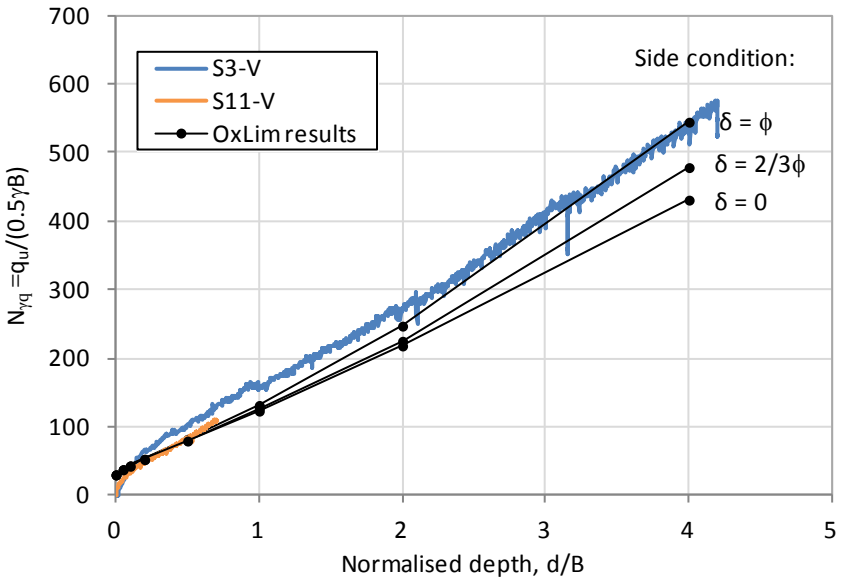

Figure 6.6: Strip foundation experimental results compared with OxLim results

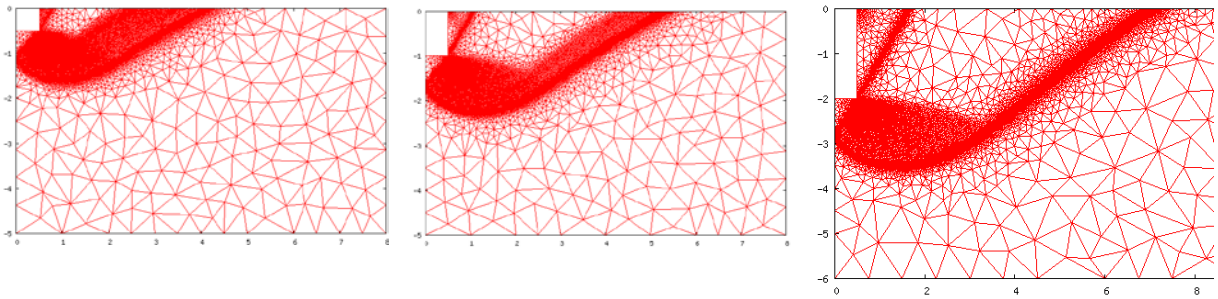

(a) $d/B = 0.5$ (b) $d/B = 1$ (c) $d/B = 2$

Figure 6.7: OxLim meshes of a strip foundation with smooth sides in sand

6.2.2 Combined loading

Combined loading tests on a single strip foundation (Type S6-1_0) have also been undertaken and compared with results from OxLim. Swipe test results in *V*:*H* load space at two embedment depths are shown in Figure 6.8. The embedment depths were z = 10 mm and z = 40 mm which correspond to z/B = 0.18 and z/B = 0.7 respectively. The results have been normalised by the maximum vertical load, V_0 experienced by the foundation prior to the swipe test. The normalised failure surface is seen to expand with increasing embedment, a feature also predicted by OxLim.

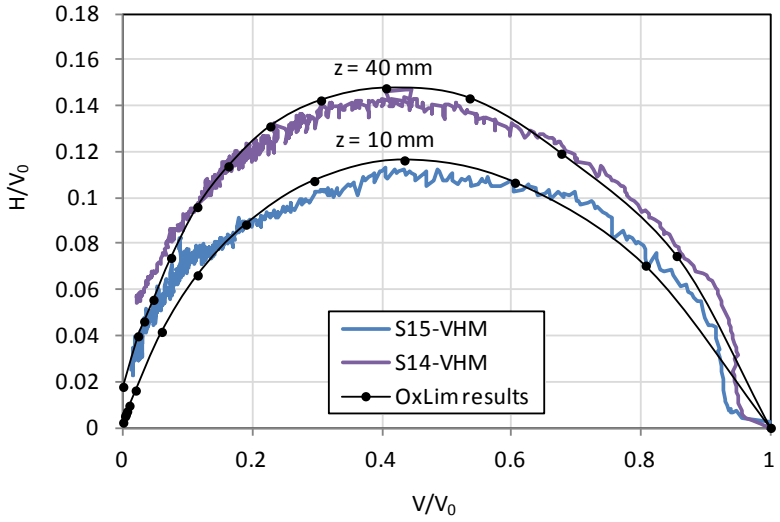

Figure 6.8: Single strip swipe test results in *V*:*H* load space compared with OxLim results

The experimental results for a strip swipe test at z = 10 mm penetration are presented in full *V*:*H*:*M* load space in Figure 6.9. The results are compared with a failure envelope defined using OxLim for a strip footing on sand. The envelope represents the average of the upper and lower bound solutions bracketed to an error of generally less than 5%. The OxLim analysis was undertaken with ϕ = 34.3° to match the experiments. The results are for a surface strip (z/b = 0) and so differ slightly from the experimental results which are for the case of z/B = 0.18. However it is seen in Figure 6.9 that the shape mapped out by the experimental load path matches well with the surface of the numerical failure envelope.

Whilst *V*:*H*:*M* failure envelopes for foundations on clay have been extensively explored using numerical analysis, this is not the case for foundations on sand. The shape of the numerical sand failure envelope was found to be roughly parabolic in the *V*:*H* and *V*:*M* planes and elliptical of anti-clockwise rotation in the *H*:*M* space, which is in line with previous experimental results (Gottardi and Butterfield, 1993, Gottardi et al., 1999). This agreement is indicated in Figure 6.10 in which OxLim results are compared with best fit expressions for previous experimental results of strip and circular footings in the *H*:*M* load space at V/V_0 = 0.5. The OxLim results are found to define a similar shape in this plane, despite the nature of the normality condition with this method.

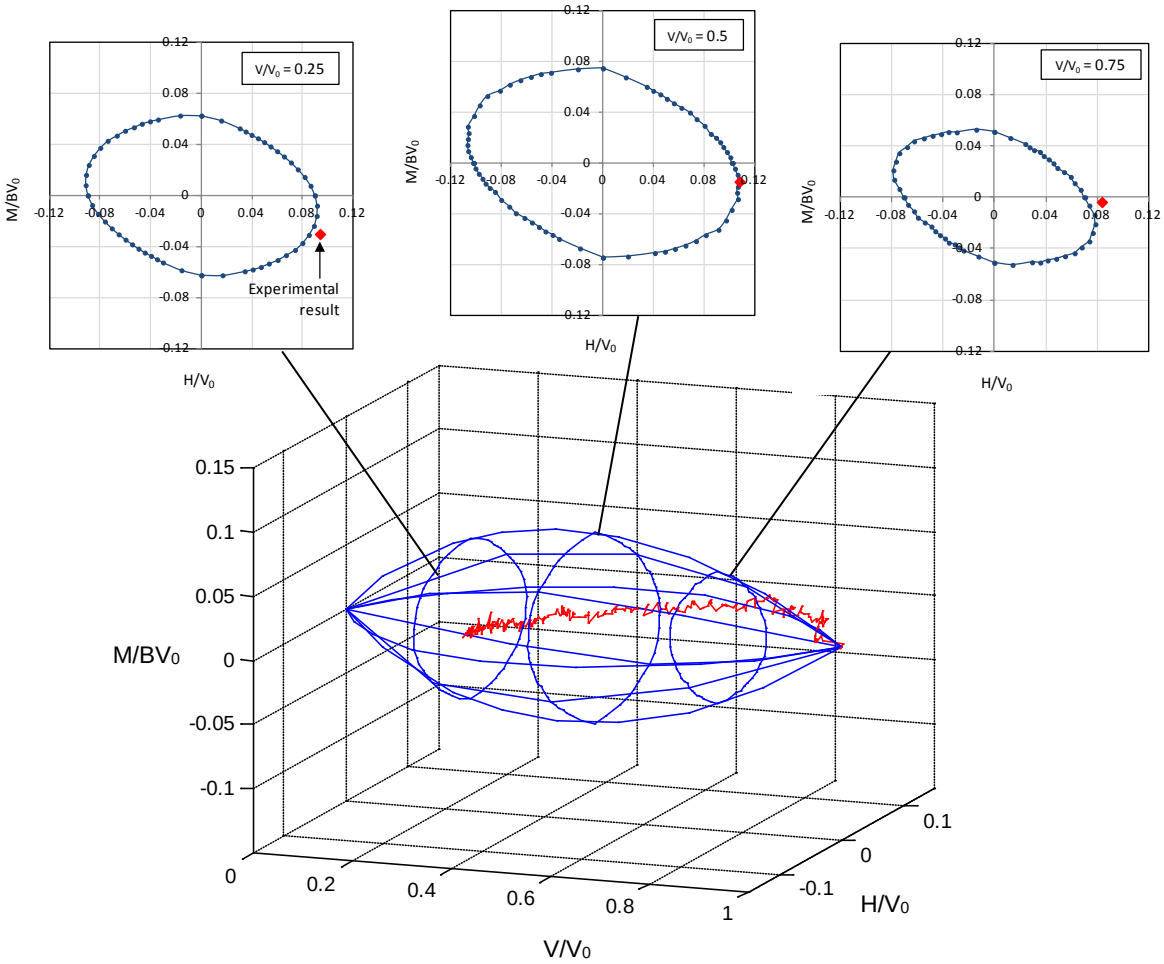

Figure 6.9: OxLim results of *V*:*H*:*M* envelope of surface strip foundation on sand, $\phi = 34.3°$, $\gamma' = 14.8$ kN/m^3

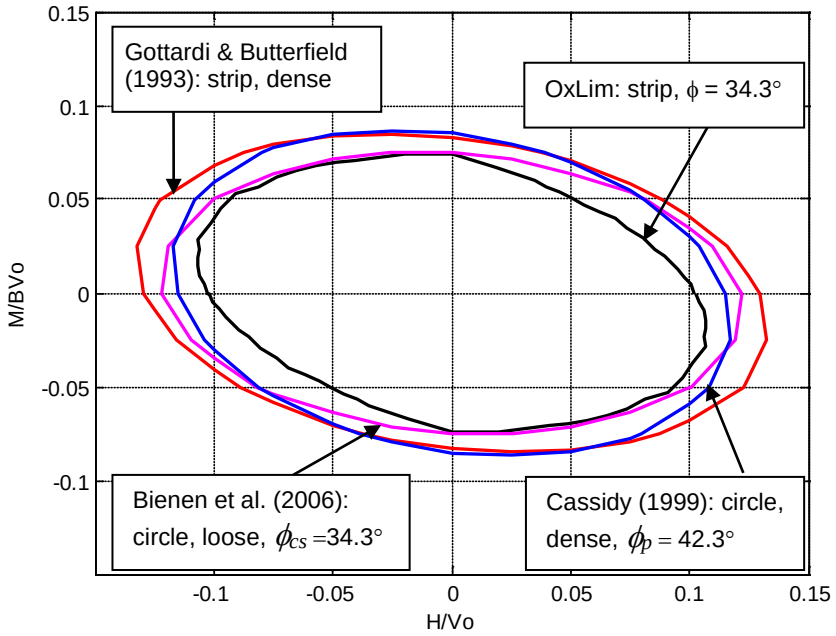

Figure 6.10: Comparison of failure envelopes for foundations on sand in *H*:*M* space, $V/V_0 = 0.5$

6.3 Grillage results

6.3.1 Vertical loading

As was discussed in Section 2.3.2.1, if the strip foundations making up a grillage are spaced closely enough then there will be interaction effects that increase the capacity beyond the sum of the individual grille capacities. For example, the failure mechanism given by Figure 6.7 (b) suggests that for the case of $z/B = 1$, interaction will start to occur when the grille edge to edge spacing is less than $10t$. As adjacent grilles penetrate into the sand, the close spacing increases the vertical and horizontal stresses between them such that arching of the sand occurs. With sufficient penetration the grillage foundation changes from 'coring' through the sand to exhibiting 'plugging' behaviour, similar to that for a tubular pile. Once the grillage foundation is in a plugged state it can be expected to have the same capacity as a flat plate foundation of equivalent overall width. The onset of plugging depends on the spacing between the grilles and their penetration depth.

Test results for grillages with six grilles ($N = 6$) and spacing ratios $s/t = 1.7$, 2.3 and 3 are given in Figure 6.11. This figure includes the penetration resistance from the single grille test (S3-V) multiplied by six for comparison. It is seen that the grillage foundations have more than double the capacity of six individual grilles, indicating the substantial effect of the grille interaction on capacity. Comparing the grillage results, it is seen that the grillage of smallest spacing ($s/t = 1.7$) initially mobilises more capacity. This is because arching between the grilles occurs at lower penetration, such that 'plugged' behaviour is reached sooner. The grillages with larger spacing ratios require more penetration to approach the plugged condition, but they subsequently mobilise more bearing capacity than the grillage with the smaller spacing ratio (because the overall width is greater).

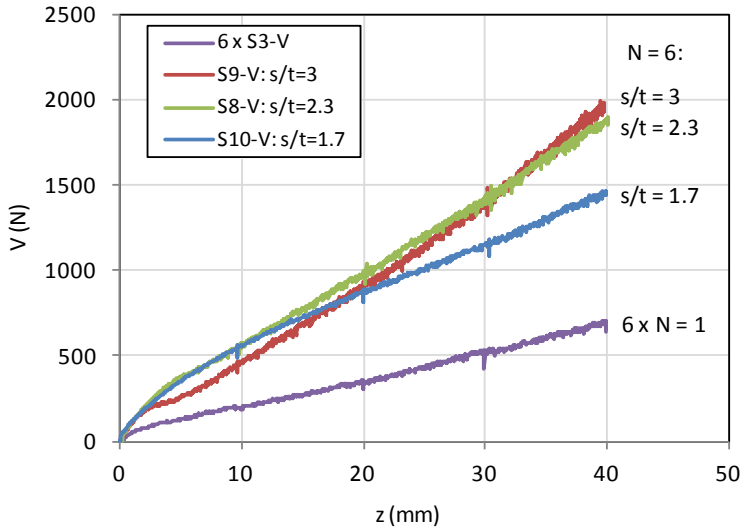

Figure 6.11: Grillage footing vertical penetration results

6.3.1.1 Design method for vertical loading

Bransby et al. (2012) proposed a method for estimating grillage foundation capacity prior to plugging. The solution treats the grilles as plane strain piles as per Equation 2.15, but with a stress enhancement due to the 'silo' effect. This leads to an increase in the overburden stress for the end bearing calculation, as well as the normal stress between the grilles, used for the side friction. For the assumption of a large number of grilles, the expression for grillage capacity is given by Equation 2.23. When full plugging has occurred the capacity can be determined using Equation 6.4 for a flat plate.

The vertical load–displacement curves for the grillages tested are compared in Figure 6.12 with i) the analytical solution for grillage penetration prior to plugging and ii) the solution for flat plate capacity. The point at which the grillage capacity and flat plate capacity lines intersect represents the penetration depth at which plugging is predicted to occur. Prior to plugging it is seen that the design method provides a reasonable match with the experimental data. However, the experimental results show a gradual transition to the plugged state whilst the design method indicates this to occur abruptly. As penetration continues in the plugged state, it is seen that the plugged capacity solution underestimates the experimental data, which is consistent with the observation made for the single foundations

tested. Based on the results shown in Figure 6.12 it is expected that the flat plate design line will be conservative in its prediction of plugging capacity.

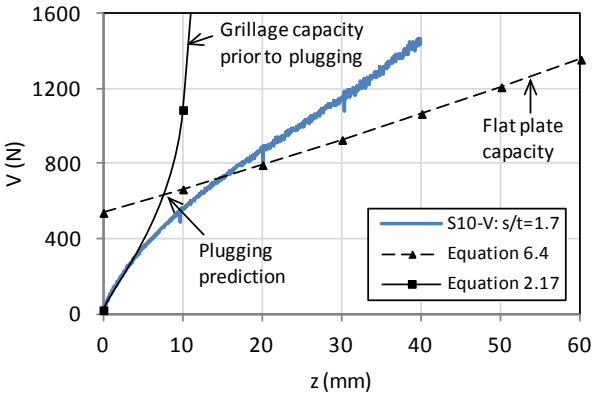

(a) s/t = 1.7 (R = 0.36)

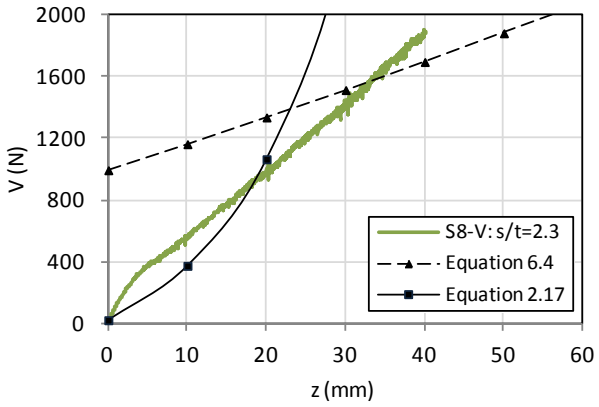

(b) s/t = 2.3 (R = 0.53)

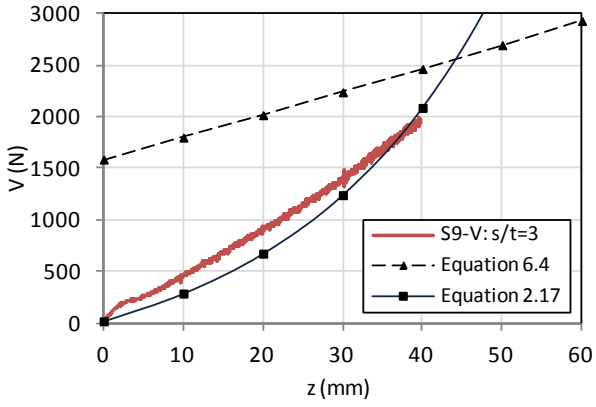

(c) s/t = 3 (R = 0.63)

Figure 6.12: Comparison of grillage vertical penetration results with design method

A key part of the design solution is the prediction when plugging will occur, since this dictates whether the grillage or flat plate expression should be used to calculate capacity. Figure 6.12 shows that a penetration depth of z = 30 mm it is predicted that the grillage with spacing s/t = 2.3 will have plugged whilst the grillage with spacing s/t = 3 will not have plugged. The deformation of the soil at this penetration depth for each test is shown in Figure 6.13. Visual inspection of the soil behaviour appears to agree with the plugging prediction from the design solution. In Figure 6.13(a) for s/t = 2.3 the sand seems to have plugged between the grilles and is being pushed down with the penetration of the foundation. In Figure 6.13(b) for s/t = 3 it appears that coring behaviour is still occurring as the sand is moving up in-between the grilles.

(a) s/t = 2.3 – plugging behaviour (b) s/t = 3 – coring behaviour

Figure 6.13: Grillages at 30 mm penetration

6.3.1.2 Comparison with numerical results

The experimental and analytical results for s/t = 2.3 are compared with vertical penetration results from OxLim in Figure 6.14. The OxLim results are initially similar to the design solution, but differ in terms of the onset of plugging. The analytical design line predicts that the grillage should plug fully within the duration of the test, whilst the OxLim results suggest further penetration is required for this to occur.

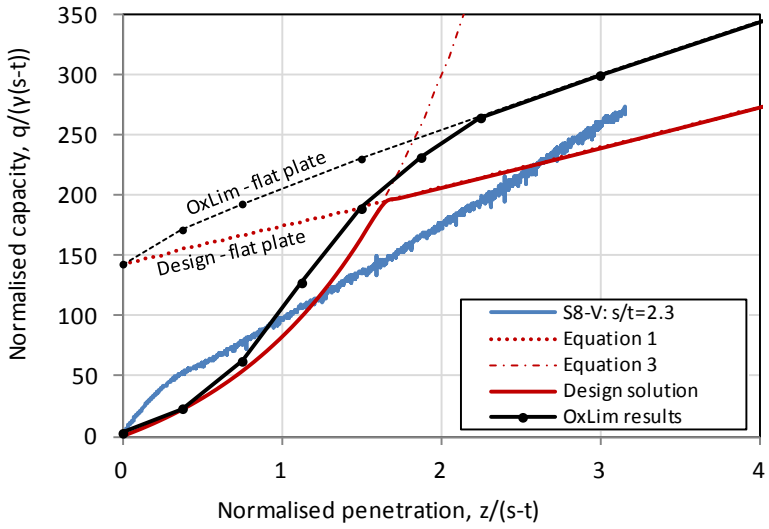

Figure 6.14: Comparison of experimental data with design solution for s/t = 2.3

The plastic regions given by the OxLim analysis with increasing penetration for s/t = 2.3 are shown in Figure 6.15. It is seen that the size of the failure mechanism inferred from the plastic region expands significantly with increasing embedment. Figure 6.15(a) & (b) are at embedment depths shown by the OxLim results in Figure 6.14 to be prior to plugging, whilst at the depth of Figure 6.15(c) plugging has occurred. This is evident in the nature of the mechanisms as in Figure 6.15(c) the mechanism is as might be expected of a solid strip. The grillages at shallower depths show that a different type of mechanism is occurring.

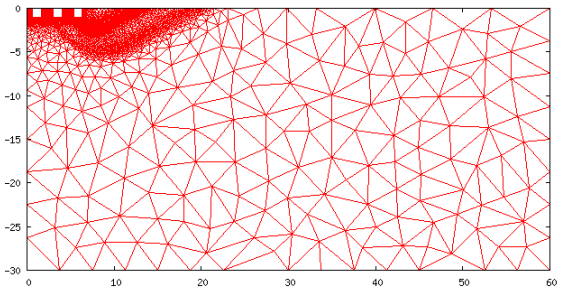

(a) z/(s – t) = 0.7 (z/B = 0.08)

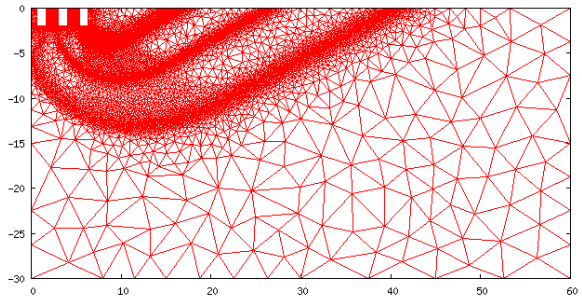

(b) z/(s – t) = 1.5 (z/B = 0.16)

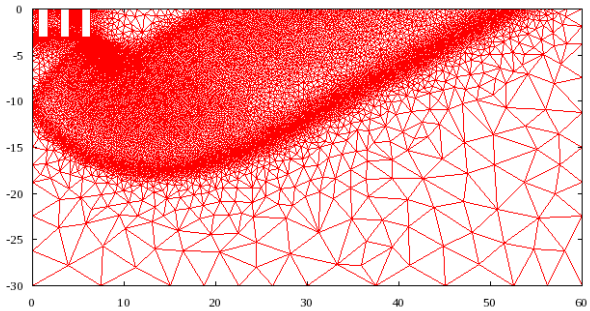

(c) z/(s – t) = 2.2 (z/B = 0.24)

Figure 6.15: Plastic regions for vertically loaded grillage, s/t = 2.3

6.3.2 Combined loading

The response of the grillage foundations to combined *V*:*H*:*M* loading was investigated by undertaking a series of swipe tests on each grillage type. Translational and rotational swipes were completed to explore different regions of the *V*:*H*:*M* load space. Swipes were undertaken at two levels of embedment. Low embedment swipes were undertaken at depths of z = 10 mm or 20 mm, while high embedment swipes were undertaken at z = 40 mm. The results of the swipe tests in the *V*:*H*:*M* plane are shown in Figure 6.16. The results have been normalised against the largest vertical load experienced prior to the swipe, V_0 to enable comparison between test results. Whilst the swipes were completed using pure horizontal translation or pure rotation, as the tests progressed moment is also generated during the translation and horizontal load is generated during rotation. With increased embedment this is seen to become more pronounced.

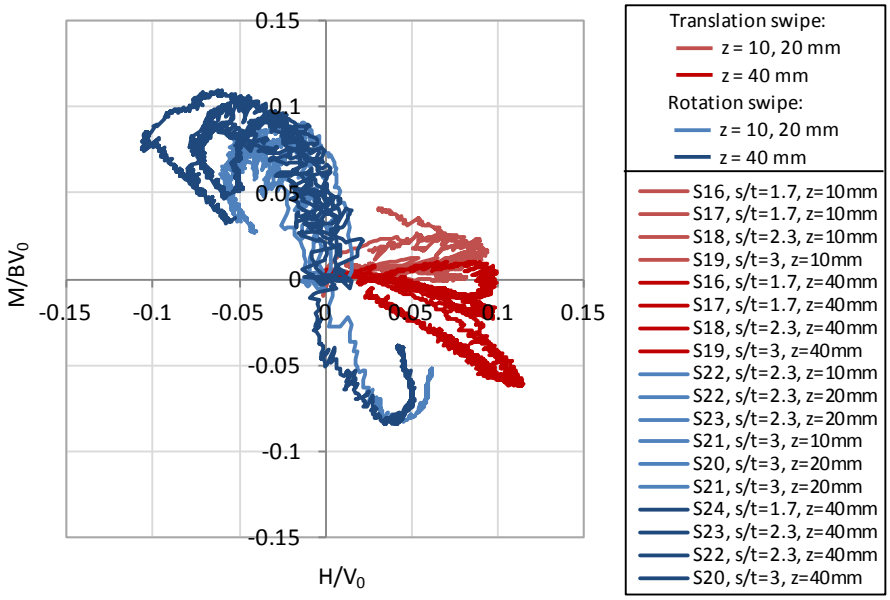

Figure 6.16: Grillage swipe tests in *H*:*M* load space for all level of V/V_0

The results of the swipe tests in the *V*:*H* plane and the *V*:*M* plane are shown in Figure 6.17, in which the penetration depths of the tests have also been identified. In each case it is seen that tests at a greater penetration depth showed a larger normalised failure surface.

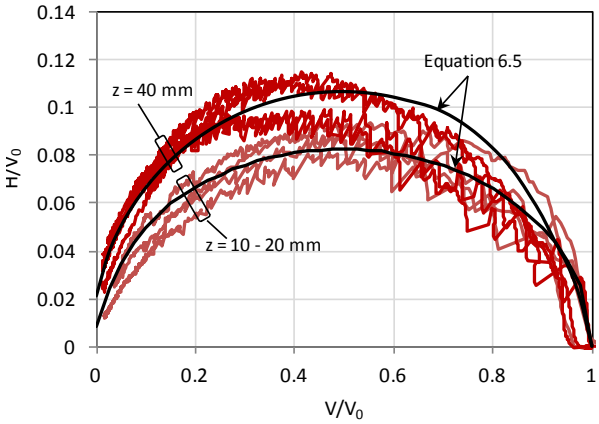

(a) *V*:*H* load space

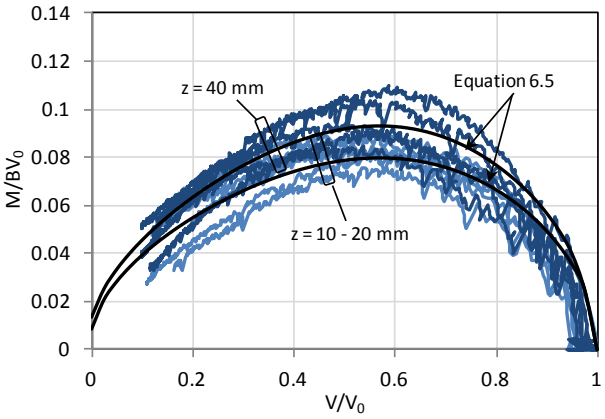

(b) *V*:*M* load space

Figure 6.17: Grillage swipe test results in *H* and *M* load planes

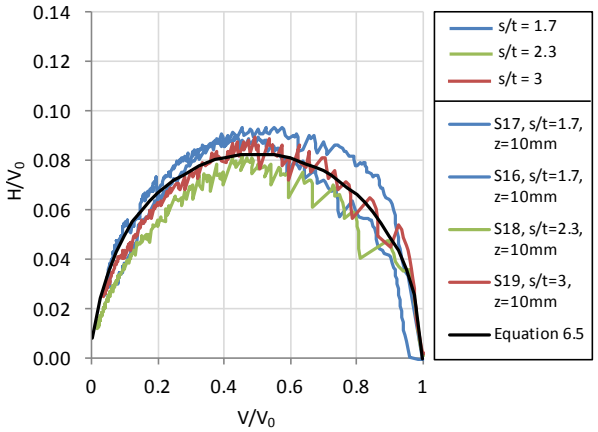

(a) *V*:*H* load space, *z* = 10 – 20 mm

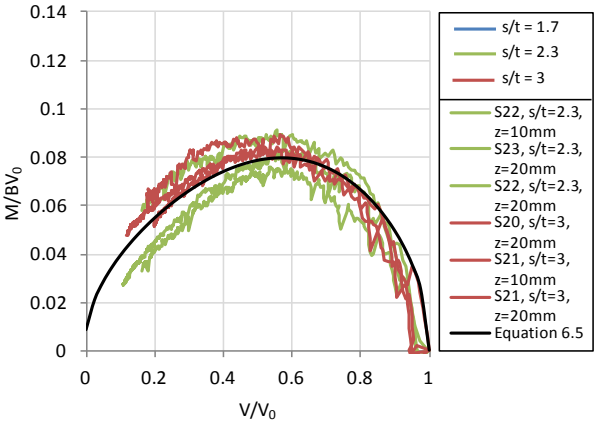

(b) *V*:*M* load space, *z* = 10 – 20 mm

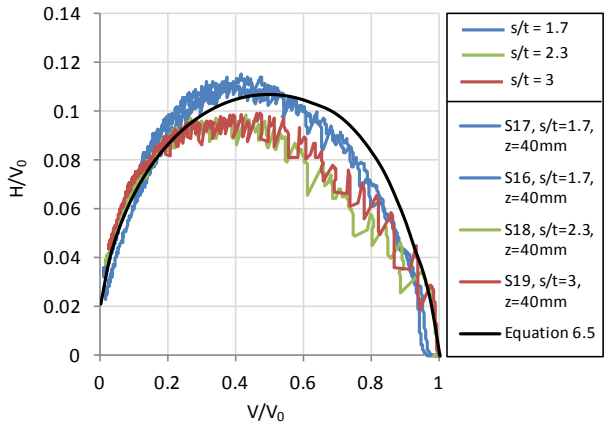

(c) *V*:*H* load space, *z* = 40 mm

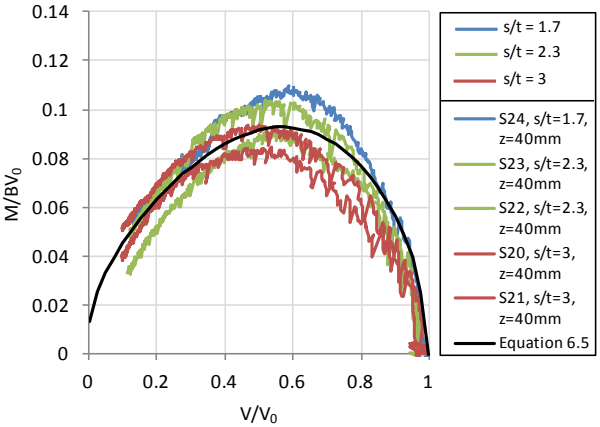

(d) *V*:*M* load space, *z* = 40 mm

Figure 6.18: Comparison of grillage results at different spacing

The experimental data is presented in Figure 6.18 to show the effect of grille spacing on combined loading capacity. Within each penetration depth category, the grillages with lower

s/*t* ratios generally had larger normalised failure surfaces. This might be expected as grillages at lower spacing are closer to the plugged capacity state.

6.3.2.1 Fitted expression for combined loading

Knappett et al. (2012) proposed an expression for the *V*:*H* failure surface of a grillage (Equation 2.24). This was adapted from the *V*:*H*:*M* failure surface expression employed by Martin (1994), following earlier work by Nova & Montrasio (1991). The expression used by Knappett et al. (2012) can be extended to incorporate moment loading as follows:

$$f = \left(\frac{h}{h_0}\right)^2 + \left(\frac{m}{m_0}\right)^2 - 2a\frac{h}{h_0}\frac{m}{m_0} - \beta_{12}(v+\chi)^{\beta_1}(1-v)^{\beta_2} = 0 \tag{6.5}$$

where:

$$\beta_{12} = \frac{(\beta_1+\beta_2)^{(\beta_1+\beta_2)}}{\beta_1^{\beta_1}\beta_2^{\beta_2}(1+\chi)^{(\beta_1+\beta_2)}} \tag{6.6}$$

and $v = V/V_0$, $h = H/V_0$, $m = M/BV_0$. Based on previous foundation studies, the eccentricity of the ellipse in the *H*:*M* plane was taken to be a = -0.22, and the failure surface shaping parameters β_1 and β_2 were both assumed to be 1. A best fit to the swipe data was made to determine the normalised horizontal load capacity h_0, normalised moment capacity m_0 and the uplift capacity parameter χ, values of which are listed in Table 6.4.

Table 6.4: Fitted parameters for Equation 6.5

Penetration depth, z (mm)	h_0	m_0	χ
10 to 20	0.085	0.081	0.005
40	0.11	0.094	0.01

Failure envelopes calculated from Equation 6.5 are shown in Figure 6.17 and are seen to give a reasonable approximation of the experimental failure surface data. In addition, shown in Figure 6.19, the *H*:*M* cross-section through the failure surface at V/V_0 = 0.4 has

been calculated for the shallow penetration range (z = 10 to 20 mm). As expected, the experimental data agrees well with the fitted failure surface of Equation 6.5.

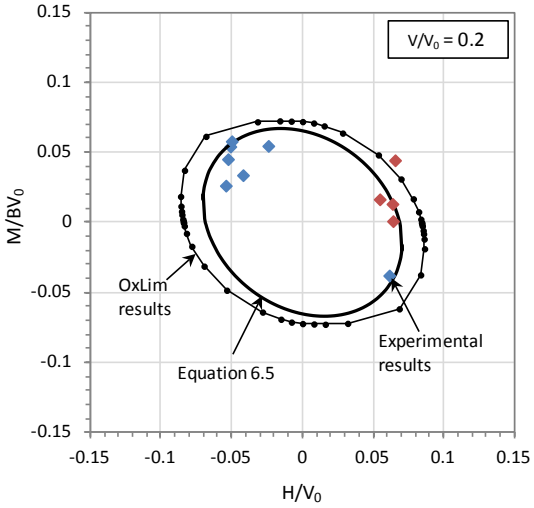

(a) V/V_0 = 0.2

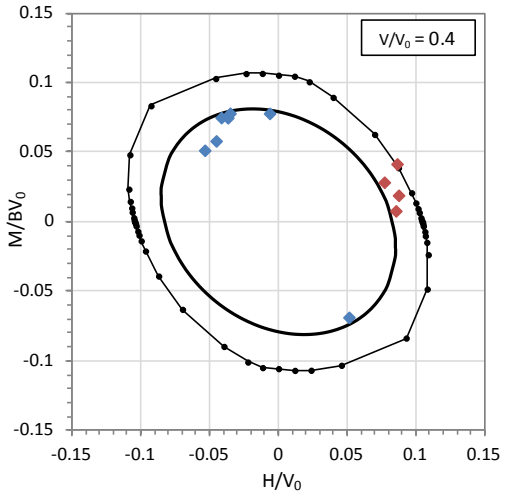

(b) V/V_0 = 0.4

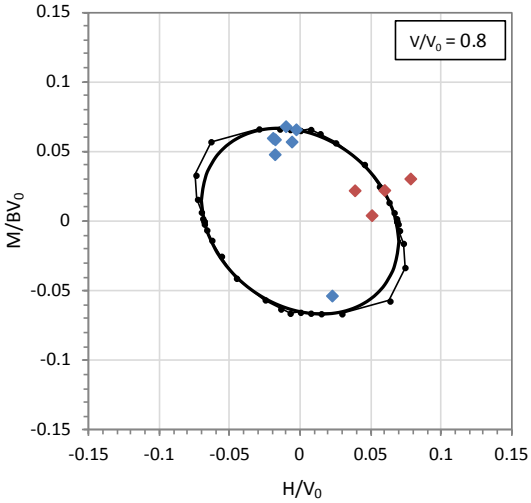

(c) V/V_0 = 0.8

Figure 6.19: Comparison of failure envelope with numerical and experimental data at z = 10 mm, t = 9.5 mm, s/t = 1.7 - 3

A comparison of the design solution given by Equation 6.5 is made with that proposed by Knappett et al. (2012) for V:H loading in Figure 6.20. The result compared from Knappett et al. (2012) is based on a grillage of N = 8, t = 5 mm and s/t = 4 on loose sand at an embedment depth of about z = 38 mm (or z/B = 0.26) and so is similar to tests undertaken in this study. From a best fit of three test data points Knappett et al. (2012) found h_0 = 0.23. This is substantially higher than h_0 = 0.11 which is why a higher capacity is shown in Figure 6.20.

The difference in test results may be a result of differences in the grillage arrangement. Further testing would be useful to help understand the differences obtained.

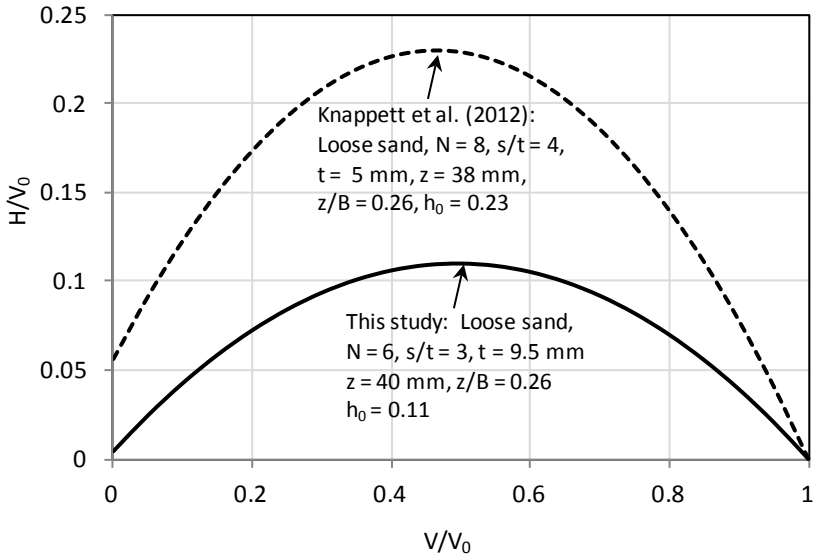

Figure 6.20: Comparison of normalised failure envelopes

6.3.2.2 Comparison with numerical results

OxLim analysis of a grillage foundation under combined loading is compared with the experimental and analytical results in Figure 6.19. The failure envelopes defined by OxLim represent the average of the upper and lower bound solutions, bracketed to an error of less than 5%. The case analysed was of a grillage with s/t = 2.3 at z = 10 mm penetration. At the base of the grilles, $\delta = \phi = 34.3°$ was adopted whilst on the side of the grilles $\delta = 2/3\phi$ was modelled. The results from the OxLim analysis undertaken are seen to broadly confirming the general shape given by Equation 6.5 and by the data. The OxLim results overestimate capacity compared with the experimental results, although the difference reduces as V/V_0 approaches 0 or 1. Adaptively refined OxLim meshes are shown in Figure 6.21 to give examples of grillage combined loading plastic regions for s/t = 2.3 at z = 10 mm embedment. Mechanisms at V/V_0 = 0.4 for the cases of (a) vertical and horizontal loading (M = 0), (b) vertical and moment loading (H = 0) and (c) vertical, horizontal and moment loading where M/H = 1.2.

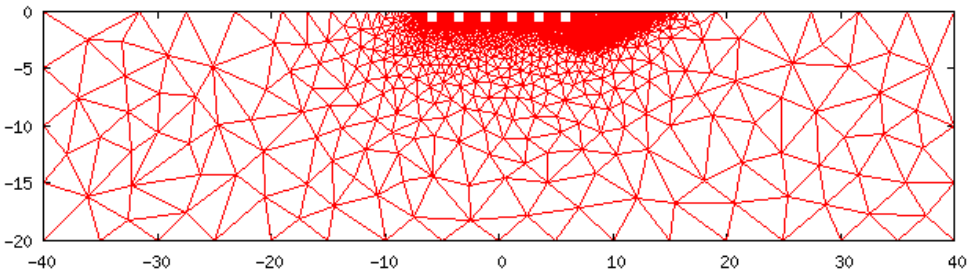

(a) *V*:*H* loading (*M* = 0)

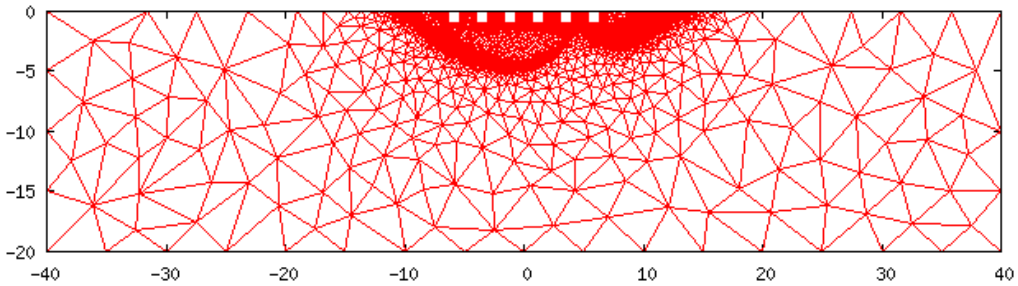

(b) *V*:*M* (*H* = 0)

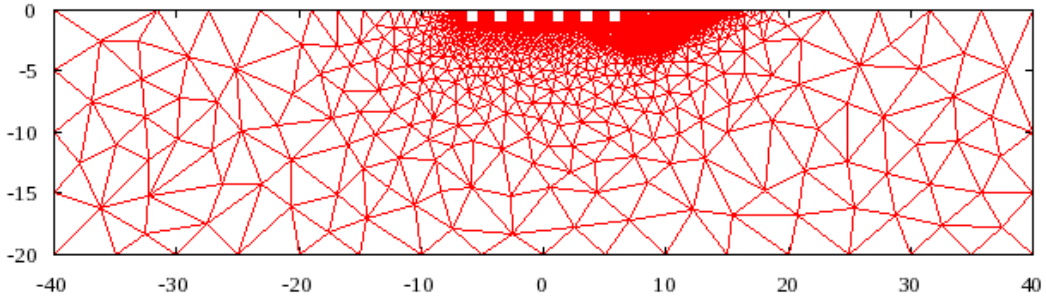

(c) *V*:*H*:*M* loading (*M*/*H* = 1.2)

Figure 6.21: OxLim meshes for grillage of *s*/*t* = 2.3 at *z*/*B* = 0.08 under VHM loading at V/V_0 = 0.4

6.4 Conclusions

This chapter has presented results from a series of vertical and combined loading tests undertaken using a 6 DOF loading rig to explore the vertical capacity and the *V*:*H*:*M* failure surface of grillage foundations on loose sand.

Initial tests investigating the vertical load–penetration response of a single grille element showed good agreement with conventional pile capacity calculations (end bearing

plus side friction, though the latter contribution is small in this case). The OxLim results compared well but slightly under predicted to the vertical capacity results. The *V*:*H*:*M* failure envelope for a strip foundation on sand was also investigated using OxLim. The results matched well with combined loading tests undertaken on a single grill. The shape of the failure envelope defined by OxLim was comparable to results from other experimental studies investigating failure envelopes for foundations on sand.

The main tests were conducted on grillages consisting of six equally spaced grille elements, with the centre-to-centre spacing being varied from 1 (no gap) to 3 times the grille thickness. At shallow penetrations, the grillages with closely spaced grilles were found to have a larger vertical capacity than those with more widely spaced grilles. At deeper penetrations, however, the grillages with more widely spaced grilles (and hence greater overall width) attained higher capacity following the onset of soil plugging, or arching. The analytical expression proposed by Bransby et al. (2011) was found to provide a reasonably good match with the experimental load–penetration curves, although did not reflect the gradual transition to plugged behaviour as observed experimentally and numerically. A new expression for the *V*:*H*:*M* failure envelope of a grillage foundation on loose sand has been proposed, based on the results of swipe tests. Comparative numerical analyses have been performed using the FELA program OxLim. These results were largely found to match quite well with the experimental data, even though FELA assumes rigid plasticity and an associated flow rule (giving excessive dilation for sands).

Chapter 7. Conclusions

This thesis has examined the bearing capacity of perforated offshore foundations. Consideration has been given to combined vertical, horizontal and moment loading conditions which are typical for foundations located offshore. Experimental work and numerical analysis has been undertaken, focusing on ring and square annular foundations on clay, and grillage foundations on sand. The results showed that perforated foundations can be an efficient foundation solution for accommodating combined loading. As a ratio of their vertical load capacity, perforated foundations can withstand higher moment and horizontal loads compared with unperforated foundations. The experimental and numerical results have been used to develop design expressions that could be employed by practitioners to estimate the vertical and combined load bearing capacity of perforated foundations. In this chapter the main findings of the thesis are summarised, and some possible areas for future work are suggested.

7.1 Main findings

The main findings are summarised in four parts in order to address each of the four aims of the thesis as stated in Section 1.2.

7.1.1 Numerical modelling with Tresca plasticity and adaptive meshing

A study was undertaken to indentify an accurate approach for modelling shallow foundations on undrained Tresca soil with finite element analysis (FEA). This was because errors are known to be associated with i) numerical approximations typically used to implement the Tresca criterion, ii) the manner in which the soil body is discretised into finite elements. The central development from this study can be summarised as follows:

1) A UMAT subroutine was developed to implement the Tresca yield criterion in 2D and 3D FEA without the use of any approximation of the yield or plastic potential surfaces. The UMAT was found to closely match known solutions for foundation capacity whereas other approaches involving surface approximations under-predict the solutions. A 2D and 3D adaptive mesh refinement scheme was also developed to reduce the error associated with discretisation of the soil geometry. This automatically refines the soil mesh based on the concentration of plastic shear strain. Validation analyses of circular foundation bearing capacity cases indicated that the combination of the Tresca UMAT and the adaptive meshing function allows the FEA solutions to converge towards the exact solution as the mesh is refined. Previous research had not demonstrated that the proper implementation of the Tresca model could achieve this in FEA.

Other key findings from this work were:

2) The required calculation time when using adaptive meshing compared to manual meshing was assessed. Adaptive meshing was more efficient in 2D analysis for obtaining an error less than about 3%, or in 3D analysis if an error less than about 7% was sought. This assessment disregards the time needed to design the manual mesh, which is not required for the automated adaptive meshing process.
3) The UMAT and adaptive meshing scheme were used to undertake a detailed study of square foundation bearing capacity so that the results could be used in the assessment of perforated foundations. A range of solutions exist in the literature, partly due to uncertainty around the nature of the failure mechanism that occurs. Examination of the refined mesh from the analyses indicated that the mechanism contained four planes of symmetry, including two diagonal planes. Square foundation bearing capacity factors of N_c = 5.44 (smooth interface) and N_c = 5.76 (rough interface) were determined, which are lower than the value of N_c = 6.17 commonly adopted in design codes.

7.1.2 Vertical load capacity of perforated foundations

Finite element analysis was undertaken to investigate the vertical bearing capacity of perforated foundations on clay over a range of perforations ratios, *R*. Centrifuge experiments were also undertaken for comparison, and to investigate skirt penetration resistance during installation and uplift capacity upon extraction. The central finding from this work was:

1) As the perforation ratio *R* increases for a surface perforated foundation the bearing capacity factor N_c was found to decrease. It reduced from N_c for a solid square or circular foundation and approached the value of N_c = 5.14 for a strip. This was the case for all levels of soil heterogeneity examined. With increasing *R* the failure mechanism varied from one where the effective strips interacted covering the width of the foundation to one where each strip acted in isolation. Curve fitting of the numerical results was used to derive a design expression to estimate the capacity of ring and square annular foundations on undrained soil (Equation 4.3). This was done by introducing a perforation ratio factor r_c to adjust the shape factor s_c to account for *R*. The centrifuge results for vertical loading matched well with the numerical results, and therefore were also well described by the expression for vertical capacity.

Other key findings included:

2) When the number of perforations N_p were varied while maintaining the same perforation ratio *R*, similar vertical capacity was achieved. For increasing soil heterogeneity the capacity of the multiple perforation foundations reduced below that for a single perforation (N_p = 1), although the difference was small. As such, it was considered that the design expression based on N_p = 1 (Equation 4.3) could be used to give a reasonable prediction for the capacity of foundations with multiple foundations, at least for cases where $kB/s_{um} \leq 5$.

3) The vertical capacity of a solid circular and square foundation (with R = 0) given by a typical design code DNV (1992) gave mixed results in comparison to the findings from FEA. For increasing soil heterogeneity, DNV (1992) gave a good prediction for circular foundations, except for kD/s_{um} < 2 for a smooth foundation, in which it was unconservative. For square foundations, DNV (1992) was unconservative in all cases. The DNV (1992) results for embedded rough circular and square foundations significantly under predicted the capacity found in FEA.
4) In general, the skirt penetration resistance measured during installation of the skirted perforated foundations in the centrifuge tests compared well with current prediction methods. It was found that using N_c = 9 for end bearing and a side adhesion value of α = 0.3 gave a reasonable match with the experimental results.
5) The uplift capacity of the foundations measured in the centrifuge tests was less than about 40% of the vertical capacity in penetration. This may have been due to the extraction rate being too slow to maintain undrained conditions, as well as soil disturbance from the foundation penetration. The peak foundation pullout load decreased as the perforation ratio increased.

7.1.3 Combined load capacity of perforated foundations

Swipe and pushover centrifuge tests were used to explore the failure envelopes for perforated foundations under combined loading. Finite element analysis was also undertaken for comparison. The main findings from this work can be summarised as follows:

1) The normalised peak horizontal capacity (h_0) increased with increasing perforation ratio R. This may have been as a result of a continuous sliding mechanism occurring across the gross area of the perforated foundations. The normalised peak moment capacity (m_0) increased with increasing R, except for the foundation with R = 0.64 where it reduced. The failure envelopes for perforated foundations were also derived using FEA. With a

full tension assumption the finite element analysis predicted a much higher peak moment capacity than the experimental results. FEA results with a zero-tension interface produced a closer match. A new design expression for the *V*:*H*:*M* failure envelope for perforated foundations has been proposed based on the experimental and numerical results (Equation 5.16). The expression is adapted from Model B (Martin, 1994) for unperforated foundations. Tension capacity is accommodated and the peak horizontal (h_0) and moment (m_0) capacity inputs are based on the perforation ratio *R*. Parameters were assessed for different embedment and interface tension conditions such that the design expression gave a reasonable match with the experimental or numerical results. Further numerical and experimental investigation could help improve the robustness of the design expression.

Other key findings were as follows:

2) Changing the foundation loading direction from 0° loading to 45° loading made minimal difference on the capacity of the foundations as a similar maximum load was obtained in both cases. This indicated that for an estimation of bearing capacity, 3D loading conditions could be simplified into a 2D loading scenario and assessed using more straightforward plane strain calculation approaches.
3) After applying a package of cycling loading to a perforated foundation, a post-cyclic monotonic test was able to reach almost twice the maximum moment load achieved in a stand-alone monotonic test. This may have been a result of consolidation having occurred during the cyclic loading. The vertical foundation displacement at the end of the cycling period was over double the amount that had occurred in the monotonic test.

7.1.4 Vertical and combined load capacity of strip and grillage foundations

Experiments at 1g were undertaken to investigate the vertical and combined load capacity of grillage foundations on loose sand. An initial investigation was also undertaken on the

capacity of a single grille (or strip). Finite element limit analysis (FELA) was also carried out for comparison. The main findings from this analysis are as follows:

1) At shallow penetrations the grillage foundations with closely spaced grilles were found to have a larger vertical capacity than those with more widely spaced grilles. At deeper penetrations the grillages with more widely spaced grilles attained higher capacity following the onset of soil plugging. The analytical expression proposed by Bransby et al. (2011) (Equation 2.23) was found to provide a reasonable match with the experimental load-penetration curves although did not reflect the gradual transition to plugged behaviour as observed experimentally (and numerically). The capacity predicted by the expression was generally conservative compared to the experimental results. For the combined loading swipe tests it was found that more closely spaced grilles generally obtained a higher capacity. A new expression for the *V*:*H*:*M* failure envelope of a grillage foundation on loose sand has been proposed based on the results of swipe tests (Equation 6.5). The shape of the failure envelope is dependent on the embedment depth of the grillage, increasing in size with increased embedment. Comparative numerical analysis results from OxLim were found to match quite well with the experimental data, and therefore the design expression.

Other key findings included:

2) Experimental tests investigating the vertical load–penetration response of a single grille element showed good agreement with conventional pile capacity calculations (end bearing plus side friction, though the latter contribution was small). The OxLim results compared well but slightly under predicted to the vertical capacity results.
3) The *V*:*H*:*M* failure envelope for a strip foundation on sand determined using FELA matched well with combined loading experiments undertaken on a single grille, even though FELA uses an associated flow rule. Whilst *V*:*H*:*M* failure envelopes for

foundations on clay have been extensively explored using numerical analysis, limited work on this had previously been undertaken for foundations on sand.

7.2 Suggested future work

Suggestions for future work coming out of the research presented in this thesis are as follows:

1) The adaptive meshing scheme developed could be updated to incorporate interface elements or contact modelling. This would allow soil-foundation interfaces with limited or no tension to be incorporated, such as was found with the centrifuge experiments. To get around this current limitation the effective width rule was used with the adaptive meshing scheme to model the case of no tension, but this is not a robust approach.
2) The numerical analysis of perforated foundations in this thesis has focused on circular and square perforated foundations. The square foundation represents the case of $B/L = 1$. Future work could examine the case of rectangular foundations in which the ratio B/L is reduced (such as was shown in Figure 3.28). It is likely that the expression for vertical loading of a perforated foundation (Equation 4.3) will still be applicable for rectangular foundation by adjusting the shape factor s_c based on the value of B/L.
3) The centrifuge results indicated the foundations to have limited vertical capacity in uplift and limited tension capacity under combined loading. Future work could examine the tension capacity under vertical and combined loading of perforated foundations in more detail.
4) The perforations examined in this thesis have principally been one central perforation, although consideration has been given to vertical bearing capacity with multiple perforations. More research could be undertaken to explore the effect of the perforated area comprising multiple perforations, particularly for the case of combined loading.

5) Whilst the vertical capacity of ring foundations was examined extensively in this thesis less work was undertaken on moment capacity. Further numerical and experimental work could be undertaken on the combined load capacity of ring foundations specifically.
6) The grillage experimental and numerical work was undertaken on a small section of a grillage with a small number of grilles (N = 6). As grillages in the field have significantly more grilles (N > 100), further work could examine how well the results transfer to a larger number of grilles.
7) The V:H:M design expressions proposed for the perforated and grillage foundations are based on a limited number of experimental and numerical results. Further work would help to refine the inputs used in these expressions.
8) The analysis undertaken in this thesis has predominantly focused on monotonic loading. Further research would be useful to investigate more thoroughly the impact of cyclic loading on bearing capacity.
9) The analysis undertaken in thesis was mostly for the case of 3 degree of freedom loading. Only a few centrifuge tests were undertaken representing additional degrees of freedom. It is suggested that more work is undertaken to understand the response of perforated foundations under 6 degree of freedom loading.

References

Abbo, A. J. & Sloan, S. W. 1995. A smooth hyperbolic approximation to the Mohr-Coulomb yield criterion. *Computers & Structures,* 54**,** 427-441.

Andersen, K. H. 2009. Bearing capacity under cyclic loading - offshore, along the coast and on land. *Canadian Geotechnical Journal,* 46**,** 513-535.

Andersen, L. & Clausen, J. 2009. Comments on "Flow rule effects in the Tresca model" by H.A. Taiebat and J.P. Carter [Computers and Geotechnics 35 (2008) 500–503]. *Computers and Geotechnics,* 36**,** 911-913.

API 2007. Recommended practice for planning, designing and construction of fixed offshore platforms. Washington, DC American Petroleum Institute.

Arup 2009. *Design Yearbook 2009*.

Arup & Clough 2008. ACE Platforms Industry Booklet.

Banimahd, M., Maconochie, A. & Oliphant, J. 2010. Numerical study of grillage foundations on sand under combined VHM loading. *Frontiers in Offshore Geotechnics II*. CRC Press.

Benien, B., Byrne, B. W., Houlsby, G. T. & Cassidy, M. J. 2006. Investigating six degree of freedom loading of shallow foundations on sand. *Geotechnique.*

Bishop, J. F. W. 1953. On the complete solution to problems of deformation of a plastic-rigid material. *Journal of the Mechanics and Physics of Solids,* 2**,** 43-53.

Bolton, M. D. & Lau, C. K. 1993. Vertical Bearing Capacity Factors for Circular and Strip Footings on Mohr-Coulomb Soil. *Canadian Geotechnical Journal,* 30**,** 1024-1033.

Bransby, M. F., Brown, M. J., Knappett, J. A., Hudacsek, P., Morgan, N., Cathie, D., Maconochie, A., Yun, G., Ripley, A. G., Brown, N. & Egborge, R. 2011. Vertical capacity of grillage foundations in sand. *Canadian Geotechnical Journal,* 48**,** 1246-1265.

Bransby, M. F., Knappett, J. A., Brown, M. J. & Hudacsek, P. 2012. The vertical capacity of grillage foundations. *Geotechnique,* 62**,** 201-211.

Bransby, M. F. & Randolph, M. F. 1998. Combined loading of skirted foundations. *Geotechnique,* 48**,** 637-655.

Bransby, M. F. & Randolph, M. F. 1999. The Effect of Embedment Depth on the Undrained Response of Skirted Foundations to Combined Loading. *Soils and foundations,* 39**,** 19-33.

Bransby, M. F. & Yun, G. J. 2009. The undrained capacity of skirted strip foundations under combined loading. *Geotechnique,* 59**,** 115-125.

Brinch-Hansen, J. B. 1970. A revised and extended formula for bearing capacity. *Bulletin of the Danish. Geotechnical Institute.* Copenhagen.

Butterfield, R. & Gottardi, G. 1994. A complete three dimensional failure envelope for shallow footings on sand. *Geotechnique,* 44**,** 181-184.

Byrne, B. W. 2000. *Investigations of suction caissons in dense sand.* DPhil Thesis, University of Oxford.

Byrne, B. W. & Houlsby, G. T. 2005. Investigating 6 degree-of-freedom loading on shallow foundations. *Proc International Symposium on Frontiers in offshore Geotechnics.* Perth Australia.

Cassidy, M. J. 1999. *Non-linear analysis of jack-up structures subject to random waves.* PhD Thesis, University of Oxford.

Cassidy, M. J. & Byrne, B. W. 2001. Drum centrifuge model tests comparing the performance of spudcans and caissons in kaolin clay. University of Oxford.

Cassidy, M. J., Byrne, B. W. & Randolph, M. F. 2004. A comparison of the combined load behaviour of spudcan and caisson foundations on soft normally consolidated clay. *Geotechnique,* 54**,** 91-106.

Clausen, J., Damkilde, L. & Andersen, L. 2006. Efficient return algorithms for associated plasticity with multiple yield planes. *International Journal for Numerical Methods in Engineering,* 66**,** 1036-1059.

Clausen, J., Damkilde, L. & Andersen, L. 2007. An efficient return algorithm for non-associated plasticity with linear yield criteria in principal stress space. *Computers & Structures,* 85**,** 1795-1807.

Das, B. M. & Larbi-Cherif, S. 1983. Bearing capacity of two closely-spaced shallow foundations on sand. *Soils and Foundations***,** 1-7.

Dassault 2009. Abaqus analysis users' manual. Providence, RI, USA: Simula Corp.

Davis, E. H. & Booker, J. R. 1973. The effect of increasing strength with depth on the bearing capacity of clays. *Geotechnique,* 23**,** 551-563.

DNV 1992. Classification notes No.30.4. *Foundations.* Det Norske Veritas.

DNV 2005. Recommended Practice E303:Geotechnical Design and Installation of Suction Anchors in Clay. Det Norske Veritas.

DNV 2009. Recommended Practice DNV-RP-H103. *Modelling and Analyses of Marine Operations.* Norway: Det Norske Veritas.

DNV 2011. Design of Offshore Steel Structures, General (LRFD Method). Det Norske Veritas.

Eason, G. & Shield, R. T. 1960. The plastic indentation of a semi-infinite solid by a perfectly rough circular punch. *Journal of Applied Mathematics and Physics,* 11**,** 33-43.

Edwards, D. H., Zdravkovic, L. & Potts, D. M. 2005. Depth factors for undrained bearing capacity. *Geotechnique,* 55**,** 755-758.

Fedorovski, V. G. 2006. Limiting pressure of rows of strip plates and the "no-force-through" effect. *Soil Mechanics and Foundation Engineering,* 43**,** 85-91.

Finnie, I. M. S. & Randolph, M. F. 1994. Punch-through and liquefaction induced failure of shallow foundations on calcareous sediments. *Seventh International Conference on the Behaviour of Offshore Structures.* Boston: Pergamon.

Fisher, R. & Cathie, D. N. Year. Gravity Based Design For Subsea Structures. *In:* Offshore Site Investigation and Geotechnics 'Diversity and Sustainability'; Proceedings of an International Conference, 2002 London, UK.

Frydman, S. & Burd, H. J. 1997. Numerical Studies of Bearing-Capacity Factor N_γ. *Journal of Geotechnical and Geoenvironmental Engineering,* 123**,** 20-29.

Galloway, M. 2004. *Interaction between adjacent footings in offshore foundation systems.* Final Year Project Report, University of Oxford.

Gottardi, G. & Butterfield, R. 1993. On the bearing capacity of surface footings on sand under general planar loads. *Soils and Foundations,* 33**,** 68-79.

Gottardi, G., Houlsby, G. T. & Butterfield, R. 1999. Plastic response of circular footings on sand under general planar loading. *Geotechnique,* 49**,** 453-469.

Gourvenec, S. 2007a. Failure envelopes for offshore shallow foundations under general loading. *Geotechnique,* 57**,** 715-728.

Gourvenec, S. 2007b. Shape effects on the capacity of rectangular footings under general loading. *Geotechnique,* 57, 637-646.

Gourvenec, S. 2008. Effect of embedment on the undrained capacity of shallow foundations under general loading. *Geotechnique,* 58**,** 177-185.

Gourvenec, S. & Barnett, S. 2011. Undrained failure envelope for skirted foundations under general loading. *Geotechnique,* 61, 263-270

Gourvenec, S., Govoni, L. & Gottardi, G. 2008. An investigation of shallow foundations on sand under moment loading. *Proceedings of the BGA International Conference on Foundations.* Dundee, Scotland.

Gourvenec, S. & Jensen, K. 2009. Effect on embedment and spacing of cojoined skirted foundations systems on undrained limit states under general loading. *International Journal of Geomechanics***,** 267-279.

Gourvenec, S. & Randolph, M. 2003. Effect of strength non-homogeneity on the shape of failure envelopes for combined loading of strip and circular foundations on clay. *Geotechnique,* 53**,** 575-586.

Gourvenec, S., Randolph, M. & Kingsnorth, O. 2006. Undrained bearing capacity of square and rectangular footings. *International Journal of Geomechanics,* 6**,** 147-157.

Gourvenec, S. & Steinepreis, M. 2007. Undrained limit states of shallow foundations acting in consort. *International Journal of Geomechanics,* 7**,** 194-205.

Gourvenec, S. M. & Mana, D. S. K. 2011. Undrained vertical bearing capacity factors for shallow foundations. *Geotechnique Letters,* 1**,** 101 - 108.

Graham, J., Pinkney, R. B., Lew, K. V. & Trainor, P. G. S. 1982. Curve-fitting and laboratory data. *Canadian Geotechnical Journal,* 19**,** 201-205.

Green, A. P. 1954. The plastic yielding of metal junctions due to combined shear and pressure. *Journal of the Mechanics and Physics of Solids,* 2**,** 197-211.

Hansteen, O. E. 1981. Equivalent Geotechnical Design Storm, Unpublished Paper Oslo: Norwegian Geotechnical Institute

Hazell, E. C. J. 2008. *Numerical and experimental studies of shallow cone penetration in clay.* University of Oxford.

Hill, R. 1950. *The mathematical theory of plasticity,* Oxford, Clarendon Press.

Hjiaj, M., Lyamin, A. V. & Sloan, S. W. 2005. Numerical limit analysis solutions for the bearing capacity factor N. *International Journal of Solids and Structures,* 42**,** 1681-1704.

Houlsby, G. T. & Martin, C. M. 2003. Undrained bearing capacity factors for conical footings on clay. *Geotechnique,* 53**,** 513-520.

Houlsby, G. T. & Puzrin, A. M. 1999. The bearing capacity of a strip footing on clay under combined loading. *Proceedings of the Royal Society of London. Series A: Mathematical, Physical and Engineering Sciences,* 455**,** 893-916.

Houlsby, G. T. & Wroth, C. P. 1983. Calculation of Stresses on Shallow Penetrometers and Footings. *Proceedings of the International Union of Theoretical and Applied Mechanics (IUTAM)/International Union of Geodesy and Geophysics (IUGG) Symposium on Seabed Mechanics.* Newcastle upon Tyne.

Hu, Y., Randolph, M. & Watson, P. 1999. Bearing Response of Skirted Foundation on Nonhomogeneous Soil. *Journal of Geotechnical and Geoenvironmental Engineering,* 125**,** 924-935.

Hu, Y. & Randolph, M. F. 1998. H-adaptive FE analysis of elasto-plastic non-homogeneous soil with large deformation. *Computers and Geotechnics,* 23**,** 61-83.

ISO 2003. Petroleum and natural gas industries, Offshore structures. *Part 4: Geotechnical and foundation design considerations (ISO 19901-4:2003).* Genva: International Organisation for Standardisation.

Kardani, M., Nazem, M., Abbo, A., Sheng, D. & Sloan, S. 2012. Refined h-adaptive finite element procedure for large deformation geotechnical problems. *Computational Mechanics,* 49**,** 21-33.

Kelly, A. 2009. Numerical analysis of offshore grillage foundation. Fourth Year Project Report, University of Oxford.

Knappett, J. A., Brown, M. J., Bransby, M. F., Hudacsek, P., Morgan, N., Cathie, D., Maconochie, A., Yun, G., Ripley, A. G., Brown, N. & Egborge, R. 2012. Capacity of grillage foundations under horizontal loading. *Geotechnique,* 62**,** 811-823.

Koiter, W. T. 1953. Stress-strain relations, uniqueness and variational theorems for elastic-plastic materials with a singular yield surface. *Quarterly of Applied Mathematics,* 11**,** 350-4.

Kumar, J. & Ghosh, P. 2007. Ultimate bearing capacity of two interfering rough strip footings. *International Journal of Geomechanics,* 7**,** 53-62.

Kumar, J. & Kouzer, K. M. 2008. Bearing capacity of two interfering footings. *International Journal for Numerical and Analytical Methods in Geomechanics,* 32**,** 251-264.

Lehane, B. M., Gaudin, C., Richards, D. J. & Rattley, M. J. 2008. Rate effects on the vertical uplift capacity of footings founded in clay. *Geotechnique,* 58, 13-21.

Lehane, B. M., O'loughlin, C. D., Gaudin, C. & Randolph, M. F. 2009. Rate effects on penetrometer resistance in kaolin. *Geotechnique,* 59**,** 41-52.

Li, R., Tang, T. & Zhang, P. 2001. Moving Mesh Methods in Multiple Dimensions Based on Harmonic Maps. *Journal of Computational Physics,* 170**,** 562-588.

Li, X., Gaudin, C., Tian, Y. & Cassidy, M. J. 2014. Rate effects on the uplift capacity of skirted foundations on clay. *(Submitted).*

Lieng, J. T. & Bjorgen, H. P. 1995. New flow-through mudmat design for Heidrun subsea structure. *Offshore Technology Conference.* Houston, Texas.

Lyamin, A. V., Salgado, R., Sloan, S. W. & Prezzi, M. 2007. Two- And three-dimensional bearing capacity of footings in sand. *Geotechnique,* 57**,** 647-662.

Mana, D., Gourvenec, S. & Martin, C. 2013. Critical Skirt Spacing for Shallow Foundations under General Loading. *Journal of Geotechnical and Geoenvironmental Engineering,* 139**,** 1554-1566.

Mana, D. S. K., Gourvenec, S. & Randolph, M. F. 2010. A numerical study of the vertical bearing capacity of skirted foundations. *Proc 2nd Int. Sym. on Frontiers in Offshore Geotechnics.* Perth.

Mandel, J. 1963. Interférence plastique de foundations superficielles. *Proc. Int. Conf. on Soil Mechanics.* Budapest.

Martin, C. M. 1994. *Physical and numerical modelling of offshore foundations under combined loads.* University of Oxford.

Martin, C. M. 2001. Vertical bearing capacity of skirted circular foundations on Tresca soil. *Proc. 15th Int. Conference on Soil Mechanics and Geotechnical Engineering.* Istanbul.

Martin, C. M. 2004. User Guide for ABC - Analysis of Bearing Capacity. University of Oxford.

Martin, C. M. 2005. Exact bearing capacity calculations using the method of characteristics. *Proc. 11th Int. Conf. of IACMAG.* Turin.

Martin, C. M. 2010. The rough guide to OxLim, Revision 1. University of Oxford.

Martin, C. M. 2011. The use of adaptive finite-element limit analysis to reveal slip-line fields. *Geotechnique Letters,* 1**,** 23 - 29.

Martin, C. M. & Hazell, E. C. J. 2005. Bearing capacity of parallel strip footings on non-homogeneous clay. *Proc. Int. Symp. on Frontiers in Offshore Geotechnics.* Perth.

Martin, C. M. & Houlsby, G. T. 2000. Combined loading of spudcan foundations on clay: Laboratory tests. *Geotechnique,* 50**,** 325-338.

Martin, C. M. & Houlsby, G. T. 2001. Combined loading of spudcan foundations on clay: Numerical modelling. *Geotechnique,* 51**,** 687-699.

Martin, C. M. & Makrodimopoulos, A. 2008. Finite-Element Limit Analysis of Mohr--Coulomb Materials in 3D Using Semidefinite Programming. *Journal of Engineering Mechanics,* 134**,** 339-347.

Meyerhof, G. G. 1953. The bearing capacity of foundations under eccentric and inclined loads. *Proc. 3rd Int. Conf. SMFE.* Zurich.

Michalowski, R. L. 2001. Upper-bound load estimates on square and rectangular footings. *Geotechnique,* 51**,** 787-798.

Michalowski, R. L. & Dawson, E. M. 2002. Three-dimensional analysis of limit loads on Mohr-Coulomb soil. *Foundations of Civil and Environmental Engineering,* 1**,** 137 - 147.

Michalowski, R. L. & You, L. 1998. Effective width rule in calculations of bearing capacity of shallow footings. *Computers and Geotechnics,* 23**,** 237-253.

Murff, J. D. 1994. Limit analysis of multi-footing foundation systems. *Proceedings of the 8th International Conference on Computer Methods and Advances in Geomechanics. Part 1 (of 4), May 22 - 28 1994.* Morgantown, WV, United states: A.A. Balkema.

Nazem, M., Kardani, M., Carter, J. P. & Sheng, D. 2012. A comparative study of error assessment techniques for dynamic contact problems of geomechanics. *Computers and Geotechnics,* 40**,** 62-73.

Nguyen, V. Q. & Merifield, R. S. 2012. Two- and three-dimensional undrained bearing capacity of embedded footings. *Australian Geomechanics,* 47**,** 25-40.

Nova, R. & Montrasio, L. 1991. Settlements of shallow foundations on sand. *Geotechnique,* 41**,** 243-256.

Pinna, R., Mcrobbie, I., Altraide, B. & Razak, S. 2009. The first Gravity Based Substructure (GBS) for the Caspian Sea. *Proc 4th Offshore Asia Conference.* Bangkok, Thailand.

Potts, D. M. & Zdravkovic, L. 1999. *Finite element analysis in geotechnical engineering: theory,* London, Thomas Telford.

Potts, D. M. & Zdravkovic, L. 2001. *Finite element analysis in geotechnical engineering: application,* London, Thomas Telford.

Prandtl, G. 1921. Eindringungsfestigkeit und festigkeit von schneiden. *Agnew. Math. U. Mech.,* 1**,** 15-20.

Puzrin, A. M. & Randolph, M. F. 2003. New planar velocity fields for upper bound limit analysis. *International Journal of Solids and Structures,* 40**,** 3603-3619.

Randolph, M. F., Cassidy, M. J., Gourvenec, S. & Erbrich, C. 2005. Challenges of offshore geotechnical engineering. *International symposium on frontiers in offshore geotechnics.* Perth.

Randolph, M. F., Leong, E. C. & Houlsby, G. T. 1991. One-dimensional analysis of soil plugs in pipe piles. *Geotechnique,* 41**,** 587-598.

Randolph, M. F. & Puzrin, A. M. 2003. Upper bound limit analysis of circular foundations on clay under general loading. *Geotechnique,* 53, 785-796.

Salencon, J. 2008. Two- and three-dimensional bearing capacity of footings in sand. *Geotechnique,* 58**,** 609-610.

Salencon, J. & Matar, M. 1982. Bearing Capacity of Circular Shallow Foundations. *Journal de mecanique theorique et appliquee,* 1**,** 237-267.

Salencon, J. & Pecker, A. 1995a. Ultimate bearing capacity of shallow foundations under inclined and eccentric loads. Part I: purely cohesive soil. *European journal of mechanics. A, Solids,* 14**,** 249-275.

Salencon, J. & Pecker, A. 1995b. Ultimate bearing capacity of shallow foundations under inclined and eccentric loads. Part II: purely cohesive soil without tensile strength. *European journal of mechanics. A, Solids,* 14**,** 377-396.

Salgado, R., Lyamin, A. V., Sloan, S. W. & Yu, H. S. 2004. Two- and three-dimensional bearing capacity of foundations in clay. *Geotechnique,* 54**,** 297-306.

Schneider, J., Randolph, M., Mayne, P. & Ramsey, N. 2008. Analysis of Factors Influencing Soil Classification Using Normalized Piezocone Tip Resistance and Pore Pressure Parameters. *Journal of Geotechnical and Geoenvironmental Engineering,* 134**,** 1569-1586.

Shewchuk, J. R. 2002. Delaunay refinement algorithms for triangular mesh generation. *Computational Geometry,* 22**,** 21-74.

Shield, R. T. 1955. On the Plastic Flow of Metals under Conditions of Axial Symmetry. *Proceedings of the Royal Society of London. Series A, Mathematical and Physical Sciences,* 233**,** 267-287.

Shield, R. T. & Drucker, D. C. 1953. The application of limit analysis to punch-indentation problems. *Journal of Applied Mechanics,* 20**,** 453-460.

Si, H. 2011. *Tetgen: a quality tetrahedral mesh generator and three-dimensional Delaunay triangulator* [Online]. Available: http://tetgen.org.

Skempton, A. W. 1951. The bearing capacity of clays. *Proc. Building and Research Congress.* London.

Sloan, S. W. & Booker, J. R. 1986. Removal of singularities in Tresca and Mohr-Coulomb yield functions. *Communications in Applied Numerical Methods,* 2**,** 173 - 179.

Stewart, D. P., Boyle, R. F. & Randolph, M. F. 1998. Experience with a new drum centrifuge. *Proc. Int. Conf. Centrifuge '98.* Tokyo.

Stuart, J. G. 1962. Interference between foundations, with special reference to surface footings in sand. *Geotechnique***,** 15 - 22.

Taiebat, H. A. & Carter, J. P. 2000. Numerical studies of the bearing capacity of shallow foundations on cohesive soil subjected to combined loading. *Geotechnique,* 50**,** 409-418.

Taiebat, H. A. & Carter, J. P. 2002. Bearing capacity of strip and circular foundations on undrained clay subjected to eccentric loads. *Geotechnique,* 52**,** 61-64.

Taiebat, H. A. & Carter, J. P. 2008. Flow rule effects in the Tresca model. *Computers and Geotechnics,* 35**,** 500-503.

Taiebat, H. A. & Carter, J. P. 2009. Reply to 'Comments on "Flow rule effects in the Tresca model" by H.A. Taiebat and J.P. Carter [Computers and Geotechnics 35 (2008) 500–503] by L. Andersen and J. Clausen'. *Computers and Geotechnics,* 36**,** 914.

Tan, F. S. C. 1990. *Centrifuge and theoretical modelling of conical footings on sand.* PhD Thesis, University of Cambridge.

Tani, K. & Craig, W. 1995. Bearing capacity of circular foundations on soft clay of strength increasing with depth. *Journal of the Japanese Geotechnical Society: soils and foundation,* 35**,** 21-35.

Terzaghi, K. 1943. *Theoretical Soil Mechanics*, John Wiley & Sons, Inc.

Tindall. 2013. *Atlas CTB: raising wind turbines to a whole new level* [Online]. Available: http://www.atlasctb.com/index.html.

Tuturea, D. P. & Jackson, G. 2002. Hang Tuah: Self-Installing, Relocatable Compression Platform. *Offshore Technology Conference.* Houston, Texas.

Ukritchon, B., Whittle, A. J. & Klangvijit, C. 2003. Calculations of Bearing Capacity Factor N[sub gamma] Using Numerical Limit Analyses. *Journal of Geotechnical and Geoenvironmental Engineering,* 129**,** 468-474.

Ukritchon, B., Whittle, A. J. & Sloan, S. W. 1998. Undrained limit analyses for combined loading of strip footings on clay. *Journal of Geotechnical and Geoenvironmental Engineering,* 124**,** 265-276.

Vesic, A. S. 1973. Analysis of Ultimate Loads of Shallow Foundations. *Journal of the Soil Mechanics and Foundations Division,* 99**,** 45-73.

Villalobos, F. 2006. *Model testing of foundations for offshore wind turbines.* DPhil Thesis University of Oxford.

Watson, P. G. 1999. Performance of skirted foundations for offshore structures. PhD thesis, The University of Western Australia.

Watson, P. G. & Humpheson, C. 2007. Foundation design and installation of the Yolla A Platform. *Proc of Offshore Site Investigation and Geotechnics.* London, UK: Society of Underwater Technology.

Westgate, Z. J., Tapper, L., Lehane, B. M. & Gaudin, C. 2009. Modelling the installation of stiffened caissons in overconsolidated clay. *Proc. 28th ASME 28th International Conference on Ocean, Offshore and Arctic Engineering.*

White, D. J., Maconochie, A. J., Cheuk, C. Y., Bolton, M. D., Joray, D. & Springman, S. M. 2005. An investigation into the vertical bearing capacity of perforated mudmats. *Proc Int. Sym. on Frontiers in Offshore Geotechnics.* Perth.

Yun, G. & Bransby, M. F. 2007. The undrained vertical bearing capacity of skirted foundations. *Soil and foundation,* 47**,** 493-505.

Zienkiewicz, O. C., Taylor, R. L. & Zhu, J. Z. 2005. *The Finite Element Method: Its Basis and Fundamentals,* Butterworth-Hienemann.

Zienkiewicz, O. C. & Zhu, J. Z. 1987. A simple error estimator and adaptive procedure for practical engineering analysis. *International Journal for Numerical Methods in Engineering,* 24**,** 337-357.

Zienkiewicz, O. C. & Zhu, J. Z. 1991. Adaptivity and mesh generation. *International Journal for Numerical Methods in Engineering,* 32**,** 783-810.